



University of Udine
Polytechnic Department of Engineering and
Architecture

Ph.D. degree in Industrial and Information
Engineering

Ph.D. Thesis

New Methodology for Automatic Process Parameters Optimization in Selective Laser Melting

Candidate:
Thomas De Monte

Supervisor:
Dott. Ing. Giovanni Totis

Thesis submitted in 2021

Ai miei figli.

Acknowledgements

Desidero ringraziare il Prof. Giovanni Totis ed il Prof. Marco Sortino per il supporto, la disponibilità ed il prezioso aiuto che mi hanno saputo fornire in questi anni, anche a distanza, visto il particolare periodo storico che stiamo vivendo.

Ringrazio inoltre tutti i colleghi e collaboratori per avermi dato la possibilità di svolgere un percorso di dottorato ricco di confronti stimolanti e di piacevoli momenti di convivialità.

Un doveroso ringraziamento va ai miei genitori Hildegard e Luciano, senza i quali non avrei mai neppure cominciato questa carriera.

Infine, il ringraziamento più caloroso va alla mia compagna Eva, a mia figlia Rose ed al futuro membro della nostra famiglia, del quale aspettiamo con gioia l'arrivo.

Abstract

Selective laser melting is one of the most promising additive manufacturing technologies, thanks to its capability to manufacture complex shaped parts with good dimensional accuracy and high mechanical performance. In recent years, this technique is starting to be adopted for the production of end-use parts, addressing high quality requirements.

To achieve the desired quality of the final product it is necessary to optimize the process parameters, possibly by reducing the build time needed for its production. However, the currently available process optimization methodologies are very time consuming and there is a lack of standards.

The aim of this work is to develop an automatic, reliable and objective process optimization technique, which can be employed to find optimal parameters combinations for different process conditions.

Therefore, it has been developed an experimental approach, based on single tracks analysis and on 3D benchmarks characterization. The main novelty of this optimization method is the automatization of samples analysis, which entailed the adoption of innovative surface metrology techniques and of novel algorithmic frameworks developed in MATLAB environment.

According to the novel method, the effects of laser power (P), scan speed (v) and laser spot size (d_s) have been investigated for the two most used materials; the extra-low-interstitial grade of Ti6Al4V alloy and the 316L stainless steel. Hence, P - v optimal combinations has been defined for each spot size level investigated, finding a first optimal region in single tracks analysis and then identifying the optimal parameter set for 3D components production.

This methodology has allowed the definition of multiple optimal parameter sets in an automatic way, limiting time and material waste. Therefore, it can be adopted in all existent production strategies that require more than one process parameter set and could allow the development of new production approaches.

Contents

Introduction	1
1 Metal AM - Powder-Bed Fusion Processes	3
1.1 History of Additive Manufacturing	3
1.2 Available Metal AM Technologies	5
1.2.1 Laser Powder Bed Fusion (LPBF)	7
1.2.2 Electron-Beam Powder Bed Fusion (EPBF)	10
1.2.3 Comparison Between SLM and EBM	11
1.3 AM Process Chain	12
1.3.1 Input Data	12
1.3.2 Build Job Preparation and Slicing	14
1.3.3 Additive Fabrication Process and Post-Processing	19
1.4 Process Advantages, Limitations, and Applications	20
2 Selective Laser Melting	25
2.1 SLM Process Workflow	25
2.2 Lasers	26
2.3 Materials	36
2.3.1 Powder Properties	36
2.3.2 Powder Production	39
2.3.3 Powder Recycling	41
2.4 Process Parameters	42
2.5 Melt Pool Physics	49
2.5.1 Rayleigh-Plateau Instability & Balling effect	51
2.5.2 Marangoni Convection	56
2.5.3 Recoil Pressure & Keyhole	59
3 Preliminary Investigation on Small Laser Spot Size	65
3.1 Introduction to process parameters optimization	65
3.2 Materials and Methods	68
3.3 Results and Discussion	71
3.3.1 Morphological classification	71
3.3.2 Track Geometry Measurements	74
3.3.3 Microstructure	74

3.3.4	Microhardness	76
3.3.5	Final Remarks	76
4	New Methodology for Process Parameters Optimization	79
4.1	Introduction	79
4.2	Equipment - Optical Profilometry	82
4.2.1	Imaging Confocal Microscopy	84
4.2.2	Focus Variation	85
4.2.3	Coherence Scanning Interferometry	86
4.3	General Methodology	87
4.4	Design of Experiments	91
4.4.1	Single Tracks DoE	92
4.4.2	3D Benchmarks DoE	95
5	Single Tracks Analysis	99
5.1	Single Tracks Recognition	99
5.1.1	Input Data	99
5.1.2	Point Cloud Pre-Processing	102
5.1.3	Segmentation Algorithm	103
5.1.4	Point Cloud Post-Processing	106
5.2	Single Tracks Classification	108
5.2.1	Input Data	108
5.2.2	Refined Segmentation Algorithm	109
5.2.3	Single Tracks Profile Analysis	111
5.3	Results & Discussion	115
5.3.1	Single Track Melting Efficiency Curve	115
5.3.2	Critical Speed Curve & Optimal Parameter Sets	117
5.3.3	Algorithm Performance	118
6	3D Benchmarks Characterization	125
6.1	Input Data	125
6.2	Profile Roughness	128
6.2.1	Point Cloud Pre-Processing	128
6.2.2	Ra Measurements	129
6.3	Areal Waviness	131
6.3.1	Point Cloud Pre-Processing	131
6.3.2	Wa Measurements	136
6.4	Boundary Characterization	138
6.4.1	Point Cloud Pre-Processing	138
6.4.2	Boundary Detection	138
6.4.3	Edges Error Computation	139
6.5	Relative Density	142
6.6	Optimal Parameter Sets	144
	Conclusions	151

List of Figures

1.1	Altitude in the painted desert in Arizona (US). The fine grained rock layers that make up these mountains contain abundant iron and manganese compounds which provide the pigments for the various colors of the region [73].	3
1.2	Cover picture of The Economist (february 10, 2011) [129].	5
1.3	AM technologies for metal components [31].	6
1.4	PBF processes binding mechanisms [38].	7
1.5	Laser-based powder bed fusion technology [138].	9
1.6	Electron-beam-based powder bed fusion technology [6].	10
1.7	AM workflow from product idea to actual component [130, 29].	13
1.8	STL file features.	15
1.9	Typical STL errors [53].	16
1.10	Examples of support structures.	18
1.11	Slicing process.	18
1.12	Metal AM process.	19
1.13	Cost vs. Complexity in AM processes and in conventional manufacturing [31].	20
1.14	Seven lattice topologies: (a) body-centred cube (BCC); (b) body-centred cube with vertical struts (BCCz), (c) gyroid, (d) matrix phase of D-gyroid, (e) face centred cube (FCC), (f) face centred cube with vertical struts (PFCC), (g) Boolean combination of BCC and FCC (F2BCC) [101].	22
1.15	Various components produced through SLM technology in the <i>LAMA^{FVG}</i> laboratory, representing some applications of metal AM.	23
2.1	SLM process workflow.	25
2.2	Phenomena describing the interaction between electrons and photons [108].	27
2.3	Scheme of a generic laser system.	28
2.4	(a) Laser beam propagation after a focusing lens and, (b) typical fiber laser beam intensity profile (Gaussian distribution).	29
2.5	Light absorptivity at different wavelengths of various materials [24].	30
2.6	Scheme of a generic fiber laser pumped with a laser diode.	32
2.7	Schematic representation of the <i>varioSCAN</i> unit [115].	33
2.8	Schematic illustration of the dynamic focusing unit operation [152].	34

2.9 Influence of the convergent and divergent nature of the laser beam on the melt pool morphology [93].	35
2.10 Absorptivity of 316L steel with a $100\mu m$ powder layer compared to the absorptivity of a bare disc at $v = 100mm/s$ (a) and $1500mm/s$ (b) [134].	36
2.11 Visualization of the relationships between powder properties, bulk powder behaviour, powder performance in process and finally the manufactured part quality as elaborated by different research groups [139].	37
2.12 Schematic representation of gas atomization process [97].	40
2.13 Example of SEM images showing characteristic morphologies of stainless steel powder: (a) gas atomized; (b) water atomized [77].	41
2.14 SLM process parameters classification [155].	43
2.15 Schematic representation of the interaction between laser beam and powder bed.	44
2.16 Top view of laser melted tracks from SS316L powder on steel substrate. Thickness of the deposited powder layer h varies in the range $0 \div 400\mu m$, laser power is $50W$ and scan speed varies in the range $0.04 \div 0.28m/s$ [148].	45
2.17 Effect of hatch distance on relative density of AlSi10Mg parts [2].	46
2.18 Different continuous exposure strategies.	47
2.19 Different layer exposure strategies.	48
2.20 Alternative scanning strategies.	49
2.21 Schematic representation of the general phenomena in the SLM process [22].	50
2.22 Water dropping from a tap [159].	51
2.23 Segmental cylinder of a liquid on the substrate: (a) non-disturbed; (b) disturbed [148].	52
2.24 SEM images showing the balling characteristics of single scan tracks under different scan speeds [76].	53
2.25 LPBF process map indicating the zones of instabilities [43].	54
2.26 Surface topologies of SS 316L simulated tracks with varying viscosities. (a) to (d) were fabricated with zero viscosity, with processing parameters of (a) $100W$ and $0.4m/s$, (b) $200W$ and $0.8m/s$, (c) $300W$ and $1.2m/s$, (d) $400W$ and $1.6m/s$. (e) was achieved with a viscosity of $2 \times 10^{-2} kg m^{-1} s^{-1}$, a power of $400W$ and scan speed of $1.6m/s$ [128].	55
2.27 Schematic representation of how “tears of wine” are generated by the Marangoni effect [23].	56
2.28 Schematic representation of the effect of surface tension gradient due to temperature gradient on the free surface of a liquid [114] (a), and of melt convection pattern in the melt pool [26] (b).	57
2.29 Marangoni convection in a weld pool: (a,b,c) low-sulfur steel, (d,e,f) high-sulfur steel [61].	58
2.30 Marangoni convection with an outward surface flow in a $NaNO_3$ pool (a), and Marangoni convection with an inward surface flow in a $NaNO_3$ pool containing $2mol\%$ C_2H_5COOK as a surface-active agent (b) [61].	58

2.31 (a) Melt pool shapes and temperature field during the keyhole collapse and porosity formation [25]; (b) Metallographic cross sections of a single track affected by keyhole porosity [59].	60
2.32 Longitudinal cross section of a single track produced with SLM technology. Voids arising from keyhole mode melting can be observed near the bottom of the melt pool [59].	61
2.33 An illustration of conduction mode (A), transition mode (B), and keyhole mode (C) melt pools in terms of the vaporized region shape [105].	61
3.1 Thermal stresses (a) when a new layer is produced and (b) when the new layer cools down [10]; (c) thermal warping during SLM fabrication of an overhanging surface [141].	66
3.2 Schematic representation of single track, multi-tracks and 3D benchmark production.	67
3.3 Characterization of Ti6Al4V powder: (a) morphology inspected by SEM; (b) particle size distribution; (c) metallographic analysis [136].	69
3.4 Design of experiments [136].	70
3.5 Schematic representation of single track scanning operation [136].	71
3.6 (a) Top view of a single track with typical defects and (b) cross section measurements, where the Heat Affected Zone is also visible [136].	72
3.7 (a) Examples of top and cross-section views of representative single tracks and (b) process map obtained [136].	72
3.8 Box plot of the (a, b) width, (c, d) depth, (e, f) height, and (g, h) contact angle of the track at different laser power and scanning speed levels [136].	73
3.9 (a) Width, (b) depth, (c) height, and (d) contact angle of the single tracks. The scan speed axis is oriented from right to left [136].	74
3.10 Microhardness trend with respect to (a) laser power, (b) scanning speed, and (c) measurement location [136].	75
3.11 Lateral face topographies of lattice structures produced with two different process parameter sets.	76
4.1 Quality descriptors for 3D benchmarks found in the literature.	79
4.2 (a) <i>Sensofar S neox Five Axis</i> ; (b) Optical schematics of a microdisplay scan confocal microscope [92].	83
4.3 Digital Micro-mirror Device [87].	83
4.4 Example of confocal microscopy image of an SLMed surface, where the slits pattern can be seen.	84
4.5 Schematic diagram of the focus variation technology [100].	85
4.6 Images of interference fringes on a curved surface with low coherence illumination [69].	86
4.7 CSI signal for a single pixel showing the modulation envelope [69].	87
4.8 Flowchart of the proposed methodology.	90
4.9 (a) Particle size distribution and (b) SEM image of SS316L powder.	92
4.10 Single tracks layout on build platform. Light-blue labels are the identification marks of the baseplates.	93

4.11 Single tracks DoE for one level of laser spot size.	95
4.12 (a) 3D benchmarks layout on build platform; (b) Factorial design applied for each spot level.	96
4.13 Design of experiments for Ti6Al4V.	97
4.14 Design of experiments for SS316L.	98
5.1 (a) Build chamber during the production of the baseplates; (b) Setup for topographies acquisition.	99
5.2 Flow chart of the methodology for single tracks analysis.	100
5.3 (a) Scanning preview of the 3D optical profiler; (b) Example of a point cloud saved as a TXT file.	101
5.4 Point cloud before and after levelling operation.	102
5.5 Two representative results of points height segmentation.	103
5.6 High points distribution of (a) a point cloud that includes a single track and, (b) a point cloud that includes only the substrate.	105
5.7 Example of a process map obtained from single track recognition.	106
5.8 (a) Filtering operation on high points and, (b) alignment operation result.	107
5.9 Cropping operations along (a) x-axis and, (b) y-axis.	108
5.10 (a) High points distribution and, (b) (y,z) view of a single track point cloud.	110
5.11 Example of single track recognition with new segmentation algorithm.	111
5.12 (a) Profile extraction and, (b) profile resampling operation.	112
5.13 Spectrum of (a) a discontinuous track profile and, (b) a continuous one.	113
5.14 (a) Example of a manual process map (result of an operator's analysis) and, (b) same process map obtained from the algorithm.	115
5.15 (a) Experimental and analytical angular coefficients of melting efficiency and, (b) discrepancy between experimental threshold and analytical one.	117
5.16 (a) Track width trend as the laser spot size varies and, (b) maximum values of v_{cr} curves for the various experiments performed.	118
5.17 Representation of the computation dataset selected through <i>Mersenne Twister</i> algorithm.	119
5.18 Accuracy function obtained by sliding e_{th} over the entire E_b -vector.	119
5.19 Melting efficiency curves at various laser spot size levels and different ma- terials.	121
5.20 Manual and automatic process maps obtained from Ti6Al4V data analysis.	122
5.21 Manual and automatic process maps obtained from SS316L data analysis.	123
6.1 (a) Build chamber during removal of residual powder and, (b) setup for topographies acquisition.	125
6.2 Scanning preview of the 3D optical profiler for (a) high magnification mea- surements and, (b) low magnification measurements.	126
6.3 Flow chart of the methodology for 3D benchmarks characterization.	127
6.4 Flow chart of profiles elaboration.	128
6.5 Raw profiles processing.	129
6.6 Box plots of roughness data as a function of spot diameter, laser power and scan speed for (a) Ti6Al4V and, (b) SS316L.	130

6.7 Roughness maps for Ti6Al4V benchmarks.	130
6.8 Roughness maps for SS316L benchmarks.	130
6.9 Surface topography before and after levelling operation.	132
6.10 Surface topography divided into two areas: the central area and the peripheral area.	133
6.11 Surface topography two-step denoising operation.	133
6.12 Topography points distribution along X axis and Y axis.	134
6.13 Surface topography before and after fill-holes algorithm application.	135
6.14 Surface topography before and after 2D Gaussian filtering ($\lambda_c = 2.5mm$ cut-off).	135
6.15 Simplified flow chart of surfaces elaboration.	136
6.16 Box plots of waviness data as a function of spot diameter, laser power and scan speed for (a) Ti6Al4V and, (b) SS316L.	136
6.17 Areal waviness maps for Ti6Al4V benchmarks.	137
6.18 Areal waviness maps for SS316L benchmarks.	137
6.19 (a) Point cloud boundary detection through <i>alpha shape</i> disk [33] and, (b) example of boundary detection on cubic samples topography.	139
6.20 Computation of edges lines.	140
6.21 Representation of the distance between boundary points and the regression line. The average value represents the edges error.	141
6.22 Box plots of edges error data as a function of spot diameter, laser power and scan speed for (a) Ti6Al4V and, (b) SS316L.	141
6.23 Edges error maps for Ti6Al4V benchmarks.	142
6.24 Edges error maps for SS316L benchmarks.	142
6.25 Schematic representation of the Archimedes method [7].	142
6.26 Box plots of relative density data as a function of spot diameter, laser power and scan speed for (a) Ti6Al4V and, (b) SS316L.	143
6.27 Relative density maps for Ti6Al4V benchmarks.	144
6.28 Relative density maps for SS316L benchmarks.	144
6.29 Quality factor maps for Ti6Al4V benchmarks (all data were included).	146
6.30 Quality factor maps for SS316L benchmarks (all data were included).	146
6.31 Quality factor maps for Ti6Al4V benchmarks. Only the data that satisfied $RD > 99\%$ and $Wa(i) > 2 \times mean(Ra)$ were considered.	147
6.32 Quality factor maps for SS316L benchmarks. Only the data that satisfied $RD > 99\%$ and $Wa(i) > 2 \times mean(Ra)$ were considered.	147

List of Tables

1.1	Features of different PBF machines [12].	11
2.1	Specifications of representative lasers for metal-AM [70].	31
3.1	Chemical composition of Ti6Al4V powder used for the experiments [136].	69
3.2	Process parameters used for the production of baseplates and single tracks [136].	69
3.3	Analysis of variance and interpolating models of the geometric features. μ_ε and σ_ε are the systematic and random relative errors, respectively [136].	75
4.1	State-of-the-Art summary table of methodologies for process parameters optimization. The main quality descriptors adopted in each work are reported.	80
4.2	Chemical composition of SS316L used for the experiments.	92
4.3	Process parameters used for the production of baseplates and single tracks.	93
4.4	Process parameters used for the production of Ti6Al4V 3D benchmarks.	97
4.5	Process parameters used for the production of SS316L 3D benchmarks.	98
5.1	Physical properties of the employed materials.	116
6.1	Comparison between Concept Laser default parameters and optimal parameters obtained with the proposed methodology.	149

Introduction

In recent years, metal additive manufacturing (Metal AM) technologies has drawn much attention as they combine high design freedom with the excellent mechanical performance of metal alloys. Among them, powder bed fusion (PBF) processes are the most used techniques in industry and, in the last decades, it has been done plenty of research. In particular, selective laser melting (SLM) is highly appreciated as it allows to produce high-performance components with good dimensional accuracy and with a better surface finish than other available AM technologies. Despite extensive work done so far by researchers and industry, there are still many improvements to be made and new materials still need to be developed. It should be remembered that this technology was released just two decades ago. Therefore, the process optimization still plays an important role today and various methodologies can be found in the literature. However, the complex physics inherent in SLM process poses great challenges in identifying general rules that interconnect process parameters, the melting process and the resulting properties of the fabricated components. For this reason, many authors based their optimization method on experimental investigations, relying on a design of experiments (DoE) approach. Although the obtainable results are consistent, the main issues of this methodology lie in the long time for production and analysis of the data and the material consumption. Another problem is related to the lack of standardised methods to objectively evaluate the process outcome. Indeed, each author defined his own methodology, making it often difficult to compare the various studies. To overcome to some extent these criticalities, an automatic, reliable and objective process optimization method has been developed in this work. Basically, the presented methodology was based on an experimental approach, which included both single tracks and 3D benchmarks production. Then, an advanced characterization of SLM surfaces has been carried out through the adoption of optical surface metrology techniques. In addition, some novel algorithmic frameworks were developed in order to automatize the specimens analysis and objectively find the optimal parameter sets for various laser spot diameters and different materials. Hence, various novel quality descriptors, for both single tracks and 3D benchmarks, were proposed, making the parameters optimization more repeatable and quantifying some geometric aspects that are complementary to the classical outputs considered in the literature.

Therefore, this dissertation is structured as follows:

- **Chapter 1:** The first chapter provides a brief introduction to metal additive manufacturing, focusing on the main two powder bed fusion processes. The AM process chain is then discussed, and the main advantages, limitations and applications of metal AM are briefly reported;

- **Chapter 2:** The second chapter is dedicated to selective laser melting, reporting an extensive state of the art. In this chapter are discussed: Laser technology, powder properties, process parameters and the main physical phenomena that occur during SLM production;
- **Chapter 3:** The third chapter describes a preliminary investigation on small laser spot size. In this work, a complete characterization of single tracks is presented. Although the experiments were carried out in an operational condition which has been never investigated before, the characterization method was developed referring to the main works found in the literature;
- **Chapter 4:** The fourth chapter gives a general description of the novel optimization method found, providing all the information necessary to introduce the following chapters. In addition, a section has been dedicated to introduce the optical metrology techniques adopted for specimens analysis;
- **Chapter 5:** The fifth chapter shows the algorithmic framework for automatic single tracks analysis. There is an extensive description of each step carried out, as well as the discussion of the obtained results;
- **Chapter 6:** The sixth chapter extensively describes the framework for 3D benchmarks characterization, involving various quality descriptors (some of which are new). Lastly, an overall quality factor has been proposed and optimal parameter sets have been determined for each material investigated.

Chapter 1

Metal AM - Powder-Bed Fusion Processes

Everything you can imagine, the nature has already created it.

Albert Einstein

1.1 History of Additive Manufacturing



Figure 1.1: Altire in the painted desert in Arizona (US). The fine grained rock layers that make up these mountains contain abundant iron and manganese compounds which provide the pigments for the various colors of the region [73].

The general term “Additive Manufacturing” (AM) refers to all those technologies that create physical objects by successive addition of material, on the basis of a geometrical representation. More specifically, in 2015 the ISO/ASTM standards define AM as the “process of joining materials to make parts from 3D model data, usually layer upon layer, as opposed to subtractive manufacturing and formative manufacturing methodologies” [50].

Although the idea of additive manufacturing (AM) is thought to have originated about 150 years ago (with proposals to build freeform topographical maps and photosculptures from 2D layers [48]), it can find an even older foundation. If we think about how sedimentary rocks are made, they are composed of layers [74]. Layers of organic or inorganic material deposited by exogenous agents (water, wind, ice, etc.) and cemented by chemical reactions between minerals and water. This very slow process has been happening before our eyes every day for millennia.

However, the development of modern AM processes historically began in 1951 with the patent of John Otto Munz, concerning a system very similar to the present-day stereolithography.

Between the 1960s and 1970s many concepts and patents concerning AM technologies were filed, thanks to research efforts and the development of computers, CAD/CAM systems, numerical control machine tools, new materials and commercial availability of lasers. The main patents filed were Swainson’s 1968 patent on photopolymerization, Ciraud’s 1972 patent on powder bed fusion technology, Nakagawa’s 1979 patent on sheet lamination and in the same year Housholder deposited one on selective laser sintering (SLS) [48, 130].

Although interest in AM technologies was high, no commercial solutions were achieved at that time. The main problems were the excessive cost of laser technology, the insufficient calculation power of computers and the printer production time was very high [41].

It was not until 1986 that Charles Hull and R. Fried founded 3D Systems company and in 1987 launched SLA-1, the first commercial AM production system based on stereolithography [126].

In the following years, an increase in patents filed and publications on AM techniques occurred and, new technologies were available on the market, such as fused deposition modelling (FDM) produced by Stratasys, laminated object manufacturing (LOM) produced by Helisys and selective laser sintering (SLS) produced by DTM. A metal-processing version of the latter technology was marketed by EOS (Germany) in 1995.

Metal powder-bed fusion technologies (full melting) were patented in the late 90s: the selective laser melting (SLM) technology patented by the Fraunhofer Institute (Aachen - Germany) in 1995 and, the electron beam melting (EBM) technique patented by the Swedish company Arcam in 1997. These two production systems were subsequently released in 2005 and 2006 respectively [126]. Thanks to the increasing interest in AM and the expiration of older patents, with the new millennium there has been a considerable expansion of available AM systems, opening the market to competition. Since the 1980s, continuous innovation and improvement of processes and products have enabled the evolution of AM applications, which has occurred in four phases [112]:

- **Rapid Prototyping**

- **Rapid Tooling**
- **Rapid Manufacturing** (or Direct Manufacturing)
- **Home Fabrication**

Therefore, it has moved from the production of conceptual or functional prototypes, to the manufacture of fixtures and tools, and then to the production of final parts. The latter phase is of great impact in many industrial sectors, such as aerospace, military, medical, dental, etc.

On the other hand, the home fabrication is similar to rapid manufacturing, but it involves consumers (or end-users) manufacturing objects themselves using 3D printing equipment they have at home. This last step is happening right now thanks to the significant reduction in the prices of commercial hobby printers (mainly FDM printers, but also photopolymerization technology can be bought cheaply).

The evolution of AM applications is making Additive Manufacturing a design paradigm in addition to a means of production.

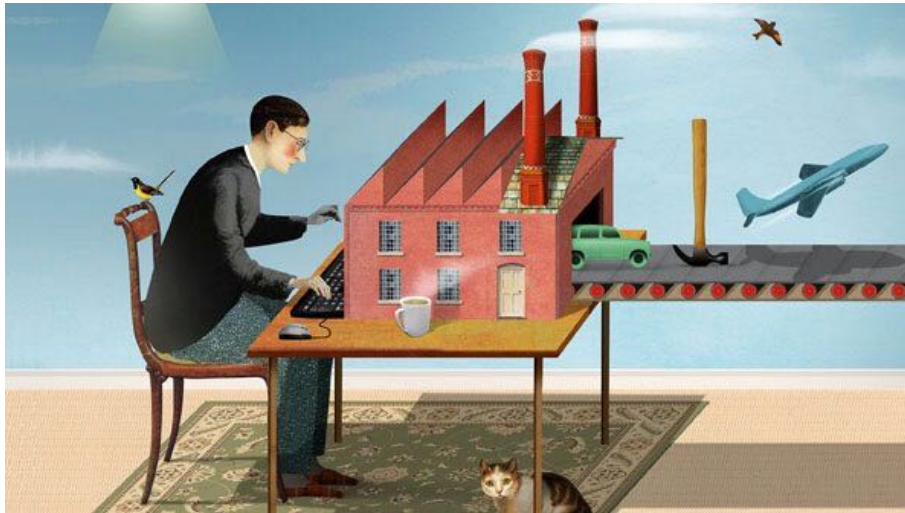


Figure 1.2: Cover picture of The Economist (february 10, 2011) [129].

1.2 Available Metal AM Technologies

Nowadays there are many 3D printing technologies, some of which have different business names that define the same production principle. However, the international ISO standard has provided clarity by defining the seven families of existing AM processes: binder jetting, directed energy deposition, material extrusion, material jetting, powder bed fusion, sheet lamination, and vat polymerization [51].








In addition to these process categories, there are production systems that integrate AM techniques (hybrid technologies) or combine them with other processes creating longer

multi-stage process chains. For example, molds can be produced by alternating printing and machining operations, parts can be printed to near net shape and then post-machined, features can be printed on top of formed components, and parts can be embedded within printed objects [130].

As can be seen in Figure 1.3, only four of the seven available technologies allow metal processing:

- **Powder Bed Fusion (PBF)** - A heat source selectively fuses regions of a powder bed;
- **Direct Energy Deposition (DED)** - A focused heat source is used to fuse materials by melting as the material is deposited;
- **Sheet Lamination (LOM)** - Sheets of material are bonded to form an object;
- **Binder Jetting (BJ)** - Liquid bonding agent is selectively deposited to join powder material;

Of these, the first two metal AM processes (PBF and DED) are the most used in industry, so much so that metal AM is often broadly classified in these two groups [12, 31] (Figure 1.3). In addition, both can be further classified according to various criteria.

Additive manufacturing technologies			
TECHNOLOGY	MATERIALS	TYPICAL MARKETS	RELEVANCE FOR METAL
 Powder bed fusion – Thermal energy selectively fuses regions of a powder bed	Metals, polymers	Prototyping, direct part	●
 Directed energy deposition – Focused thermal energy is used to fuse materials by melting as the material is deposited	Metals	Direct part, repair	◐
 Sheet lamination – Sheets of material are bonded to form an object	Metals, paper	Prototyping, direct part	◑
 Binder jetting – Liquid bonding agent is selectively deposited to join powder material	Metals, polymers, foundry sand	Prototyping, direct part, casting molds	◑
 Material jetting – Droplets of build material are selectively deposited	Polymers, waxes	Prototyping, casting patterns	○
 Material extrusion – Material are selectively dispensed through a nozzle or orifice	Polymers	Prototyping	○
 Vat photopolymerization – Liquid photopolymer in a vat is selectively cured by light-activated polymerization	Photopolymers	Prototyping	○

AM technologies for metal objects

Figure 1.3: AM technologies for metal components [31].

As the topic is very broad, the following will briefly describe only the PBF technologies (which contain the technique examined in this dissertation).

The main classification criterion for PBF technologies is the energy source, which can be of two types: laser based or electron beam based [12, 31].

Regardless of the energy source, PBF processes generally occur in an inert atmosphere or in partial vacuum to protect powder and molten material from oxidation. A coating mechanism or roller takes the processing material from the powder feeder and deposits a

thin powder layer (called powder bed).

According to the geometry of the first cross-section of the part (first layer), afterwards an energy source selectively melts the already laid powder. When the first layer is scanned, the build platform goes downward by a defined layer thickness and the coating system deposits another powder layer. This cycle is repeated layer-by-layer, until the complete 3D object is produced. At the end of the process, the component is immersed in the unprocessed powder and the part is not visible until the latter is removed [12].

This basic description of the manufacturing process refers to each powder fusion technology. Clearly each technique has its own features and will be briefly discussed in the following paragraphs.

1.2.1 Laser Powder Bed Fusion (LPBF)

The first LPBF technology developed was selective laser sintering, which was originally used for the production of plastic prototypes by exploiting a point-wise laser scanning technique. Over the years, this approach has been extended to other materials, such as metals and ceramics, and many technically different variants have been developed. Each new PBF technology developer introduced its own terminology to name the process (most popular names include the word “sintering” or “melting”), leading to ambiguities.

Uncertainty about terminology is linked to the existence of four different fusion mechanisms: solid state sintering, chemically induced binding, liquid phase sintering and full melting (Figure 1.4). On the basis of powder characteristics and of energy input utilized, each PBF technology can adopt any mechanism, often even more than one [38].

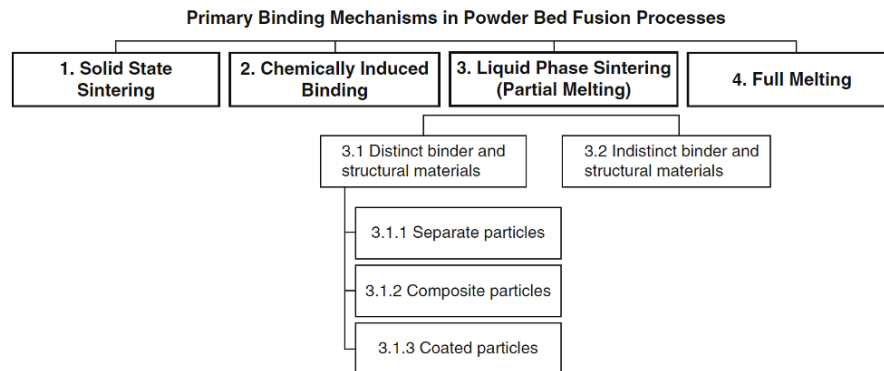


Figure 1.4: PBF processes binding mechanisms [38].

The first fusion mechanism, solid state sintering, refers to the classic meaning of sintering, which is the fusion of powder particles without melting at elevated temperatures (generally between the half of absolute melting temperature and the melting temperature). The main mechanism behind sintering is matter diffusion between packed powder particles, which causes the typical sinter necking. To achieve very low porosity of the resulting material, long sintering time is required. Accordingly, only few PBF techniques use solid state sintering as a primary fusion mechanism.

Chemically induced binding is the second fusion mechanism, and it's based on thermally activated chemical reactions between two types of powders or between powders and gas atmosphere to form a by-product which binds the powder together. Generally, the materials involved in this fusion mechanism are ceramic powders (SiC , ZrB_2 , AlN , etc.), and the resulting component is characterised by high part porosity. Thus, post-process infiltration or high-temperature furnace sintering is often needed to achieve better mechanical performance. However, the use of chemically induced binding in commercial machines is limited by these post-processing operations, as they're expensive and time-consuming. The third mechanism is the liquid phase sintering, or partial melting, which consists of melting a portion of constituents within a collection of powder particles, while another portion remains solid. There are many ways in which this mechanism can be utilized in PBF processes:

- **Separate particles** – A combination of binder and structural powder particles are mixed together and then processed;
- **Composite particles** – Both the binder and the structural material are contained within each powder particle;
- **Coated particles** – Structural powder particles are coated with the binder material;
- **Indistinct mixtures** – No distinct binder or structural materials are present. In metals, this is possible by melting smaller powder particles and the outer regions of larger ones without melting the entire structure, or by melting only lower-melting-temperature constituents in an alloyed structure (this was the method used in the early EOS Direct Metal Laser Sintering machines).

The latest fusion mechanism, as well as the most commonly associated with PBF technologies for metal alloys processing, is full melting. During the process, the energy source completely melts the material to a depth greater than the layer thickness. Therefore, also a portion of the previously solidified layer is re-melted, creating a well-bonded, highly dense and high-performance part [38]. Indeed, rapid melting and subsequent rapid solidification lead to unique mechanical performance of the components, which are different from those of cast or wrought parts and, in many cases, are more desirable.

The most common commercial LPBF processes that make use of full melting are “Selective Laser Melting” (SLM), “Direct Metal Laser Sintering” (DMLS) and “Laser Cusing” (“Cusing” comes from the abbreviation of the term “concept” and the word “fusing” [12]). This dissertation will focus on these technologies that can fully melt metal powder materials by using a laser energy source. From now on, these processes will be referred to as SLM. A representative scheme of the SLM technique is shown in Figure 1.5.

Most of these processes use one or more fiber lasers of 200W to 1kW as energy source to melt the powder material. The output laser beam is diverted to the powder bed through a galvanometric mirror system, whose inertia may limit the scanning speed during the process. Depending on the material and the process parameters (e.g. laser power, scanning speed and beam spot size), the dimension of the melt pool can vary between 0.1 and 0.5mm. So minimum feature size is around $0.1 \div 0.2mm$. The accuracy of the process is

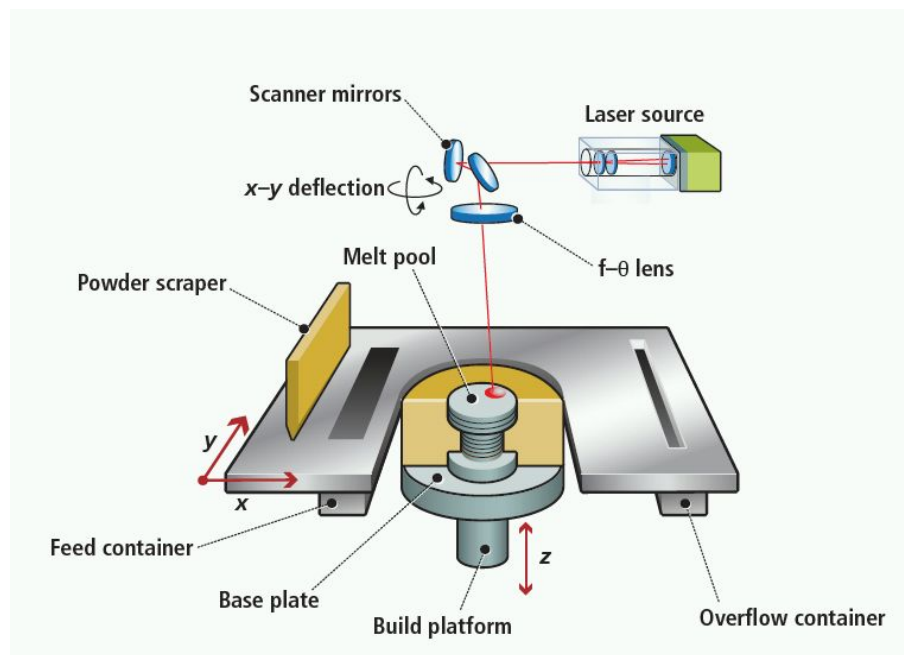


Figure 1.5: Laser-based powder bed fusion technology [138].

approximately 0.1mm , while the surface roughness of the components produced can vary between 4 and $11\mu\text{m}$, depending on surface slope relative to the growth direction [12].

Another parameter that affects the parts quality is the layer thickness, which can vary between 20 and $100\mu\text{m}$, depending on the size and distribution of the powders (generally, particle fraction varies between 10 and $60\mu\text{m}$ [139]).

Because of rapid heating and cooling of the powder layer, the produced parts are characterized by residual stresses. To reduce thermal gradients during the process, many machine manufacturers have developed powder preheating systems, such as special build platforms with heating elements inside that can bring powders to $100 \div 200^\circ\text{C}$. Nevertheless, a post heat treatment of produced parts is typically required.

In general, the build chamber is provided with inert atmosphere of argon gas, reaching oxygen values of 0.1% during production. For nonreactive materials, also nitrogen gas can be used. As will be discussed below, limiting the oxygen content during production is critical to achieve high-performance components.

Dimensions of a medium-sized machine is $250 \times 250 \times 325\text{mm}^3$, so producible components are medium-small sized. The largest industrial machine currently reaches $800 \times 400 \times 500\text{mm}^3$ (Concept Laser X Line 2000R) with multi-laser technology [37], but the cost of these machines is still very high.

Finally, LPBF processes are generally characterised by low build rates of $5 \div 20\text{cm}^3/\text{hour}$. However, using the latest versions of multi-laser technique, it is possible to achieve build rates up to $100\text{cm}^3/\text{hour}$ [12].

1.2.2 Electron-Beam Powder Bed Fusion (EPBF)

Another PBF process is electron beam melting (EBM) in which the powder bed layer is selectively melted by an electron beam in a vacuum chamber. A representative scheme of the EBM technique is shown in Figure 1.6.

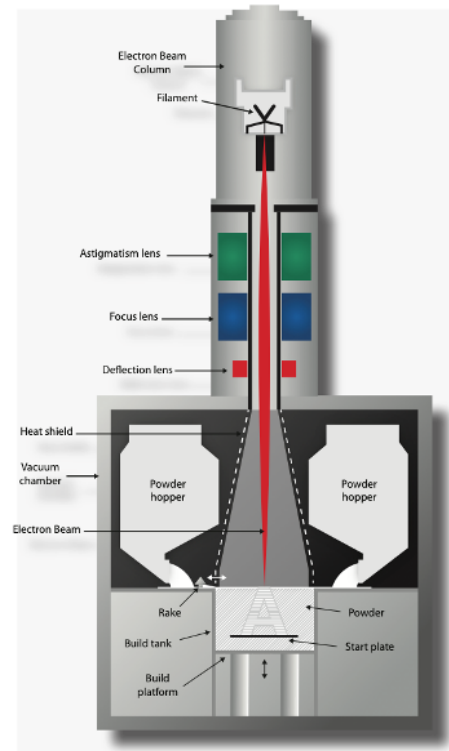


Figure 1.6: Electron-beam-based powder bed fusion technology [6].

The main characteristic of EBM is the energy source: a heated tungsten filament emits a stream of electrons moving near the speed of light. The electron beam is then focused and deflected magnetically by the focus coil and the deflection coil.

Since magnetic coils have an almost immediate response, an electron beam can be moved instantaneously ($1 \div 10\text{km/s}$ max speed) from one point to another without needing to traverse the area in-between [38]. The resulting high scanning speeds allow the EBM technology to reach high build rates, up to $80\text{cm}^3/\text{hour}$.

Generally, an EBM energy source ranges from 1 to 3kW : when the voltage difference is applied to the heated filament, the electrical energy is converted into the electron beam very efficiently. When electrons come in contact with the powder particles, their kinetic energy is converted in thermal energy and the powder bed melts.

The melt pool size varies from 0.2 to 1.2mm depending on the material and the process parameters, such as beam current and scan speed. Consequently, the minimum feature size and accuracy are generally worse than SLM ($100\mu\text{m}$ and $0.2 \div 1.2\text{mm}$ respectively). Even the achievable surface roughness of produced parts is high; R_a ranges typically from

1.2. Available Metal AM Technologies

Manufacturer	Model	Energy Source	Build Volume [mm]	Build Rate [cm^3/hr]	Scan Speed [m/s]
EOS	EOS M400	1 kW fiber laser	400 x 400 x 400	NA	7
EOS	EOSM280 / M290	200 W or 400 W fiber laser	250 x 250x 325	5÷20	7
SLM Solution	SLM 500HL	2x400 W lasers and 2x100 W lasers (optional)	500 x 250 x 325	Up to 70	Up to 15
SLM Solution	SLM 280	400 W and 1000 W (optional) lasers	280 x 280 x 350	20÷35	Up to 15
Concept Laser	M2 Cusing	200 W or 400 W fiber laser	250 x 250 x 280	2÷20	7
Renishaw	SLM 500	200 W or 400 W fiber laser	250 x 250 x 300	5÷20	7
ARCAM	Q 10	3000 W electron beam	200 x 200 x 180	Up to 80	1000 max
ARCAM	Q 20	3000 W electron beam	350 x 380	Up to 80	1000 max

Table 1.1: Features of different PBF machines [12].

50 to $200\mu m$ [12].

To avoid deflections due to the interaction of electrons with gas atoms at atmospheric pressure, the whole process takes place under high vacuum. Another characteristic of EBM is that the powder bed must be conductive to absorb electrons. Therefore, only powders of conductive materials, such as metals, can be used. Because of repulsive forces of neighboring negatively charged particles, the mean powder particle size is generally higher in EBM with respect to SLM (varies from 50 to $150\mu m$). Thus, the layer thickness has higher values, ranging from 50 to $100\mu m$ [139].

With respect to thermal stresses, the parts produced with EBM technique are characterized by residual stresses (similarly to SLM), due to the rapid heating and cooling of the powder layer. However, by scanning in two stages the powder bed, it is possible to reduce thermal gradients very effectively [12, 38]. Indeed, by defocusing the electron beam and scanning very rapidly the entire powder bed, it can be preheated evenly to any pre-set temperature (typically $700 \div 1100^\circ C$ [139]).

After the pre-heating stage, a low current beam with low scan speed is used in the melting stage. Thanks to this strategy, it is possible to significantly reduce the thermal gradients and therefore also the residual stresses within produced parts (generally, no post heat treatment is required).

Typical build volume of an EBM machine can vary between $200x200x180mm^3$ and $350x380mm^3$ ($\varnothing x H$). Hence, the dimension of parts that can be produced by this technology is medium-small. Details of some PBF machine models are given in the Table 1.1.

1.2.3 Comparison Between SLM and EBM

SLM and EBM technologies are both based on the PBF technique, but there are some substantial differences that can be summarized as follows:

- Thanks to the almost instantaneous response of magnetic coils, EBM has in general higher build rates with respect to SLM. For instance, in the production of truss-like structures (lattice structures), the immediate electron beam motion from one location to another can considerably speed up the component fabrication [38];
- On the other hand, the use of an electron beam does not allow to achieve the same dimensional accuracy as a laser, and even the surface quality is much lower [12];
- In EBM, the process takes place under high vacuum, which reduces thermal convection, thermal gradients, and avoids contamination and oxidation of the melt pool

and the powder bed. In contrast, SLM uses an inert gas environment that avoids the oxygen content in the process chamber and removes the vaporized powder condensates;

- Another difference relates to the preheat systems that these technologies use. In the SLM, the preheating temperature of the powder bed is generally low and therefore the parts undergo strong thermal gradients during the process. Thus, thermal post-treatments are needed to reduce residual stresses. On the other hand, in EBM the pre-set temperature is much higher (thanks to the pre-heating scanning stage) and no thermal post-treatment is needed;
- The pre-heating stage of EBM allows to hold powder particles together, which can act as support structures for overhanging surfaces. Thus, in EBM less supports are needed with respect to SLM;
- Moreover, by maintaining the powder bed at an elevated temperature, the typical EBM part microstructure is characterized by larger grain size than SLM one. This clearly has an effect on mechanical properties, which are slightly different for the two technologies. The tensile strength of SLM samples is typically greater than the one of EBM samples; whereas the ductility is lower.

Both technologies have advantages and disadvantages, but the most common technique currently is SLM, due to its better accuracy, flexibility and lower machine cost with respect to EBM.

1.3 AM Process Chain

As mentioned above, there are many AM technologies available and each has its own operating principle. However, each of these techniques has in common a general process chain, which can be seen in Figure [1.7](#). The main steps of the work flow will be clarified in the following paragraphs.

1.3.1 Input Data

Each metal additive manufacturing process starts with a virtual CAD 3D model [\[29, 130\]](#). Generally, a product idea can be modelled directly using any CAD software. Due to the typical geometric complexity of AM parts, there is a growing interest in free-form modelling software, although classic feature-based modelling is often used (whose principles are related to subtractive technologies).

The AM chain can also start from a set of 2D images like those obtained from medical computed tomography (CT) scans. The stack of CT images is typically stored in Digital Imaging and Communications in Medicine (DICOM) format, which is a standard for handling, storing, printing, and transmitting information in medical imaging [\[91\]](#). The 3D reconstruction consists in transforming rectangular or cubic (voxel) data into curved data [\[89\]](#). All images are filtered first, reducing noise and increasing both sharpness and contrast (image enhancement).

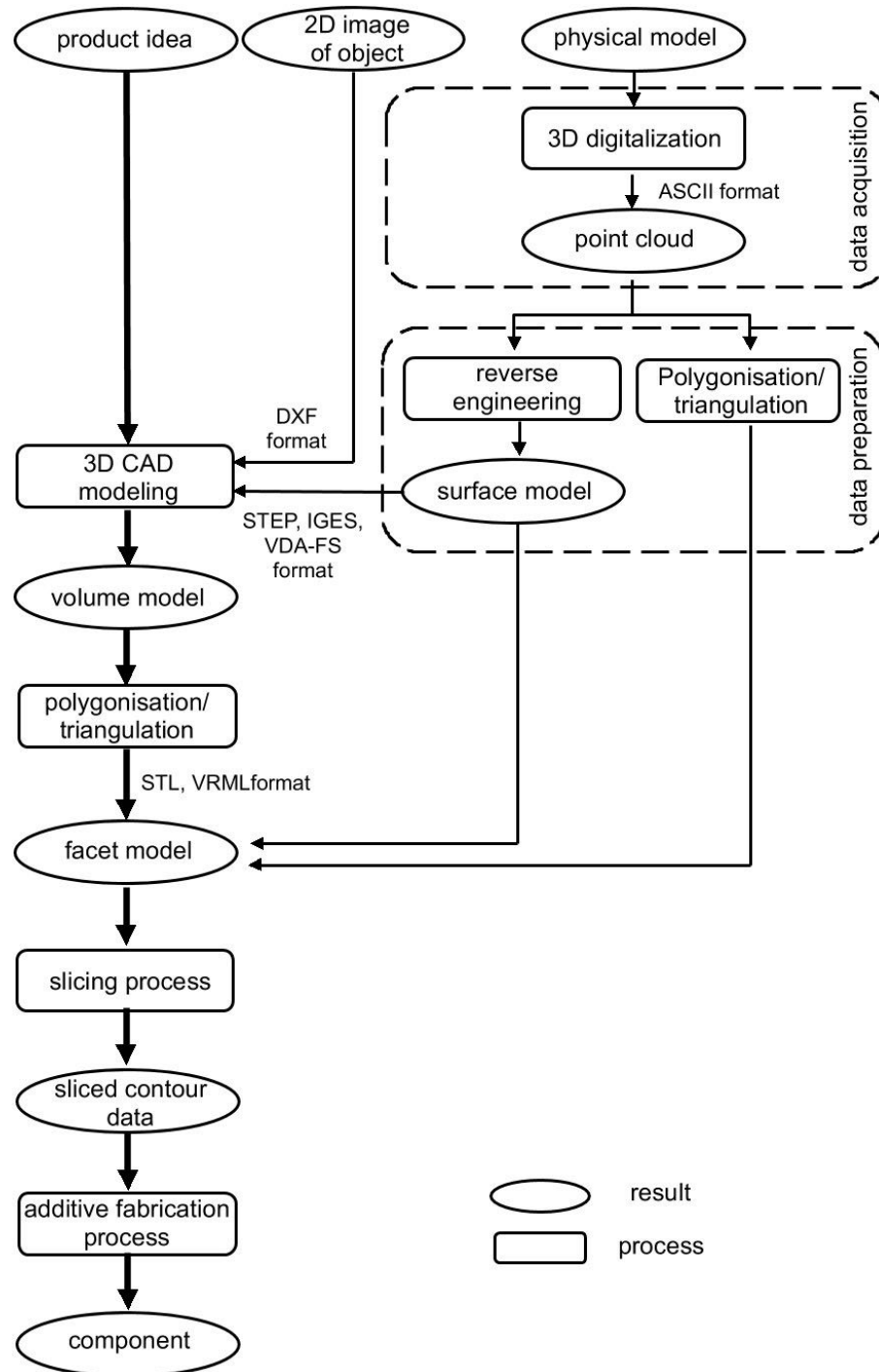


Figure 1.7: AM workflow from product idea to actual component [130, 29].

After that, a classification algorithm solves alignment issues between slices (2D images) and, through a segmentation algorithm, the digital image is partitioned into multiple seg-

ments (set of pixels). By doing so, the contours of the 3D object are detected and with a surface extraction algorithm (contour-based surface reconstruction, marching cube, etc.) the entire 3D surface of the scanned part is reconstructed [67].

Over the past decade, thanks to the increase in power and resolution of X-ray systems, computed tomography has also been used for industrial metrology. In addition to quality control, industrial CT devices can reconstruct both the internal and external geometry of an object without the need to cut it through and destroy it [66]. Although these systems dovetails very well with AM, they have limitations due to the high cost of the machines and the materials that can be scanned: low-density materials (plastic, lightweight alloys, titanium, etc.) can be easily scanned, while high-density materials (steel) require very powerful sources and radiation penetration may be limited.

Input data for AM processes can also be obtained via optical metrology, by scanning a physical model. This approach is the basis of reverse engineering and can be done with different technologies, such as 3D laser scanners, fringe projection, focus variation, etc.

Regardless of the adopted technique, the external surface of the physical model is digitized by points; during scanning phase, the metrological tool saves a large set of points in space, which define the surface of the scanned object. The point dataset, called “point cloud”, contains the X, Y and Z spatial coordinates of each single point.

After point cloud acquisition, there are several algorithms to transform the point dataset in a triangulated surface (e.g. Delaunay triangulation).

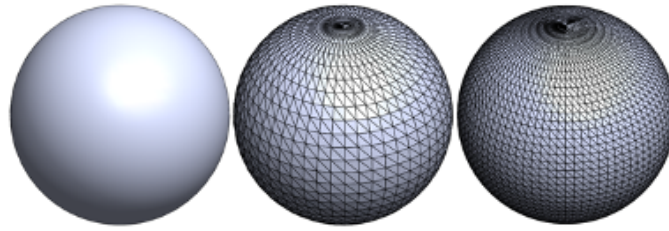
These facet models are the ones required in AM processes. Indeed, even if the CAD model is a volumetric model, it must be converted to a triangular mesh (tessellation). The quintessential format for AM is the STL, which is the STereoLithography format or Standard Tessellation Language that was developed by the 3D Systems in the 1990s [38]. An STL file describes the triangulated surface by the unit normal and vertices (ordered by the right-hand rule) of the triangles, using a three-dimensional Cartesian coordinate system (Figure 1.8(a)). The higher the resolution of the STL file, which means the more triangles that discretize the surface, so the better the quality of the model [29]. Nowadays any CAD software allows files to be saved in STL format and in the export phase it is possible to set the triangulation resolution. Nevertheless, increasing the resolution above a certain value is also not recommended, as it brings no additional benefit: very small features cannot be produced with AM, so the size of the file will be unnecessarily increased, making it more difficult to handle in the next steps of the process chain.

1.3.2 Build Job Preparation and Slicing

Once the STL file is ready, it is possible continue the AM process chain with the build job preparation. The first operation consists in STL model correction: conversion from CAD to STL format may result in errors in the model, especially for objects with complex shape (large number of triangles).

An STL file is producible if each triangular facet obeys the following rules [53]:

- **Vertex to vertex** – Each facet must share one, and only one, edge with each of its adjacent triangles. In other words, each edge is connected to exactly two faces;



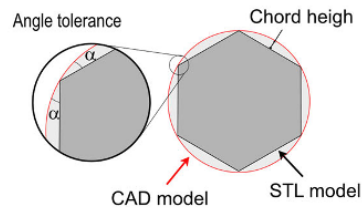
(a) Examples of STL model resolution [1].

```

Solid name
  facet normal  $n_i$   $n_j$   $n_k$ 
    outer loop
      vertex  $x1$   $y1$   $z1$ 
      vertex  $x2$   $y2$   $z2$ 
      vertex  $x3$   $y3$   $z3$ 
    endloop
  endfacet
endsolid name

```

(b) STL file structure.



(c) STL discretization error [16].

Figure 1.8: STL file features.

- **Facet orientation** – The orientation of each facet is specified in two ways, which must be consistent. Firstly, by convention, the direction of the normal vector is facing outwards of the 3D object. Secondly, the vertices are listed in a counter-clockwise-order when looking at the object from the outside.

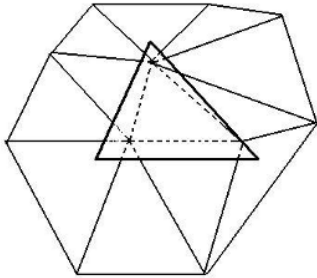
This way the surface of the facet model is perfectly closed (watertight) and without any ambiguity. Typical errors that affect STL files are [53]:

- **Reversed normal vector** – the direction of the normal vector of a triangle is facing inwards of the 3D object;
- **Holes** – the facet model has missing triangles;
- **Overlapping facets** – two or more triangles intersect with each other;
- **Degenerate facets** – a geometrical degeneracy of a facet occurs when all of the facet's edges are collinear, even though all its vertices are distinct;
- **Non-manifold conditions** – when a model is composed by two tangent parts (e.g. model obtained from a Boolean union), it is possible that during tessellation one edge (or more) is shared by more than two adjacent facets (non-manifold facet).

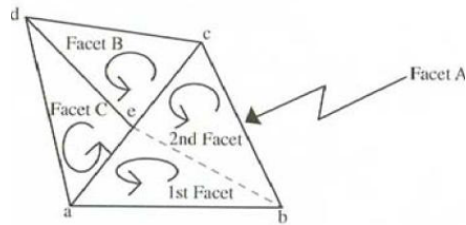
Several software, such as *Magics RP* developed by *Materialise* (Belgium), are available to fix these errors automatically or even manually. So, it is good practice to check the STL models, avoiding issues in the next steps.



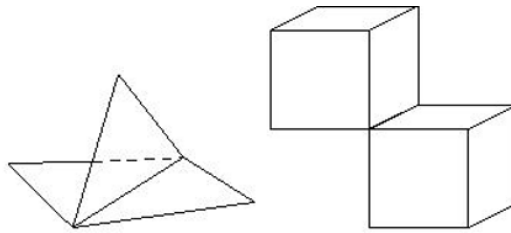
(a) Holes (Missing triangles).



(b) Overlapping facets.



(c) Degenerate facets.



(d) Non-manifold conditions.

Figure 1.9: Typical STL errors [53].

After STL model correction, the part to be printed has to be oriented and positioned on the virtual build platform in the most suitable way for production. For industrial applications, the criterion of minimum production time is typically sought, but it must be taken into account that the component orientation has also an influence on part surface quality and mechanical properties. For instance, the parts produced with some AM processes have a highly anisotropic microstructure, resulting in a different mechanical behaviour depending on the part orientation with respect to the growth direction. Typically, components result weaker along the growth direction [29]. In many technologies, also surface roughness is orientation dependent: e.g. in LPBF, the overhanging surfaces have a worse quality due to the presence of partially fused particles that adhere to the surface [16]. So, it is important to consider these aspects when orienting a component on the build

platform.

Furthermore, it is quite common to produce more than one component during a single printing process. A copy function can be used in case of multiples of the same component, or completely different STL files can be loaded. Some applications may require also linear scale function to slightly reduce or enlarge part size to account for shrinkage or coatings [38].

These tasks can be done in the specific AM machine's software, or with generic software such as *Magics RP*, where the specific virtual build platform can be loaded.

If necessary, additional support structures may often be added after the part positioning and orientation. These structures are necessary when the part to be produced is unable to withstand stresses inherent within the manufacturing process [54]. In particular for metal PBF processes (but not only) this is a limit of potential design freedom offered by AM. Geometrical limitations regard downward facing (overhanging) surfaces; beyond a critical overhang angle, part features cannot be printed with the desired quality. The critical angle is typically about 45° [68]. Therefore, the main functions of support structures are [54]:

- Withstand to deformation or even collapse of processed material caused by gravity during the manufacturing process;
- Mitigate the effects of thermal gradients generated during production, especially for metal AM. Thermal distortions may lead to cracks, curling, sag, delamination and shrinkage. In other words, supports play the role of both heat diffuser and rigidity enhancer;
- Anchor the part to the build platform. In some cases, this may balance the part to be produced during the process;
- In PBF, they stop any layer shifting during the re-coating phase.

Although support structures can be very useful and often essential, their presence leads to feedstock material, time and energy waste [54]. This is because adding supports means the addition of material to the produced part, which will have to be removed during post-processing operations (often manually). Therefore, processing more material requires more build time and energy consumption. Furthermore, post-processing may significantly affect the final cost of the produced part and, after supports removal, the overhanging surface may have poor surface finish.

Limiting the use of support structures, it is possible by efficiently orienting the part, minimizing overhanging surfaces. In many cases, actions can be taken on component design, making support structures an integral part of the component. Although it is not always permissible, part modifications can make the component fully self-supporting without strongly affecting performance. This is the concept of “permanent support structures” [68].

In addition, a huge number of supports types exist for every need, and several optimization approaches have been developed to minimize the volume of material used for support structures. Some support structures examples can be seen in Figure 1.10.

Once finished the build job preparation, all elements present on the build platform can be sliced. The latter term suggests what happens during this operation: all STL models

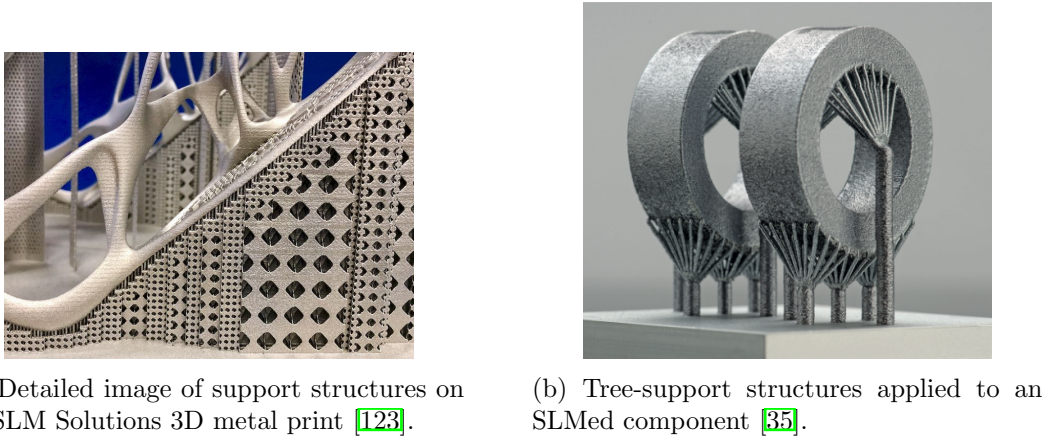


Figure 1.10: Examples of support structures.

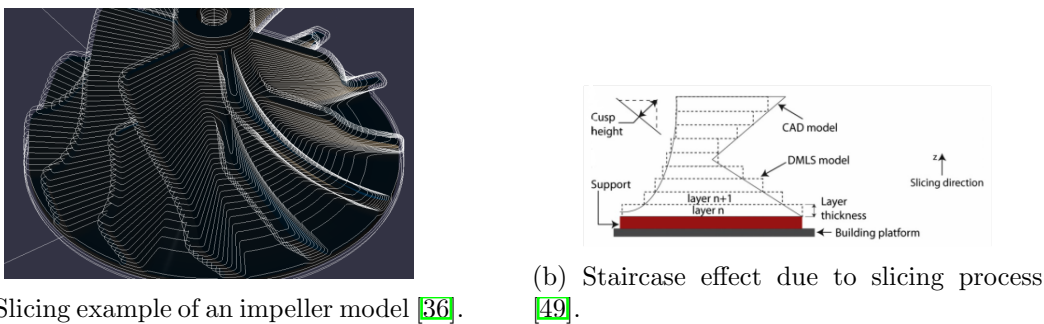


Figure 1.11: Slicing process.

(and their supports), that were previously placed and oriented on the build platform, are literally sliced into thin layers by an algorithm. The traditional slicing method separates the STL model along a predefined direction (orthogonal to the build platform) with a series of parallel planes (see Figure 1.11), generating the build part instructions for the AM machine. The smaller the layer thickness, the more accurate the component; however, production time also increases (more layers need to be built).

During the slicing setup, some software allow to set other process parameters, including fill patterns, speed, temperatures, material, etc. [29].

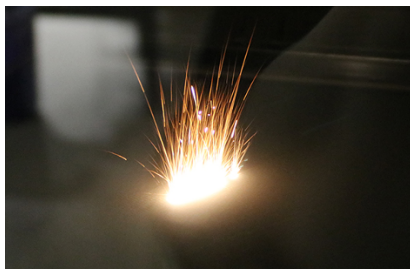
Although the most widely used method in AM is the traditional one, there are also other approaches. For instance, the traditional method can be further divided into basic slicing (the one described above) and adaptive slicing. For complex components with features of various sizes, the last method adapts the layer thickness to the real need for precision of the given layer. This allows to increase the productivity, while maintaining the component accuracy. In PBF processes this method is difficult to apply as it is not possible to vary the layer thickness without changing the other process parameters.

Another method is the multi-directional slicing, which is used to slice the STL model with several sets of planes in different directions. This approach is particularly suitable

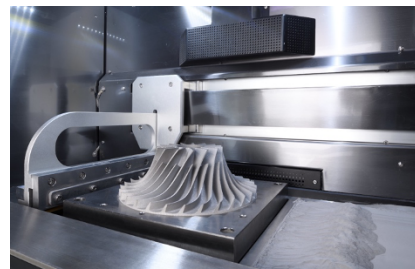
for complex parts that are composed of regular features, especially with several main directions and overhanging surfaces.

Furthermore, for the free-form components such as revolving parts, the non-layer-wise slicing method can be used, cutting the model with free-form surfaces [146]. However, the last two methods cannot be used in any AM process, but are suitable only for techniques that allow to change the growth direction of part during the process, such as the DED technology.

1.3.3 Additive Fabrication Process and Post-Processing



(a) Side image of spatters during selective laser melting [95].



(b) Impeller produced with powder bed fusion technology [107].

Figure 1.12: Metal AM process.

Once the slicing software has generated the build instructions file, it can be sent to the AM machine.

Before starting the process, some machines may require to set some specific process parameters that were not yet established in the previous step. In flexible machines it is also possible to have some parameters that require optimization to suit the specific part that is to be build. However, other machines may have very closed systems, in which only material and resolution can be set.

When all settings are made, the AM process can be started: the first few steps of the AM procedure are semi-automated tasks that may require considerable manual control, interaction, and decision making. Subsequently the automated layer upon layer process starts and the part begins to take shape.

As discussed above, there are different printing techniques and various materials that can be elaborated. The process can take a few hours, up to several days, depending on the number and size of the parts, as well as their orientation on the build platform and the process parameters used.

At the end of the process, the output of the AM machine should ideally be ready for use. Although this is possible in some applications, post-processing is often required: part separation (from build platform), manual support removal, manual finishing, cleaning, machining, shot peening or tumbling operations can be performed as needed.

As mentioned above, some metal AM processes need also a stress relieving heat treatment before separating the part from the build platform or a hot isostatic pressing (HIP) to reduce material porosity and enhance mechanical properties [38, 29].

Once obtained the desired outcome, parts are ready for use in various applications, which will be briefly mentioned in the following paragraph.

1.4 Process Advantages, Limitations, and Applications

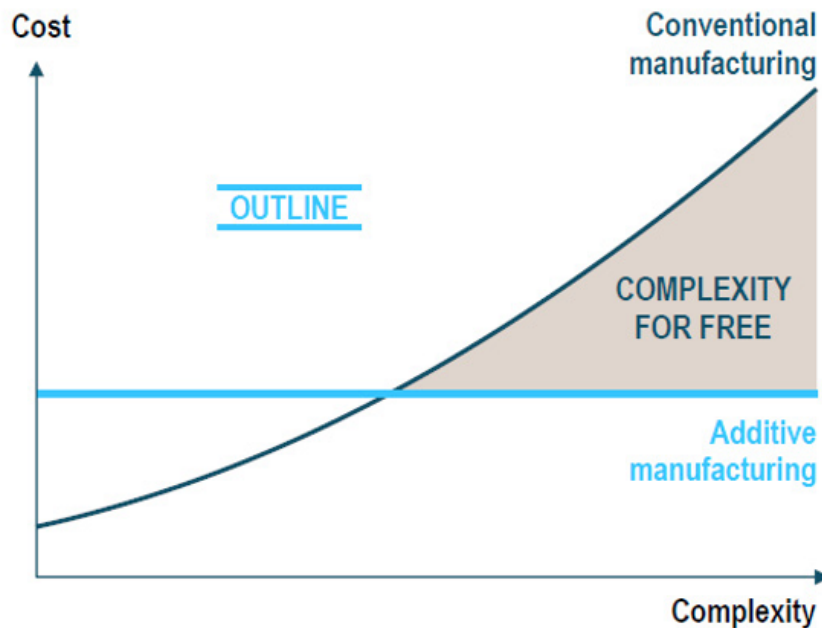


Figure 1.13: Cost vs. Complexity in AM processes and in conventional manufacturing [31].

AM technologies underpin a production concept that is opposing to subtractive techniques. Adding material instead of removing it from a solid block brings several benefits. The first among these is the greater freedom of design with respect to traditional manufacturing [29]. Because of constraints of conventional processes, designers often have to find a compromise between aesthetics, functionality and costs at the risk of losing the essence of their initial concept. Every detail added involves extra processing, so as geometric complexity increases, the associated production cost also increases.

On the other hand, in AM processes, the geometrical complexity of components is for free: the more geometrically complex the part is, the more suitable it is for AM (see Figure 1.13). Although there may be limitations due to overhangs and the use of supports (in some cases are difficult to remove), the AM technology can produce geometric details that would be otherwise unfeasible. Even with 5-axis milling or the most complex injection moulding or die-casting systems, it is impossible to achieve certain features, especially internal ones. The clearest examples are internal cooling channels, especially conformal ones, which are often unfeasible with traditional technologies. Conformal cooling channels follow the external geometry of the component to enhance heat transfer with a refriger-

ant liquid. Industrial injection moulding case studies have confirmed that these cooling systems lead to more uniform temperature distributions, reduced cycle times, reduced corrosion, longer maintenance intervals and part quality improvement [130]. Thanks to the achievable internal features, injection moulding and heat exchangers are application fields where it makes sense to use additive techniques.

Thus, the greater design freedom and the consequent achievable geometrical complexity entail a series of advantages if used properly. Another example is replacing several simpler parts with a single more complex one, reducing assemblies and inventory costs. This approach is named Part Consolidation and in some cases it can be extended to complete assemblies with moving parts (Instant Assemblies) [29, 31]. To produce complete assemblies, a minimum gap between the moving parts is needed. The material in these gaps is not processed and can be removed after production, leaving the surrounding parts free to move. By reducing the number of components to be produced, there may be the elimination of production steps and potentially also tooling (costly and time-consuming). Similar considerations can be made in general for all complex objects that are produced in one process step with AM.

Another way to use design freedom is light-weighting; by performing a finite element analysis, it is possible to iteratively remove unnecessary material from component, maintaining its mechanical performance. Topology optimization is not a recent design approach; however, at present it is possible to take full advantage of its potential, thanks to AM technologies [29]. Lightweight structures are especially used in aerospace and automotive industries, where the reduction in weight can lead to significant energy savings over the entire product life [130].

In these industrial fields, AM technologies lead also to another advantage: the reduction of the buy-to-fly ratio, which is the ratio of input material weight to final part weight. For traditional manufacturing processes, buy-to-fly ratio for aerospace components can be as high as 10:1 up to 20:1.

On the other hand, the near net shape products obtained with AM processes can potentially have a 1:1 ratio, which means 10-20 times less wasted material (supports and allowances have to be taken into account) [31].

To reduce components weight, with AM it is also possible to implement lattice or cellular structures. These structures are topologically ordered, three-dimensional open-celled structures composed of one or more repeating unit cells. There are several types of cells and are defined by dimensions and connectivity of their constituent strut elements, which are connected at specific nodes. By tuning cell topology (connectivity) and geometry (cell size and strut dimensions), lattice structures can produce unique mechanical, electrical, thermal and acoustic properties [86].

In addition to aerospace applications, these structures can also be used in the biomedical field: the reduction in stiffness, due to special lattice structures, allows the medical implant to resemble the natural mechanical behaviour of the human bone. Moreover, the porosity of the material due to these structures, facilitates osteointegration. These two features reduce a common problem of medical implants, the stress shielding effect [86]. This phenomenon occurs when metal implants are used to repair fractures or in joint replacement surgery. Although rigid metal plates stabilize the fracture site, the higher stiffness of the

implant results in bone loss (bone density reduction) as a result of decreased physiologic loading of the bone [96].

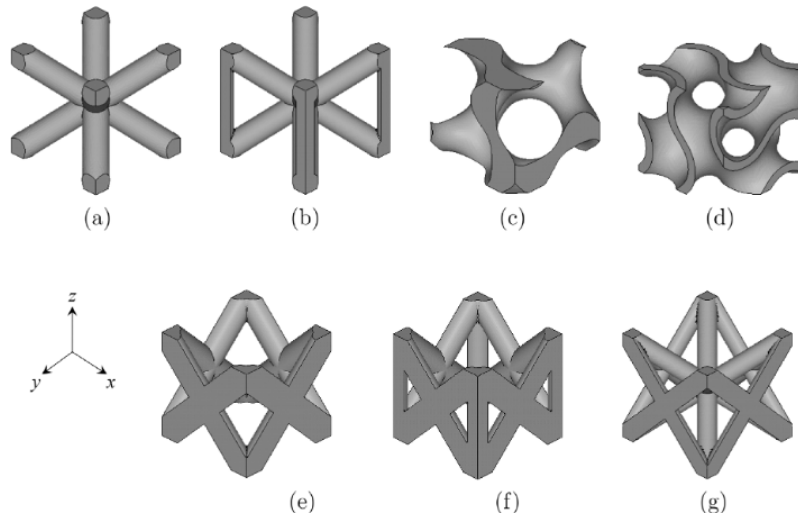


Figure 1.14: Seven lattice topologies: (a) body-centred cube (BCC); (b) body-centred cube with vertical struts (BCCz), (c) gyroid, (d) matrix phase of D-gyroid, (e) face centred cube (FCC), (f) face centred cube with vertical struts (PFCC), (g) Boolean combination of BCC and FCC (F2BCC) [101].

Moreover, producing components with AM allows mass customization. Indeed, the typical short time-to-market of new products offered by AM opens the door to components that are customized to the needs of each individual customer. This advantage is often exploited in the medical and dental fields, where the medical device design starts from CT of the target patient, thus allowing the perfect coupling between bone and prosthesis [29]. Customization is not unusual also in the jewellery industry: many companies allow to customize their jewellery, sometimes allowing the customer to design himself the desired object to be produced with AM.

Although AM techniques are used in various fields of application nowadays, they still present some issues. As these technologies are relatively new, there is still a lack of regulation: in recent years ISO and ASTM standards have introduced new AM regulations, but metrology and quality control are still challenging. These challenges are related to the part materials, geometries, and surfaces. Since the part material and geometry are created simultaneously in AM, components must be inspected for defects in the bulk material (unexpected porosity, larger internal voids, inclusions, etc.). It is worth noting that AM materials have not the same properties as their bulk counterparts. Thus, special characterization techniques are needed for additive materials [130].

Furthermore, in many metal AM processes, the resulting material may be affected by growth direction; in some cases, microstructure (anisotropy), surface quality and dimensional accuracy may vary with part orientation. This is also due to the presence of supports structures, which may affect the part quality and require considerable effort to remove them, affecting the cost. Indeed, post-processing operations may significantly affect the

component cost.

The challenge grows when process parameters are changed to achieve different component performance, so considerable effort is required for application design and for setting process parameters [31].

From the production economy point of view, it is true that the time-to-market of new products is typically low, but the build rates of AM technologies are also very low. Combined with the high cost of both the machines and materials used, this entails a very high cost of production, especially for metal AM. Moreover, AM techniques are discontinuous processes and therefore economies of scale cannot currently be applied [31].

Generalizing, it can be claimed that metal AM technologies are convenient in the production of parts that have a high buy-to-fly ratio, have a complex shape and/or internal features, have a high cost of raw material, have slow machining rates and are difficult and expensive to machine [31].

At the same time, the design freedom and unique features offered by AM processes require different process-specific design rules and tools, which make up the so-called Design for Additive Manufacturing (DfAM) [29, 130]. To achieve the maximum benefit of AM technologies, designers need to change their mindset and overcome the “cognitive barriers” imposed by past experience and conventional processes [130].

Eventually, to overcome process and materials limitations, further research effort is needed to increase machines capabilities (dimensional accuracy, surface roughness, mechanical performance, etc.) and expand available materials that can be used.

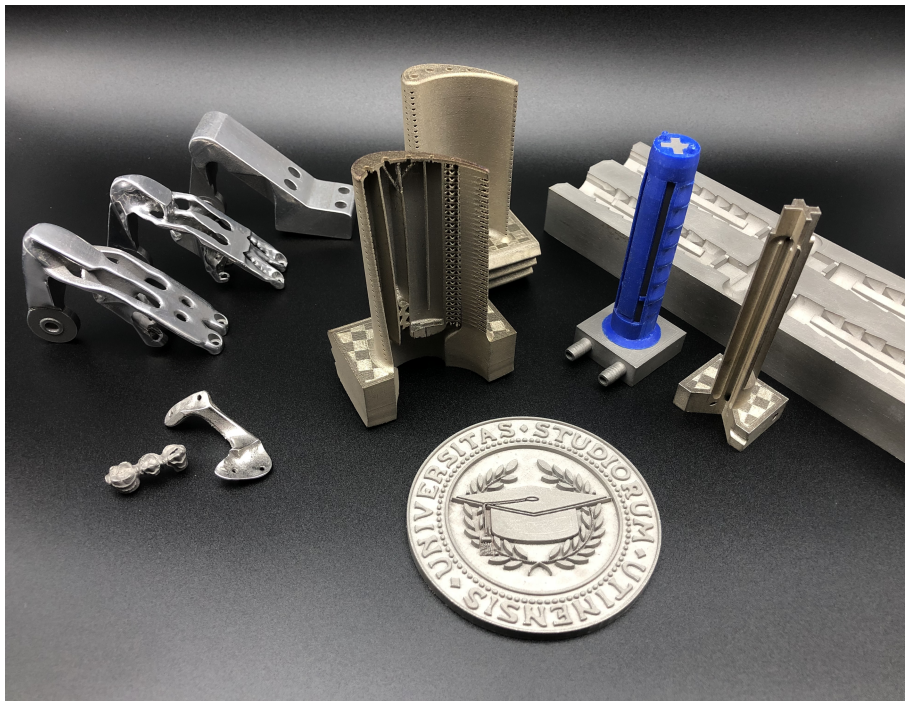


Figure 1.15: Various components produced through SLM technology in the *LAMA^{FVG}* laboratory, representing some applications of metal AM.

Chapter 2

Selective Laser Melting

2.1 SLM Process Workflow



Figure 2.1: SLM process workflow.

In the previous chapter, a general AM process chain has been described, focusing mainly on the build job preparation. From an operational perspective, the latter step is typically carried out in *Magics RP* environment, where STL model correction, positioning, supports generation and slicing operations can be performed.

Once the slicing files are generated, they can be loaded into the SLM machine to proceed with further settings. In the *Concept Laser M2 Cusing*, the machine used in this work, the process parameters have to be assigned to each workpiece when the respective file is loaded. The adopted material has also to be defined in the machine user interface in order to automatically set the inert gas flow parameters, such as the target oxygen percentage during the production and the flow speed.

Before starting the production process, a new build platform (grinded and shot blasted) and a new powder scraper (coater) has to be installed. Both components have to be manually adjusted in order to place the build platform to laser focus distance and align the powder scraper to get a constant layer thickness.

If there is not enough powder, the feed container is filled with fresh powder (this aspect will be discussed later) and the first layer is generally laid manually by the operator in order to verify that everything is fine. At this stage, the process chamber is filled with the inert gas (Nitrogen or Argon), which acts as a shielding, avoiding unexpected reaction of gaseous particles with the materials (burning and explosion). It is worth recalling that some materials are susceptible to oxygen even at room temperature (e.g. titanium and aluminium alloys); therefore, also preliminary operations have to be carried out in inert atmosphere.

When the oxygen content of the build chamber reaches the target value, the process start button can be pressed and the laser starts to selectively melt the powder bed, layer upon layer. The process can take from a few hours, for smaller parts, up to 1-2 weeks of continuous manufacture for larger workpieces. After production, the fabricated parts are immersed in the unprocessed powder. Therefore, the remaining powder has to be removed in order to release the components and thus to detach the build platform from the machine.

Due to the high thermal stresses inherent in SLM process, a stress relieving heat treatment is often required before removing the workpieces from the build platform. Basically, it consists in heating and maintaining a temperature close to the tempering temperature, followed by slow cooling in order to avoid the formation of new internal stresses.

When the workpieces (and the build platform) reach the room temperature, they can be removed from the build platform with a sawing machine (slow but quick) or through a wire erosion machine. Any support structures must subsequently be removed manually or through machining operations. Shot peening and tumbling processes can also be carried out in order to increase the surface finish, being careful not to reduce dimensional accuracy. Eventually, the components produced and post-processed are ready for end-use applications.

2.2 Lasers

One of the technological elements behind the SLM process is the LASER, which stands for Light Amplification by Stimulated Emission Radiation. Its operation is based on the stimulated emission of photons (first enunciated by A. Einstein in 1917 and subsequently considered at the application level around the 1950s). This physical phenomenon consists of the stimulation of an excited atom by a photon, producing the decay of electrons

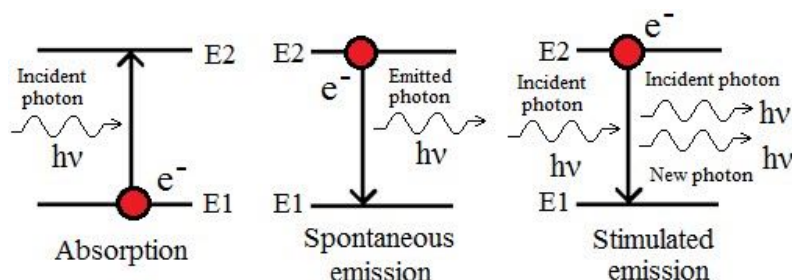


Figure 2.2: Phenomena describing the interaction between electrons and photons [108].

from the unstable high energy orbit (high energy state), to the stable one at lower energy (ground state). The result is an emission of two photons, all strictly with the same frequency and phase [47].

It is worth noting that not all atoms are in the ground state because they always have some thermal energy above absolute zero. Moreover, an atom in ground state can make a transition to a higher energy level when it absorbs a photon with sufficient energy (absorption).

Under normal conditions (i.e. if the emission is not stimulated), atoms in a high energy state can make a transition to a lower state whenever they “wants to”: electrons decay into the lower orbit at completely random successive moments, returning the energy in the form of photons, all with the same light energy, but directed in any direction. This natural phenomenon is called spontaneous photonic emission.

The laser, on the other hand, is able to produce multiple stimulated emissions and channel photons into a single unidirectional, monochromatic, and perfectly phased beam. To do this, lasers have a particular structure, which consists of three parts: the active medium (solid, gaseous, semiconductor or even liquid), the pumping system (electric current, flash lamps or laser diodes), and the resonant, which is a mirrors system that forms an optical cavity. In a generic laser system, the active medium is placed between a high reflective mirror and a partially reflective mirror (see Figure 2.3). Since the distance between them is a whole multiple of half a wavelength of laser radiation, the mirror system constitutes a resonant optical cavity. Once the pumping system starts emitting light (or electrical energy), excited atoms begin the state transition and photons are forced to oscillate back and forth between the mirrors producing a cascade of photons that amplifies the light. To ensure this light amplification, the majority of atoms in the active medium must be in an excited state, so spontaneously emitted photons are more likely to stimulate emission than to be absorbed by atoms in the ground state. This is called a population inversion, because the population is inverted from the normal situation in which more atoms are in lower levels than in higher levels [47].

When the radiation reaches a certain intensity, the photons penetrate the partially reflective mirror and produce a coherent (photons have same wavelength and phase) unidirectional beam, typically characterized also by a small divergence angle (beam divergence depends on the nature of the resonator, the width of the emitting area, and diffraction). Once the laser beam is focused using an appropriate optical system, the free-propagated

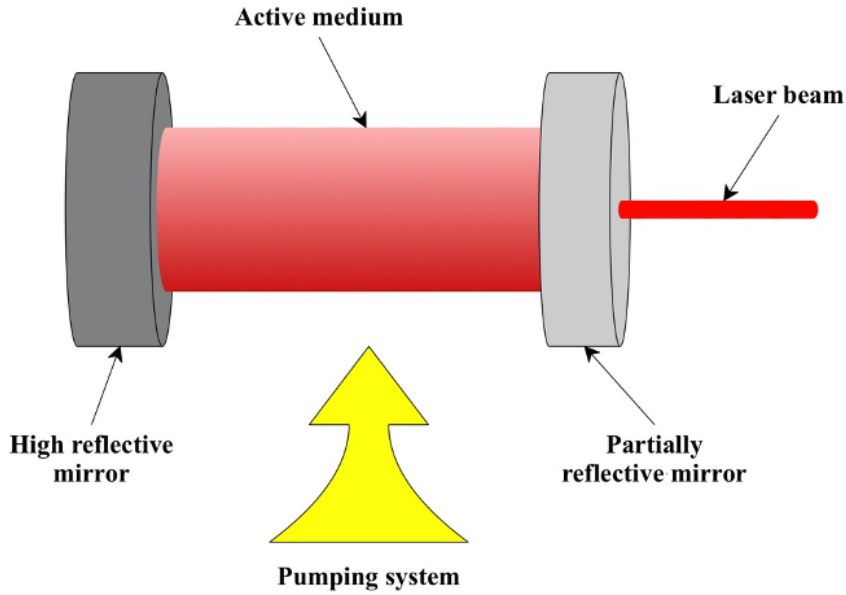


Figure 2.3: Scheme of a generic laser system.

radiation naturally converges until it reaches the focal point, where the beam diameter is minimal (d_0 , beam waist), and then diverges with a certain divergence angle that gradually grows along the beam axis. When the laser hits a perpendicular surface, the diameter of the intersection area is called spot diameter (d_s) and its size depends on the defocus distance. The transmitted intensity profile on processed surface strongly depends on the beam quality, which can be defined with the beam propagation factor (M^2)[\[47\]](#):

$$M^2 = \frac{\pi w_0 \theta}{\lambda} \quad (2.1)$$

where θ is the beam divergence angle, w_0 is the beam radius at the waist ($d_0/2$) and λ is the wavelength. The minimum M^2 value is 1 for a diffraction-limited Gaussian beam.

From the viewpoint of energy, the laser efficiency can be measured in different ways; the most used measurement typically is the overall or wall-plug efficiency, which is the fraction of the energy delivered to the laser that emerges in the laser beam [\[47\]](#). This overall efficiency, in turn, depends on the efficiency of each step needed to convert the energy provided by the wall-plug into a laser beam.

Considering a generic electrically powered laser, the steps are the following:

- Electrical energy enters the laser system through a power supply, which converts much of the input energy into drive current that is passed through the active medium (the related efficiency is called *power-supply efficiency*);
- Much of the electrical energy is deposited in the active medium (related efficiency is *energy-deposition efficiency*);
- Much of the deposited energy excites atoms (or molecules) to produce a population inversion (related efficiency is *excitation efficiency*);

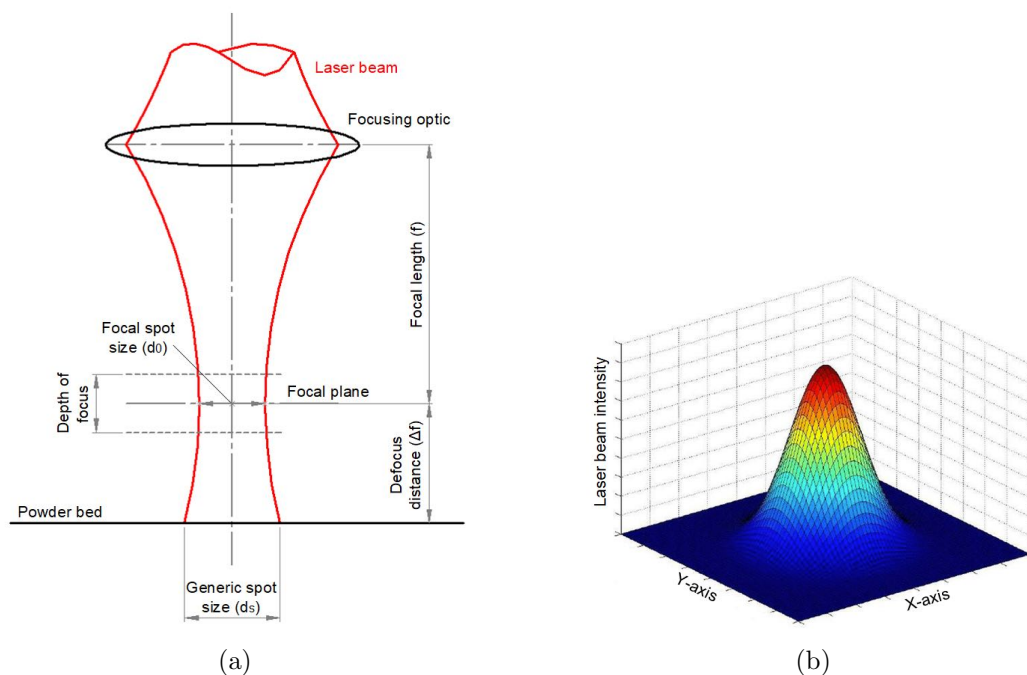


Figure 2.4: (a) Laser beam propagation after a focusing lens and, (b) typical fiber laser beam intensity profile (Gaussian distribution).

- The laser system converts much of the energy of the population inversion into light by stimulated emission (related efficiency is *laser transition efficiency* – for optical pumping it is called *quantum efficiency*);
- Much of the stimulated emission emerges in the laser beam through the optical cavity (related efficiency is *energy extraction efficiency*)

In every step, there is a loss of energy, so the wall-plug efficiency is the product of all step efficiencies. Similar considerations apply to optically pumped lasers (e.g. solid-state lasers), which have some extra steps, although many are more efficient than most gas lasers (electrically powered).

As can be imagined, the overall efficiency depends on the laser type; in particular on the pumping system and on the active medium used.

Concerning the latter, those commonly used in industrial systems are:

- Gaseous blend of electrically excited carbon dioxide (CO_2);
- Neodymium-doped Yttrium-Aluminum crystal ($Nd:YAG$);
- Ytterbium-doped glass (Yb) drawn in thin fibers (optical fiber).

The CO_2 laser is one of the earliest and most widespread gas lasers. In this laser type, the gas state medium fills a discharge tube that is electrically pumped by a DC or AC

current to induce the population inversion for lasing.

Due to its high efficiency ($5 \div 20\%$), high output power ($0.1 \div 20kW$) and low cost, the CO_2 lasers are extensively used for cutting, drilling, welding and marking operations. However, their emission is relatively non-stable because of thermal expansion and contraction of the system structure due to the heat generated in the energy pumping process. Due to these thermal stresses, the overall optics should be checked for fatigue every 2000 hours [70].

Although they were used in the first metal-SLS machines, CO_2 lasers are no longer used in metal-AM nowadays. As a matter of fact, the long infrared operation wavelength of CO_2 lasers ($10.6\mu m$) results in limited throughput due to low light absorption coefficient of metals in the infrared region. Nevertheless, $10.6\mu m$ wavelength is particularly suitable for polymeric materials processing and therefore CO_2 lasers are widely used in SLA and SLS technologies.

A more suitable laser for metal processing is the $Nd:YAG$ laser, in which the solid medium ($Nd^{3+} : Y_3Al_5O_{12}$) is optically pumped along the radial direction by a flash lamp or pumped by an $808nm$ laser diode in the axial direction, to produce a near infrared wavelength of $1064nm$. As can be seen in Figure 2.5, at this operating wavelength the light absorption coefficient of metals is far greater than that in the infrared region [70]. Furthermore, comparing the wavelengths of CO_2 and solid-state lasers ($10\mu m$ and $1\mu m$ respectively), the shorter wavelength of $Nd:YAG$ allows to reduce the minimum spot size, leading to greater precision in laser processing. In fact, by specifying the waist radius in equation 2.1, it can be seen that it is directly proportional to the wavelength. So, if the wavelength is reduced from ($10\mu m$ to $1\mu m$, the waist radius is also reduced by $1/10$).

$Nd:YAG$ lasers can reach an output power similar to CO_2 ones (up to $16kW$) and the

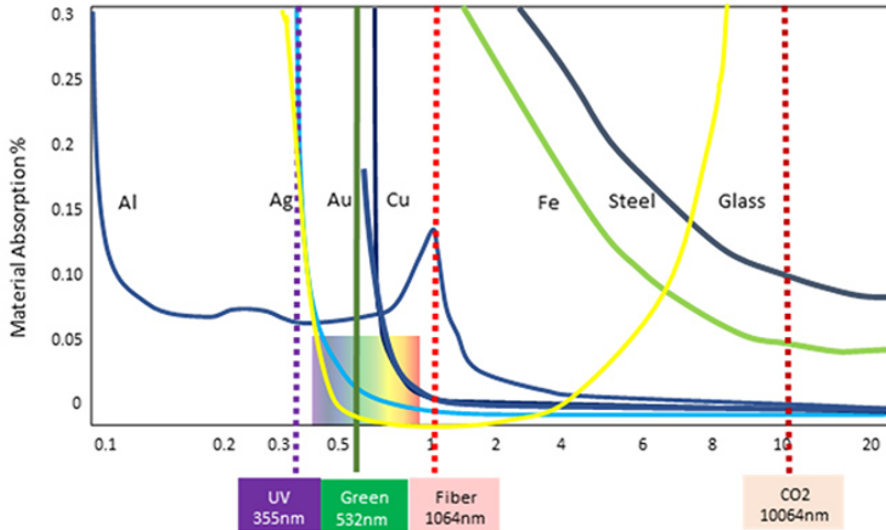


Figure 2.5: Light absorptivity at different wavelengths of various materials [24].

light beam can be delivered by flexible optical fibers, thanks to their particular operating wavelength. Therefore, the delivery efficiency of $Nd:YAG$ lasers is higher with respect to CO_2 lasers, which have a lack of optical fibers that can deliver their wavelength range.

Lasers	<i>CO</i> ₂ laser	<i>Nd:YAG</i> laser	<i>Yb</i> -fiber laser
Application	SLA, SLM, SLS, DED	SLM, SLS, DED	SLM, SLS, DED
Operation wavelength	10.6 μ m	1.06 μ m	1.07 μ m
Efficiency	5 \div 20%	Lamp pump: 1 \div 3%, Diode pump: 10 \div 20%	10 \div 30%
Output power (CW)	Up to 20kW	Up to 16kW	Up to 10kW
Pump source	Electrical discharge	Flashlamp or laser diode	Laser diode
Operation mode	CW & PW	CW & PW	CW & PW
Fiber delivery	Not possible	Possible	Possible
Maintenance periods	2000 hours	200 hours (Lamp life), 10'000 hours (Diode life)	Maintenance free (25'000 hours)

Table 2.1: Specifications of representative lasers for metal-AM [70].

Conventional *Nd:YAG* lasers are typically pumped by Xenon flash lamps, which are characterized by low electrical-to-optical efficiency. The unabsorbed energy is dissipated as heat, which enhances the temperature of the optical elements, inducing unexpected thermal lensing and birefringence effects and, therefore poor beam quality.

Another weakness of *Nd:YAG* lasers is the short lifetime of the flash lamps (200 hours). Nevertheless, this issue can be overcome by using laser diodes as pumping system, which have also a higher electrical-to-optical efficiency (the overall power efficiency can increase up to 5 times the lamp-pumped laser one). Although *Nd:YAG* lasers are heavily used in AM research works, over the past decade they have been replaced by more compact and efficient *Yb*-fiber lasers [70].

These lasers are typically pumped by laser diodes with 950 \div 980nm wavelength and are capable of producing near-infrared laser beams in 1030 \div 1070nm output wavelength (as for *Nd:YAG*, very suitable for metal processing). The active medium of this laser type consists of a rare-earth doped optical fiber. Among the various rare-earth elements used for fiber doping, Ytterbium is the most suitable for high power generation because of high quantum efficiency (\sim 94%).

With respect to early gas and solid-state lasers, *Yb*-fiber lasers have in general much higher wall-plug efficiency, reducing operating costs and making higher laser powers practical. Moreover, the high surface-to-volume ratio of fibers and the general system compactness eases the heat removal, limiting both the laser beam quality degradation and the need for active cooling. In fact, given the high quality of the fiber laser beam, the intensity profile is generally considered to be perfectly Gaussian ($M^2 = 1$).

In addition, as a fiber laser is made, no optical surface is exposed to dirt and dust, from the pumping diode to the end of the fiber delivering the laser beam. This is a major advantage because surface damages are avoided and the maintenance needs are radically reduced, with respect to the other laser types (at least 25000 hour of use). Therefore *Yb*-fiber lasers are by far the most used in industry, and are the ones referred to by the

term "fiber laser" [47].

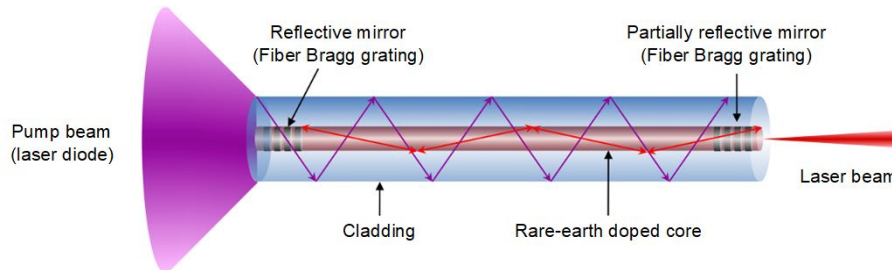


Figure 2.6: Scheme of a generic fiber laser pumped with a laser diode.

With regard to the modulation of laser power, it is typically done directly by controlling the energy provided by the pumping system. Indeed, direct modulation is particularly suitable for semiconductor diode lasers, in which the light can be electronically modulated. As a matter of fact, laser diodes are reasonably linear over much of their operating range, so they can be modulated with continuously varying analog signals. By modulating the laser diode, it can therefore be easily modulated also a diode-pumped solid-state laser [47]. Another crucial feature of lasers is the duration of emission in the time domain: laser operation modes can be classified into continuous wave mode (CW) and pulsed wave mode (PW) [18, 47, 70]. A CW laser emits a beam continually (many lasers can emit stably for hours, days, or longer); whereas in PW mode, lasers emit only within a short pulse duration at fixed repetition rate.

The operation mode can be managed by the pumping system and internal devices thus many lasers can operate in both conditions. However, lasers are most commonly operated in CW mode in metal-AM, due to the higher volumetric deposition (2 – 3 times higher) and, more generally, the higher build rate (higher scan speed) [18]. On the other hand, PW mode reaches better process resolution, due the minor thermal energy dissipation to the material surrounding the melt pool. For instance, Caprio et al. [18] determined process resolution through single track width measurements in SLM technology and noticed greater accuracy with PW mode (from $350\mu\text{m}$ of CW to $200\mu\text{m}$ of PW).

The SLM system used in the experiments described in this dissertation is the *Concept-Laser M2 Cusing*, in which a continuously operated *Yb*-fiber laser with 1067nm wavelength is mounted. The laser beam produced is then delivered through an optical fiber to a galvanometric scanning system, whose commercial name is *varioSCAN*. This optical system is mainly composed of three devices:

- The scan head, which is in turn composed of two galvanometric mirrors that allow the deflection of the laser beam on the X-Y plane of the build platform;
- The F-theta lens (optional in the *varioSCAN* module), which is a particular lens used to eliminate the static defocus error in the region close to the center of the processing field;

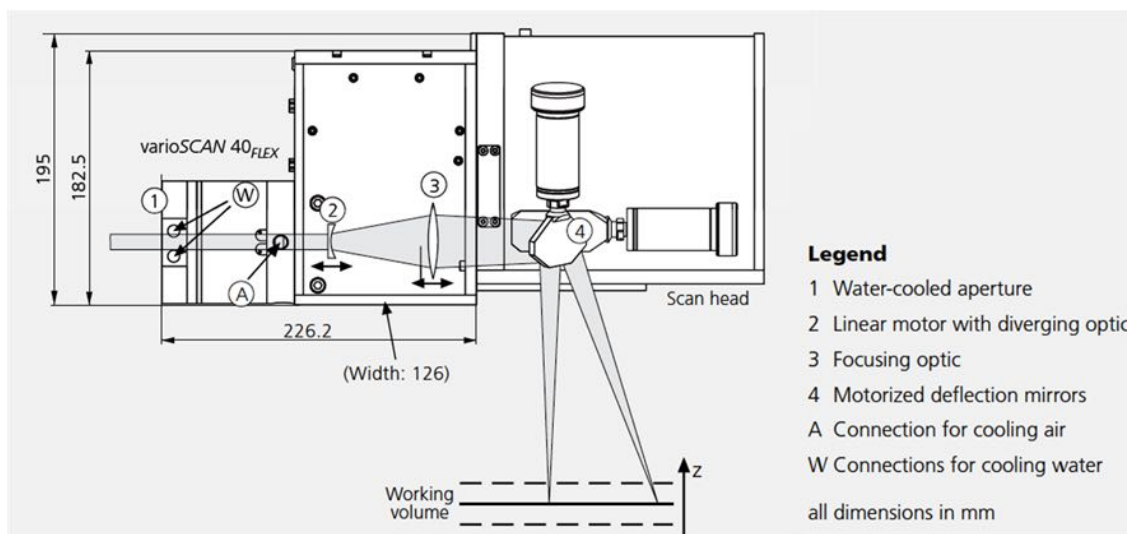


Figure 2.7: Schematic representation of the *varioSCAN* unit [115].

- The dynamic focusing unit, which is a particular mirror system that allows to continuously adjust the image field size, working distance and spot size over the full processing field.

Concerning the scan head, the two mirrors are mounted on very small rotary motors (called galvanometers) and are positioned orthogonally to each other such that the rotary motion of the two mirrors translates to linear motion in X- and Y-axis of the laser beam. The small size of the motors provides high-speed positioning, short settling times, and high acceleration and deceleration, which is ideal for high-speed, short-distance motion.

The F-theta lens are widely used in laser-AM of metals as it allows to easily reduce the static defocus error, due to the fixed focus length of typical static focusing units. Indeed, without the F-theta lens, the image field of the scan head would be spherical on the entire build platform. By installing a F-theta lens, instead, there is a flattening of the image field that allows to consider perfectly flat at least the region close to the center of the processing field. However, as can be seen in Figure 2.8, an imprecise focusing of the laser beam still occurs at the edge of the processing field [152]. This may be acceptable for machines with a small build platform, but for larger industrial machines with greater build volumes is often needed also a dynamic focusing unit to eliminate this error. Actually, this unit could solve the problem of static defocus error without needing an F-theta lens (so much so that in the *varioSCAN* system the latter lens is an optional), but it is not unusual to find systems that mount both devices.

Basically, referring to the Figure 2.8, the defocus error can be resolved by moving the expander lens so that the focal spot lies back on the build platform. Thus, by giving an appropriate adjustment of the beam expander lens position, the laser can be focused in any region of the flat focal plane.

In addition to the static error, the focus unit also allows to correct dynamic errors due to the inertia of the galvanometric mirrors and permits to change laser spot diameter during

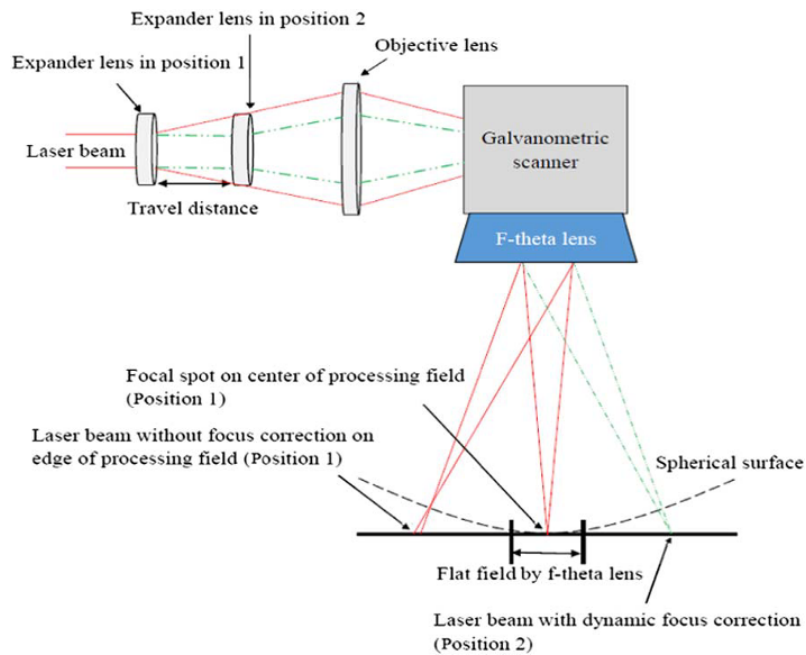


Figure 2.8: Schematic illustration of the dynamic focusing unit operation [152].

the process according to a specific scanning strategy. Basically, the *varioSCAN* converts the two-dimensional scan head (X-Y plane) into a three-dimensional laser deflection unit. It is worth noting that changing the spot diameter with the *varioSCAN* unit is not the same as laser defocusing, in which a defocus distance is intentionally introduced. Indeed, in the literature there are various studies in which authors changed the spot size by defocusing the laser beam to increase the productivity (up to 840%). For instance, Metelkova et al. [93] pointed out that the increase of the beam diameter without changing the optical setup for each diameter lead to different results with respect to an in-focus beam with the same theoretical diameter. Furthermore, there are also differences between positive and negative defocusing:

- In case of negative defocus distance, the convergent nature of the beam enhances the efficiency of the laser penetration, “drilling” deeper inside the material (melt pool is deeper);
- For positive defocus distance, this phenomenon is attenuated as the beam is divergent. Being less energy efficient, the process is less sensitive to heat input variations, leading to a more stable melt pool.

In other words, defocusing lead to different types of laser-material interactions, which are not only governed by the beam diameter, but also by its convergent or divergent nature [93].

Regarding laser-material interaction, it is worth noting that in laser-PBF processes the laser interacts with a powder-coated substrate and not with a bare one, as happens in

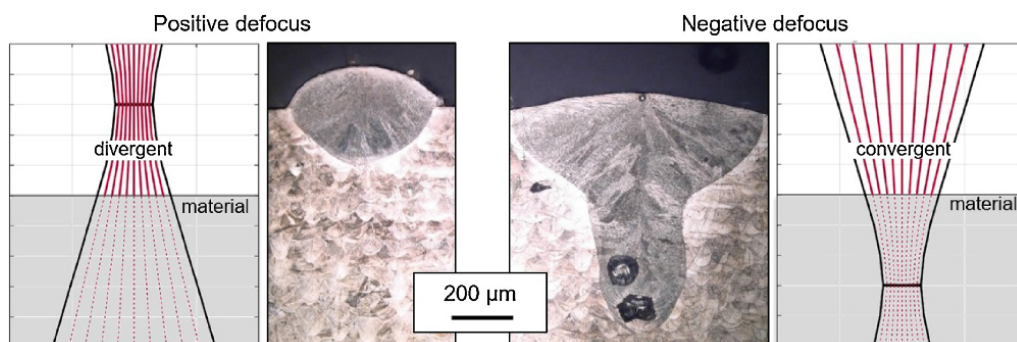


Figure 2.9: Influence of the convergent and divergent nature of the laser beam on the melt pool morphology [93].

laser welding. There are several physical differences in processing powder instead of dense material, the main of which is the absorption coefficient (absorptivity) of the material. Indeed, several studies can be found in literature where it is experimentally proven that the powder absorption is significantly higher than the one of the same dense material (about two times higher). As the absorption coefficient is the ratio of energy absorbed by the material to the input energy, this means that LPBF process efficiency is higher compared to conventional laser processes. The higher absorptivity can be explained by the multiple reflections and scattering of the laser radiation in the powder material, which also result in higher optical penetration depth [134, 153].

However, as for dense materials, the powder absorptivity is not a constant value, but it varies according to energy input parameters and powder properties. This makes it rather complicated to determine the energy effectively absorbed by powders during the process. For instance, Trapp et al. [134] studied the effective absorptivity of CW 1070nm laser light for bare and powder-coated discs for three different materials by using direct calorimetric measurements. Laser power and scan speed were also varied to investigate their influence on powder absorptivity. As can be seen in Figure 2.10, they have found that the absorptivity curve as function of laser power can be divided in three regimes:

- *Regime I* – At low power, the powder absorptivity is about two times higher compared to the dense material one. Indeed, in this regime not all the powder is completely fused. The increase in the fraction of powder being molten with the increasing power is consistent with the dramatic decrease in absorptivity. As the material is completely fused (minimum in the curve), the powder-coated substrate and the dense material have a qualitatively comparable absorption coefficient;
- *Regime II* – By increasing the laser power even more, the material starts to evaporate, and the resulting recoil pressure generates a keyhole (this phenomenon will be discussed later). The multiple laser light scattering on keyhole walls results in a dramatic enhancement of absorptivity;
- *Regime III* – At high power, the fast absorptivity growth saturates as part of the laser radiation is absorbed by the vapours and only a part of the laser intensity hits

the keyhole (as mentioned above, the laser has a Gaussian distribution).

Also scan speed have an effect on absorptivity: by increasing the scanning speed, the entire curve along the power-axis becomes stretched, shifting the trends described above to higher power levels.

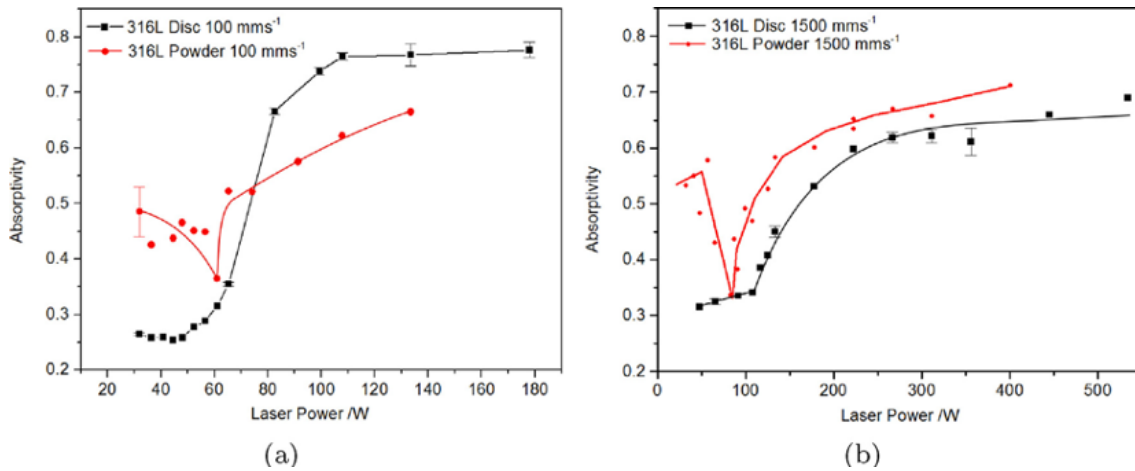


Figure 2.10: Absorptivity of 316L steel with a $100\mu m$ powder layer compared to the absorptivity of a bare disc at $v = 100mm/s$ (a) and $1500mm/s$ (b) [134].

As can be seen in Figure 2.10, absorptivity is highly dependent on laser parameters and its trends are distinctly different for powders and dense material.

Concerning powder properties, powder size and powder distribution also have an influence on the laser absorptivity. Spierings et al. [14] compared three different particle size distributions and two layer thicknesses of SS 316L powder and found that finer particles are easier to be melted and therefore are beneficial for high part densities and high mechanical strength. On the other hand, bigger particles enhance the breaking elongation, nearly reaching the values of conventional stainless steel.

Furthermore, Zhang et al. [156] investigated experimentally and through simulation the influence of particle size on laser absorption, confirming that the powder layer absorptivity diminished while increasing particle size. Indeed, small particles enhance the multiple reflections in powder bed, strengthening the interaction between neighbouring particles and therefore promoting absorption.

These studies only showed some of the possible effects of powder properties in laser-PBF processes. In the following paragraph, the material properties will be deepened, pointing out their effects on the process.

2.3 Materials

2.3.1 Powder Properties

Powder properties play a key role in the quality of additively manufactured parts and the assessment of the complex interaction between these two aspects is of paramount

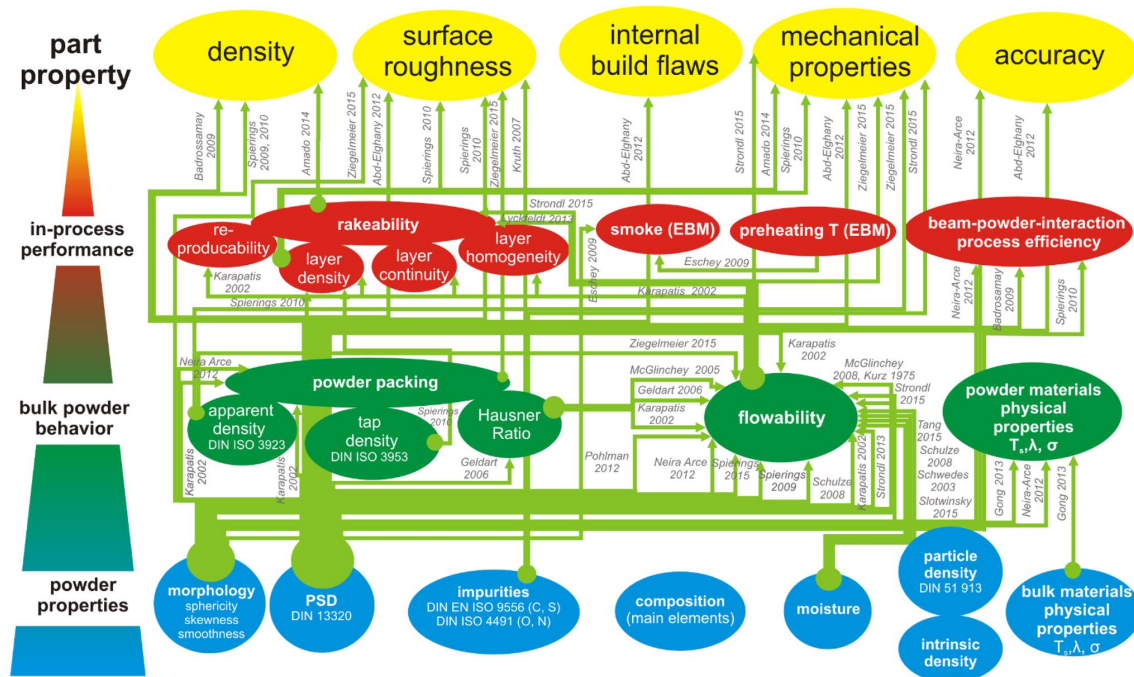


Figure 2.11: Visualization of the relationships between powder properties, bulk powder behaviour, powder performance in process and finally the manufactured part quality as elaborated by different research groups [139].

importance. Although there is still a lack of a comprehensive understanding of powder property-part quality relationship, numerous investigations focusing on this topic have been published in recent years.

Vock et al. [139] provide a comprehensive overview on past and current research activities focusing on the influence of powder quality on different aspects of the PBF processes and part properties. As can be seen in Figure 2.11, the powder-related properties can be categorized into multiple levels and each distinct property can influence multiple features of the building process, which in turn affect different aspects of the part quality.

The first level (the lowest) describes the pure physical and chemical properties of individual powder particles, which are particle morphology, particle size distribution (PSD), impurities content, chemical composition, moisture, particle density and material physical properties.

The second level describes the behaviour of the powder ensemble as a whole; in other words, the achievable powder packing density, the complex behaviour of powders when subjected to movement or stress (flowability) and the physical properties of the bulk powder material. These features are strongly influenced by the powder properties and the interaction between particles (interparticle forces), such as electrostatic interaction, surface tension, Van der Waals forces, friction, etc.

The third level describes the behaviour of powder under process-specific conditions, namely the laser-powder interaction (previously discussed), the powder bed behaviour at preheat-

ing temperature, the sudden scattering of powder during the process (called smoke) and the rakeability, which quantifies the layer forming quality (layer homogeneity, density, continuity and reproducibility). Lastly, the sum of various aspects in each level reflects on part quality features, such as density, accuracy, surface roughness, mechanical properties and internal build flaws.

As can be seen from the complexity of the scheme in Figure 2.11, interconnecting the properties of the individual powder particle with bulk powder behaviour, in-process performance and part quality is a challenging task and there is still a great deal to be done. For the sake of brevity, the most relevant results on the mainly studied aspects in the literature will be summarized below:

- *Particle size distribution* – PSD has a significant influence on bulk powder behaviour. Indeed, Karapatis et al. [55] found that PSD influences the layer density in LPBF: a wide PSD, biased towards fine particles, leads to high powder bulk density, while conversely, a narrow PSD worsens layer density, but improves flow properties. Confirming this last statement, many authors found that flowability increases with decreasing width of the PSD and with the increase of particle size (coarser particles flow better) [139]. Furthermore, bulk powder physical properties are also influenced by PSD. For instance, Gong et al. [39] stated that thermal conductivity is sensitive to PSD, finding that smaller particles show a higher conductivity. Lastly, as discussed in the previous paragraph, PSD influences also laser absorption: small particles promote laser absorption due to the enhancement of multiple reflections in powder bed [14, 156];
- *Powder morphology* – the impact of particle shape on bulk powder behaviour, in-process performance and final part quality is complex to be described and general statements are difficult to be made. According to Schulze [116], particle morphology affects flow properties: coarse spherical-shaped particles (typically smooth) have better flow properties than rough, sharp-edged, non-spherical particles. However, in case of small particles, which are more prone to adhesive forces, rough particles may exhibit a better flow behaviour. Karapatis et al. [55] confirmed that sphericity lead to good flow behaviour, optimal packing density, and good layer deposition, while Spierings et al. [122] found that an increase of ellipticity (deviation from perfect spherical to ellipsoidal form) improves flowability in general;
- *Flowability* – this term generally defines the behaviour of powder when it is mobilized or subjected to stress. For a better understanding, imagine two powder samples contained in jars, one is granulated sugar and the other is flour. Rolling the jar containing sugar on its side will produce a fluid movement in the powder (the sugar will fall smoothly), keeping a constant flow pattern. If rotating the flour container instead, the powder movement will be intermittent, mostly of agglomerates. In this case it is possible to slightly move the jar and find that nothing happens, and then an avalanching event occurs as the powder collapses to a new position. In this loose packing state, these two powders lie at opposite ends of the flowability spectrum: sugar would be described as "free-flowing" and flour as "cohesive". The challenging

task is how to assess and quantify flowability: as Vock et al. reported, several methods can be found in the literature which attempt to quantify flow characteristics (such as flow energy, angle of repose, avalanching behaviour, etc.) and typically correlate them with the powder physical properties and the quality of powder layer formation. However, Vock et al. pointed out that flow characteristics should be tested with equipment as close as possible to the process conditions in order to have reliable results and the term flowability must be specified with regard to the applied testing method (details and references about available testing devices can be found in Vock et al.'s review [139]);

- *Rakeability* – this is the most investigated in-process performance aspect related to PBF. For instance, Karapatis et al. [55] investigated the factors that influence the quality of the powder layer, identifying powder flow and powder packing as the most contributing properties. Furthermore, Lyckfeldt et al. [84] found that the degree of cohesion has to be low to promote good flow properties but in the same time the powder layer should stay uninfluenced by shear stresses when depositing the next powder layer. This implies a high enough flow energy driven by a high tap density rather than cohesive forces. Spierings and Amado correlated in-process performance with part properties: Spierings et al. [14] found that coarser powders lead to a lower powder layer density and an increased surface roughness of the produced part, while Amado et al. [4] stated that powder spreading quality influences the mechanical properties and homogeneity of the part density. In addition, Sun et al. [125] address experimentally the powder layer formation with a powder deposition system (identical to the PBF machine one) in which a digital camera was installed. This enabled the authors to rake the powder under conditions very close to the process ones and to study raking quality by a statistical analysis of the images acquired with the camera. Despite this work, very few studies that use similar setups can be found in the literature, therefore more systematic studies will be necessary to correlate the impact of rakeability on final part quality in conditions as close as possible to the analysed process.

2.3.2 Powder Production

The key in manufacturing high quality components by L-PBF processes is to control the fundamental properties of the powder [9]. Although there are several systems for metal powder production (details can be found in Dixon's review [30]), nowadays the most common methodology is gas atomization. In fact, this production system allows to obtain small particles of predominantly spherical shape. As discussed above, these features are very important to ensure good flowability and rakeability, hence good final part quality. For instance, Li et al. [77] studied the densification behaviour of gas and water atomized SS 316L powder during SLM and confirmed that samples fabricated from gas atomized powder achieved denser structure than samples obtained from water atomized powder (water atomization is another widely used powder production technology). Indeed, authors found that gas atomized powder allow higher packing density with respect to water atomized ones, which generally have an irregular shape (see Figure 2.13).

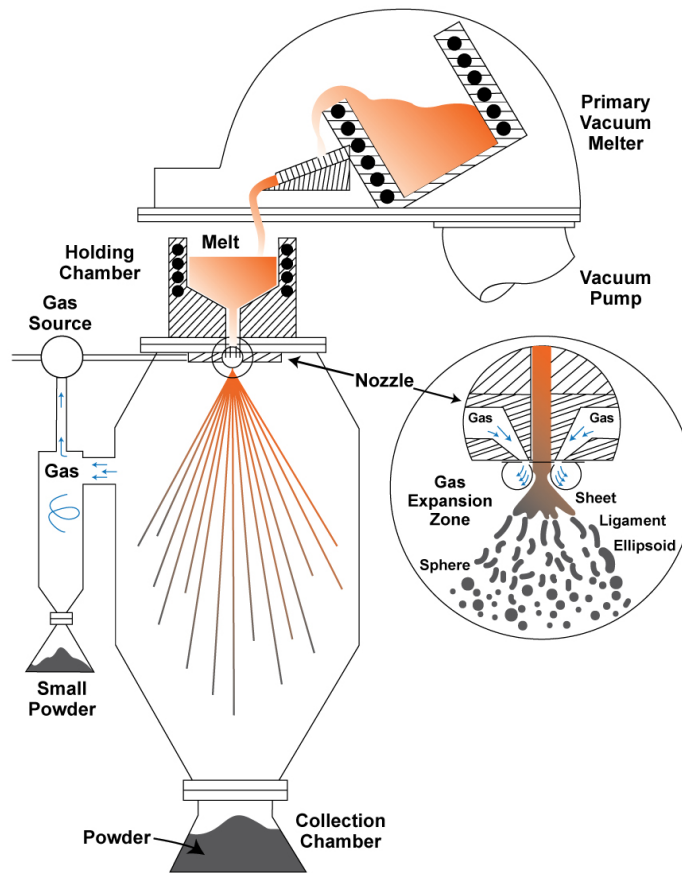


Figure 2.12: Schematic representation of gas atomization process [97].

Furthermore, gas atomized powders have lower oxygen content, leading to better wetting ability for SLM process. Indeed, the whole gas atomization process is generally carried out in vacuum or under an inert atmosphere, allowing the protection of the alloying elements from oxidation.

Typically, these systems are designed for dry powder collection and their height can reach about 6-10 meters, ensuring complete solidification of particles before reaching the bottom of the tank [9]. An example of a gas atomization system can be seen in Figure 2.12.

In this system, the metal to be atomised is first melted and then exposed, through a special nozzle, to a high velocity gas jet which causes the liquid metal to break up into small droplets. To control the particle size, it is possible to vary the design of the atomizing nozzle, the gas pressure, and the size of the metal stream [30]. The droplets subsequently solidify in flight to form the powder, which includes a wide range of sizes. Powders are then classified, usually by sieving or by air classification, into size ranges appropriate for various applications [135].

It is worth noting that although smaller particles can reach a diameter of about 1 micron, they are composed of millions of atoms. It is therefore clear that the term "atomization"

is strictly inaccurate, however it has become the generally accepted term to describe the production of particles below 150 microns.

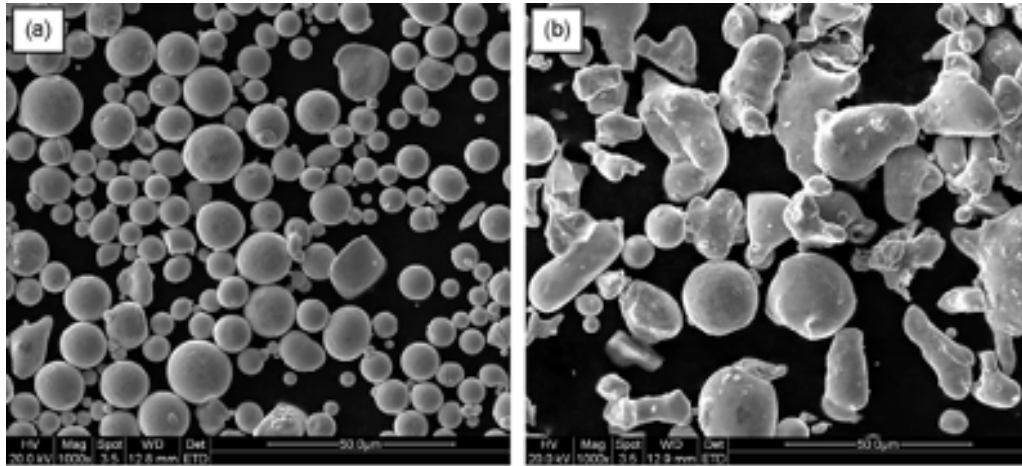


Figure 2.13: Example of SEM images showing characteristic morphologies of stainless steel powder: (a) gas atomized; (b) water atomized [77].

2.3.3 Powder Recycling

In SLM process, only a portion of the powder laid in the building volume is actually lasered to build up a component. The powder surrounding the part remains predominantly unchanged. This fact makes LPBF techniques potentially resource efficient processes; un-melted powders can be collected and recycled in the subsequent build jobs. However, process efficiency is highly dependent on the condition of un-melted powders and on the recycling strategy.

Concerning the latter, powder recycling can be done according to four main strategies [139]:

- *Strategy A* – used and sieved powder is mixed with virgin powder after each build job in constant proportion;
- *Strategy B* – used powder is mixed with powder of the same age after each cycle;
- *Strategy C* – reintroduction of sieved powder after each build job without mixing with other powders;
- *Strategy D* – used and sieved powder is added to the top of the unused virgin powder, no mixing takes place.

In the first strategy, the continuous batch refresh by adding virgin powder to the used one allows to slow down the degradation of the powder over time. However, this recycling strategy results in a large number of different powder conditions and small powder fractions can reach an extremely high cycle age. Furthermore, mixing together powders of

different production batches prevents the traceability of feedstock material, often required by certifications [83].

In the strategy B, the powder batch is allocated to as many build jobs as possible, leaving a residue powder, which is subsequently mixed with powder of the same condition. This strategy results in a collective degradation of powder and therefore it is more suitable for high requirements regarding traceability. According to Vock et al.'s review, Strategy C is the most used in published recycling studies. This is probably due to the absence of powder mixing, which ensures traceability. Indeed, the whole powder batch used is in the same condition and the effects of recycling on powder properties can be systematically studied.

The last strategy (Strategy D) is very practical from a production point of view, as the powder used and sieved is reintroduced without removing the remaining powder of the previous build job and without performing any mixing operation. However, homogeneity of the powder batch is compromised, and this could be reflected on produced parts quality.

In the literature, numerous studies on recycled powders effects can be found, in which authors correlated powder cycle age with powder properties and part quality, finding the maximum number of powder reuse.

For instance, Lutter et al. [83] determined the maximum number of possible use cycles for recycling strategy B regardless of powder quality degradation. This study gives the natural upper limit of the number of use cycles, which varies around an average of 35 cycles (ranging from 1 to 117 cycles) for various production scenarios. As confirmed by Vock et al.'s review, most of the published recycling studies on LPBF stay well below the upper natural cycle limit calculated by Lutter et al., ranging from 2 up to 38 cycles (average value is 12 cycles). This may be due to the different recycling strategy adopted (mainly strategy C), to the limited number of tests performed in some studies and to different regulations adopted for powder quality assessment.

Summarizing these works, the authors have found a general increase of oxygen content in the analysed powders, a slight shift of PSD to larger particle sizes, a slight modification of morphology (particles become rougher and less spherical) and the possible presence of by-products, such as condensates and spatters. Powder degradation, in turn, may have an effect on part quality: many studies revealed a decrease of UTS, yield strength, ductility and impact toughness, while surface roughness has been increased.

However, the literature showed scattered results and often very different from each other (improved, decreased, or even unaffected), despite referring to similar starting alloys and process parameters. These results may be due to the slight effect that, in many cases, powder recycling has on part quality, but it also highlights the need for a standardised methodology for recycled powder assessment.

2.4 Process Parameters

The SLM technology presents over 50 different process input variables that impact the characteristics of the finished part, creating a significant challenge in understanding process physics and developing an effective process control strategy [121]. Broadly speak-

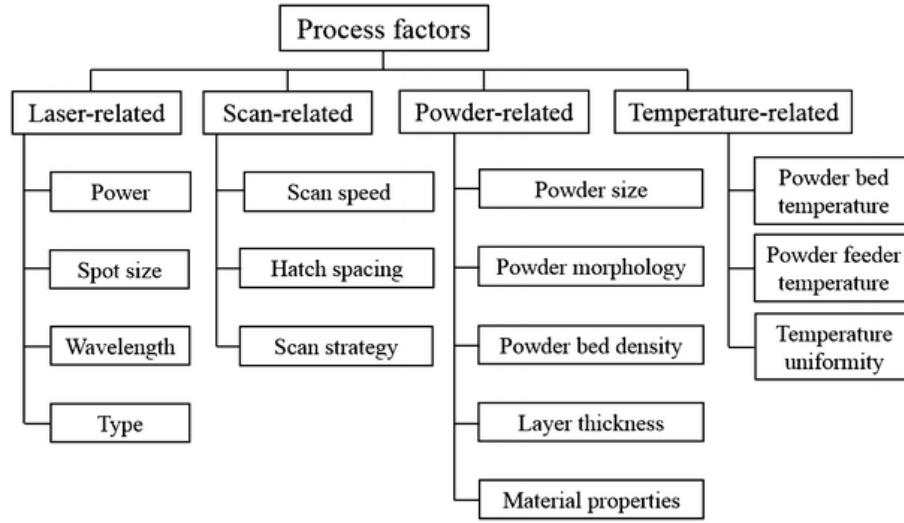


Figure 2.14: SLM process parameters classification [155].

ing, these factors can be classified into four main categories: laser-related, scan-related, powder-related and temperature-related [155]. In Figure 2.14, a simple classification of the main process parameters can be seen.

Most of laser-related variables (laser type and wavelength) and powder-related factors (powder characteristics and material properties) have already been discussed in the previous sections. These variables can be considered as "predefined parameters" because, once chosen, they cannot be manipulated during a typical build process with current technologies. Then, there are other variables defined as "controllable" that can be modified to achieve the desired process performance. These are mainly laser power (P), laser spot size (d_s), scan speed (v), layer thickness (t), hatch spacing or hatch distance (Hd), scan strategy and powder bed temperature.

Since the process itself consists of supplying energy to a powder bed using a laser source, it is reasonable that the first process parameters to take into account are the ones that determine the amount of input energy. In fact, laser power and spot size define the irradiance of the laser (power per unit area - W/cm^2), which is:

$$I_0 = \frac{2P}{\pi(d_s/2)^2} \quad (2.2)$$

for a Gaussian beam at the focal plane. It is worth noting that for most machines used in the literature works, the laser spot size is fixed and therefore the irradiance is determined only by laser power.

Another parameter related to the input energy density is the scan speed, that is, the speed at which the laser moves on the X-Y plane in the work area. Indeed, for lasers operating in continuous mode, this parameter defines the exposure time of the lasered surface and, together with laser power, expresses the *Linear Energy Density* (LED or ED_L):

$$ED_L = \frac{P}{v} \quad (2.3)$$

whose unit of measure is W/mm . This is the simplest expression that is often used as a metric to compare SLM process results under different sets of laser power and scan speed, since these two parameters are the most investigated in the literature, keeping constant the other factors.

Thus, laser power and scan speed effects are typically not studied separately, but rather by making more general considerations about LED: when the LED is too low, the energy delivered to the powder bed is insufficient and the poor melting conditions lead to the retention of a high number of macroscopic pores (from tens to hundreds of microns in size) in the final parts. These pores have a deleterious effect on mechanical properties, such as tensile strength and fatigue resistance. In addition, low LED values lead to low thermal stresses and thus low component warps, while surface quality is typically poor due to melt pool instabilities (this aspect will be treated later).

On the other hand, when the LED is too high, the melt pool becomes very deep and re-melting of multiple layers occurs. In this condition, the melt pool can reach the metal boiling temperature and vaporization of the alloy can take place, leading to intense melt pool convection flows and vapour driven gas bubbles can be trapped in the material, increasing again porosity. Furthermore, The higher the LED, the more severe the contraction of the molten metal in the solidification process. In this condition, components are characterized by high residual stresses and thermal warps, while the surface quality is typically high [11, 85, 155].

Therefore, it is fundamental to define the right LED window in which a compromise between residual porosity, mechanical performance, surface quality and geometrical accuracy can be found.

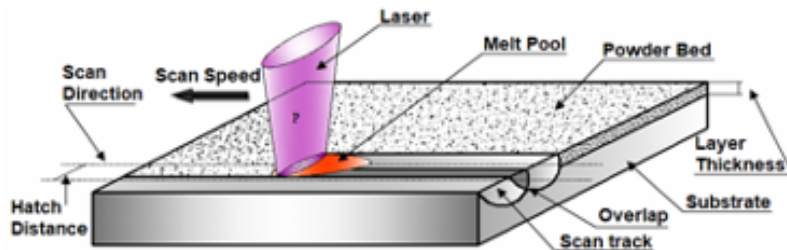


Figure 2.15: Schematic representation of the interaction between laser beam and powder bed.

However, LED involves only two of the main process parameters and its validity is limited to experiments in which only power and speed are modified. Campanelli et al. [17] formulated an alternative expression of energy density that takes into account also the laser spot size:

$$ED_P = \frac{P}{vd_s} \quad (2.4)$$

whose unit of measure is W/mm^2 . The spot size defines the area exposed to the laser radiation and therefore it is of great influence on process resolution and productivity:

keeping constant the energy density, the smaller the spot diameter, the smaller the melt pool width [21].

Liu et al. [79] investigated the effect of the laser spot size in SLM using SS 316L powders. For a reduction in beam size from 48 to 26 μm , improvements in the part density, surface finish, and mechanical properties were reported. Makoana et al. [88] used two different systems with different spot diameters (80 and 240 μm) to investigate the effect of spot size variation during laser-based PBF. It was found that a smaller beam diameter and smaller laser power resulted in a narrower and shallower molten pool, leading to smaller hatch spacing and layer thickness.

Despite extensive research efforts in SLM, it is worth noting that only few researches on spot size effect can be found in the literature, especially on the feature resolution. Since the laser spot size is fixed in most literature works, the aforementioned expression of energy density is not common and no additional information is added compared to the LED.

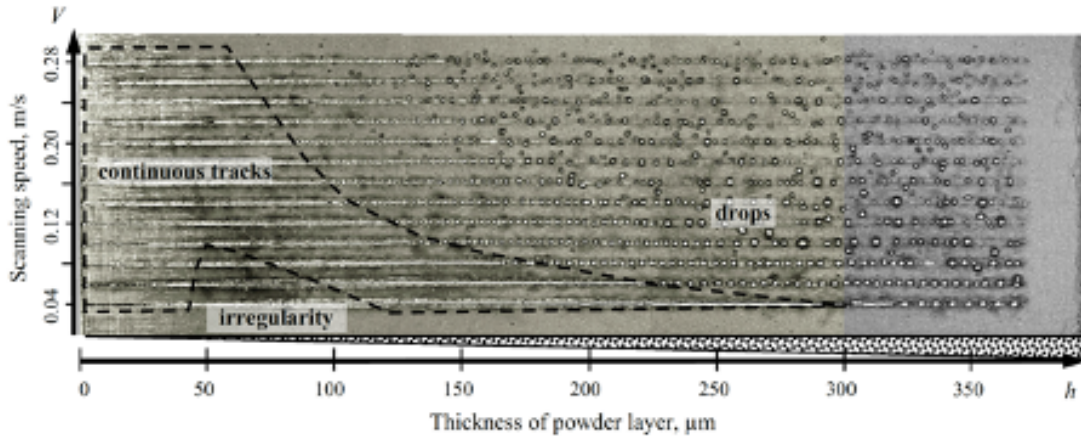


Figure 2.16: Top view of laser melted tracks from SS316L powder on steel substrate. Thickness of the deposited powder layer h varies in the range $0 \div 400\mu\text{m}$, laser power is 50W and scan speed varies in the range $0.04 \div 0.28\text{m/s}$ [148].

A more common expression is the *Volumetric Energy Density* (VED or ED_V), which includes also the layer thickness:

$$ED_V = \frac{P}{vtd_s} \quad (2.5)$$

whose unit of measure is W/mm^3 . The thickness of the powder layer raked multiple times during the whole process has a substantial influence on the material response to laser radiation and considerably affects the process productivity and resolution. Basically, the thickness of a raked layer determines how much powder will be melted by a single laser scan.

Generally, the choice of this parameter stems from a trade-off between the build rate and the resolution: the lower the layer thickness, the higher the resolution (low staircase effect) and the lower the productivity. On the contrary, the higher the layer thickness, the lower the resolution and the higher the productivity. Actually, Yadroitsev and Smurov [147]

found that thinner layer thicknesses provide a stabilizing effect for the laser melted tracks and allow to increase the scan speed. Thus, the reduction in build rate due to the decrease in layer thickness is mitigated by the fact that for thin layers it is possible to operate at higher speeds, as shown in Figure 2.16. It is worth noting that layer thickness is strongly related also to powder properties and to the adopted recoating system [99]. Thus, the choice of this parameter should also take into account the rakeability aspect, especially for thin layers.

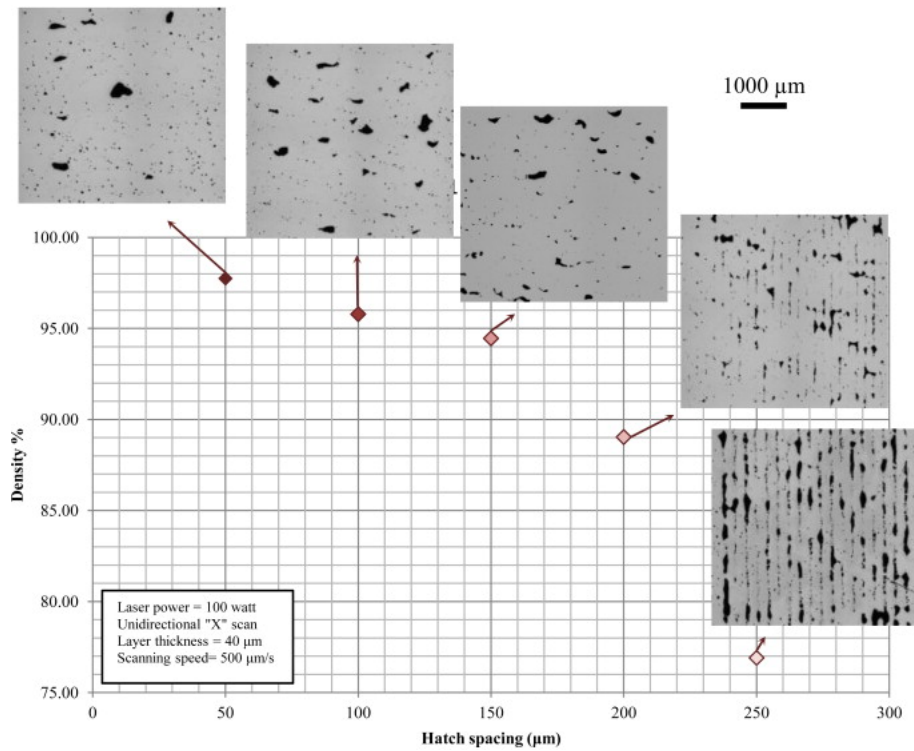


Figure 2.17: Effect of hatch distance on relative density of AlSi10Mg parts [2].

As for VED, there is another formulation from literature in which the spot size is replaced by the hatch distance:

$$ED'_V = \frac{P}{vth_d} \quad (2.6)$$

whose unit of measure is still W/mm^3 . As, can be seen in Figure 2.15, the hatch distance represents the shift between two neighbouring tracks in the plane of beam scanning and defines the overlap rate between them. Indeed, the overlap rate O_r can be defined as:

$$O_r = \frac{W - h_d}{W} 100\% \quad (2.7)$$

where W is the track width, whose value has to be measured from single tracks experiments or estimated (based on spot size considerations).

The hatch distance has a great impact on laser beam – material interaction: a variation

of hatch distance entails thermo-physical modifications of the process. Indeed, after first scanned track formation, the laser beam directly interacts not only with the powder bed, but also with a portion of the previous melted track. Thus, the already formed tracks will inevitably have a heat effect on the next track, impacting on the energy density needed for a good layer formation [28].

Basically, low hatch distance can cause high VED values. As a result, vaporization may become severe and pores can be formed due to trapped gas bubbles. Meanwhile, the large overlapping area due to low hatch distance promotes the enhancement of surface roughness, which is unfavourable for powder spreading and subsequent printing. Therefore, more pores can be formed at the corner of the overlapped melt tracks because of the rough surface [158].

On the contrary, increasing hatch distance increases the gap between two neighbouring tracks, until reaching their isolation (no overlapping area). At high hatch distance values, poor surface finish and large irregular pores can be observed in the final parts. Such pores may arise from gaps between neighbouring tracks, due to lack of overlap. Moreover, the gaps are hard to be filled up due to the high melt pool viscosity and low penetration depth of the melts, which are related to low VED (hatch distance is inversely proportional to energy density) [149, 158].

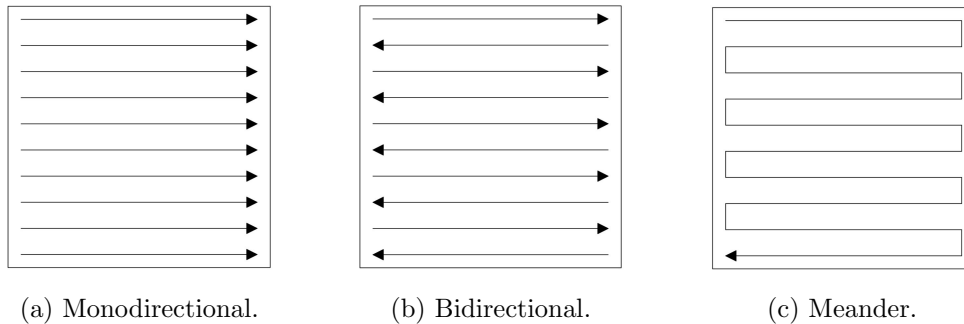


Figure 2.18: Different continuous exposure strategies.

Another factor that significantly affects the process outcome, especially in terms of porosity and residual stresses, is the scan strategy. There are numerous ways to scan the layer surface and several studies on this topic can be found in the literature.

The continuous line scanning is the basic scan strategy, in which the scan vectors of the laser path are continuously scanned with a constant hatch distance over the entire layer. As can be seen in Figure 2.18, continuous scanning can take place according to 3 different exposure approaches: monodirectional, bidirectional and meander. In the continuous monodirectional scanning each scan vector has the same direction, while in the continuous bidirectional scanning neighbouring vectors have opposite direction. The meander strategy is similar to the bidirectional one, but the laser does not interrupt the exposure passing from a scan vector to the other.

However, scanning large areas with continuous scan strategy could induce high residual stresses due to the high thermal difference in the opposite ends of the scanning vectors [63, 65].

Thus, the direction of scan vectors is typically rotated at a certain angle for each layer (see Figure 2.19). Rotating layer-by-layer the exposure direction promotes isotropy and porosity distribution uniformity.

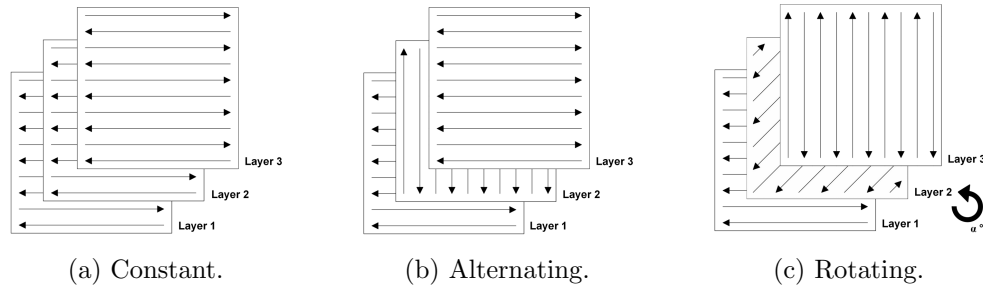


Figure 2.19: Different layer exposure strategies.

In some cases, different process parameters within a single layer can be beneficial for part production, thus the *hull and core* or *skin and core* strategy can be used. In this strategy, the layer is divided into two areas: the outer contour, which is the skin area, and the central region, which is the core area. This approach allows to set high layer thickness in the core area, hence reducing the build time, and low layer thickness in the skin area, to maintain a high accuracy and good surface finish. However, this scan strategy requires a preliminary process parameter optimization step, in order to define optimal sets of parameters for both scanning areas. In addition, its impact on the part performance remains poorly understood [27].

The most used scan strategy for industrial applications is the island strategy, which consists in splitting the entire layer area into numerous local squared areas (islands) that are scanned in a random order. As can be seen in Figure 2.20b, at each successive layer, the islands scan vectors are rotated by 90 degrees and shifted by 1 mm along both X and Y axis.

By applying this scan strategy, the accumulation of defects in same location is avoided and the residual thermal stresses in the final part are lower and more balanced. The idea behind this strategy is the minimization of scan vector length and the random distribution of layer heat accumulation. Indeed, Kruth et al. [65] investigated the effect of scan vector length on residual thermal stresses and found that the lower the scanning length, the lower the thermal stresses.

Concerning thermal stresses, also powder bed temperature plays an important role. For instance, Buchbinder et al. [15] investigated the effect of preheating temperature on thermal distortions of aluminium components during SLM process. The experiments were performed at different build platform temperatures, starting at room temperature up to 250°C . The authors found that increasing preheating temperature the thermal gradients during production are reduced, thus distortions can be drastically lowered, and cracks caused by thermal stresses can be prevented. Vrancken et al. [140] performed similar investigation on Ti6Al4V, finding a reduction in residual stresses of 50%. Casati et al. [19] investigated preheating effect on mechanical properties of the AlSi10Mg alloy and found that the highest level of hardness and tensile strength of specimens can be achieved when

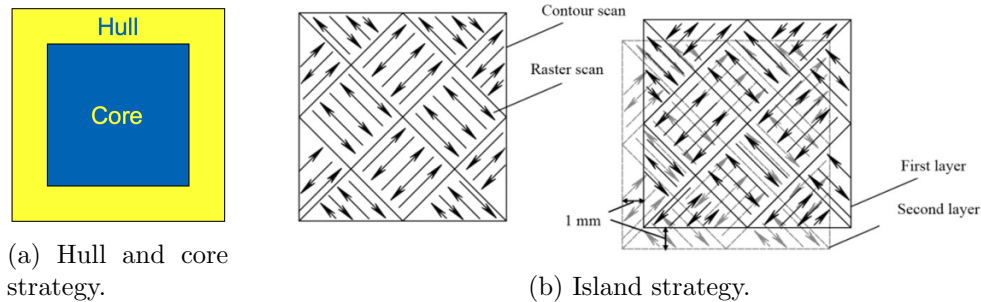


Figure 2.20: Alternative scanning strategies.

the build platform is at room temperature. With the preheated platform there is drop of mechanical performance instead. It is supposed that the rather long holding times spent at high temperature during the process could induce a substantial overaged temper in the components.

Kempen et al. [56] found that preheating temperature also influences the part density: increasing build platform temperature, an increment of relative density can be observed. Furthermore, the higher the preheating temperature, the lower the energy input is needed to melt the powder. Therefore, the authors observed that higher scan speeds can be used for higher preheating temperatures, producing equally dense samples.

It can be concluded that understanding the effects of each parameter on the observed process output is a challenging task because of the mutual interaction between the effects of process variables. The various energy density expressions can be useful to make different considerations on final parts quality under different sets of process parameters. Nevertheless, it is worth noting that these formulations are not able to model accurately the complex physics of the process. Indeed, Bertoli et al. [11] investigated the reliability of VED as a design parameter by comparing single tracks of SS 316L produced with different sets of process parameters and found that VED does not accurately describe the track shape evolution. Indeed, the VED is able to reduce the combinations of parameters needed for the detection of the process window but is unable to identify the latter accurately.

For better understanding the limits of energy density formulations, the melt pool physics will be discussed in the following section.

2.5 Melt Pool Physics

SLM process involves complex physical phenomena such as absorption and scattering of laser radiation, heat transfer, phase transformation, fluid flow within the molten pool, evaporation, emission of material, and chemical reactions [71, 148].

When the laser beam interacts with the powder bed, most of the energy flux is absorbed by the powder particles, leading to localized melting. Although this process is similar to laser beam welding, the laser – powder particles interaction adds significant complexity to the process physics, as discussed in the previous paragraphs. The melted region, called

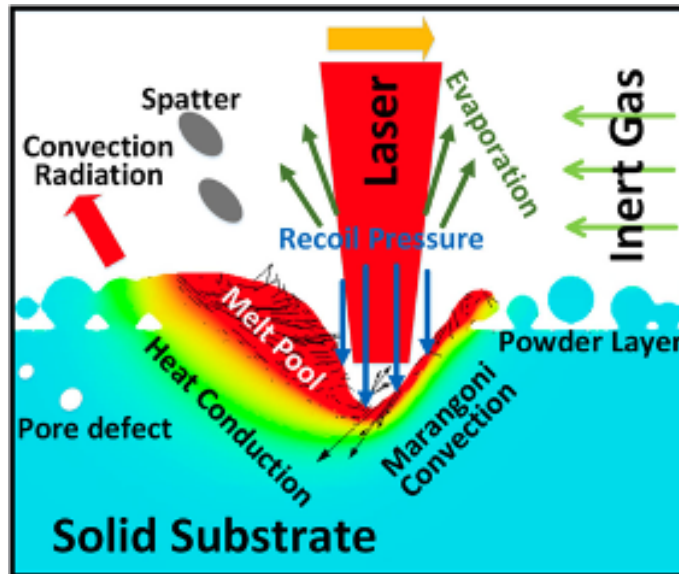


Figure 2.21: Schematic representation of the general phenomena in the SLM process [22].

melt pool, has typically higher width than the beam spot size and it has an elongated circular shape in the opposite direction of scanning. As can be seen in Figure 2.21, the melt pool depth is greater than powder layer thickness and re-melting of solid substrate takes place. Partial melting of preceding layer is paramount to form a solid part and achieve high density and good mechanical performance. Furthermore, the molten track can be subdivided in three regions: a *depression region* placed at the laser spot, a *tail end region* located near the end of the melt track, and a *transition region* in between [58].

Because of typical laser intensity profile (Gaussian distribution) and of heat transfer mechanisms, the melt pool is characterized by a high temperature gradient between the central region below the laser spot and the melt pool boundary. Indeed, the surface temperatures below the beam spot can become high enough to reach boiling values. Once the material evaporates, the resulting recoil pressure creates a melt pool surface depression, which gives the name to the region below the laser. Moving towards the melt pool boundary, temperatures drop until reaching the solidification value. At the boundary region, there is a transition between liquid and solid phase where both states of matter coexist. This region is denoted as *mushy zone* (yellow area in Figure 2.21) and it is characterized by a high capability in adhering powder particles onto it due to high viscosity and a very rapid cooling rate [103].

Since the heat of laser source can be transmitted up to hundreds of microns from the melt pool, in the region close to it a *heat affected zone* can be formed (green area in Figure 2.21).

After laser exposure, the melted region rapidly solidifies due to heat conduction with the solid substrate and, convective and radiative heat transfer with the inert gas atmosphere. The metallurgical properties of the resulting solid track depend on cooling rate and on melt pool stability. As a matter of fact, the melt pool is highly dynamic and its shape con-

stantly evolves during the process [60, 103]. The main driving forces that affect the melt pool shape evolution are surface tension forces, recoil vapour pressure and viscous forces [128]. These ones are highly dependent on temperature distribution thus on energy input, which in turn is defined by process parameters. Therefore, depending on the technological parameters, the melt pool reshaping can range from a quasi-stationary shape (with little deviations) to significant changes in geometry.

The main physical phenomena that affect this dynamic behaviour are Rayleigh-Plateau instability, Marangoni convection and recoil pressure, which will be briefly discussed in the following sections.

2.5.1 Rayleigh-Plateau Instability & Balling effect



Figure 2.22: Water dripping from a tap [159].

The most obvious physical phenomenon that affects the melt pool dynamics is the Rayleigh-Plateau instability, or capillary instability. First observed by Savart [113] and later explained by the experiments of Plateau [106] and Rayleigh [111], this phenomenon is well known in fluid dynamics. Indeed, to detect such instability it is sufficient to observe the jet of water issuing from a tap. By slowly closing the faucet, the cylindrical liquid flow gradually reduces its diameter until separating in small droplets (Figure 2.22). This phenomenon is mainly related to liquid surface tension, or rather to surface energy minimization of the system. Basically, when the aspect ratio (diameter/length) of the liquid cylinder is lower than a certain threshold, the system tends to separate into droplets with equal volume in order to minimize surface area and thus surface energy of the system. By applying axial harmonic disturbances with different wavelengths to a vertically falling liquid stream (liquid cylinder), Lord Rayleigh found the stability limit condition of the system, which is defined as follows:

$$\frac{\pi D}{L} > 1 \quad (2.8)$$

where D is the cylinder diameter and L is the perturbation wavelength [148]. In a real system, tiny perturbations are always present. For instance, in the case of faucet there is a vibration due to friction between the liquid stream and the nozzle. Resolving the perturbations into sinusoidal components, it can be observed that some components grow with time and other decay. Among the growing components, the one that grows faster dominates the stream shape evolution if there is enough time to increase perturbation amplitude. Basically, if the dominant perturbation wavelength (L) exceeds the jet circumference (πD), the fluid system becomes unstable and the liquid stream breaks up into drops (Equation 2.8).

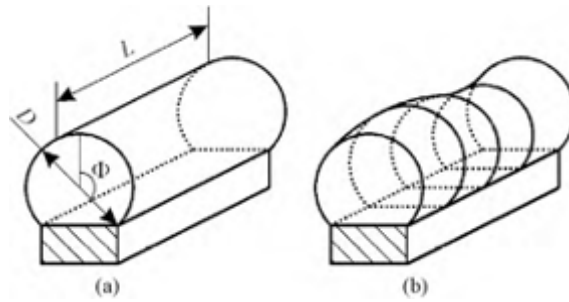


Figure 2.23: Segmental cylinder of a liquid on the substrate: (a) non-disturbed; (b) disturbed [148].

Yadroitsev et al. [148] extended the analysis of this phenomenon to single tracks formation in SLM. Authors modelled a melted track as a liquid segmental cylinder attached to a solid substrate by a contact band with a fixed width. As shown in Figure 2.23a, the contact width is specified by angle Φ . Considering the equation of a segmental cylinder with harmonically disturbed radius (Figure 2.23b), they found that the system is stable at any perturbation wavelength if $\Phi < \pi/2$ (less than a half cylinder). On the other hand, if $\Phi > \pi/2$, the stability condition becomes:

$$\frac{\pi D}{L} > \sqrt{2} \sqrt{\frac{\Phi(1 + \cos 2\Phi) - \sin 2\Phi}{2\Phi(2 + \cos 2\Phi) - 3 \sin 2\Phi}} \quad (2.9)$$

In the limit case $\Phi = \pi$, the Equation 2.9 gives:

$$\frac{\pi D}{L} > \sqrt{\frac{2}{3}} \quad (2.10)$$

which is less than the limit for the free circular cylinder of Rayleigh-Plateau because the segmental cylinder with $\Phi = \pi$ is still attached to the substrate by a line and deforms with the loss of the axial symmetry. Thus, the segmental cylinder is in general more stable than the free circular one. Basically, the lower the angle Φ , the greater the stability of the melt pool. On contrary, if Φ is high and the circumference-to-length ratio is low, the melt pool becomes unstable and it breaks up into droplets. In early studies on SLM process, this instability was named *balling effect*, since the resulting melted track consisted of a series of “balls”. In literature the term balling is widely used and identifies a process region in

which the melt pool is affected by the Rayleigh-Plateau instability. In terms of processing conditions, balling regime occurs at low energy input and lack of fusion takes place. In this condition, the temperature ranges between solidus and liquidus temperatures and there is insufficient substrate penetration (Φ angle is close to π). According to Yadroitsevs et al. [148] experimental results, substrate penetration (i.e. a decrease in Φ angle) is crucial for stabilizing the melt pool. This can be obtained by increasing laser power or by decreasing scan speed. Furthermore, the authors found that a decrease in scan speed decreases melt pool length and increases its width. This leads to greater circumference-to-length ratio, which is beneficial for stability.

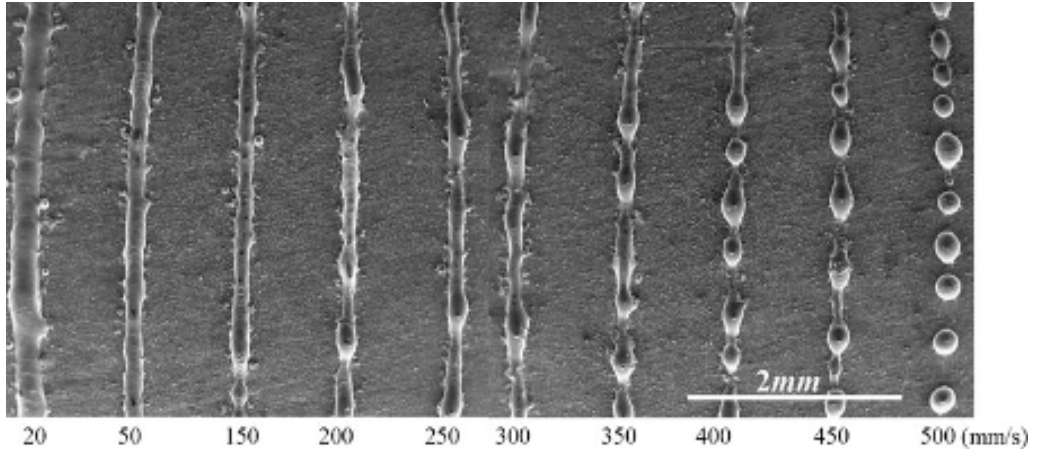


Figure 2.24: SEM images showing the balling characteristics of single scan tracks under different scan speeds [76].

Wang et al. [143] performed a dimensionless analysis on the energy equation controlling the SLM process and proposed a dimensionless number that allows to define the threshold below which lack of fusion occurs: the so-called *single track melting efficiency*. This parameter represents the ratio of the energy density of laser to the one required by sufficient fusion below the laser spot, and it can be written as follows:

$$N_m = \frac{AP}{\pi w_0 t v \rho c (T_m^{eff} - T_0)} = \frac{\frac{AP}{\pi w_0 t v}}{\rho c (T_m^{eff} - T_0)} = \frac{E_v^*}{\rho c (T_m^{eff} - T_0)} \quad (2.11)$$

where A is the absorptivity, P is the laser power, v is the scan speed, t is the layer thickness, ρ is the density, c is the heat capacity and T_0 is initial powder temperature, while w_0 is the beam radius at the waist. Assuming that the focal plane is coplanar with powder bed, $w_0 = d_s/2$.

Here, T_m^{eff} is the effective melting point, that is:

$$T_m^{eff} = T_l + \frac{L_m}{c} \quad (2.12)$$

where T_l is the liquidus temperature and L_m is the latent heat of melting.

In Equation 2.11, the authors defined the volumetric energy density E_v^* as follows:

$$E_v^* = \frac{AP\tau}{\pi w_0^2 t} \left(= \frac{APw_0}{\pi w_0^2 tv} \right) \quad (2.13)$$

where τ is the time that the laser needs to cover a characteristic length w_0 .

According to Equation 2.11, the energy density of laser should be higher than the sum of sensible and latent heat to ensure single track continuity ($N_m > 1$). $N_m \leq 1$ condition is typically obtained at low laser power and high scan speed, or high values of layer thickness or spot size. So, by increasing laser power or by reducing scan speed, layer thickness or spot diameter, the formation of a continuous and smooth single track can be ensured. This is in accordance with the work of Yadroitsev et al. [148].

Although this threshold can be useful to predict the process region in which balling

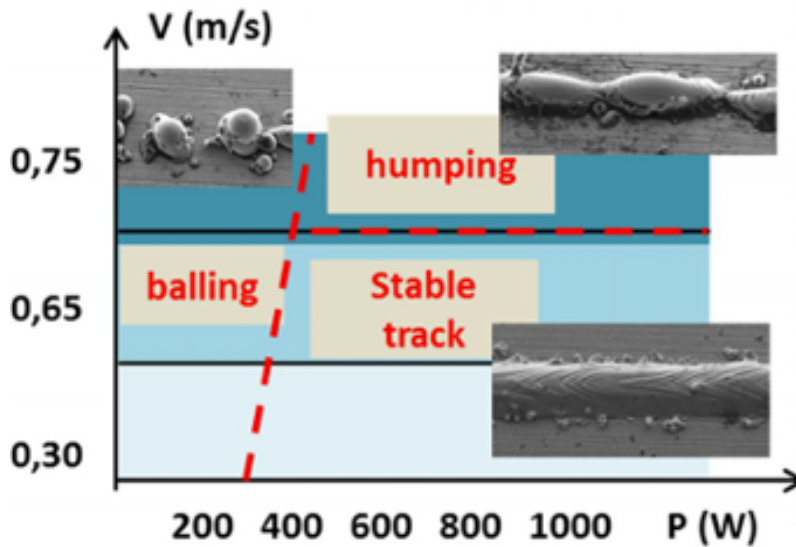


Figure 2.25: LPBF process map indicating the zones of instabilities [43].

phenomenon may occur and therefore to reduce the number of processing conditions to be investigated for process optimization, the *single track melting efficiency* cannot accurately describe the balling occurrence. As a matter of fact, these simple analytical models are not able to fully capture the process complexity and the mutual interaction between physical phenomena.

For instance, in the case of balling phenomenon, the Rayleigh-Plateau instability is not only related to lack of fusion, but it can also occur with high laser power and high scan speed values.

In this particular processing condition, there is a sufficient substrate penetration. Nevertheless, the temperature below the laser spot reaches boiling values and material evaporation takes place. The consequent recoil pressure (which will be discussed later) interacts with Rayleigh-Plateau effect and viscous shear forces, leading to the periodic formation of humps and valleys in the resulting melted track [43]. Since the track shape resembles the one obtained in case of lack of fusion (a series of droplets), this processing condition

was often related to balling phenomenon. However, in recent studies, high-power and high-speed instability has been called *humping effect*, so that it can be distinguished from balling phenomenon (see Figure 2.25). In addition, Tang et al. [128] provided insights into

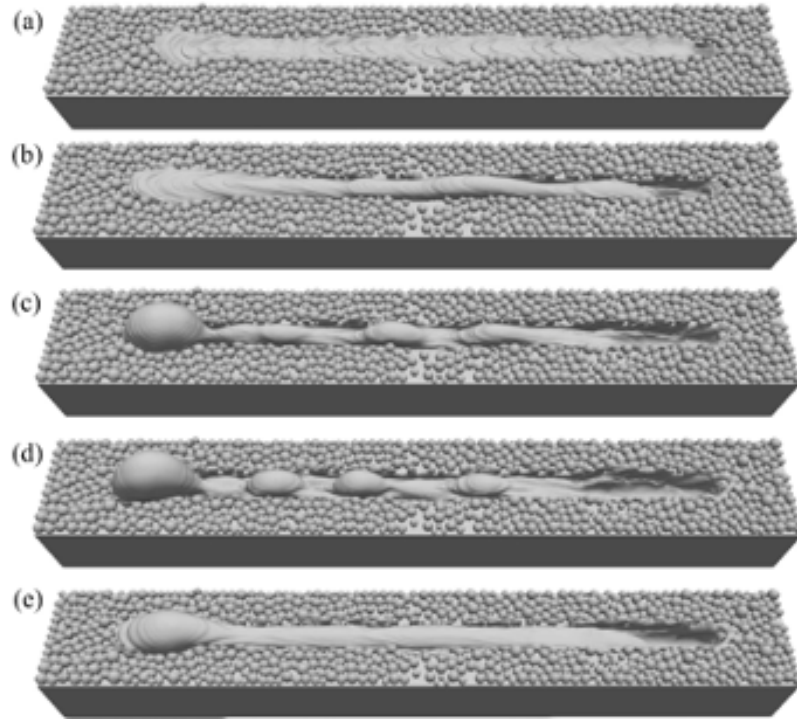


Figure 2.26: Surface topologies of SS 316L simulated tracks with varying viscosities. (a) to (d) were fabricated with zero viscosity, with processing parameters of (a) 100W and 0.4m/s, (b) 200W and 0.8m/s, (c) 300W and 1.2m/s, (d) 400W and 1.6m/s. (e) was achieved with a viscosity of $2 \times 10^{-2} \text{kg m}^{-1} \text{s}^{-1}$, a power of 400W and scan speed of 1.6m/s [128].

the underlying mechanisms of humping formation through simulation approach, which was subsequently experimentally validated. According to the authors, humping is triggered by material evaporation at high-scan speed condition. The resulting recoil pressure produces a backward momentum that moves the molten material backward to the transition region of melt pool. In this stage, the intense flow inertia tends to eject molten material at the tail end region, whereas high surface tension has an opposite effect. For high-speed LBPF (elongated melt pools), also viscous shear stresses can decelerate the backward fluid flow and reduce flow inertia. Thus, the competition between surface tension and flow inertia results in the accumulation of molten material at the tail end region. Since the rear part of melt pool is close to a thin liquid cylinder attached to a solid substrate, the molten material preferentially breaks into separated droplets with smaller surface area. With the occurrence of Rayleigh-Plateau instability, the swelling in the tail end region accounts for the formation of humps after solidification.

To better appreciate the effects of viscous forces, the authors performed simulations with

different viscosities and found that humping defects become more severe in absence of viscous forces. Referring to Figure 2.26, case (d) and case (e) were simulated with same process parameters, but different viscosities were applied. In the first case, viscous forces were not considered, while in the second case a viscosity of $2 \times 10^{-2} \text{ Kg m}^{-1} \text{ s}^{-1}$ was applied. It is evident that high viscous shear stresses prevent humping defects, whereas their absence exacerbates melted track instability. Furthermore, considering case (a) to (d) in Figure 2.26, the authors confirmed that tracks produced with same energy density, but different sets of laser power and scan speed, lead to different results, as experimentally observed by Bertoli et al. [11]. In other words, this result shows the limits of energy density analysis, which can be used to roughly exclude process instability zones but cannot accurately define the right process window.

2.5.2 Marangoni Convection

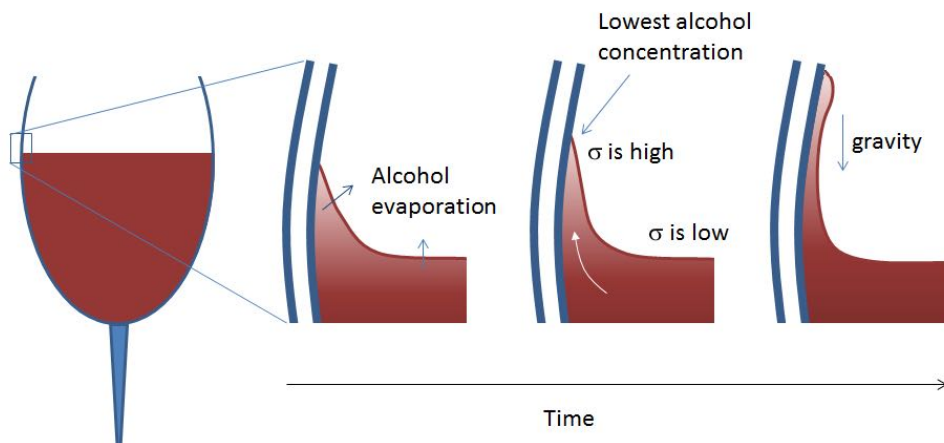


Figure 2.27: Schematic representation of how “tears of wine” are generated by the Marangoni effect [23].

The Marangoni effect is the mass transfer at the interface between two phases (typically liquid and gas) due to a surface tension gradient, which in turn is due to thermal gradients and/or concentration gradients [23].

This effect was first observed in the so-called “tears of wine” by James Thomson (Lord Kelvin’s brother) in 1855 [131]. However, it was the Italian physicist Carlo Marangoni who explained the nature of this phenomenon, presenting his experimental results in the doctoral thesis published in 1865 [90].

As already mentioned, the Marangoni effect can be easily observed by looking at a glass of strong wine. Since ethanol and water have different evaporation rates, a concentration gradient takes place. The resulting surface tension gradient lifts liquid upwards against gravity along the surface of the glass by some millimeters.

Another way to obtain the Marangoni effect is through thermal gradients. As a matter of

fact, surface tension of any substance is a decreasing function of temperature. Considering a liquid-gas interface having a hot region and a cold region (Figure 2.28a), surface tension will have high values in the cold region and low values in the hot region. This imbalance in surface tension will cause a surface motion from the warmer to the colder liquid surface regions. Furthermore, because of liquid phase viscosity, the surface motion will propagate within the liquid, giving rise to convective flows. This phenomenon is called *thermal Marangoni convection* or *thermo-capillary convection*.

In the SLM process, Marangoni convection is the basis of melt pool dynamics. Because

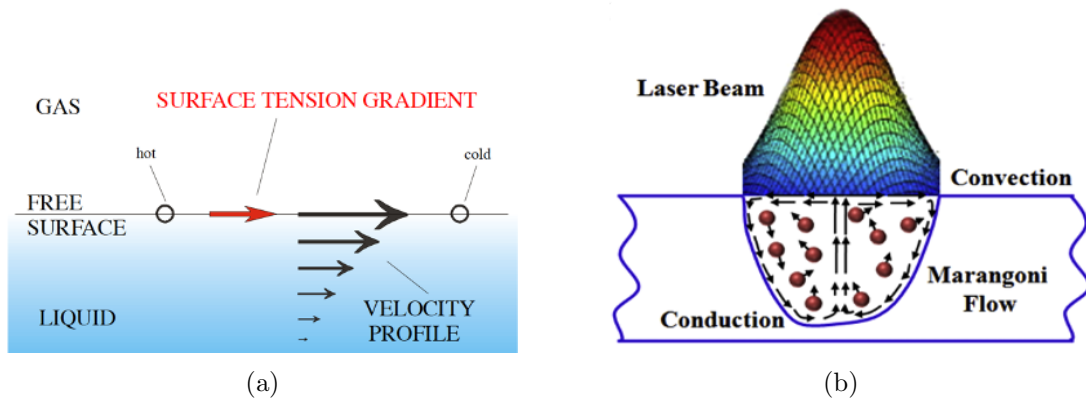


Figure 2.28: Schematic representation of the effect of surface tension gradient due to temperature gradient on the free surface of a liquid [114] (a), and of melt convection pattern in the melt pool [26] (b).

of laser intensity profile (Gaussian distribution) and of heat transfer mechanisms, the processed material will be hotter below the laser spot and colder at melt pool boundary. The resulting thermal gradient triggers a convective flow that moves the fluid along the free surface from the center to the edges of the melt pool. When the flow reaches the edges, it deflects down the liquid-solid interface and reverses up to the center, getting a full counterclockwise (or outward) convection pattern (see Figure 2.28b).

In case of thermal gradients, the intensity of Marangoni flow can be expressed by the so-called *Marangoni number* (dimensionless) [81]:

$$Ma_{Thermal} = \frac{d\gamma}{dT} \Delta T \frac{L}{\mu \alpha} \quad (2.14)$$

where $d\gamma/dT$ is the surface tension gradient ($N/(m \cdot K)$), ΔT is the temperature difference along the melt pool radius (K), L is the characteristic length of the free surface (m), μ is the dynamic viscosity ($Pa \cdot s$ or $Kg/(m \cdot s)$), and α is the thermal diffusivity (m^2/s). Alternatively, the Marangoni number can be expressed also by the following: [42]:

$$Ma'_{Thermal} = \frac{\Delta\gamma_T L}{\mu \nu} \quad (2.15)$$

where $\Delta\gamma_T$ is the surface tension difference (N/m), L is the characteristic length of the free surface (m), μ is the dynamic viscosity ($Pa \cdot s$ or $Kg/(m \cdot s)$), and ν is the kinematic

viscosity (m^2/s).

A good outward flow intensity is essential for melt pool stability [20]. In fact, the melt flow recirculation is beneficial to increase the melt pool size (width, length and for metals also depth) and to cool down the surface region beneath the laser spot, reducing vaporization. Generally, a high surface tension gradient helps the smoothness of the resulting melted track, reducing balling occurrence. However, an excessive Marangoni flow leads to material splashing and, combined with high recoil pressure, can generate the so-called “keyhole” phenomenon, which will be treated later. The right Ma value can be achieved by setting the correct process parameters. Indeed, Dai et al. [26] found that the Marangoni number approximately increases in a linear relationship with the enhancement of the applied energy density.

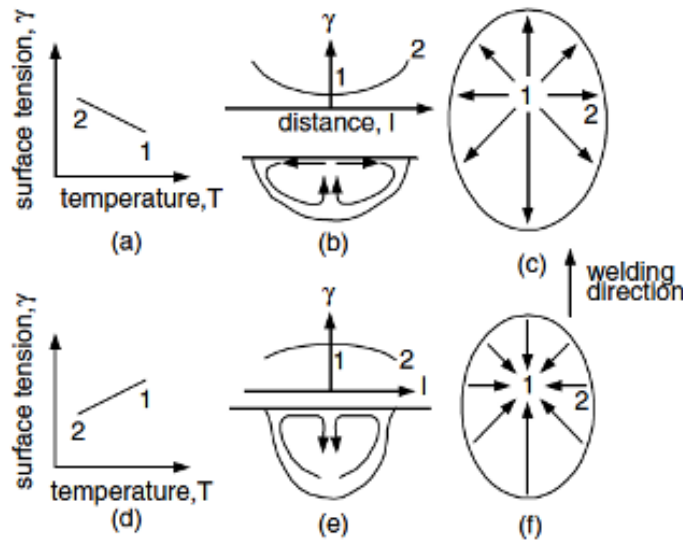


Figure 2.29: Marangoni convection in a weld pool: (a,b,c) low-sulfur steel, (d,e,f) high-sulfur steel [61].

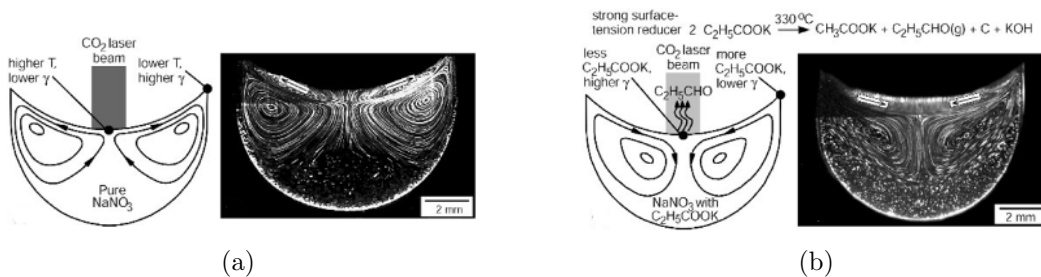


Figure 2.30: Marangoni convection with an outward surface flow in a $NaNO_3$ pool (a), and Marangoni convection with an inward surface flow in a $NaNO_3$ pool containing $2mol\%$ C_2H_5COOK as a surface-active agent (b) [61].

However, it is not always possible to manage convective flows inside the melt pool using process parameters. Although the surface tension gradient is generally negative for metals, there are conditions in which it becomes positive, hence the resulting convective flow is reversed (clockwise or inward).

One of the main causes of the Marangoni flow inversion (from outward to inward) is the presence of surface-active elements within the melt pool. In SLM and welding of metals, the most critical surface-active elements are oxygen and sulfur. In addition, element enrichments of a multi-element alloy can also be surface-active. For instance, *Si*, *Cr*, *Mo* can be rejected during the austenitic solidification in SS 316L and cause local surface tension variations; the same can happen with the precipitation of Si in Al-Si alloys [157].

The resulting convective flow pulls the liquid material from free surface edges to the centre, modifying melt pool shape: width and length are reduced, while the surface height becomes irregular (formation of hills and valleys). Because of this, positive tension gradients negatively affect the melt pool stability, leading to balling phenomenon [20, 26].

The intensity of solutal Marangoni flow can reach 3-5 times that of thermal flow and it can be defined as [5, 81]:

$$Ma_{Solutal} = \frac{d\gamma}{dC} \Delta C \frac{L}{\mu D} \quad (2.16)$$

where $d\gamma/dC$ is the surface tension gradient, ΔC is the concentration difference of the surfactant, L is the characteristic length of the melt pool, μ is the dynamic viscosity, and D is the surfactant diffusivity.

In SLM research works, solutal Marangoni flow is often studied in case of oxidation. For instance, Dai et al. [26] developed a simulation model in which the influence of *O* element on fluid flow driven by surface tension gradient was considered. The material used was AlSi10Mg, which was considered firstly pure and after in presence of oxidation. Their simulation confirmed that the surface tension can be dramatically decreased by $\sim 20\%$ as the oxidation is formed in the melt pool. In such condition, the convective flow reverses to form a clockwise circulation and experiments confirmed that balling effect takes place. Despite the extensive works that can be found in literature, especially for thermal Marangoni flow, very few studies have taken into account both Marangoni effects together. To do this, the general equation of surface tension variation has to be considered [157]:

$$\frac{\delta\gamma}{\delta T} = -A - R\Gamma_s \ln(1 + K_{seg}a_i) - \frac{K_{seg}a_i}{1 + K_{seg}a_i} \frac{\Gamma_s \Delta H^0}{T} \quad (2.17)$$

where A is a temperature coefficient, R is the gas constant, Γ_s is the saturated surface excess, K_{seg} is the equilibrium absorption coefficient of surface-active elements, a_i is the activity of surface-active elements, and ΔH^0 is the standard heat of adsorption. Through this formulation, temperature and concentration variations of melt pool can be taken into account. However, all coefficients in the equation must be known.

2.5.3 Recoil Pressure & Keyhole

In L-PBF processes the depth of the molten pool is typically controlled by conduction of heat in the underlying solid material. However, under certain conditions, the melt pool

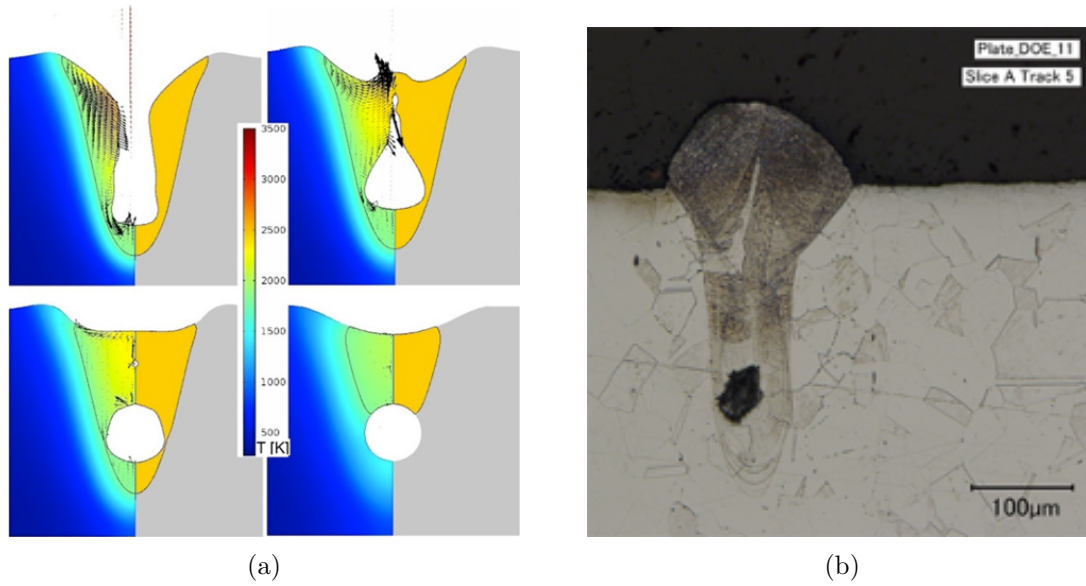


Figure 2.31: (a) Melt pool shapes and temperature field during the keyhole collapse and porosity formation [25]; (b) Metallographic cross sections of a single track affected by keyhole porosity [59].

evolution can be controlled by material evaporation. As previously stated, the surface temperatures below the beam spot can become high enough to reach boiling values. When the molten material begins to evaporate, there is an instantaneous volume increase, which generates the so-called recoil pressure [59]. According to Qiu et al. [109], the recoil pressure can be defined as follows:

$$p_{recoil} = p_0 \exp \left[\frac{\Delta H_v}{R} \left(\frac{1}{T_v} - \frac{1}{T_m} \right) \right] \quad (2.18)$$

where p_0 , ΔH_v and R are atmospheric pressure, enthalpy change due to evaporation and universal gas constant, respectively, while T_m is the melting temperature and T_v is the boiling temperature.

The recoil pressure causes a melt pool surface depression, which forms a vapour cavity. If the laser energy input is high enough to evaporate a large portion of the molten material, this cavity becomes deeper and multiple reflections of the laser beam take place within it, enhancing radiation absorption. This causes further deepening of melt pool, which can reach depths of hundreds of microns (the laser literally “drills” the substrate). As long as the radiation is applied, the melt pool is ejected upward under the effect of recoil pressure, keeping most of the molten material at the top (see Figure 2.31a).

Due to high thermal gradients, Marangoni convection is the dominant mode of heat transfer and it also has an influence on melt pool upward ejection. Indeed, the top region of the melt pool is wide due to the strong outward Marangoni flow, whereas the bottom of the melt pool is narrow. The resulting melt pool cross-section view resembles the shape of a keyhole (see Figure 2.31b), so this operational regime is called *keyhole mode*.

Once the laser has moved away, vaporization and therefore recoil pressure are immediately stopped. Accordingly, due to gravity and surface tension forces, the upper part of melt pool rapidly collapses from above the keyhole, entrapping gas inside it. Indeed, the small quantity of liquid in the lower part moves too slowly to fill the keyhole from the bottom and a residual porosity at the end of solidification is almost always formed in this particular operational regime [25]. Therefore, keyhole mode should be avoided during L-PBF processes in order to obtain components with low residual porosity.

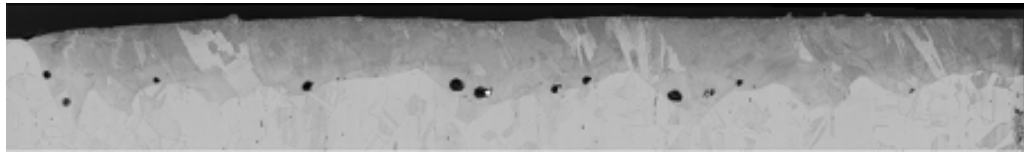


Figure 2.32: Longitudinal cross section of a single track produced with SLM technology. Voids arising from keyhole mode melting can be observed near the bottom of the melt pool [59].

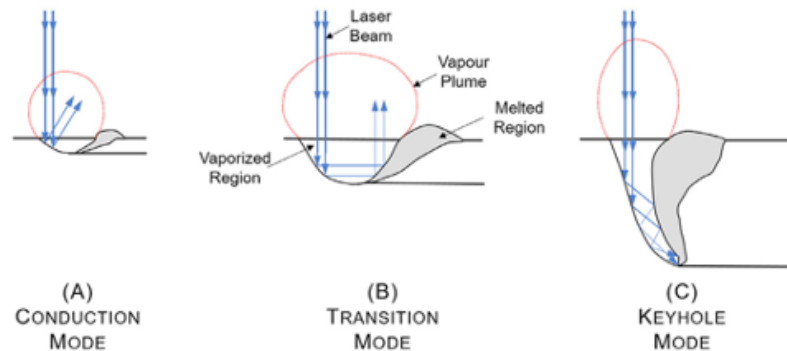


Figure 2.33: An illustration of conduction mode (A), transition mode (B), and keyhole mode (C) melt pools in terms of the vaporized region shape [105].

It is worth noting that in laser processes which involves melting, there are mainly two different operational regimes: conduction mode and keyhole mode. As can be expected, heat conduction is the dominant heat transfer mechanism for conduction mode, while heat convection is the dominant mechanism for keyhole mode melting [105]. Depending on processing conditions, one heat transfer mechanism prevails over the other and determines the operational regime type. In addition, Patel et al. [105] defined a transition mode, which lies between the two main regimes. This regime occurs when both heat transfer mechanisms are involved and the melt pool shape evolution is dependent on fluctuating laser absorptivity, which in turn is a function of the number of reflections between the vaporization walls, in addition to the energy input. For the sake of simplicity, the transition mode will not be considered hereinafter.

In the literature, various authors have found a threshold separating the two main operational regimes, which is generally called *keyhole threshold*. Firstly, Hann et al. [46] found that the melt pool depth normalized by the beam size (δ^*) is a function of normalized

enthalpy:

$$\delta^* = f\left(\frac{\Delta H}{h_s}\right) = f\left(\frac{AP}{h_s\sqrt{\pi\alpha v d_s^3}}\right) \quad (2.19)$$

where ΔH is the specific enthalpy, h_s is the enthalpy at melting, A is the absorptivity, P the laser power, α is the thermal diffusivity and d_s is the laser spot size.

This result agrees with the physical interpretation of the analyzed problem: material cannot melt or vaporize unless the local enthalpy is high enough for phase change to occur [46].

In a later work, King et al. [59] assumed that the condition for keyhole mode to occur is:

$$T_{max} \geq T_b \quad (2.20)$$

where T_{max} is the melt pool peak temperature and T_b is the boiling temperature of material.

By using Hann's et al. definition and after some substitution and assumptions, the authors found the threshold for keyhole formation in terms of normalized enthalpy:

$$\frac{\Delta H}{h_s} = \frac{AP\sqrt{\alpha}}{\kappa T_m \sqrt{\pi v d_s^3}} \geq \frac{\pi T_b}{T_m} \quad (2.21)$$

where κ is the thermal conductivity and T_m is the melting temperature. This keyhole threshold can be rewritten also in terms of process parameters:

$$\frac{P}{\sqrt{v d_s^3}} \geq \frac{\kappa T_b \sqrt{\pi^3}}{A \sqrt{\alpha}} \quad (2.22)$$

This formulation suggests that keyhole threshold is directly defined by laser power, scan speed and spot size. However, Yang et al. [151] confirmed that also layer thickness has an effect on keyhole occurrence. Therefore, authors suggested a modified specific enthalpy definition:

$$\frac{\Delta H}{h_s} = \frac{0.865AP\alpha}{\kappa T_m \sqrt{\pi v t d_s}} \geq \frac{\pi T_b}{T_m} \quad (2.23)$$

which takes into account also the layer thickness t .

Also, Equation 2.23 can be rewritten in terms of process parameters:

$$ED_v = \frac{P}{v t d_s} \geq \frac{\kappa T_b \sqrt{\pi^3}}{0.865 A \alpha} \quad (2.24)$$

This modified threshold has been validated with single track experiments and authors found an excellent agreement with experimental results for Ti6Al4V alloy. However, the model developed by Yang et al. for predicting melting mode threshold has been experimentally validated only for one material. Thus, further tests with different materials should be done to ensure overall validity of the model.

According to King et al. [59] and Patel et al. [105], it cannot be expected that these analytical models can accurately explain the complex physics of the process. As a matter of fact, the oversimplification of layer thickness effects, the assumption of temperature

independent physical properties and various other assumptions related to SLM-machine properties can contribute to the model uncertainty. Nevertheless, these models can be helpful for narrowing down the initial selection of process parameters for new alloys or for new process optimization strategies.

Chapter 3

Preliminary Investigation on Small Laser Spot Size

3.1 Introduction to process parameters optimization

Despite the obvious potential of SLM technology, process parameters optimization still plays a very important role today. As reported in the previous chapter, various complex phenomena can occur during the production and can lead to the formation of various workpiece defects. The main issues that can take place are the following:

- Porosity
- Residual stresses
- Geometrical defects
- Surface defects

Among all, porosity is the main defect to avoid, as it harms the mechanical performance of the components produced. As a matter of fact, unwanted porosity entails defects in the workpiece microstructure and affects both mechanical strength and fatigue behaviour. The main causes of porosity are related to overheating phenomena (e.g. keyhole) and, on the other hand, to lack of fusion (bad connection between tracks and/or layers).

Another issue that in general affects SLM components are residual stresses. Indeed, it is well known that the rapid heating and subsequent rapid cooling, due to the fast laser scan during the process, entail high thermal gradients in the workpiece. Basically, when a new layer is produced, its temperature is far above the underlying layers. Thus, the new layer will first expand uniformly, and the cooler underlying part will restrict this expansion, resulting in compressive stresses that act on it (see Figure 3.1a). When the laser stops to scan, the new layer will cool down faster than the part below, resulting in the development of tensile stresses in the new layer (see Figure 3.1b). The magnitude of these stresses is typically high, and it can reach the yield strength of material, due to the elevated and localized energy input provided by the laser [10]. This typically happens at high energy density levels. Hence, the resulting high thermal gradients and the enormous cooling rates

can lead to permanent warps, which can involve macroscopic geometrical defects. In fact, high thermal stresses are the main cause of part geometry defects. However, it can be also due to equipment issues (e.g. damaged coater, beam deflection not correctly calibrated, etc.) or wrong design choices (e.g. insufficient support structures, wrong part orientation, etc.).

Lastly, surface defects include all those defects that increase the surface roughness. In

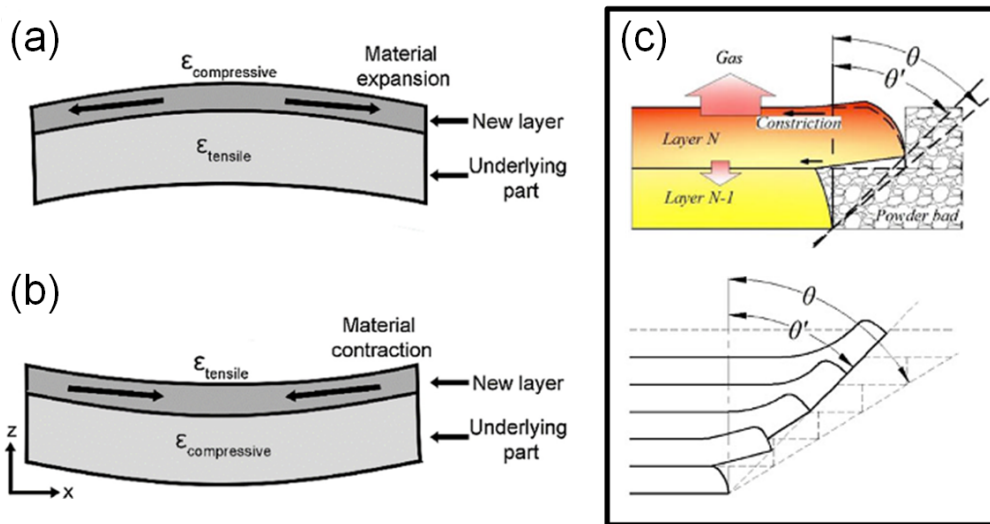


Figure 3.1: Thermal stresses (a) when a new layer is produced and (b) when the new layer cools down [10]; (c) thermal warping during SLM fabrication of an overhanging surface [141].

agreement with Balbaa et al. [8], the main cause of surface defects is the formation of periodic humps that are composed by adjacent scan tracks on the top surface. In practice, large and well overlapped tracks lead to smoother surfaces, while thinner tracks and low overlap rates entail higher roughness. Clearly, tracks shape is related to energy input, thus, to process parameters. As a consequence, low roughness can be obtained at high energy density levels, while high roughness is the result of low energy density applied during the process.

Other factors that affect the worsening of surface finish are tracks irregularities, balling and humping phenomena, and the ejection of molten material (spatters) due to intense convective flows and high recoil pressure. All these phenomena entail the formation of pseudo-spherical signatures on the workpiece surface, which were named “globules” by Lou et al. [82].

It can be noticed that every aforementioned defect is related to process parameters. Therefore, to reduce the entity of these defects and to obtain high quality components, process parameters optimization is of great importance.

Despite the large number of analytical and numerical approaches (simulating the SLM process performance) that can be found in literature, the experimental approach is often adopted to obtain reliable results.

As regards the latter approach, three different variations can be found in the literature:

- 3D benchmarks experiments
- single tracks + 3D benchmarks experiments
- single tracks + multi-tracks + 3D benchmark experiments

The first variation is widely adopted as it is the simplest approach; some representative 3D components are produced by varying the main process parameters, typically according to a Design of Experiments. Through this method, an optimal parameter set can be surely obtained. Nevertheless, it may not be the most efficient method in terms of material consumption, as a large number of specimens has typically to be produced.

Another of the most used optimization approaches entails two experimental steps. The first step consists in the production of a series of single tracks on top of a base plate by applying for each track a combination of process parameters (according to a full-factorial Design of Experiments). Tracks morphology is then analysed to restrict the parameters domain by avoiding anomalies, such as lack of fusion and keyhole. Thus, an optimal process region (process window) is obtained and, some 3D benchmarks are accordingly fabricated and analysed, identifying the optimal parameters set for 3D components production.

Although this method requires an additional step, it could be very convenient, as the

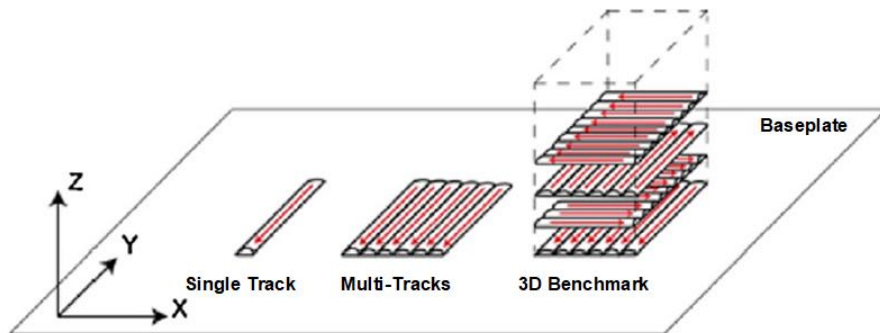


Figure 3.2: Schematic representation of single track, multi-tracks and 3D benchmark production.

material consumption can be considerably reduced. As a matter of fact, single tracks experiments require a very small amount of material and they reduce also the number of 3D samples to be produced in the next step. The third approach entails also an intermediate step; the multi-track experiments. Basically, a single layer (multiple tracks) is produced on a base plate, according to the process window previously defined by single tracks experiments. Then, a new process window can be obtained through the analysis of single layers and it can be subsequently adopted for 3D benchmarks production.

The latter method is not very common; however, it is theoretically the most complete approach for process optimization.

With regard to the process parameters investigated, laser power, scan speed and layer thickness are typically analysed in each experimental phase involved, while hatch distance (or overlap rate) and scan strategy are only studied in multi-track and/or 3D benchmarks experiments.

It is worth recalling that laser spot size is often ignored and only few studies on this topic can be found in the literature. However, Makoana et al. [88] studied the spot size effect by producing single tracks with two different LPBF systems that had different laser spot diameters ($80\mu\text{m}$ and $240\mu\text{m}$). The authors found that track width was significantly reduced when the smallest spot diameter was applied.

This result entails a higher process resolution and therefore smaller and more accurate geometrical details can be produced, as suggested by Chen et al. [21]. As a confirmation of this, a novel SLM technology has been recently developed; the micro-SLM. This technique is similar to SLM technology; however, very small laser spot and ultra-fine powder are involved in the process. These peculiarities result in a considerable increase in both system complexity and costs. Further details on micro-SLM can be found in the review of Nagarajan et al. [99]. It is worth reporting that no commercial machines have been found at the moment.

In this work, starting from the idea that a smaller spot diameter involves a higher process resolution, the conventional SLM process was investigated when the smallest available laser spot diameter was applied. Thus, the aim was to investigate laser power and scan speed effects through single tracks experiments, in order to find the optimal process window for $50\mu\text{m}$ spot size.

In the following sections, the powder material and the SLM equipment is described, as well as the methodology adopted for specimens production and analysis. Eventually, the morphological and geometrical characterization of tracks, as well as their microstructure and microhardness are discussed. It is worth reporting that the work described in this chapter was published in the journal *Data in Brief (Elsevier)* [136].

3.2 Materials and Methods

The material chosen to carry out the experiments was the extra-low-interstitial grade of Ti6Al4V alloy, as it is widely adopted in many strategic industrial sectors such as aerospace, automotive, energy and biomedical. Most applications in these industrial fields require very small and/or complex geometric features.

The characteristics of the Ti6Al4V powder applied in this research are given in Table 3.1 and in Figure 3.3. The powders were characterized by using a scanning electron microscope (*Zeiss Evo 40*) equipped with an energy dispersive X-ray spectroscopy (*INCA X-sight*). The grains had a spherical shape (Figure 3.3a), with diameters ranging from $6.5\mu\text{m}$ to $80\mu\text{m}$ with a slight negative skewness. The median diameter value was $35.88\mu\text{m}$, whereas the 10th and 90th percentiles were $21.45\mu\text{m}$ and $52.19\mu\text{m}$ respectively, as illustrated in Figure 3.3b. A sample of the powder was embedded in epoxy resin and underwent metallographic preparation in order to obtain a mirror like surface. Afterwards the specimen was etched by applying Kroll's reagent for *1min* and then analysed by an *Olympus SX-41*

Chemical element	Al	V	Fe	O	C	N	H	Ti
Ti6Al4V (% weight)	6.5	4.14	0.18	0.1	0.008	0.007	0.003	89.06

Table 3.1: Chemical composition of Ti6Al4V powder used for the experiments [136].

optical microscope in order to determine the microstructure of the powders. The microstructure was composed by Ti martensite, obtained by a rapid cooling of molten metal during the production of the spheres (see Figure 3.3c).

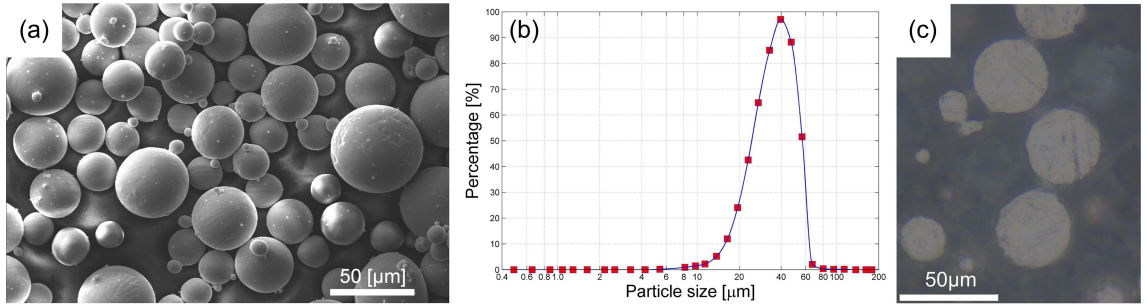


Figure 3.3: Characterization of Ti6Al4V powder: (a) morphology inspected by SEM; (b) particle size distribution; (c) metallographic analysis [136].

Parameters	Ti6Al4V Baseplate	Single Tracks	Levels
Laser Power	225W	50 ÷ 400W	8
Scan Speed	1300mm/s	250 ÷ 2500mm/s	10
Spot Size	155μm	50μm	1
Layer Thickness	25μm	25μm	1
Overlap Rate	40%	-	-
Scan Strategy	Islands	-	-

Table 3.2: Process parameters used for the production of baseplates and single tracks [136].

The specimens were manufactured with a *Concept Laser M2 Cusing* machine equipped with a 400 W single-mode CW ytterbium-doped fiber laser. The beam intensity had a Gaussian distribution with the beam quality factor $M^2 = 1.08$, and the emission wavelength was $1067nm$. The spot size was regulated to $50\mu m$, according to the $1/e^2$ classical definition that was also adopted by Xiang et al. [144]. The optical system of the machine included a *Scanlab intelliSCAN 30* two-axis scanning system and a *Scanlab varioSCAN 40i* dynamic focusing unit.

Both the laser power and the scan speed were varied in a wide range, as highlighted in the design of experiments shown in Table 3.2. The layer thickness was $25\mu m$ throughout all the experiments. All the single tracks were scanned in counterflow with respect to the protective gas flow. This choice was made in order to avoid the interaction between the laser

beam and the process fumes, as well as to prevent the precipitation of slags on the material to be processed. To mimic standard operating conditions, single tracks were printed on the top surface of basic structures that were produced during the previous layers of the same job. All the basic structures were printed by using the same parameters, and top layer passes were set at an angle of 45° with respect to the track direction. The adoption of such bases as single track substrates did considerably simplify the experimental activity by concurrently better reproducing the real process conditions. Single tracks distribution on such substrates is shown in Figure 3.4

After platform removal the tracks were classified according to their morphology seen from

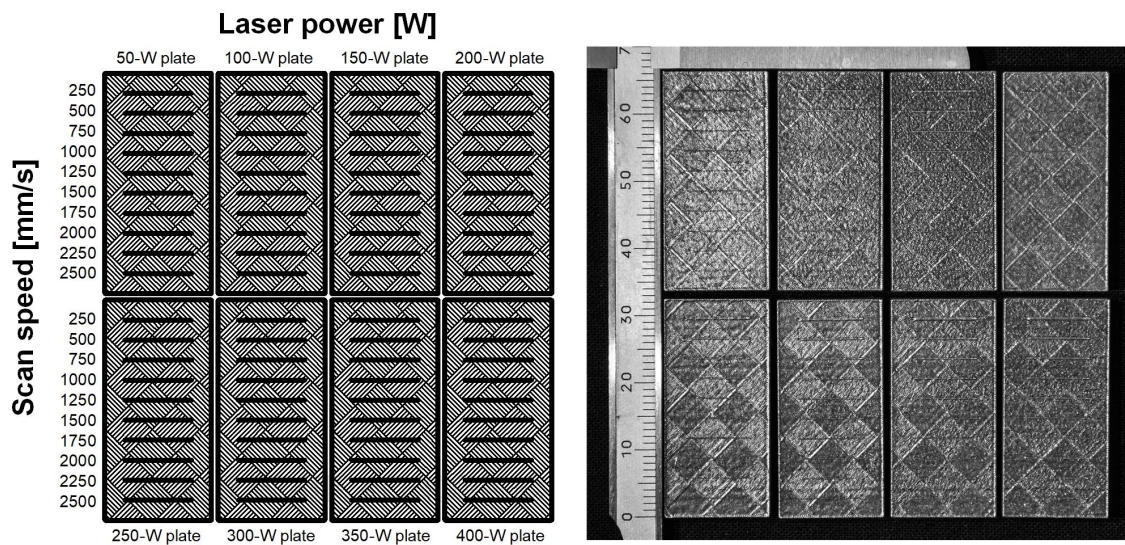


Figure 3.4: Design of experiments [136].

the top by using the same SEM/EDXS device adopted for powder characterization. Afterwards, all the specimens were cross sectioned by an abrasive refrigerated wheel, embedded in epoxy resin and then ground and polished to obtain a mirror like surface. The last polishing step of the material was done by using colloidal silica. The sections were then etched using Kroll's reagent for $1min$ and then analysed by the optical microscope. Eventually, the cross-section microstructure was examined as well as the presence of melting defects (voids, gas porosity, and inclusions) in order to achieve a complete track characterization. To determine the presence of *Heat-Affected Zones* in the proximity of the scan track, or of different microstructures between the base and the scan track, a Vickers microhardness profile (load of $0.05kgf$ for $15s$) across the scanned track was acquired starting at a depth of $50\mu m$ with respect to the base top surface.

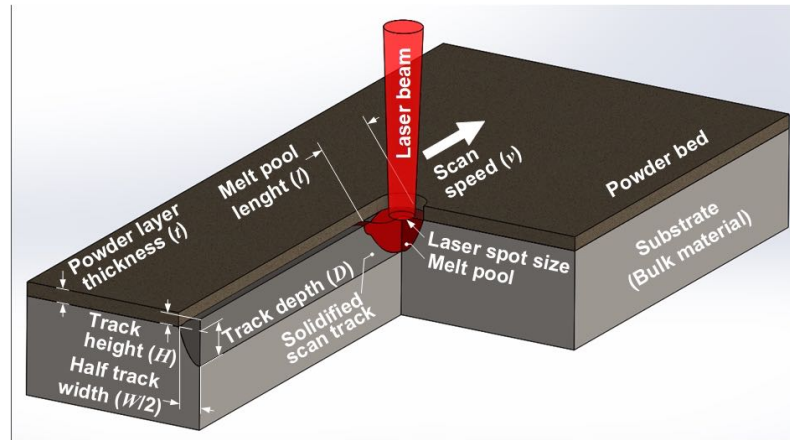


Figure 3.5: Schematic representation of single track scanning operation [136].

3.3 Results and Discussion

3.3.1 Morphological classification

Single tracks were firstly analysed to determine their morphology, and then metallographic analysis and dimensional measurements of their cross sections were carried out. Single track scanning is schematically illustrated in Figure 3.5. An example of single track top and cross section views is given in Figure 3.6, where most of the typical defects affecting track morphology are visible.

As can be seen from Figure 3.7a, different kinds of single track morphology were obtained. Specifically, the tracks were classified into five distinct categories according to their morphology, as follows:

- **Strongly discontinuous (I)**: the track was absent or only some isolated solidified drops caused by the balling phenomenon were found;
- **Discontinuous (II)**: a partial track formation was achieved owing to a slightly higher energy density;
- **Continuous but irregular (III)**: substrate alteration was continuous; however, the resulting track was strongly jagged. Moreover, at low laser power levels, many partially melted particles were found near the track;
- **Regular and thin (IV)**: the track was continuous and predominantly regular. Track width was about twice the laser spot diameter. A high-power level combined with medium-to-low scanning speeds promoted a stable melt pool;
- **Regular and thick (V)**: the track was continuous and regular like in the previous case; however, its width was higher and its depth was much deeper because of the higher energy density. Tracks were affected by the typical keyhole porosity owing to excessive material evaporation. The effects of flows inside the melt pool can be seen in the top views.

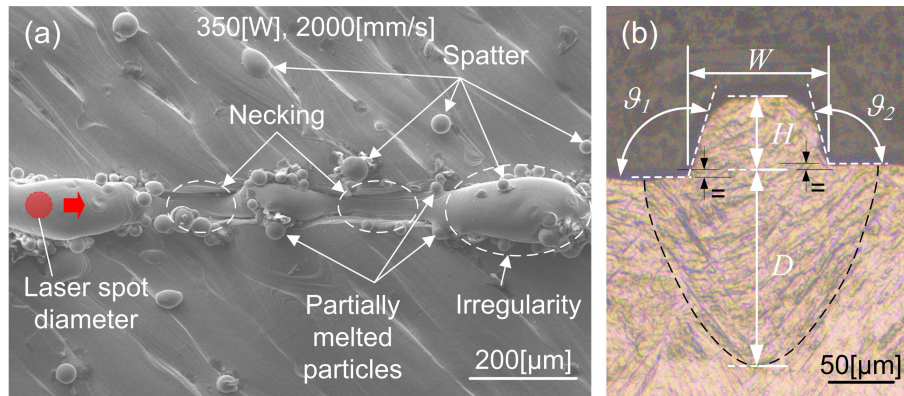


Figure 3.6: (a) Top view of a single track with typical defects and (b) cross section measurements, where the Heat Affected Zone is also visible [136].

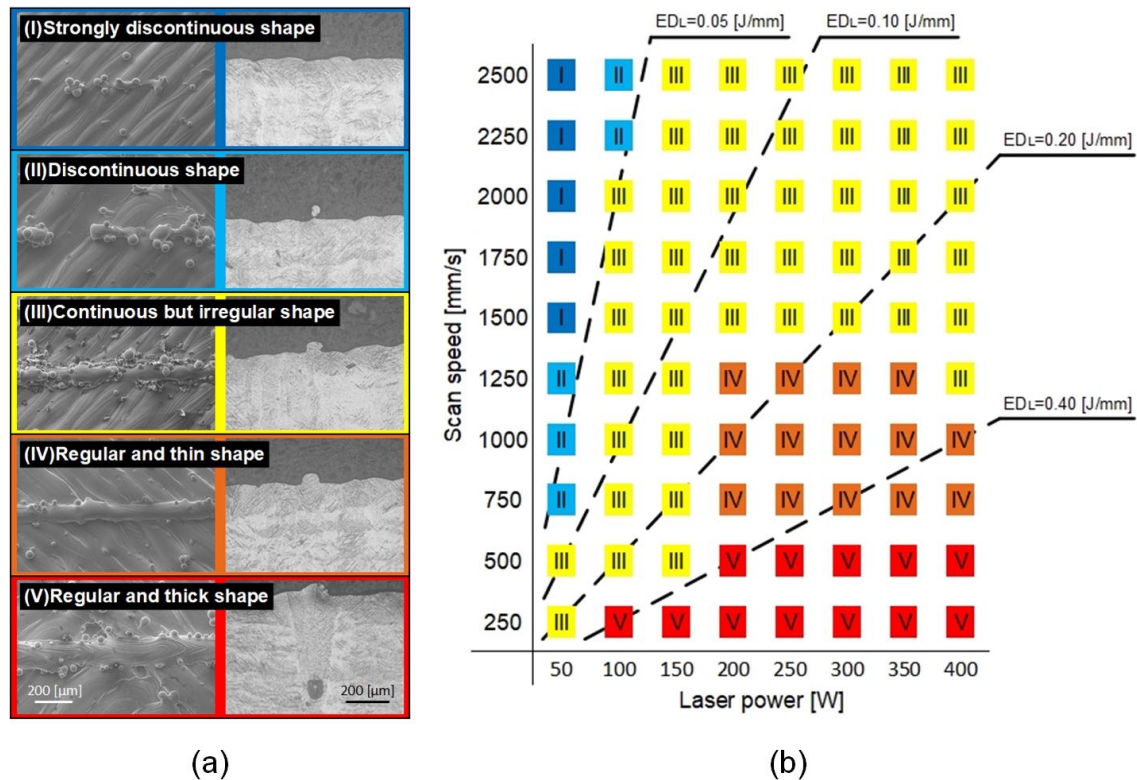


Figure 3.7: (a) Examples of top and cross-section views of representative single tracks and (b) process map obtained [136].

The process map obtained is reported in Figure 3.7b. As done in recent research works [75], single track results can be roughly classified by using the linear energy density ($ED_L = P/v$).

From the results presented in Figure 3.7b, no track or a strongly discontinuous track was

formed (categories I and II) when ED_L was less than $0.05J/mm$ owing to the insufficient amount of energy transferred to the powder and to the balling phenomenon. For ED_L levels in the range between $0.10J/mm$ and $0.20J/mm$ (category III), several morphological defects were found, as shown in Figure 3.6a. Specifically, single tracks of category III were affected by irregularities and necking. Partially melted powders together with spatter generation were also observed under these conditions. On the other hand, continuous and regular shapes can be observed for ED_L values between $0.20J/mm$ and $0.40J/mm$, whereas above $0.40J/mm$ a substantial evaporation of materials takes place. This enhances the energy absorption of the laser source, thus causing an excessive track penetration. In addition, vapor cavity collapses during the cooling phase and typical keyhole voids can be seen in the cross-section views. This gives rise to single tracks of category V. From the top views, the only visible difference between category IV and category V is the considerably greater thickness of the tracks belonging to the latter category.

In short, the best single tracks were found when $0.20 \leq ED_L \leq 0.40J/mm$. However, this window does not ensure an adequate 3D printing of bulk parts because of the expected heat accumulation effects in the presence of multi-track and multi-layer configuration [28]. Process parameters corresponding to lower energy densities – from 0.1 to $0.2J/mm$ – should be considered as the best candidates for a successful 3D printing.

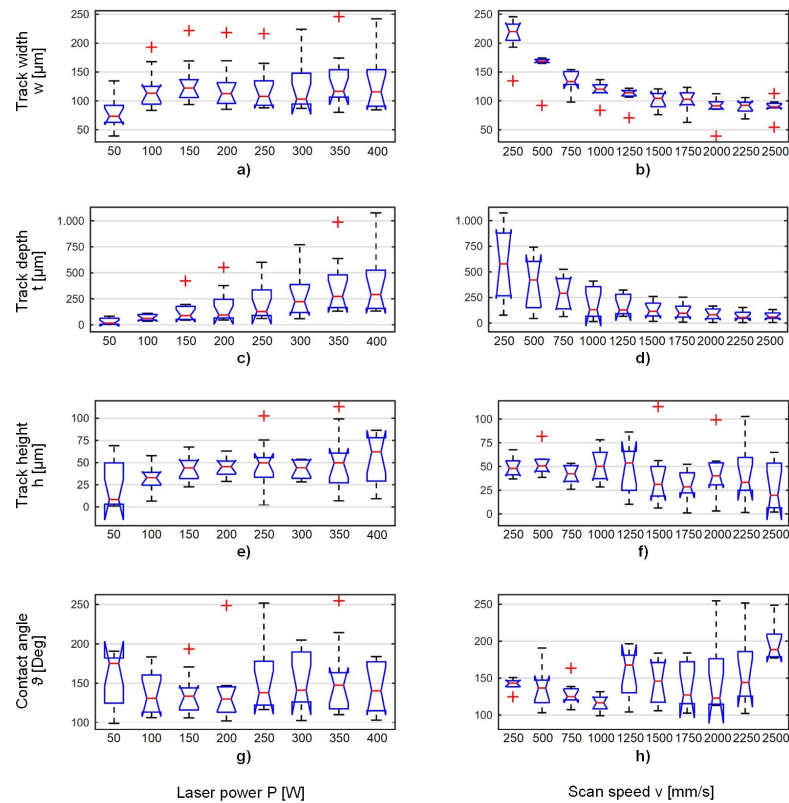


Figure 3.8: Box plot of the (a, b) width, (c, d) depth, (e, f) height, and (g, h) contact angle of the track at different laser power and scanning speed levels [136].

3.3.2 Track Geometry Measurements

From the analysis of SEM images, the following characteristics were determined: the track width W , height H , depth D and contact angle θ were evaluated and are defined in Figure 3.6b. Statistical boxplots showing the behaviour of the observed quantities are reported in Figure 3.8. The analysis of variance was carried out in order to determine the most important dependencies between the observed variables and the process parameters. Eventually, the interpolating models represented in Figure 3.9 were determined through the stepwise regression algorithm that was executed both in natural and logarithmic scale. The results from the analysis of variance and from linear regression are reported in Table 3.3.

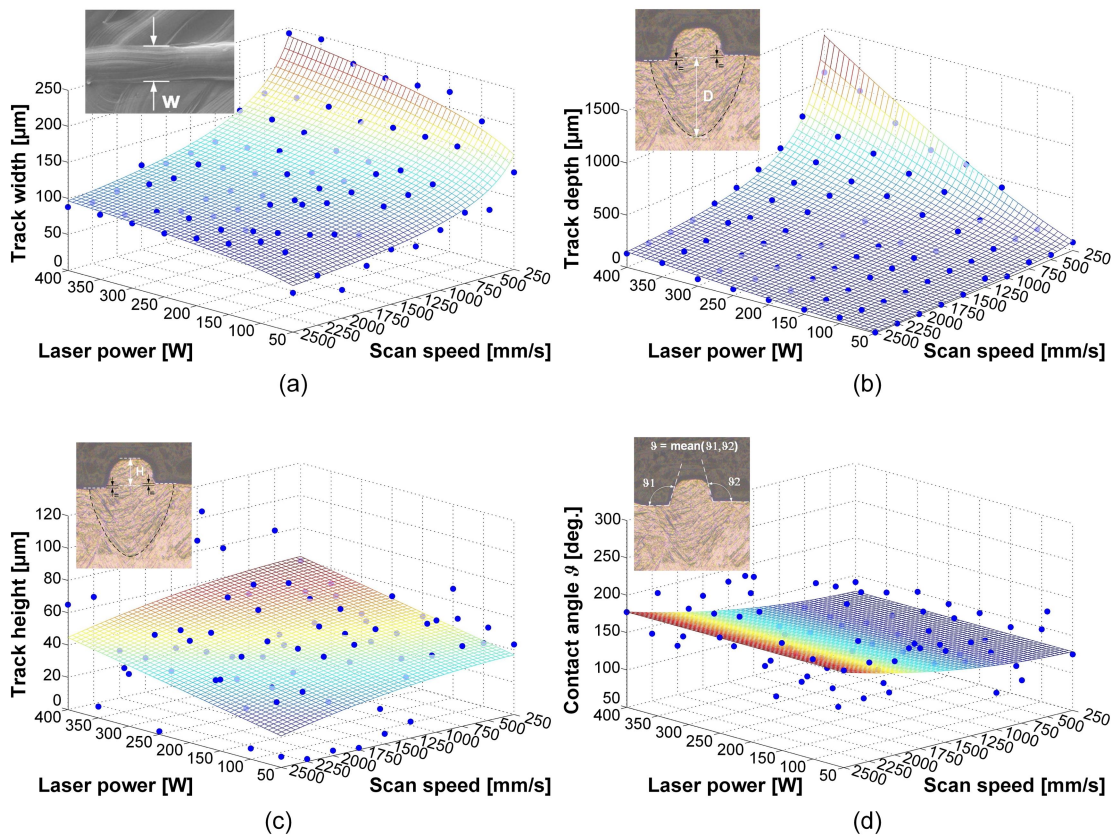


Figure 3.9: (a) Width, (b) depth, (c) height, and (d) contact angle of the single tracks. The scan speed axis is oriented from right to left [136].

3.3.3 Microstructure

Metallographic analysis was also carried out in order to achieve a complete physical characterization of the single tracks and of the underlying substrate. As it is visible in Figure 3.6b, the microstructure was fully composed of Ti martensite. This indicates that the

Geometric feature	ANOVA (p-value)		Model	R^2	μ_ϵ [%]	σ_ϵ [%]
	P [W]	v [mm/s]				
Track width	7.59e-15	1.95e-32	$645P^{0.2}v^{-0.4}$	0.90	9	11.4
Track depth	2.29e-11	1.91e-14	$120.3P^{1.3}v^{-1}$	0.94	18	31.9
Track height	0.071	0.3296	$26.7 + 7.2 \cdot 10^{-2}P$	0.13	38.8	50.3
Contact angle	0.4455	0.0004	$126.8 + 8.14 \cdot 10^{-6}v^2$	0.20	18.2	22.4

Table 3.3: Analysis of variance and interpolating models of the geometric features. μ_ϵ and σ_ϵ are the systematic and random relative errors, respectively [136].

material underwent high cooling rates during and after the solidification. The formation of martensite was likely due to the high difference between the volume of the single track and the volume of the base that was already solidified when the single track study was carried out. The microstructure did not depend on the process parameters, and no secondary phases generated by the reheating of the material were detected in the *Heat-Affected Zones*.

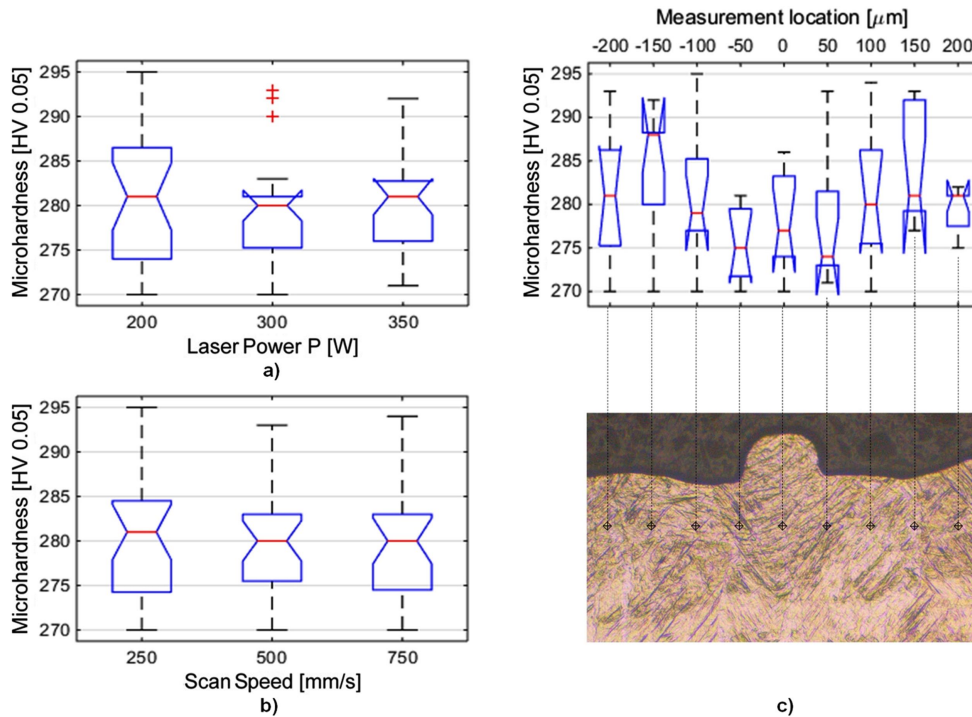


Figure 3.10: Microhardness trend with respect to (a) laser power, (b) scanning speed, and (c) measurement location [136].

3.3.4 Microhardness

The microhardness analysis was carried out by considering only the samples obtained with a laser power of 200W, 300W and 350W with a scanning speed of 250mm/s, 500mm/s and 750mm/s. For each of these combinations, microhardness was inspected every 50μm along the horizontal axis as shown in Figure 3.10c. The hardness profiles were in agreement with the microstructure of the scan track. No appreciable differences in hardness values were found. The mean hardness corresponded to a Ti martensite phase.

3.3.5 Final Remarks

In this work, an experimental study on the SLM process of Ti6Al4V powder when using 50μm laser spot diameter was carried out. For this purpose, the effects of both laser power and scan speed on single tracks formation were investigated, according to a full-factorial Design of Experiments.

A complete characterization of single tracks was carried out in order to establish the optimal process window, develop statistical models on track geometrical features and evaluate the microstructural characteristics of the specimens produced.

Lastly, a preliminary 3D benchmark production was carried out in order to verify the enhancement of process resolution due to the adoption of 50μm spot parameter set. In

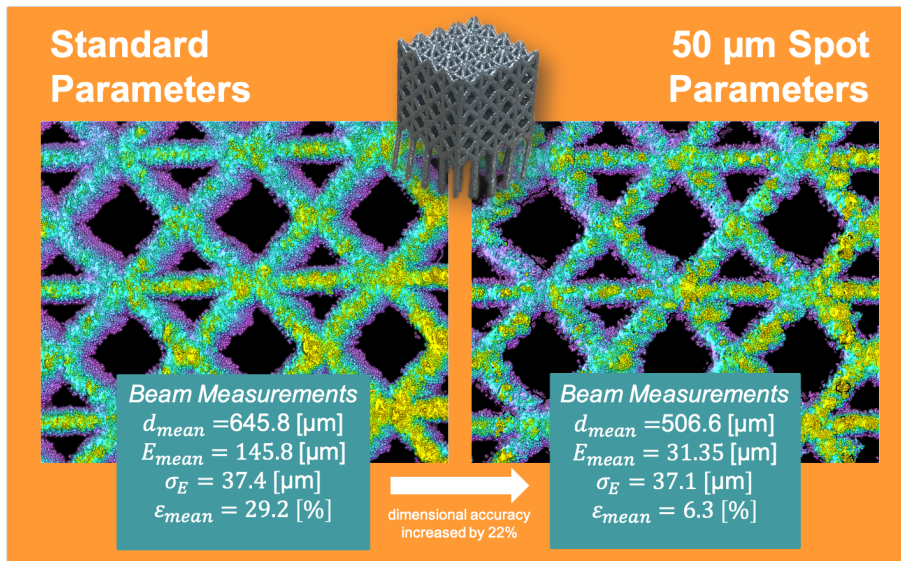


Figure 3.11: Lateral face topographies of lattice structures produced with two different process parameter sets.

accordance with Di et al. [28] work, which studied the heat accumulation effect due to multi-track and multi-layer production, the optimal parameter set was chosen in the upper left region above the category IV region (referring to (P, v) plane). In particular, the adopted laser power and scan speed were 150W and 1500mm/s, respectively. Thus, two 3D benchmarks were produced in order to compare standard parameters (reported in

Table 3.2) with $50\mu m$ spot parameters. The benchmark geometry chosen was a Face and Boundary Centred Cube with vertical struts (FBCCz) lattice structure and the nominal beam diameter was $d_{nominal} = 0.5mm$.

After samples production, the surface topography of a lateral face of the structures was acquired through a 3D optical profiler (which will be described in the following chapter). Ten beam diameter measurements were then carried out for each lattice structure produced. Subsequently, the mean diameter (d_{mean}), the mean absolute error (E_{mean}), the standard deviation of the absolute error (σ_E) and the mean relative error (ϵ_{mean}) were computed. As can be seen from the results reported in Figure 3.11, the reduction in spot diameter from 155 to $50\mu m$ led to an increase of 22% in dimensional accuracy. This confirmed that small spot size parameters are suitable for the production of more accurate lattice structures. Therefore, further investigations into the spot size effect could be of great interest, as it would allow the development of production strategies that adapt the parameters to the part geometry a priori.

Chapter 4

New Methodology for Process Parameters Optimization

4.1 Introduction

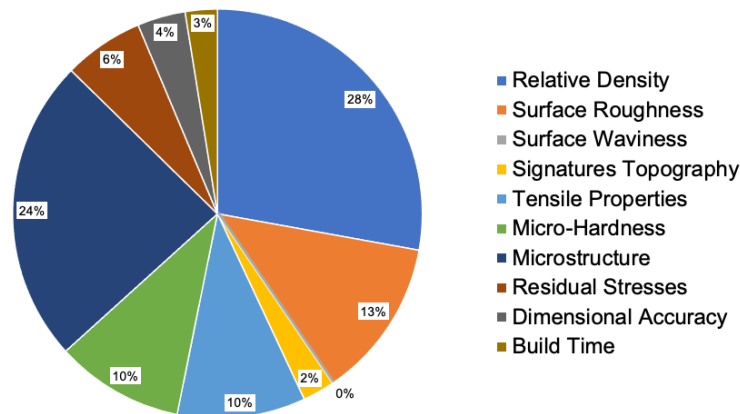


Figure 4.1: Quality descriptors for 3D benchmarks found in the literature.

Nowadays, there are various process parameters optimization methodologies available in the literature. As reported in the previous chapter, these can be divided into analytical, numerical or empirical approaches. Since this work deals with an empirical method, only approaches based on experimental testing will be discussed.

With respect to this type of methodologies, in Table 4.1 are reported various studies found in the literature, which were published in the last three years. Summarizing Table 4.1, the most adopted optimization method consists directly in the production and evaluation of 3D benchmarks. The second most commonly used method entails the analysis of both single tracks and 3D benchmarks.

Ref.	Year	Single-Tracks	Multi-Tracks	3D Benchmarks	Simulation	Material	Track Geometry	Flow Phenomena	Heat Transfer Related	Relative Density	Surface Roughness	Surface Waviness	Signatures Topography	Tensile Properties	Micro-Hardness	Microstructure	Residual Stresses	Dimensional Accuracy	Build Time
[34]	2018	x			x	Alumina	x	x	x					x	x				
[45]	2018			x		AlSi10Mg	x			x	x						x	x	
[62]	2018			x		Inconel 625			x	x	x		x		x				
[64]	2018	x		x	x	Ti-18Zr-14Nb	x		x	x	x			x			x	x	
[102]	2018	x	x	x		AlCuMg	x	x		x				x	x	x			
[119]	2018	x		x		Ti6Al4V	x	x		x			x		x				
[120]	2018	x		x		Ti6Al4V	x	x	x	x									
[144]	2018	x			x	Ti6Al4V	x	x	x										
[3]	2019	x	x			STS 630	x				x								
[13]	2019	x		x		AlSi10Mg+4Cu	x	x		x				x	x				x
[52]	2019			x		W-7Ni-3Fe				x				x		x			
[72]	2019	x		x		Sc- & Zr- 7075 Al	x	x		x	x			x	x				
[80]	2019	x	x	x	x	SS 316L	x		x	x	x								
[104]	2019	x		x		Cu7.2Ni1.8Si1Cr	x	x		x				x		x			
[127]	2019			x		NiTi	x			x						x		x	
[145]	2019	x		x		Ag	x			x					x	x	x		
[150]	2019			x		Invar 36, SS316L				x				x		x	x		
[154]	2019			x	x	AlSi10Mg			x	x						x			
[8]	2020	x		x		Inconel 718	x	x		x	x					x	x		
[32]	2020			x		SS 316L							x						
[40]	2020			x	x	Ti6Al4V		x	x	x									
[44]	2020			x		Inconel 738LC		x	x	x	x		x	x		x	x		
[57]	2020			x		NiTi				x	x					x			
[78]	2020			x		FeCoCrNi				x				x		x			
[132]	2020			x		CoCr				x	x				x	x			
[137]	2020	x	x	x		Ti6Al4V+3Cu	x	x		x					x	x			
[142]	2020			x		ODSN								x		x			

Table 4.1: State-of-the-Art summary table of methodologies for process parameters optimization. The main quality descriptors adopted in each work are reported.

It is worth noting that multi-track experiments (that are a single layer or multi-layer single tracks) are not very common.

Regarding materials, Ti6Al4V is still the most investigated one, followed by SS 316L and AlSi10Mg. However, the current trend is to investigate new materials and new alloys that were not available before for this technology.

By analysing literature works, 13 quality descriptors were defined (see Table 4.1).

In studies that include single track analysis, the most investigated ones were track geometry and melt pool flow phenomena. In particular, track width and track depth were the most measured features, while balling and keyhole phenomena were mainly recognized. Through the observation of various process signatures on track morphology, a process map is often defined. However, no standardized methodology was found, and each author defined their own method, based on their expertise. Furthermore, the bibliographic research has highlighted that height profile of single tracks has not been investigated with the aim of process parameters optimization.

In studies that include simulation, heat transfer mechanisms and thermal modelling of the process were considered, thus the temperature distribution and the thermal history were studied.

As can be seen from Figure 4.1, the most adopted quality descriptors for 3D benchmarks were relative density, surface roughness, tensile properties, micro-hardness and microstructure, while individual topographic features, residual stresses, dimensional accuracy and build time were less investigated.

It is worth noting that no literature work has been found in which the surface waviness has been taken into account for process parameters optimization. As a matter of fact, the review performed by Townsend et al. [133] on surface texture metrology for metal AM confirmed that surface texture characterisation is mostly based on computing ISO 4287 texture parameters on profiles and Ra parameter is by far the most widely adopted.

In a more recent work, even Lou et al. [82] noticed from their state-of-the-art summary that the majority of published works on PBF processes characterize the surface following the traditional routes (i.e. Ra or Sa parameters are considered), without giving special consideration on the unique characteristics of PBF surfaces. In addition, the authors proposed a novel surface characterization framework based on automatic extraction of individual topographic features. A similar approach was developed also by Senin et al. [118]. Nevertheless, there are no scientific works that apply these novel characterization techniques on process parameters optimization.

With respect to the main process parameters investigated and the size of the DoE adopted, the same considerations can be made as in Chapter 3.

From the state-of-the-art and from the work described in Chapter 3, a range of criticalities of current available process optimization methodologies were found, which can be summarized as follows:

- Single tracks analysis gives very useful information; however, most authors prefer directly analyse 3D benchmarks. This is probably due to the long time needed for single tracks inspection, especially for cross sections;
- There is a lack of objective quality descriptors for single tracks analysis (tracks

characterisation is based on author's expertise);

- Surface characterization of 3D Benchmarks is almost based on roughness measurements, without considering other specific quality descriptors;
- In general, there is a lack of standard methodologies for process parameters optimization.

In this work, a novel process parameters optimization technique will be proposed in order to overcome to some extent the aforementioned critical issues. In particular, the aim is to develop an automatic, reliable and objective methodology for process optimization based on optical metrology. Basically, the methodology consists of single tracks analysis and subsequent 3D benchmarks characterization. However, an original algorithmic approach based on optical metrology data has been developed for both single tracks and 3D benchmarks surface characterization. This allows to automatize to some extent the data analysis phase, defining new descriptors that make the methodology reliable and objective.

Due to its quickness, various process parameters can be analysed in a wide range, and one or more optimal parameter sets can be defined. This is particularly useful for strategies that adapt parameters to part-geometry, such as adaptive slicing, hull and core strategies (or similar) and multi-laser production, which require more than one process parameter set.

4.2 Equipment - Optical Profilometry

The investigation of SLM process output through surface characterization plays an important role in the presented methodology. Therefore, it is worth introducing some available measurement techniques for this purpose.

The most prevalent imaging methods for areal topography measurements are *Imaging Confocal Microscopy* (ICM), *Focus Variation* (FV) and *Coherence Scanning Interferometry* (CSI) [69, 92]. Although these techniques have distinct features and different operating logics, all three technologies can work in the same machine (with appropriate adjustments). As a matter of fact, the 3D optical profiler used in this work, the *Sensofar S neoX Five Axis* [94], allows to operate with all aforementioned techniques by easily applying different software and hardware settings. The optical schematics of *S neoX* can be seen in Figure 4.2 (b).

The main peculiarity of this microscope is the *Digital Micro-mirror Device* (DMD), also called reflective microdisplay (see Figure 4.3). The device consists of an array of micro-mirrors, each of which has only two possible states: switched on (behaving as reflective) and switched off (no light is reflected). Basically, when the light source is collimated and directed onto the microdisplay, various illumination patterns can be obtained by switching on a set of micro-mirrors with different logics. Passing through the optical path, the light subsequently illuminates a portion of the workpiece surface and the light reflected or scattered from the latter is imaged back to the camera (detector), which records a signal for each pixel [92].

In addition, to acquire the whole surface topography, the objective has to be linearly

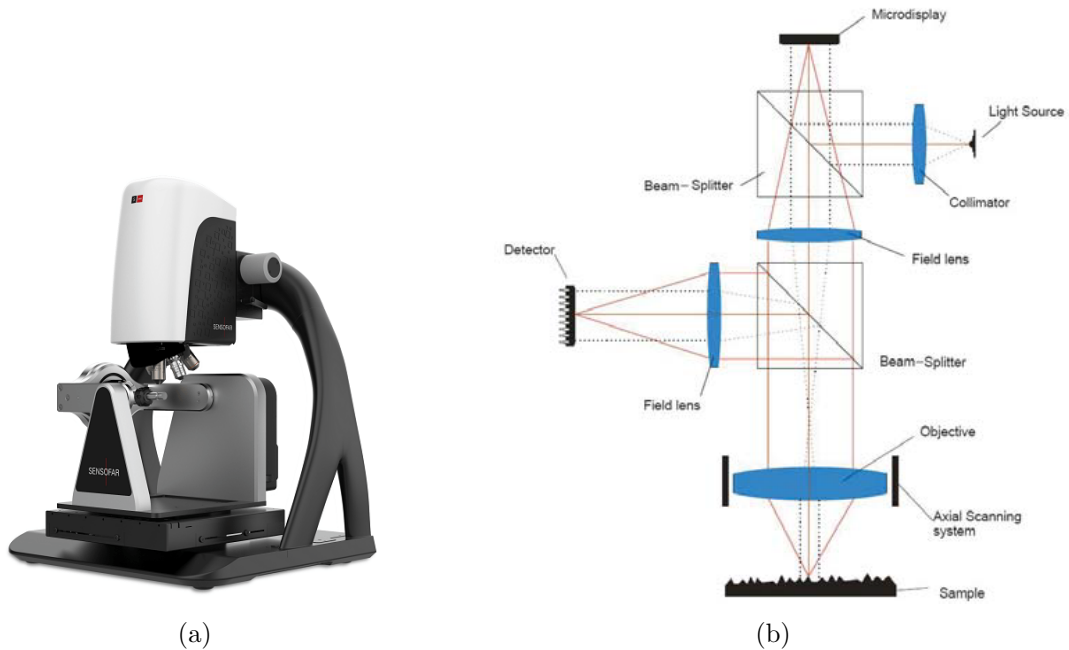


Figure 4.2: (a) *Sensofar S neoX Five Axis*; (b) Optical schematics of a microdisplay scan confocal microscope [92].

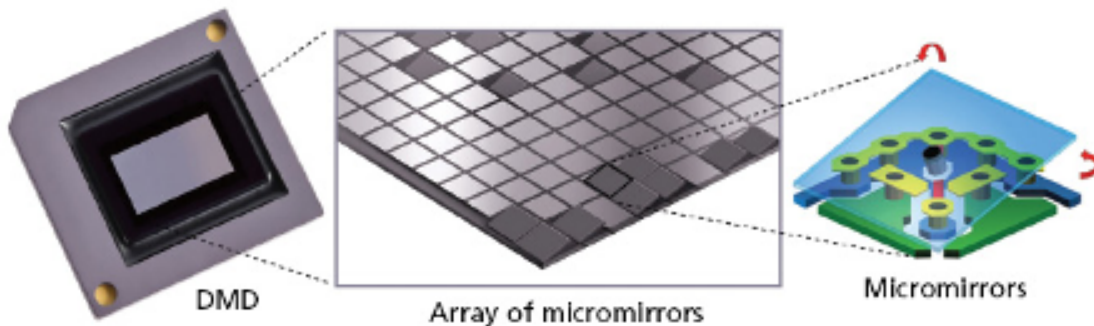


Figure 4.3: Digital Micro-mirror Device [87].

moved along the optical axis (Z axis stage) through a vertical scanning system. This allows the focal plane to cross the vertical range from below to above the surface. If the latter is larger than a field of view (FoV), the workpiece has also to be moved with X and Y axis stages and more scanning operations are required to obtain the entire surface topography. The *S neoX* used in this work has also the 4th and the 5th axis, allowing more complex positioning of the workpiece. However, these additional axis were not used in the presented methodology.

In conclusion, depending on the logic adopted by the microdisplay to reflect light, on the camera recording mode and according to the type of objective mounted, the *S neoX* can switch from a measurement technique to another. The following will briefly describe the

functional operation of each technique, highlighting their pros and cons.

4.2.1 Imaging Confocal Microscopy

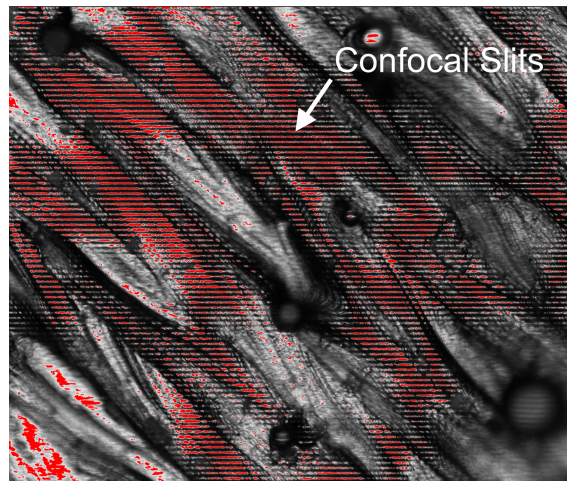


Figure 4.4: Example of confocal microscopy image of an SLMed surface, where the slits pattern can be seen.

Sensofar S neox is in all respects a confocal microscope. As a matter of fact, if only one micro-mirror is switched on, the light source illuminates only a single point of the workpiece surface. So, if the light reflected or scattered from the latter is recorded by only one pixel of the camera, optical sectioning light rejection can be achieved. In this configuration, the machine actually behaves as a classical confocal microscope; the microdisplay represents the illumination pinhole and the camera behaves as a confocal aperture pinhole and detector simultaneously [92].

However, point by point scanning (such as laser scanning microscopes) is very slow and typically other faster scanning strategies are applied. Basically, to obtain an optically sectioned image, the illuminated regions on the workpiece have to be restricted by a structured illumination pattern and the reflected or backscattered light has to be detected by a second pattern, identical to the illumination one. The detection pattern blocks the light that comes from surface regions out of the focal plane [69]. So, by moving the objective along the optical axis, the camera records only the points belonging to the focal plane at each Z stage step. The final result is an image representing the entire surface topography of the scanned workpiece.

Structured illumination and detection patterns can be a set of equally distributed pixels, slits or any other pattern that restricts the amount of illumination (*S neox* uses slits).

Concerning the objective, this technique requires an episcopic objective (EPI - light travels through the objective twice) with very low depth of field. The achievable height resolution is dependent on numerical aperture (NA), thus on magnification. At the highest NA in air (0.95), the height resolution is about 1 nm and the highest measurable local slope is about 72° [92]. However, the higher the NA (higher magnification), the smaller the working

distance and the FoV. Thus, with high magnification objectives, only flat components can be scanned, and measurements can take long time. On the contrary, with low magnification (low NA) objectives, the working distance and FoV become greater and also the shape of quite rough components can be measured, however losing height resolution and measurable local slope angle. In practice, confocal technique is the middle way between the technologies considered.

4.2.2 Focus Variation

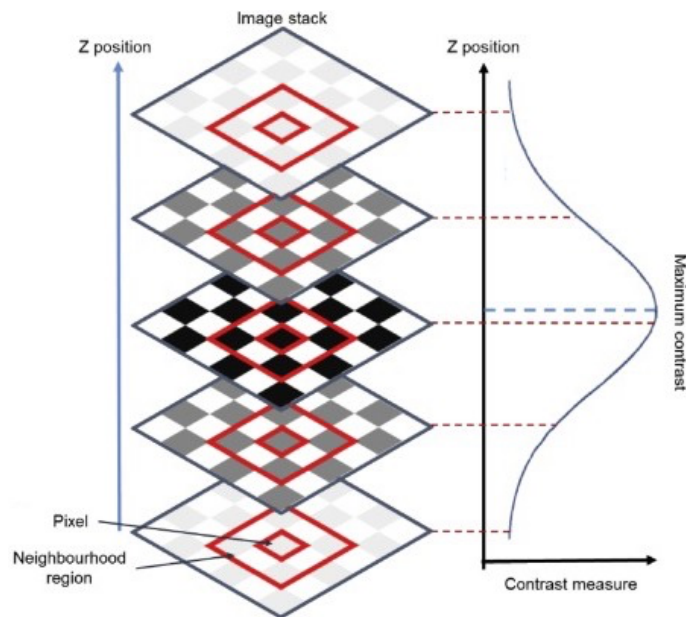


Figure 4.5: Schematic diagram of the focus variation technology [100].

Focus variation works with brightfield images, which can be obtained by switching on all micro-mirrors of the microdisplay and recording a simple image with the camera. This technique is another way to take advantage from low depth of field objectives and vertical scanning. Indeed, confocal microscopy and focus variation can be applied with the same type of objectives.

The basic operation of focus variation starts by recording a sequence of images while the optics is vertically moved along the optical axis. The result is a stack of brightfield images (vertical image stack). Subsequently, the local contrast of each pixel within an image is measured by algorithmically combining information about the surrounding bright and dark pixels (this results in a lateral resolution that is less than the pixel size). The procedure is repeated for the same pixel in all the images of the vertical stack (see Figure 4.5). After these computations, a contrast curve is available for each pixel, spanning the whole set of vertically stacked images. Finally, the z location of each pixel is computed by an algorithm that determines the maximum contrast value for each curve [100]. In other words, the final image is composed by pixels that have the maximum contrast value,

which means that all saved pixels are exactly in focus position.

Height resolution is difficult to establish for this technique, since it depends on various factors, such as texture contrast, applied algorithms, numerical aperture and light wavelength.

From the practical point of view, surfaces with no evident texture (smooth surfaces) cannot be measured, as no focus position can be retrieved [92]. To try to overcome this problem, wavelength or magnification (thus NA) can be changed: an optically smooth surface may appear optically rough when wavelength or magnification is reduced.

On the contrary, the main advantage of focus variation lies in the ability to measure high local slopes and in its rapidity. As a matter of fact, this technique is most typically used with low magnification objectives for shape and form acquisition of components with rough surfaces (thus it is highly suitable for metal AM components). Roughness measurements can also be performed as long as the analysed surface has high values of Ra (or Sa).

4.2.3 Coherence Scanning Interferometry

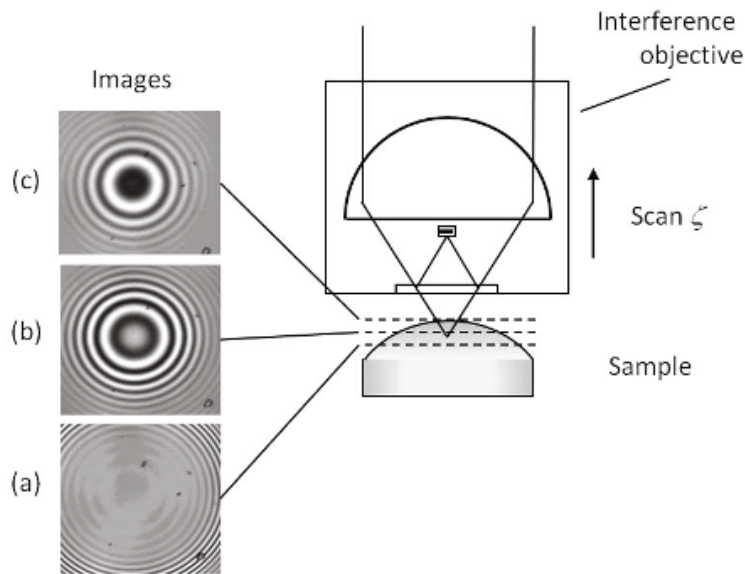


Figure 4.6: Images of interference fringes on a curved surface with low coherence illumination [69].

Coherent scanning interferometry uses a broadband light (white light) as illumination source, since the broadening of the spectral emission reduces its coherence length. Indeed, this method is also denoted as low coherence interferometry or white light interferometry [110].

The typical imaging system is analogous to that of a confocal microscope except for a modification in the optical path. As a matter of fact, to use interferometry with the Sensofar microscope, all micro-mirrors have to be switched on and a special objective has to be mounted: a two-beam interference objective. This kind of optical system allows to

divide the incoming coherent light into two beams of equal intensity, directing one beam onto a reference mirror and the other onto the workpiece. Both light waves are then reflected and directed to the detector. Their combination produces interference fringes, which permit to measure the optical path difference.

The height information is obtained by stepwise moving of the objective (vertical scanning) and taking an image at each step. The final surface image results from combination of the single step images.

More in detail, during scanning operation, the camera records intensity data for each pixel in successive camera frames. The intensity measured at one pixel results in a curve as it is displayed in Figure 4.7. The intensity correlogram consists of a periodic signal modulated by a Gaussian envelope and it can be used to find the best focus position for each pixel through an algorithm. Basically, surface heights are deduced by noting where the interference effect is stronger.

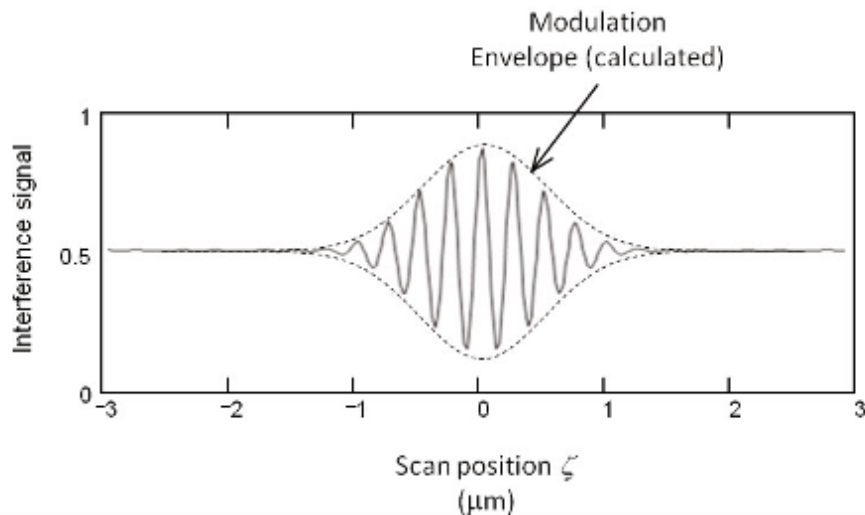


Figure 4.7: CSI signal for a single pixel showing the modulation envelope [69].

The achievable height resolution is about 0.1 nm regardless of magnification of the objective; hence this technique is the highest precision measuring technology considered. In practice, CSI allows to have a fine autofocus at every point of field of view and suppression of spurious interference from scattered light (very low noise). Nevertheless, the main drawbacks of this technique are the impossibility of measuring optically smooth surfaces with relatively high local slopes and, its slowness [92].

4.3 General Methodology

This section will provide an overview of the general methodology, summarizing all the steps required to achieve process parameters optimization. The first five steps can be included to single tracks analysis, while the other steps can be related to 3D benchmarks characterization. For each macro group, an entire chapter will be devoted later, in order

to explain in detail all stages necessary to achieve the final goal.

STEP 1 - Single Tracks Production

The methodology starts with the production of a series of single tracks, according to a full factorial DoE. Single scan lines have to be produced by varying the main process parameters. Typically, laser power and scan speed are investigated at this step. However, due to rapidity of analysis steps, also laser spot size and/or layer thickness can be included in the DoE. For the sake of simplicity, only spot size has been considered in this work. Since single tracks production requires a small amount of material, it is also convenient to consider a large range of process parameters levels in order to analyse a process map as wide as possible. This will not significantly affect cost and time of production.

STEP 2 - Surface Topography Acquisition of Single Tracks

After samples production, single tracks top surface can be acquired by an optical metrology technique. For this purpose, coherence scanning interferometry is preferred, because of its high precision and because it requires less processing steps during results analysis (noise is practically absent). In addition, the equipment used for samples scanning allows to acquire the whole topography of each single track in an automated way. As a matter of fact, it is possible to take a reference position at the beginning of the first scanned track and, by knowing the (x,y) coordinates of each scanned track, a grid scan strategy can be applied for the automatic acquisition of all tracks topographies. Since the working area of the optical profiler is limited, single tracks should be produced on a small build platform or on SLMed plates that has to be later removed from platform and held together with a customized samples holder (3D printed).

The output of scanning operation is a point cloud that represents the (x,y,z) coordinates of the acquired surface, which is composed of single track surface and a portion of the substrate where the single track was produced.

STEP 3 - Single Tracks Recognition

Once all point clouds of each single track are automatically acquired, it is possible to perform a first classification step. Through a statistical distribution analysis of points that compose a single point cloud, it is possible to automatically recognize the presence of a single track (segmentation algorithm). By doing so, point clouds are divided in two categories: point clouds that include a single track and point clouds that include only the substrate (no single track is recognized).

This step is completely automatic and it is performed by using MATLAB programming platform.

STEP 4 - Single Tracks Classification

For this second classification step, only point clouds that include a single track are considered. Firstly, a more accurate segmentation algorithm is used for single track detection.

Afterwards, single tracks can be divided into two categories: continuous and discontinuous tracks. The track continuity (i.e. the stability) is determined by a novel descriptor, which is based on spectrum analysis of track profile. Basically, this step separates tracks with evident balling or humping phenomena from continuous and smooth ones. The whole classification procedure has been developed with MATLAB and it is completely automated. It is also worth noting that by detecting the points belonging to a single track, it is possible to automatically measure track width, which is essential for hatch distance selection in 3D benchmarks production.

STEP 5 - Process Window

The two-steps classification algorithm allows to define a process map in the (P, v) plane (for each level of spot size), in which three categories can be defined: insufficient energy density, continuous and discontinuous tracks. In addition, two curves can be computed: the single track melting efficiency curve and the critical scan speed curve ($v_{cr} = v_{cr}(P)$). The first curve defines an energy density limit below which no single tracks are formed (separation between point clouds that include a single track and point clouds in which no track is recognized), while the second curve defines a scan speed limit above which track stability is compromised. The latter is the most interesting curve, as it can be used to define the process window for later 3D benchmarks experiments. As a matter of fact, by defining the process window in the neighbourhood of the maximum value of critical speed curve, it is possible to:

- maximize productivity, as the maximum of the critical speed curve represents the maximum scan speed for which a stable track is obtained; hence a good quality 3D component is likely to be produced in this process condition;
- be as far away from the keyhole as possible, thus also avoiding the need of cross section analysis.

Therefore, a small DoE centred at the maximum of the critical speed curve can be defined for next production step.

STEP 6 - 3D Benchmarks Production

After the definition of the process window for single tracks, it is necessary to compute hatch distance through track width measurements while preserving a fixed overlap rate. At this step, also the scan strategy has to be chosen in order to set all main process parameters for production of 3D components. For the sake of simplicity, overlap rate and scan strategy have not been investigated in this work. However, this methodology is suitable also for further investigation on these two parameters.

It is also worth noting that the process window defined for single tracks drastically reduces the process region to be investigated.

Consequently, a DoE of 3D benchmarks with 3 levels of power and 3 levels of speed (centred at the maximum of critical speed curve) can be produced for each level of spot size and/or layer thickness taken into account. A three-dimensional cube of side 8 mm

has been chosen as benchmark geometry, as it is the simplest and the most common shape used for process optimization.

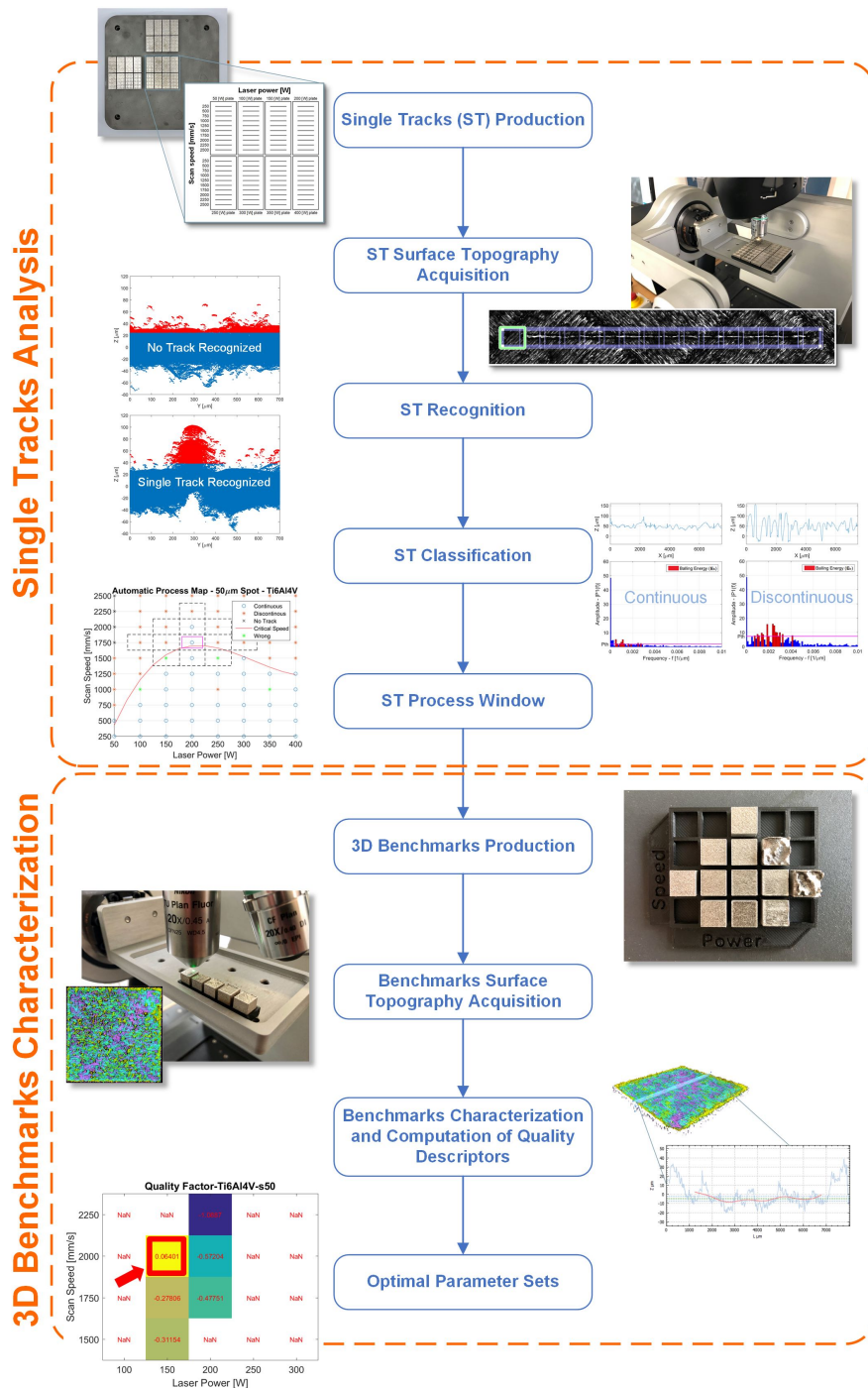


Figure 4.8: Flowchart of the proposed methodology.

STEP 7 - Surface Topography Acquisition of Benchmarks

The cubes produced have then to be removed from the build platform and collected in specific holders for subsequent surface measurements. The cube-holders (3D printed) are required for a precise positioning of samples below the 3D profiler objective. As for single tracks measurements, by taking a reference position at the first cube and by knowing the (x,y) coordinates of the other samples, it is possible to automate the acquisition of the surface topography of each cube. However, with respect to single tracks, cubes surface is significantly greater and acquisition with interferometry would take a long time.

Therefore, focus variation technique is preferable, as it is the fastest available methodology and roughness of SLMed surfaces is enough high for a good topography acquisition.

The output of scanning operation is a point cloud that represents only the top surface of the cube sample, since it will give enough information for process parameters selection at this optimization step.

STEP 8 - Benchmarks Characterization

From the generated point clouds, it is possible to extract profiles for roughness analysis and consider the whole surface for areal topography characterization. With respect to the latter, a novel descriptor has been defined and an automated procedure has been developed in MATLAB environment.

Density measurements must also be carried out, since relative density is a descriptor of mechanical performance of produced parts (low porosity means high mechanical performance). For density measurements, Archimedes method is recommended, as it is rapid, non-destructive, and gives sufficiently accurate data.

Eventually, through roughness profiles, areal topography characterization and density measurements, it is possible to compute a series of quality descriptors.

STEP 9 - Optimal Parameter Sets

Once defined the quality descriptors, dimensionless values are computed for each descriptor in order to sum the results and obtain a final descriptor that takes into account all investigated aspects. The benchmark with higher value of this final quality parameter represents the optimal parameter set.

This procedure has to be done for each level of layer thickness or spot size, in order to define the various optimal parameter sets needed for the target adaptive production strategy (e.g. skin and core or adaptive slicing strategy).

4.4 Design of Experiments

In this work, a design of experiments approach has been applied for the production of both single tracks and 3D benchmarks. The factors investigated were laser power, scan speed and laser spot size, while the other process parameters were kept constant. In particular, layer thickness was set to $25\mu m$, the gas flow was against the scanning direction and no build platform pre-heating was performed. The same experimental approach was applied

Chemical element	Fe	Cr	Ni	Mo	Mn	Si	P	C	S
316L stainless steel (% weight)	Rest	17,7	12,6	2,35	1,14	0,61	<0,045	0,025	0,004

Table 4.2: Chemical composition of SS316L used for the experiments.

for two different materials: Ti6Al4V and SS316L.

These two materials are widely applied in SLM production and were chosen to validate the proposed method. As a matter of fact, it will then be possible to compare the results of the methodology with the process parameters used by the machine manufacturer.

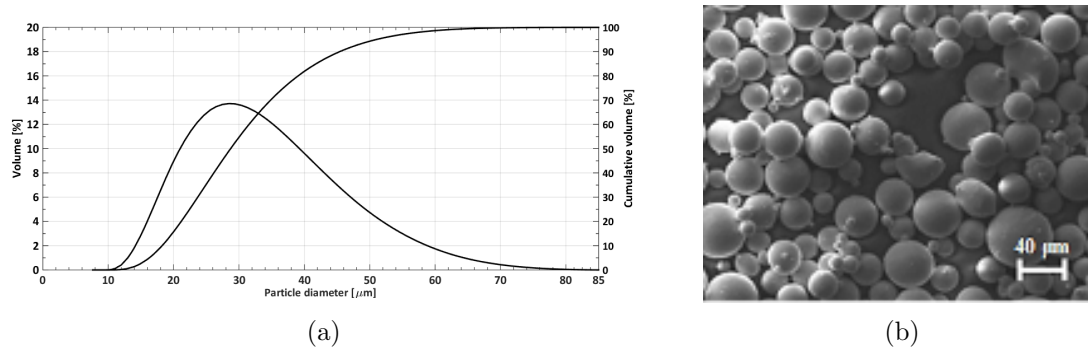


Figure 4.9: (a) Particle size distribution and (b) SEM image of SS316L powder.

Titanium powder was identical to that used in experiments described in Chapter 3, while stainless steel powder characteristics are given in Table 4.2 and Figure 4.9. Even stainless steel powder was analysed by the scanning electron microscope – SEM *Zeiss Evo 40* equipped with EDXS INCA X-sight. Thus, a sample of powder was embedded in epoxy resin and underwent lapping and etching for optical metallographic inspection, as shown in Figure 4.9 b). It can be noticed that particles had a spherical shape (typical of gas-atomized powder) with diameters at 10th and 90th percentile equal to $18.169\mu\text{m}$ and $45.436\mu\text{m}$, respectively. The 50th percentile diameter was $28.719\mu\text{m}$. All specimens were manufactured with the *Concept Laser M2 Cusing* machine, equipped with a 400W single-mode ytterbium-doped laser (1067nm wavelength) and a *varioSCAN* dynamic focusing unit (spot size range was $50 \div 500\mu\text{m}$).

4.4.1 Single Tracks DoE

With respect to single tracks experiments, a full factorial DoE with 3 factors has been carried out. In particular, eight levels of laser power ($50 \div 400\text{W}$), ten levels of scan speed ($250 \div 2500\text{ mm/s}$) and three levels of laser spot size ($50 \div 250\mu\text{m}$) were investigated. Therefore, 240 specimens were fabricated for each material (480 total samples). Details of DoE are summarized in Table 4.3.

Referring to the DoE ranges, the P -range was defined as large as possible, while an upper limit was set for the v -range. As a matter of fact, the maximum speed that can be set in the M2 Cusing is 7500mm/s . However, this value is very high and no literature work was

Parameters	Ti6Al4V Baseplate	SS316L Baseplate	Single Tracks	Levels
Laser Power	225W	180W	50 ÷ 400W	8
Scan Speed	1300mm/s	600mm/s	250 ÷ 2500mm/s	10
Spot Size	155 μ m	120 μ m	50 ÷ 250 μ m	3
Layer Thickness	25 μ m	25 μ m	25 μ m	1
Overlap Rate	40%	30%	-	-
Scan Strategy	<i>Islands</i>	<i>Islands</i>	-	-

Table 4.3: Process parameters used for the production of baseplates and single tracks.

found in which an optimum scan speed has reached such a high value. Thus, considering both literature works and Concept Laser parameters for various materials, it was chosen an upper limit of 2500mm/s, which is 1000mm/s above the standard parameters with higher speed provided by the machine manufacturer. The step sizes, on the other hand, were chosen in order to limit the number of experiments to a reasonable, albeit high, value. It is worth reporting that the choice of a full factorial DoE is due to the need to validate the methodology. Indeed, the performance evaluation of the algorithmic framework that will be discussed in next chapter requires as much data as possible and, every operating condition must be tested. Furthermore, the adoption of a full factorial DoE will also allow to compute some experimental curves, such as the melting efficiency curve and the critical speed curve, that otherwise would not be possible to identify.

It is also worth recalling that single scan lines were produced on the top surface of

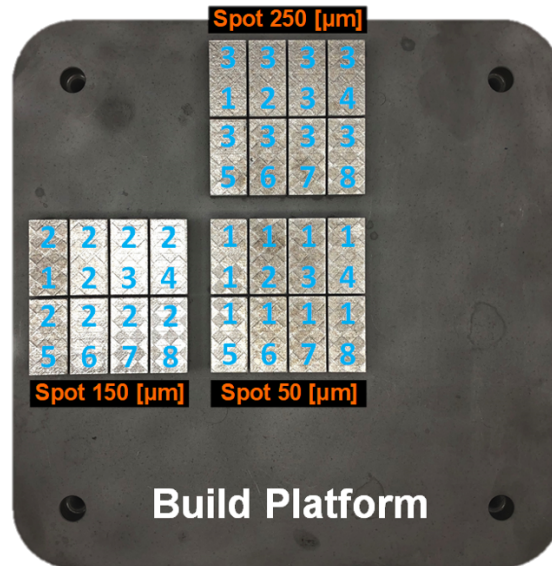


Figure 4.10: Single tracks layout on build platform. Light-blue labels are the identification marks of the baseplates.

rectangular baseplates that were 3D printed during the previous layers of the same job. All baseplates were fabricated using default parameters and island scan strategy was applied. Hence, scan lines that make up the top layer of baseplates were printed at an angle of 45 degrees with respect to single tracks.

The reason behind this design choice lies in various advantages that baseplates printed together with the single track specimens entail:

- the layer thickness can reasonably be assumed to have the desired value. As a matter of fact, the layer thickness reaches a stable value after the production of first layers;
- the substrate surface is as similar as possible to that obtained in operating conditions. Thus, the laid powder bed would have more representative characteristics;
- the substrate temperature is higher than room temperature. This allows to some extent to compensate for the heat accumulation effect due to multi-layer production, which would not happen in the case of tracks produced directly on build platform.

These statements were confirmed to some extent by Mishra et al. [98]. As a matter of fact, the authors studied the effect of surface morphology on the melt pool geometry in single tracks production. Basically, three types of substrates were used in a single tracks study, keeping constant the process parameters (except laser power): polished, shot blasted and laser deposited substrates were investigated. The authors found that the track geometry features (width and height) can vary up to 30% when different substrates are applied. Moreover, the same authors did also suggest that laser deposited substrates should be generally preferred for single track analysis, since they better represent the substrate characteristics under real operative conditions; the process typically takes place on a laser deposited surface for almost the entire production time. Thus, more reliable results will be obtained, especially for track width measurements, which are crucial for hatch distance selection and the suppression of porosity due to bad connection between tracks.

Nevertheless, it is worth noting that the adoption of SLMed substrates implies the need to have default parameters for their production. This could be a limit for the presented methodology, since it is not possible to apply this experimental approach in case of new materials development. However, further investigations on the effect of the substrate topography could be performed, in order to find some kind of correction factor that takes into account the differences between substrates applied in single tracks studies.

From the algorithmic point of view, track recognition on a polished (or shot blasted) substrate would be easier (the substrate would be almost flat); therefore, excellent results are expected in this case.

The layout of the specimens produced can be seen in Figure 4.11, where it can be noted that ten single tracks per baseplate have been placed, maintaining a distance of 3 mm from each other and from the edges of the single baseplate. Overall, 24 baseplates were included for each build job, in groups of 8 for each spot size level. This means that the samples needed for the investigation of one material were all fabricated in the same build platform. As can be seen from Figure 4.10 and Figure 4.11, an intuitive spatial distribution was applied, as samples number was quite high and, by doing so, the risk of errors during

the analysis has been suppressed. However, location effects and gas flow consequences could be expected. Therefore, spatial randomization will be a point of interest for future development of the methodology.

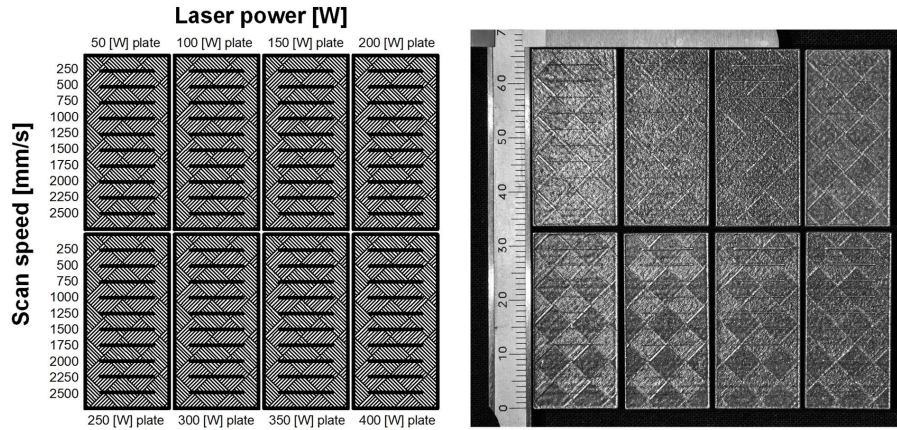


Figure 4.11: Single tracks DoE for one level of laser spot size.

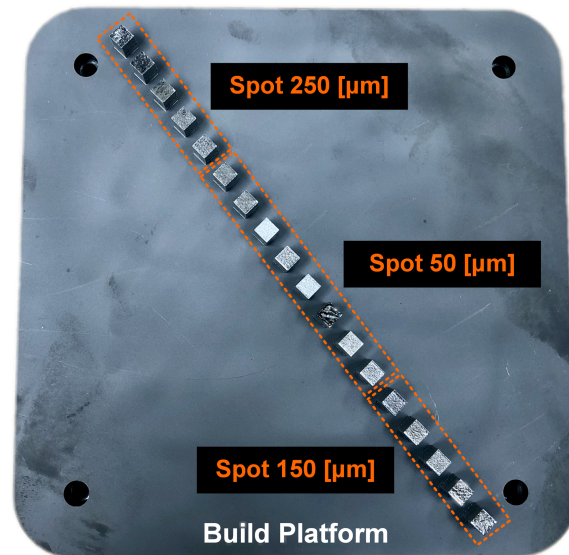
4.4.2 3D Benchmarks DoE

Even the DoE used for 3D benchmarks characterization includes 3 factors: laser power, scan speed and laser spot size. The experiment size needed in this step is small: a factorial design with 3 levels for each factor is sufficient ($3 \times 3 \times 3 = 27$ samples). Nevertheless, some extra levels for laser power and scan speed were added to the experiment in order to better validate the methodology.

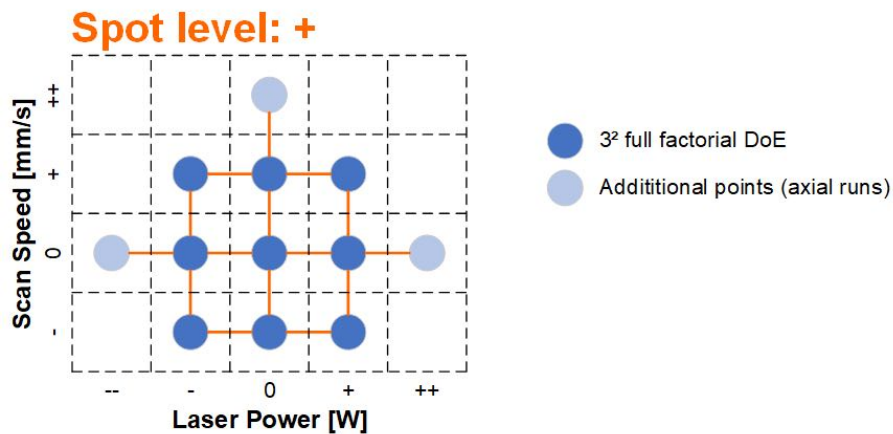
In practice, 36 samples were fabricated for each material investigated (72 total samples). While the levels of laser spot size were the same of single tracks DoE, the selection of laser power levels and scan speed levels was more articulated. As a matter of fact, for each material, 3 different process maps were obtained from single tracks analysis: one (P, v) map for each spot size level. In every map, a critical speed curve was defined and the ideal 3×3 (P, v) DoE was centered at the maximum of the aforementioned curve. Hence, different laser power and scan speed values have been taken into account for each spot size level.

For the sake of clarity, the DoE of every spot level can be seen in Figure 4.13 and Table 4.4 for Ti6Al4V, while the ones for SS316L are reported in Figure 4.14 and Table 4.5. As can be seen in Figure 4.12b, the main factorial design is basically composed by a 3×3 full factorial design and by 3 axial runs. These additional points will be used to ensure that the optimum processing condition is inside the core DoE.

It is also worth noting that only 18 samples were positioned on each build platform; hence, two build platforms were needed for each of the investigated materials (Job 1 and Job 2). Indeed, by placing the samples along a negative slope diagonal line (see Figure 4.12 a), the maximum number of sample for build platform is limited. However, by doing so, each cube will be singularly engaged by a portion of the coater blade and interaction between



(a)



(b)

Figure 4.12: (a) 3D benchmarks layout on build platform; (b) Factorial design applied for each spot level.

samples during the powder spreading phase will be avoided. As a matter of fact, if a cube damages the coater blade, the other samples will not be affected by that damage and a good powder spreading will be guaranteed.

After production, all samples were removed from build platform and no thermal treatment was performed. Afterwards, support structures were manually removed from samples and each 3D benchmark was collected in a special holder for subsequent analysis.

Ti6Al4V				
Parameters	Spot 50 μm	Spot 150 μm	Spot 250 μm	Levels
Laser Power	100 \div 300W	100 \div 300W	150 \div 350W	3+2
Scan Speed	1500 \div 2250mm/s	1000 \div 1750mm/s	500 \div 1250mm/s	3+1
Layer Thickness	25 μm			1
Overlap Rate	30%			1
Scan Strategy	<i>Bidirectional&AlternatingExposure</i>			1

Table 4.4: Process parameters used for the production of Ti6Al4V 3D benchmarks.

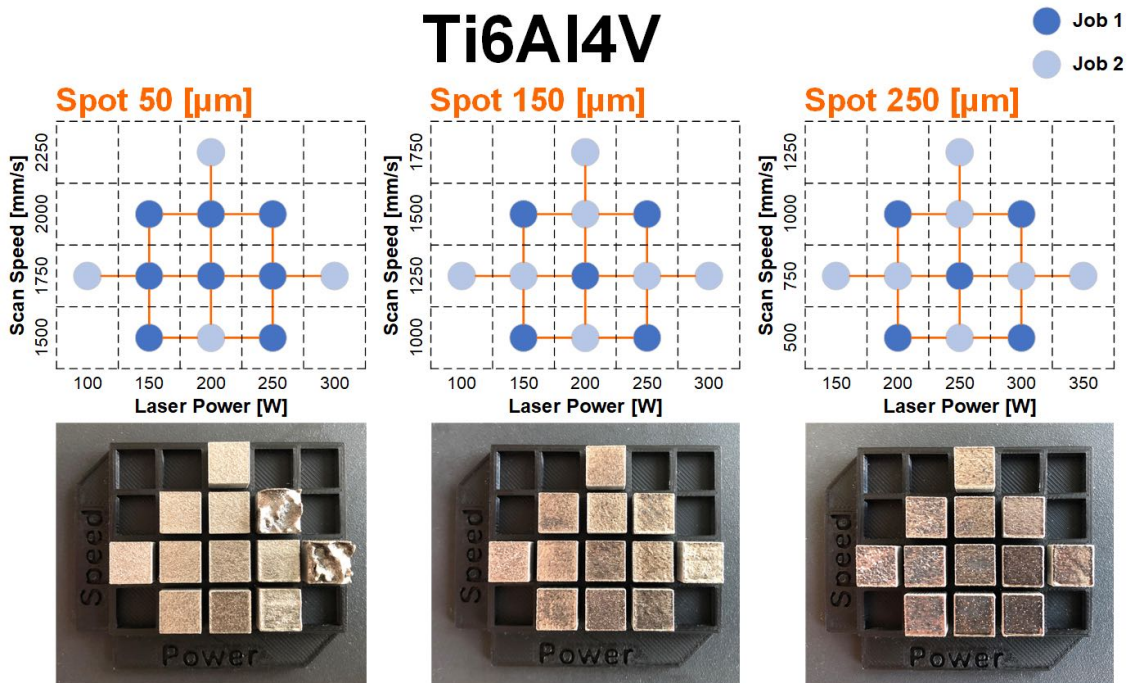


Figure 4.13: Design of experiments for Ti6Al4V.

SS316L

Parameters	Spot 50 μ m	Spot 150 μ m	Spot 250 μ m	Levels
Laser Power	50 \div 200W	50 \div 250W	150 \div 350W	3+2
Scan Speed	250 \div 1000mm/s	250 \div 1000mm/s	250 \div 1000mm/s	3+1
Layer Thickness	25 μ m			1
Overlap Rate	30%			1
Scan Strategy	<i>Bidirectional&AlternatingExposure</i>			1

Table 4.5: Process parameters used for the production of SS316L 3D benchmarks.

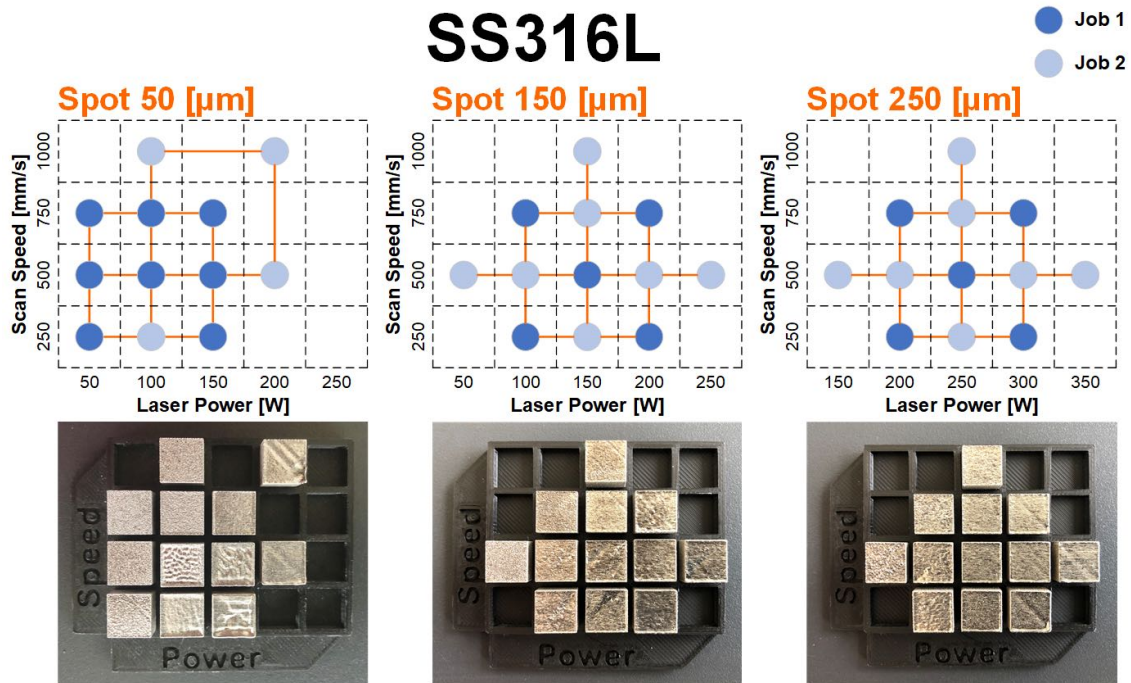


Figure 4.14: Design of experiments for SS316L.

Chapter 5

Single Tracks Analysis

5.1 Single Tracks Recognition

5.1.1 Input Data

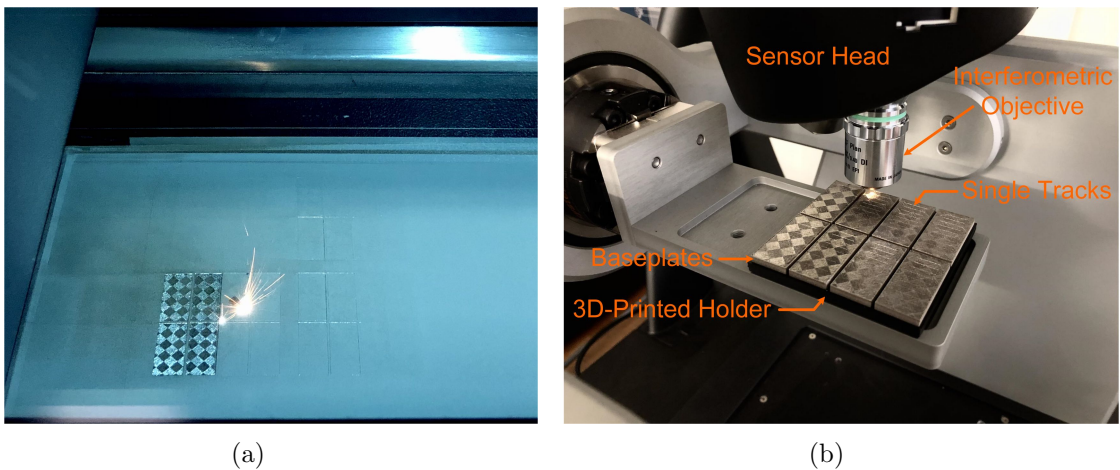


Figure 5.1: (a) Build chamber during the production of the baseplates; (b) Setup for topographies acquisition.

The full factorial DoE of single tracks was produced on a single build platform for each material. After production and some post-processing operations, single tracks were collected in 3D-printed holders for subsequent topography acquisition. The 3D profiler was the *Sensofar S neox Five Axis* and the objective mounted was the *Nikon DI-20x*, which is an interferometric objective with a magnification of $20x$ and a working distance of $4.7mm$. The field of view (FoV) was $845 \times 707 \mu m^2$; with a resolution of $0.69 \mu m/pixel$ (pixel size can be set by the operator), that corresponds to 1224×1024 pixels. A stitching area composed by one row and 16 columns with an overlap rate of 15% was necessary for the acquisition of the whole topography of one single track. This means that the scanning area was composed by 16 FoVs and the nominal area dimension was

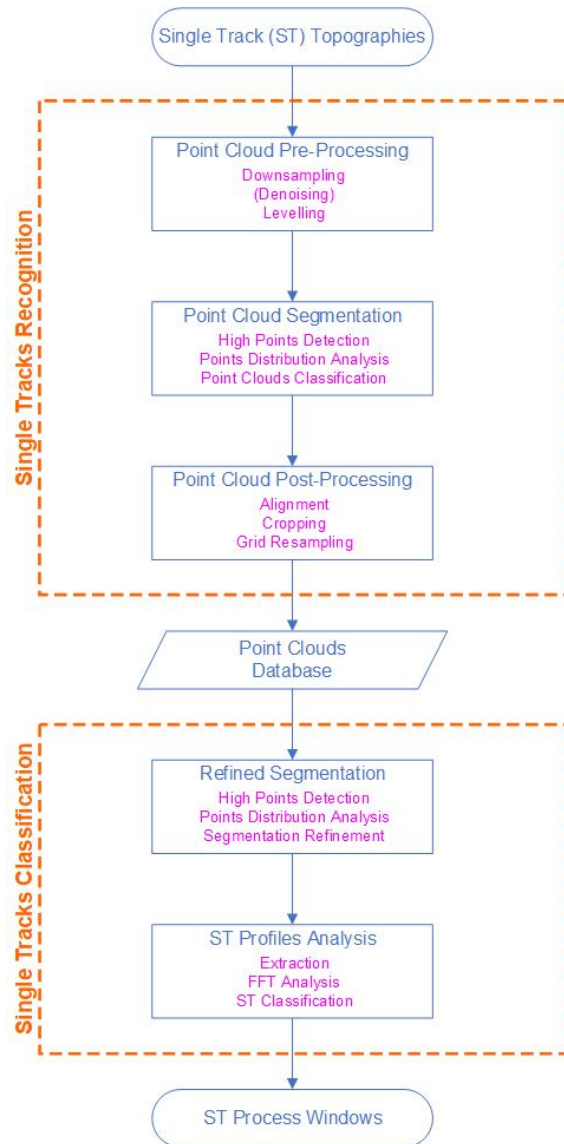


Figure 5.2: Flow chart of the methodology for single tracks analysis.

$11.61 \times 0.71 \text{mm}^2$, or $16830 \times 1024 \text{pixels}$. In addition, the Z stage acquisition range was $370 \mu\text{m}$, 6% of white light intensity was used and autofocus algorithm was applied at each FoV.

Once defined the acquisition recipe for one single track (SMR - *Single Measurement Recipe*), the Multi-Measurement Recipe (MMR) was defined in order to acquire automatically, in one scanning operation, all single tracks belonging to a sample holder. Actually, the MMR for one holder was divided into two blocks (see Figure 5.3a) due to the large amount of data. As a matter of fact, the high resolution of topography acquisition implies large files dimension; approximately 400 MB per file (~ 15 million points). Hence, the

number of tracks acquired in one scanning operation were halved (from 80 to 40 samples per scan) in order to be managed more easily.

The result was a collection of TXT files (one for each single track) containing the spatial coordinates of each surface topography. An example of a TXT file can be seen in Figure 5.3b. It is worth recalling that each topography obtained from the 3D profiler consists in an image (or an image stack). However, a point cloud can be obtained by computing pixels intensity with a properly calibrated conversion factor. The centre position of pixels defines the (X,Y) coordinates, while the pixels intensity can be converted to Z coordinates. It is also worth reporting that each topography has not exactly the same area dimensions. Indeed, the number of measured points varies between scans as the acquired topography is not always the same and critical local slopes can be present (metal AM surfaces are characterized by high roughness values). Nevertheless, the measured points rate was always over 90% and its variation was small. Therefore, the small variation of area dimensions can be practically neglected.

Once all topography files were generated, each of them was automatically renamed with a string containing the values of the process parameters investigated in the DoE (e.g. 's50P150v2000.txt' means a track produced with a spot size of 50 μ m, a laser power of 150W and a scan speed of 2000mm/s).

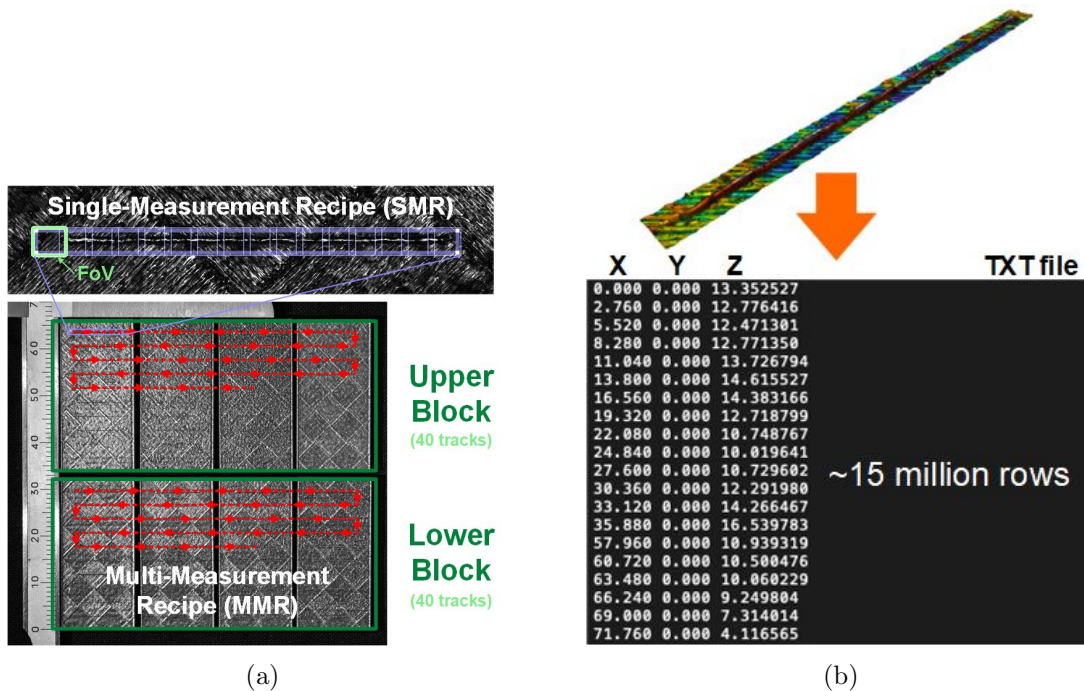


Figure 5.3: (a) Scanning preview of the 3D optical profiler; (b) Example of a point cloud saved as a TXT file.

5.1.2 Point Cloud Pre-Processing

Downsampling

After point clouds generation, TXT files were one by one automatically imported and processed in *MATLAB* environment. The first operation was points downsampling, which was necessary to reduce the calculation time of the next steps. No sophisticated algorithm was applied to resample the point clouds, as there were no particular conditions to be met in terms of point spacing (e.g. uniformity). Basically, one point every twenty was considered from the coordinates list. This means that the number of points was reduced from ~ 15 millions to ~ 750000 points.

Nevertheless, the original point clouds were preserved in order to apply the various modifications computed at each step. In other words, the computations of thresholds, statistical models, etc. were performed only on downsampled point clouds, while the operations that modify the point cloud were applied also to the original ones.

Denoising

Traditional algorithms for point cloud denoising largely rely on local surface fitting or on local/non-local averaging and permits to remove outliers and noise from dense point clouds. However, noise is very low in case of topography measurements with low coherence interferometry. Therefore, denoising step was ignored in this work in order to optimize the computation time of the whole analysis. As a matter of fact, denoising operation could take a long time, especially for point clouds with a large number of points.

Eventually, even if some noise was present in the analysed point clouds, the described methodology was enough robust to overcome this problem.

Levelling

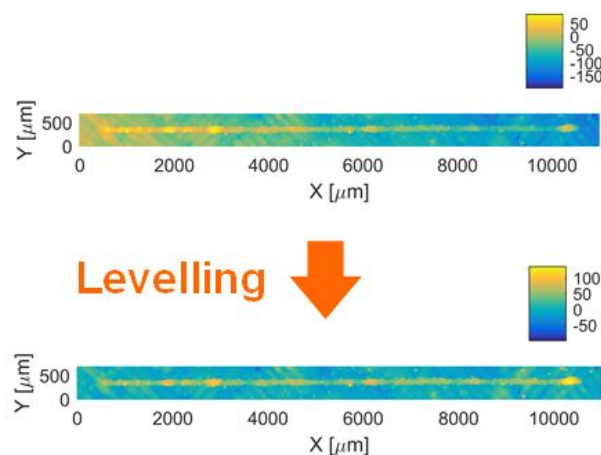


Figure 5.4: Point cloud before and after levelling operation.

The last operation of pre-processing step was the levelling of point clouds. Basically,

the tilt of a point cloud was adjusted by interpolating a plane and subtracting it from the topography.

The canonical equation of a plane is:

$$aX + bY + cZ + d = 0 \quad (5.1)$$

where a, b, c, d are real numbers, while X, Y, Z are coordinate vectors. This equation can be rewritten as follows:

$$Z = \beta_0 + \beta_1 X + \beta_2 Y \quad (5.2)$$

where $\beta_0 = -d/c$, $\beta_1 = -a/c$ and $\beta_2 = -b/c$. If we consider Z_E (Z estimated) as the response of a multiple linear regression and, X, Y of target point cloud as predictors, coefficient estimates $(\beta_0, \beta_1, \beta_2)$ can be computed by regression:

$$Z_E = \beta_0 + \beta_1 X_{ptCloud} + \beta_2 Y_{ptCloud} (+ \epsilon) \quad (5.3)$$

where ϵ is the vector of residuals. Equation 5.3 represents the plane that interpolates the target point cloud. Once the vector Z_E was defined, it was subtracted from the Z coordinates of the target point cloud in order to remove the topography tilt:

$$\Delta Z = Z_{ptCloud} - Z_E \quad (5.4)$$

where ΔZ is now the updated Z coordinate vector of the leveled point cloud. After levelling operation, the whole point cloud was also shifted in order to place the origin of z-axis at the mean value of Z coordinates.

5.1.3 Segmentation Algorithm

High Points Detection

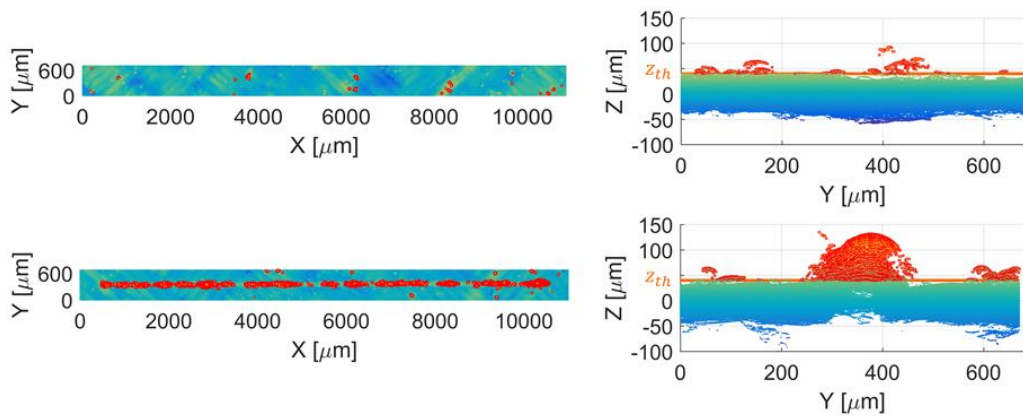


Figure 5.5: Two representative results of points height segmentation.

The segmentation algorithm starts with the detection of points that lie above a certain Z threshold. As a matter of fact, the single track surface should be in theory higher than

the substrate, since it was produced in the layer after the end of baseplate production. However, this is not entirely true due to the high roughness of the substrate and the presence of spatters and macro-humps, whose points could fall within the threshold. To partially overcome this problem, three substrate topographies (no track presence) were investigated and a threshold ($z_{th,sub}$) was defined on the basis of a statistical consideration:

$$z_{th,sub} = mean(Z_{ptCloud}) + 3 * std(Z_{ptCloud}) \quad (5.5)$$

As a matter of fact, a point cloud representing only the substrate, that is the baseplate surface, is characterised by a gaussian distribution of Z coordinates, centred on the origin. Thus, by considering only the points above 3 standard deviations from the mean, it can be reasonably assumed that the $\sim 99.7\%$ of points belonging to the substrate are ignored. The threshold was computed for three substrate topographies and then the average value was chosen as z_{th} :

$$z_{th} = mean(z_{th,sub}^I, z_{th,sub}^{II}, z_{th,sub}^{III}) = 40[\mu m] \quad (5.6)$$

Once defined z_{th} , points higher than the threshold were automatically detected and saved separately ($Z_{ptCloud} > z_{th}$). Two representative results of points height segmentation can be seen in Figure 5.5. It can be noticed that in the point cloud containing a single track, also some spatters and portions of substrate were detected. Therefore, the z_{th} threshold is not sufficiently accurate for track detection and additional steps are required for this purpose.

High Points Distribution Analysis

Once separated the high points from the rest, their spatial distribution was analysed. In particular, the points distribution with respect to y-axis (transverse to the direction of the track) was considered. Two representative distributions can be seen in Figure 5.6. It can be noticed that if a track is present, the distribution resembles a Gaussian one (Figure). Thus, the number of points for each central bin was way higher than in case of the substrate alone. Therefore, a threshold on number of points per bin was defined:

$$n_{th} = mean(N) + std(N) \quad (5.7)$$

where N is the vector of number of points per bin. Basically, the higher the $N(i)$ value, the higher the number of points belonging to the (x,z) plane passing through a specific y coordinate. In this case, n_{th} is a mobile threshold and depends on spatial distribution of points.

In case of track presence, the distribution of elements belonging to vector N resembled a half Gaussian distribution with a highly positive Kurtosis (leptokurtic). Thus, n_{th} was a high threshold and only a portion of points that belonged to a single track were satisfying the condition $N > n_{th}$. On the other hand, n_{th} value was very low in case of point clouds that didn't had a single track and more points were considered.

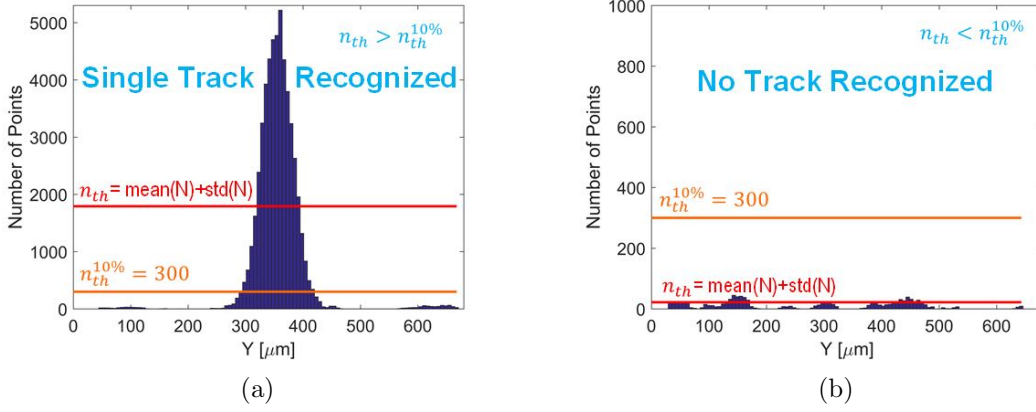


Figure 5.6: High points distribution of (a) a point cloud that includes a single track and, (b) a point cloud that includes only the substrate.

Point Clouds Classification

The n_{th} mobile threshold was used in the previous step for the detection of high points that had a relevant numerosity along the x axis (single track axis). However, n_{th} is not only a threshold, but it can be further used as a statistical descriptor of point clouds distribution. This implies that point clouds can be classified on the basis of n_{th} value. As a matter of fact, point clouds that include a single track will have high values of n_{th} . On the contrary, point clouds that include only the substrate will have very low n_{th} .

With a view to make a distinction between point clouds containing a single track and point clouds that include only the substrate, a threshold on n_{th} value was defined. To compute this new threshold, a point cloud with a continuous single track was analysed (in general, a continuous and well-formed track can be found at very high energy density levels). Once performed the first steps of the analysis, it was verified that the n_{th} threshold had kept the points for the entire length of the single track. Afterwards, the 10% of the n_{th} value of that track was taken as a reference:

$$n_{th}^{10\%} = (n_{th})_{ST_{continuous}} * 10\% \simeq 300pt \quad (5.8)$$

Therefore, $n_{th}^{10\%}$ was used as a new threshold for point cloud classification: if a point cloud had a n_{th} value greater than $n_{th}^{10\%}$, then a single track was present. On the contrary, the point cloud included only the substrate ($n_{th} < n_{th}^{10\%}$). Thus, energy density wasn't enough for consistent powder melting.

Clearly, this threshold depends on the total number of points of the topography. Therefore, if the data acquisition settings are modified (resolution, etc.), then the $n_{th}^{10\%}$ must be calibrated again.

The practical meaning of this new threshold is the following: if the length of molten material along the scan path of a single track is higher than the 10% of the total length of the nominal track, then a track can be recognized. This includes both discontinuous tracks (presence of balling or humping) and continuous ones. On the contrary, if the length of

molten material is less than the 10%, then it can be reasonably assumed that no track is present.

From the physical point of view, the $n_{th}^{10\%}$ threshold allowed to define an empirical single track melting efficiency curve.

An example of a computed process map can be seen in Figure 5.7, in which point clouds with no track were distinguished from point clouds that include a single track.

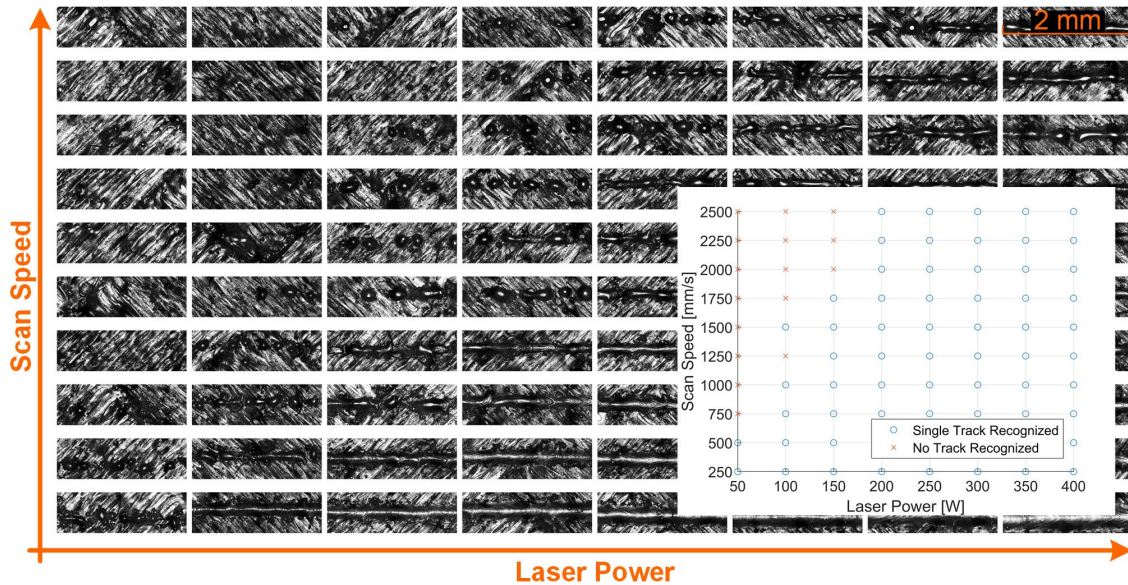


Figure 5.7: Example of a process map obtained from single track recognition.

5.1.4 Point Cloud Post-Processing

The following operations were performed only on point clouds that include a single track. Indeed, the point clouds in which no track was recognized were ignored in the following steps of the analysis.

Point Cloud Alignment

Once the point clouds that not include a single track were removed from the analysis, the remaining point clouds were post-processed for further analysis steps.

The first operation was the point cloud alignment, that is the alignment of the single track with the x-axis. This step is essential for an accurate track detection, since a part of the logic behind the next segmentation algorithm lies in defining some thresholds along the y-axis. Thus, if the track is not correctly aligned with the x-axis, then a relevant error will be introduced.

Previously, a portion of single track points were detected through z_{th} and n_{th} thresholds. However, n_{th} threshold was ignored in this step and the points that only satisfied the z_{th} criterion were considered. As previously mentioned, these points may include also points

that do not belong to a single track. Therefore, a simple filter on Y coordinates distribution was applied in order to roughly consider only single track points. Basically, the average (μ) and the standard deviation (σ) of the Y coordinates vector of high points were computed. Afterwards, all points outside the $\mu \pm 2\sigma$ range were removed (see Figure 5.8a). With respect to the (x,y) plane, the remaining points were then used for the interpolation of a straight line, which represents the single track axis. The explicit equation of a straight line belonging to the (x,y) plane is $y = mx + q$. Thus, the regression model of the line that interpolates the points detected can be written as follows:

$$Y_{highpt} = mX_{highpt} + q \quad (5.9)$$

where m is the slope of the line and q is the y intercept.

Once computed the regression, coefficient m can be used in a rotation matrix R for the alignment of single track axis. The rotation matrix has to rotate the entire point cloud around the z-axis in order to align the single track with the x-axis. Thus, the rotation was computed as follows:

$$\begin{pmatrix} X' \\ Y' \\ Z' \end{pmatrix} = \begin{bmatrix} \cos(\theta) & -\sin(\theta) & 0 \\ \sin(\theta) & \cos(\theta) & 0 \\ 0 & 0 & 1 \end{bmatrix} \begin{pmatrix} X \\ Y \\ Z \end{pmatrix} \quad (5.10)$$

where $\theta = \text{atan}(m)$.

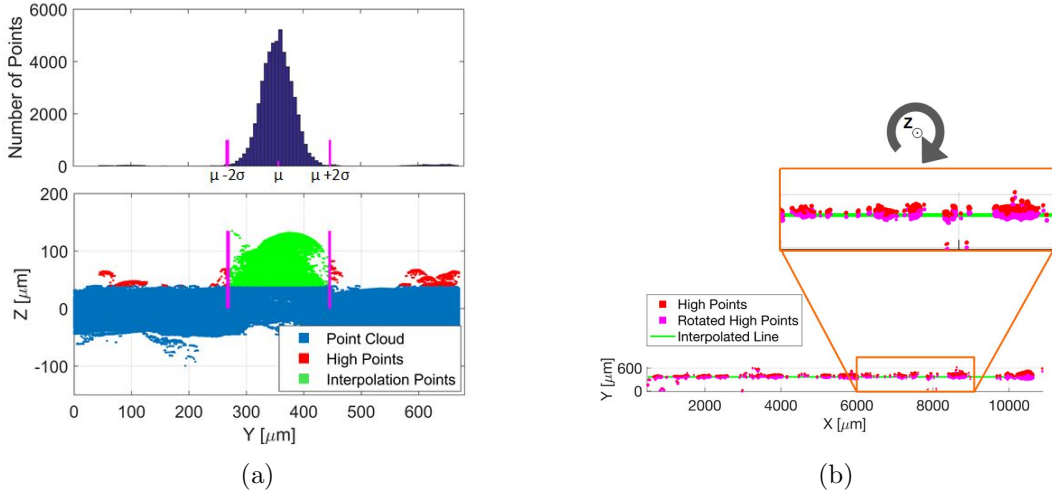


Figure 5.8: (a) Filtering operation on high points and, (b) alignment operation result.

Point Cloud Cropping

Nevertheless, the rotation of the point cloud entailed also a misalignment of point cloud borders with respect to the (x,y,z) reference system. Therefore, a two-step cropping operation was needed to regain a rectangular area aligned with the reference system. The first cropping operation was performed along x-axis. Basically, after computing the centre of

the single track, the extremes of the point cloud were removed and a point cloud of $8mm$ of length was considered (see Figure 5.9a). This operation was necessary also to remove the side effects of track shape, which are the typical initial hump and the final depression zone.

After x-cropping, to regain a rectangular area, also a cropping operation along y-axis was necessary. Therefore, two extreme slices of the point cloud were considered and local Y minimum and maximum were computed (see Figure 5.9b). Afterwards, points not within the two limits (Y_{max} and Y_{min}) were removed and a rectangular area was obtained.

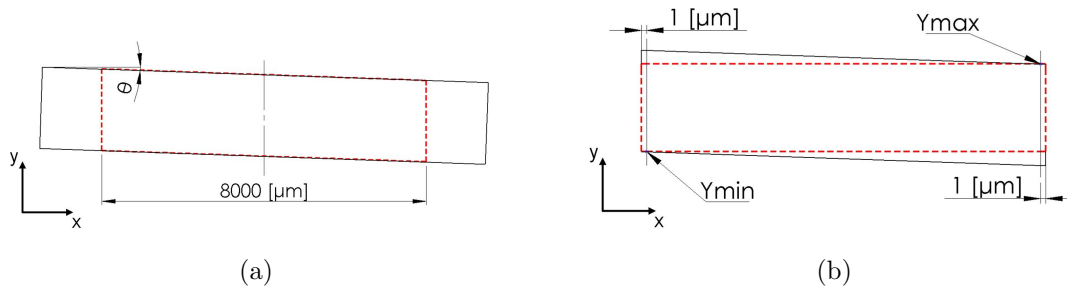


Figure 5.9: Cropping operations along (a) x-axis and, (b) y-axis.

Grid Resampling

The previous steps, in particular levelling and point cloud alignment, had a negative effect on point spacing. As a matter of fact, points were no longer evenly spaced with respect to (x,y) plane. Therefore, a resampling algorithm was developed to retrieve the uniform spacing of points. In practice, a grid with a cell size of $2\mu m$ was applied to the (x,y) plane and the z -coordinates of the points within each cell were averaged. By considering the centre position of each cell as (x,y) coordinates and the average results as z -coordinates, a new equally spaced point cloud was obtained.

Database Generation

Eventually, all point clouds (and related data) were saved in a MATLAB database. The conversion of point cloud format, from TXT to MAT files, entailed a memory space saving of more than 90%. Indeed, approximatively 30 GB per set of single tracks (there was one set for each spot level and material) were reduced to about 2 GB. This memory space optimization was of great relevance for the next analysis steps, in terms of computation time.

5.2 Single Tracks Classification

5.2.1 Input Data

The second step of single tracks analysis entailed a further classification phase. The previously generated databases were loaded in MATLAB environment and only point

clouds that include a single track were considered in this step. The main features of these topographies were the following:

- point clouds were levelled (no tilt) and z-axis origin was set to the average value of Z-vector;
- single tracks were aligned with the x-axis;
- with respect to (x,y) plane, point clouds had a rectangular area and 8mm of the single track was considered (initial hump and final depression zone were removed);
- the point spacing was $2\mu m$, however, some missing data (small holes) were present in the point clouds.

5.2.2 Refined Segmentation Algorithm

High Points Detection

Since the point clouds were not the same as in the previous step, high points were again detected. In this case, the threshold was chosen again on the basis of a statistical analysis of three substrate topographies. Thus, the threshold value was $z_{th} = 40\mu m$ and all points with a z-coordinate below the z_{th} were removed from the analysed point cloud.

Points Distribution Analysis

High points distribution was again investigated; however, the purpose was different with respect to the earlier step. Previously, the aim of tracks recognition was to identify a portion of points belonging to the track, removing as many points as possible of the substrate. A statistical descriptor of the point cloud was then defined. To do this, a high threshold was applied in order to avoid false positives. However, many track points had been removed along with the substrate points. To include more points and overcome this problem, a lower threshold was defined in this phase:

$$n_{th}' = mean(N) + 0.5 * std(N) \quad (5.11)$$

where N is the vector of number of points per bin. It can be noticed that the standard deviation value was halved, with respect to Equation 5.7. This is because the distributions of N-vector had high values of standard deviation and, by halving $std(N)$, n_{th}' was sufficiently reduced. However, the reduction of the threshold value entails the possibility that points in the substrate will be included. Thus, further segmentation step was needed to better recognize track boundaries and make the algorithm more reliable. It is worth highlighting that no substrate points were included in each track analysed in this work (more than 300). Nevertheless, it is an eventuality that could happen due to the high variability of track shape and of substrate topography, especially in case of highly discontinuous tracks (low ED).

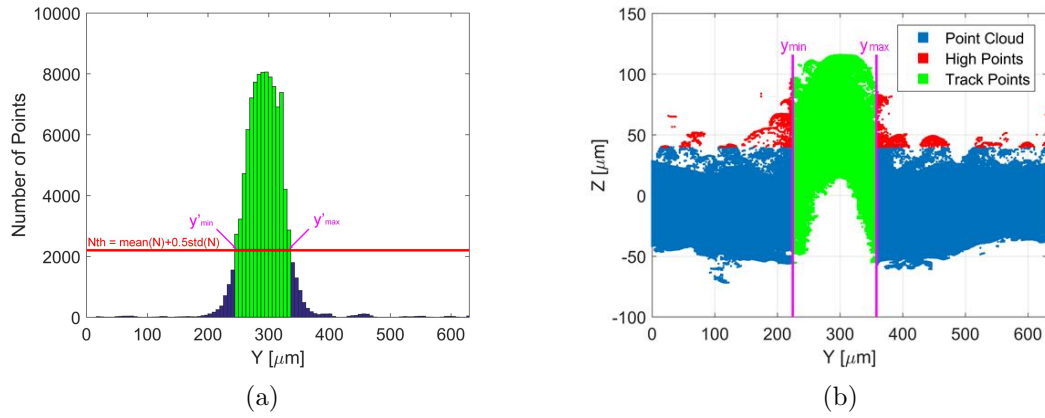


Figure 5.10: (a) High points distribution and, (b) (y,z) view of a single track point cloud.

Segmentation Refinement

This step represents the main difference with respect to the previous segmentation algorithm.

Once defined n_{th} , the elements of N-vector that exceed the threshold were analysed. Thus, an algorithm that finds the maximum y-interval in which $N(i) > n_{th}$ was developed. Basically, each y-interval that satisfied the aforementioned condition was saved separately. Afterwards, the one that had the maximum Δy was identified. Thus, the first-attempt values y'_{min} and y'_{max} were saved. However, these y-limits were not exactly the track boundary limits. This is because z_{th} and n_{th} detect only high points that have a relevant numerosity along x-axis (track axis). Thus, points that belong to the edges of the track were ignored and only the central region was taken. To consider also track edges, a further statistical analysis was performed: the average value and the standard deviation of y-coordinates satisfying the maximum-interval condition were computed and new y_{min} and y_{max} were defined as follows:

$$y_{min} = \text{mean}(Y_{interval}) - 2 * \text{std}(Y_{interval}) \quad (5.12)$$

$$y_{max} = \text{mean}(Y_{interval}) + 2 * \text{std}(Y_{interval}) \quad (5.13)$$

where $Y_{interval}$ is the vector of y-coordinates between first-attempt values of y_{min} and y_{max} . By doing so, most of track points were considered, as can be seen in Figure 5.10b. Therefore, the new y-interval was used for track points detection and automatic track width measurements:

$$W = y_{max} - y_{min} [\mu m] \quad (5.14)$$

where W represents the track width. Afterwards, a different interval was defined also for substrate points. The purpose of this operation was to define a new z-reference for subsequent steps. To ensure track points removal, a wider y-interval for single track points

was defined:

$$y_{min} = mean(Y_{interval}) - 5 * std(Y_{interval}) \quad (5.15)$$

$$y_{max} = mean(Y_{interval}) + 5 * std(Y_{interval}) \quad (5.16)$$

This new interval was then removed from original point cloud and the average of z-coordinates of the remaining points was computed:

$$z_{ref} = mean(Z_{substrate}) \quad (5.17)$$

where z_{ref} is the new z-reference value. Thus, z_{ref} was subtracted to the Z_{track} vector in order to align the point cloud of the track with the mean height of the substrate.

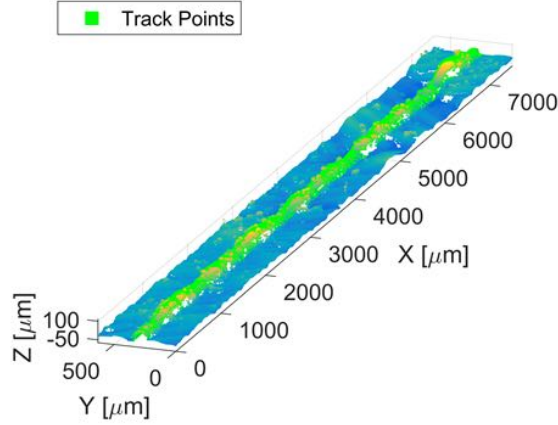


Figure 5.11: Example of single track recognition with new segmentation algorithm.

5.2.3 Single Tracks Profile Analysis

Profile Extraction

In the previous step, points that belonged to the substrate were removed from the point cloud. Thus, only single track points were considered. To evaluate the continuity of a single track, it was decided to extract a profile along the track-axis (x-axis). For each track, the profile was positioned at the mean value of the Y-vector of the point cloud:

$$y_{profile} = mean(Y_{track}) \quad (5.18)$$

where Y_{track} is the vector of y-coordinates of a single track point cloud. From the practical point of view, a small y-interval was actually chosen to extract the track profile ($y_{profile} \pm 1[\mu m]$). This was necessary for numerical reasons and it entailed a small drawback. As a matter of fact, by considering a small range of y-coordinates instead of a precise coordinate, more than one point (maximum two) could be taken for each x-coordinate of

the profile. The height difference of multiple-points case was investigated in order to assess the extent of the z-coordinate error. It was found that the height difference between profile points with same x-coordinate was in the order of magnitude of tens of nanometers, thus, negligible.

The extracted profiles presented also another issue: points were not entirely equally spaced, since there were some missing data due to small holes in the original point cloud.

Both issues (multiple points and missing data) were easily solved by a resampling operation. By using the MATLAB function *resample*, the profile data were resampled in order to obtain a uniform spaced signal in the spatial domain. Basically, *resample* function uses a polyphase antialiasing filter to resample the signal with a specific sampling frequency F_s . In this case, the sampling frequency was not referring to the temporal domain, but to the spatial domain. Thus, its unit of measure was $1/\mu m$ and the value was set to $F_s = \frac{1}{2}[1/\mu m]$, since the point spacing of original point cloud was $2\mu m$.

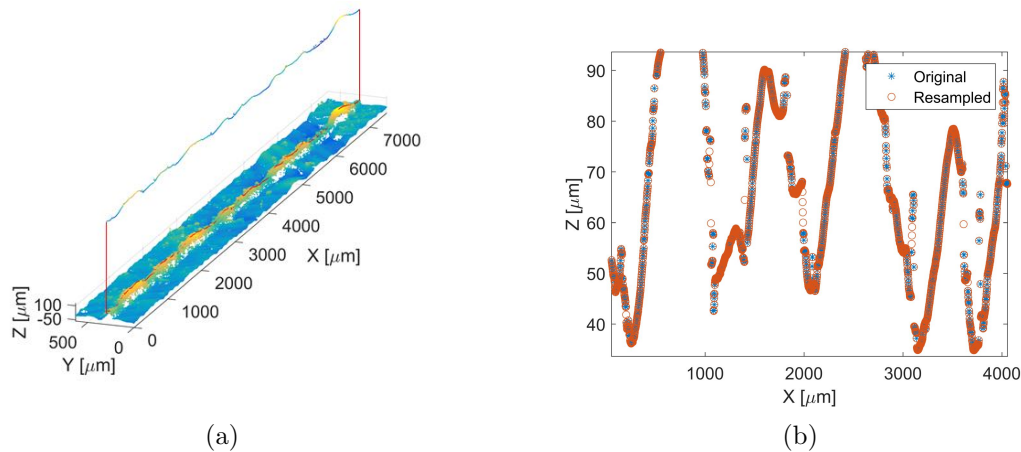


Figure 5.12: (a) Profile extraction and, (b) profile resampling operation.

Profile Analysis

Once extracted and resampled the profiles, the average height and the standard deviation of the spatial domain signal were computed as preliminary investigation. The mean value of the signals was not particularly interesting, since the tracks affected by evident balling or humping phenomena had similar values to those of well-formed tracks. As a matter of fact, a “ball” or a hump is typically higher than a regular-shaped track. So even though the tracks were discontinuous, their average height was high enough to be comparable to the height of a continuous track. On the contrary, the standard deviation of the signal was more representative. To deepen the analysis, a *fast Fourier transform* (FFT) was applied to convert the profile signal from spatial domain to frequency domain representation.

It is worth recalling that the aim of this step was to find a descriptor that distinguishes discontinuous tracks from continuous ones. In other words, the purpose was to recognise the occurrence of balling or humping effects on track shape.

With respect to the frequency domain representation, a well-formed track should have a

high fundamental frequency (f_0) and some noise at high frequency (in practice, a flat spectrum). On the other hand, a discontinuous track should be characterized by some relevant low-frequency components, since the balling and humping are pseudo-periodic phenomena with a relatively low frequency (strong balling effects can be observed with the naked eye).

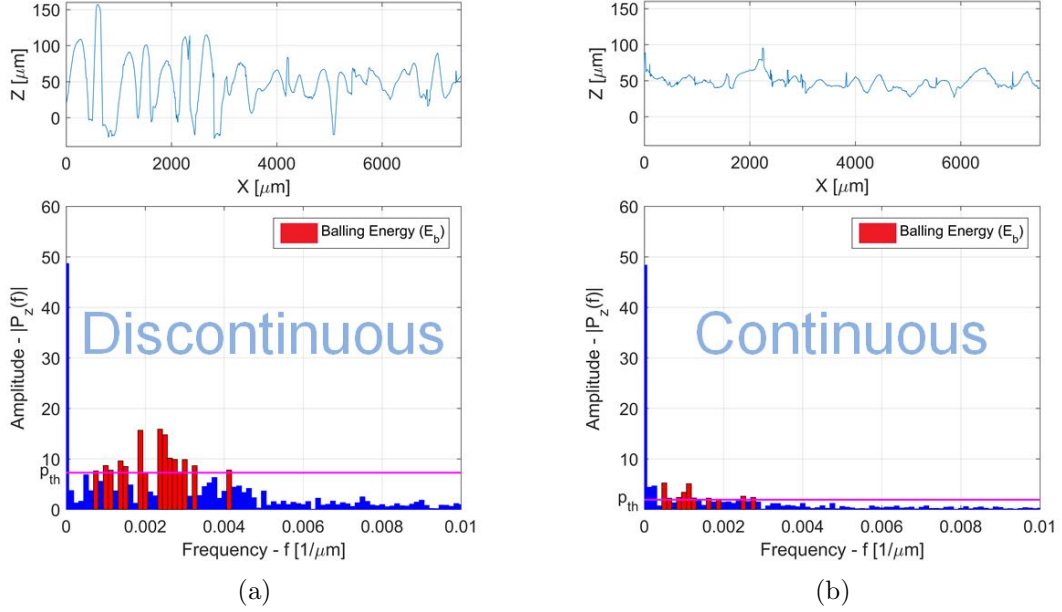


Figure 5.13: Spectrum of (a) a discontinuous track profile and, (b) a continuous one.

Based on this reasoning, a novel descriptor was defined to quantify the extent of discontinuity of the analysed tracks. In other words, the energy associated with the frequency components due to balling or humping phenomena was measured and used as a descriptor of track continuity. This descriptor was named *balling energy* (E_b).

Since the fundamental frequency actually represents the average height of the profile, the first five frequency components were cutted-off in order to remove the profile mean value effect, which was not representative for continuity analysis. Even frequency components above $f = 0.025$ [1/μm] were removed in order to reduce the high-frequency noise.

After this operation, a threshold on the amplitude of frequency components ($|P_z(f)|$) was defined in order to detect relevant components:

$$p_{th} = \text{mean}(P_z) + 2 * \text{std}(P_z) \quad (5.19)$$

Thus, only frequency components that satisfied the condition $P_z > p_{th}$ were considered. Some examples of results obtained from the application of this threshold can be seen in Figure 5.13. Lastly, all amplitudes detected were added up:

$$E_b = \sum_i P_b(i) \quad (5.20)$$

where P_b is the vector of amplitudes that satisfied the condition $P_z > p_{th}$ and E_b is the *balling energy*. As a matter of fact, the sum of all P_b values actually represents the area of that components in the amplitude spectrum, which is the energy associated with those frequency components.

Single Tracks Classification

In the previous step, the balling energy was computed for each scanned track. This descriptor quantifies the extent of track discontinuity. Hence, a threshold on E_b was found in order to distinguish continuous tracks from discontinuous ones. To do this, an empirical threshold was defined by analysing all data available. Firstly, single tracks were manually analysed by an operator and a reference process map was defined for all spot size levels and for each material (six process maps). In each process map, single tracks were classified as follows:

- **Continuous:** single tracks that belong to this category were well formed and regularly shaped;
- **Discontinuous:** tracks were affected by balling or humping phenomena;
- **Ambiguous:** in some cases, the operator was not able to interpret the status of a track, since its shape was a middle ground among continuous track and discontinuous one.

The latter track category was removed from analysis, since it would had introduced uncertainty in the reference data. It is worth reporting that ambiguous tracks were about 7% of the total amount of scanned tracks (5% of all point clouds).

After manual classification, an optimization algorithm was developed in order to find the energy threshold (e_{th}) that maximizes the accuracy of the automatic classification based on *balling energy*. Basically, a mobile e_{th} threshold was defined. By sliding it over the entire E_b -vector of each data set, the energy threshold was fixed at the value that maximizes the classification accuracy, which was defined as follows:

$$accuracy = 0.5 * \left(\frac{n_{00}}{n_{00} + n_{01}} + \frac{n_{11}}{n_{11} + n_{10}} \right) * 100 [\%] \quad (5.21)$$

where

- n_{00} is the number of discontinuous tracks that satisfied $E_b < e_{th}$ (OK)
- n_{01} is the number of discontinuous tracks that satisfied $E_b \geq e_{th}$ (BAD)
- n_{11} is the number of continuous tracks that satisfied $E_b \geq e_{th}$ (OK)
- n_{10} is the number of continuous tracks that satisfied $E_b < e_{th}$ (BAD)

An example of process map obtained from automatic classification can be seen in Figure 5.14b.

It is worth reporting that ambiguous tracks were also classified by the automatic methodology. Once performed the classification, the curve that separated continuous tracks from discontinuous ones was defined for each process map. The maximum value of that curve was then used as centre for next 3D benchmarks DoE.

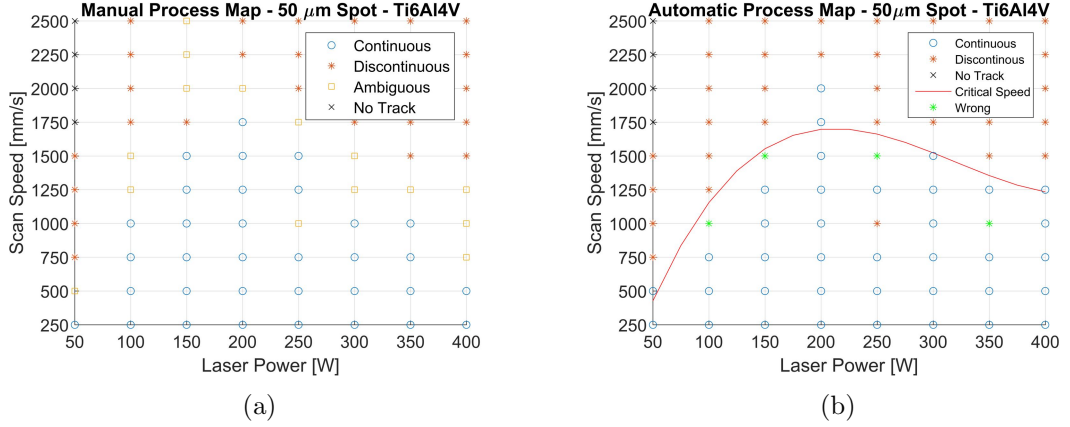


Figure 5.14: (a) Example of a manual process map (result of an operator’s analysis) and, (b) same process map obtained from the algorithm.

5.3 Results & Discussion

5.3.1 Single Track Melting Efficiency Curve

With single track recognition, point clouds containing a scanned track were distinguished from those that include only the substrate topography. To do this, a novel statistical descriptor (n_{th}) was defined in order to classify point clouds in an automatic and objective manner.

The boundary line that separates the two point cloud categories had also a physical interpretation. As a matter of fact, this line defines an empirical energy density threshold, below which the energy input of the laser is not enough to complete powder melting. According to Wang et al. [143], this threshold was named *single track melting efficiency*. In addition, the authors defined an analytical formulation of this energy density threshold, as mentioned in Chapter 2. For convenience, it is worth recalling the equation of *single track melting efficiency*:

$$N_m = \frac{AP}{\pi w_0 t v \rho c (T_m^{eff} - T_0)} \quad (5.22)$$

where A is the absorptivity, P is the laser power, v is the scan speed, t is the layer thickness, ρ is the density, c is the heat capacity and T_0 is initial powder temperature, while w_0 is the beam radius at the waist. The condition $N_m = 1$ represents precisely the meaning of point cloud threshold computed in single track recognition step. Therefore, the following relation was computed for each process map in order to compare the analytical equation

Parameter	Sym.	Units	Ti6Al4V	SS316L
Density	ρ	Kg/m^3	4220	7950
Heat capacity	c	$m^2/(s^2 \cdot K)$	546	450
Latent heat of melting	L_m	m^2/s^2	3.65×10^5	2.713×10^5
Melting point	T_l	K	1923	1723
Laser absorptivity	A	–	0.38	0.33

Table 5.1: Physical properties of the employed materials.

with experimental results:

$$v = coeff_A P \quad (5.23)$$

where $coeff_A$ is an analytical term obtained from Equation 5.22:

$$coeff_A = \frac{A}{N_m \pi w_0 t \rho c (T_m^{eff} - T_0)}. \quad (5.24)$$

The physical parameters adopted for the computation are reported in Table 5.1. It is worth noting that the values of ρ and c were chosen in the solid phase, since the heat accumulation process mainly happens before melting. This assumption was in accordance with Wang et al. [143].

As can be seen from Figure 5.19, analytical formulation tended to overestimate the energy density threshold at high laser spot size, while it tended to underestimate the threshold at $50\mu m$ spot size. It can be also noticed that the discrepancy increased mainly as the laser spot size increased. The reason behind this could be related to laser absorptivity of the powder bed. As a matter of fact, more particles will be processed through the laser beam when the spot diameter is increased (spot area is greater). This means that more beam reflections will occur in the powder bed, increasing the absorptivity to an asymptotic value. On the contrary, the spot diameter will be comparable with the average powder particle size and absorptivity will be smaller when d_s is minimal. In order to identify a correction factor for the analytical formulation, the discrepancy between experimental threshold and analytical one was investigated. The discrepancy was defined as follows:

$$\Delta c = coeff_E - coeff_A \quad (5.25)$$

where $coeff_E$ is the coefficient of Equation 5.23 obtained from experimental data. In Figure 5.15b are plotted the Δc values for both materials investigated and the regression curve that interpolates the data. The equation of the latter was the following:

$$\Delta c = f(d_s) = \beta_0 + \beta_1 d_s + \beta_2 d_s^2 = -11.29 + 0.17 d_s - 4.39 * 10^{-4} d_s^2 \quad (5.26)$$

Basically, Δc represents the correction function for Equation 5.23 and can be useful for the prediction of “no track” region. However, further investigations would be needed to achieve a more reliable Δc function and a deeper understanding of the phenomenon.

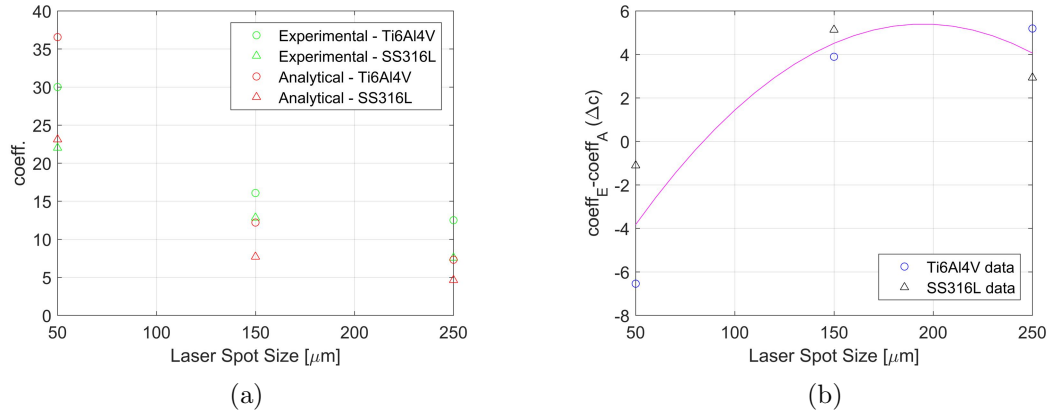


Figure 5.15: (a) Experimental and analytical angular coefficients of melting efficiency and, (b) discrepancy between experimental threshold and analytical one.

5.3.2 Critical Speed Curve & Optimal Parameter Sets

The single tracks classification algorithm divided continuous tracks from discontinuous ones. The whole algorithm was essentially based on track profiles data analysis. Indeed, the track classification was performed by the FFT analysis of profile signals and by the definition of the *balling energy* threshold (e_{th}). The result was a series of process maps, which can be seen in Figure 5.20 for Ti6Al4V and in Figure 5.21 for SS316L.

Through the distinction between continuous and discontinuous tracks, a boundary curve was computed, as for single track recognition. In this case, the curve cannot be interpreted as an energy density threshold, given its nonlinearity in the (P, v) plane. Therefore, it was considered as the function of the maximum permissible speed above which the scanned tracks become discontinuous. In other words, the speed value belonging to this curve is the highest value for which a continuous track is obtained, given an arbitrary laser power value. This curve was named *critical speed curve* (v_{cr}). As can be seen in Figure 5.20 and Figure 5.21, the v_{cr} -curve was generally characterized by a growing segment and a subsequent decreasing segment. The first growing section divided tracks affected by balling from continuous ones, while humping tracks were separated by the decreasing segment. Nevertheless, it was not possible to distinguish balling from humping phenomenon through the classification algorithm (it wasn't part of the purpose of this work). Thus, further investigations would be necessary to identify a characteristic that distinguishes the two phenomena automatically.

From the point of view of process productivity, the maximum of v_{cr} function represents the operative condition that maximises the productivity, maintaining track continuity and therefore producing high-quality components. On the basis of this hypothesis, the DoEs of 3D benchmarks were centred at the maximum value of v_{cr} curve. Thus, in the next chapter, 3D benchmarks quality will be investigated in order to validate this hypothesis.

With respect to maximum values of the various v_{cr} curves defined in this work, it was possible to investigate the spot size effect on process stability. Interestingly, it was

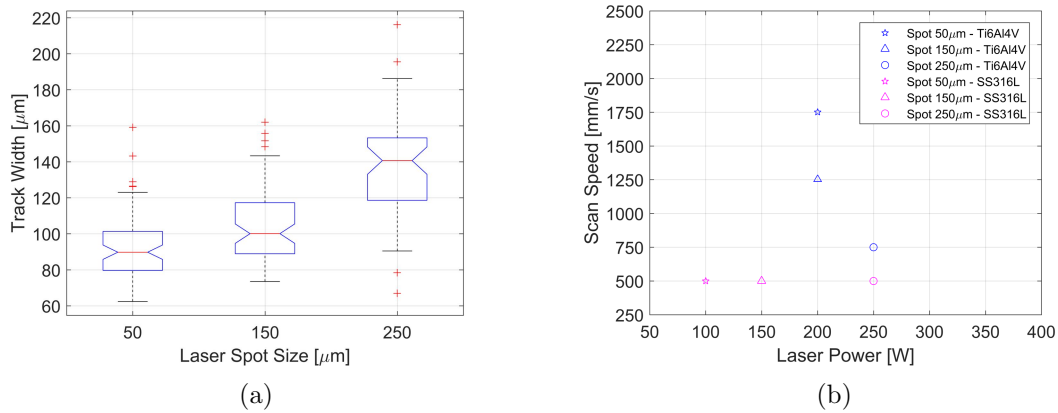


Figure 5.16: (a) Track width trend as the laser spot size varies and, (b) maximum values of v_{cr} curves for the various experiments performed.

noticed that the process stability was increased as the spot size decreased, in case of Ti6Al4V process maps. This result would appear to be at odds with the stability condition ($\pi D/L > \sqrt{2/3}$) defined by Yadroitsev et al. [148], as the track width decreased with the reduction of spot diameter ($\sim 20\%$ reducing the diameter by $100\mu\text{m}$). However, by reducing d_s , even melt pool length may decrease. To confirm this hypothesis, it would be necessary to measure the melt pool length during the production using an in-line monitoring system.

Furthermore, this effect was not recognized in SS316L single tracks, where an increase in spot size entailed only an increase in laser power. This was probably due to the excessive step size used to define power and speed levels in SS316L DoEs. As a matter of fact, the continuous regions were small in stainless steel experiments. Thus, a different criterion for the selection of scan speed levels would be needed in order to better investigate the process region of interest. In this work, P -range was defined as large as possible, while the v -range was limited to 1000mm/s above standard parameters with higher speed (thus, the upper limit was 2500mm/s). However, a lower speed limit would have been enough in case of SS316L DoEs, thus allowing to intensify the experiments in the optimal process region. Since only two materials were investigated in this work, it was not possible to find a novel criterion for the upper limit selection of scan speed.

5.3.3 Algorithm Performance

To establish the algorithm performance, the single track classification was analysed, since it was the main step of the proposed methodology. Therefore, the topography data of single tracks was divided into two datasets on the basis of manual continuity analysis: continuous-tracks and discontinuous-tracks datasets. It is worth reporting that point clouds without a single track (no track region) and those with a track manually classified as ambiguous were ignored in the analysis.

Afterwards, the datasets were further divided into computation and validation datasets.

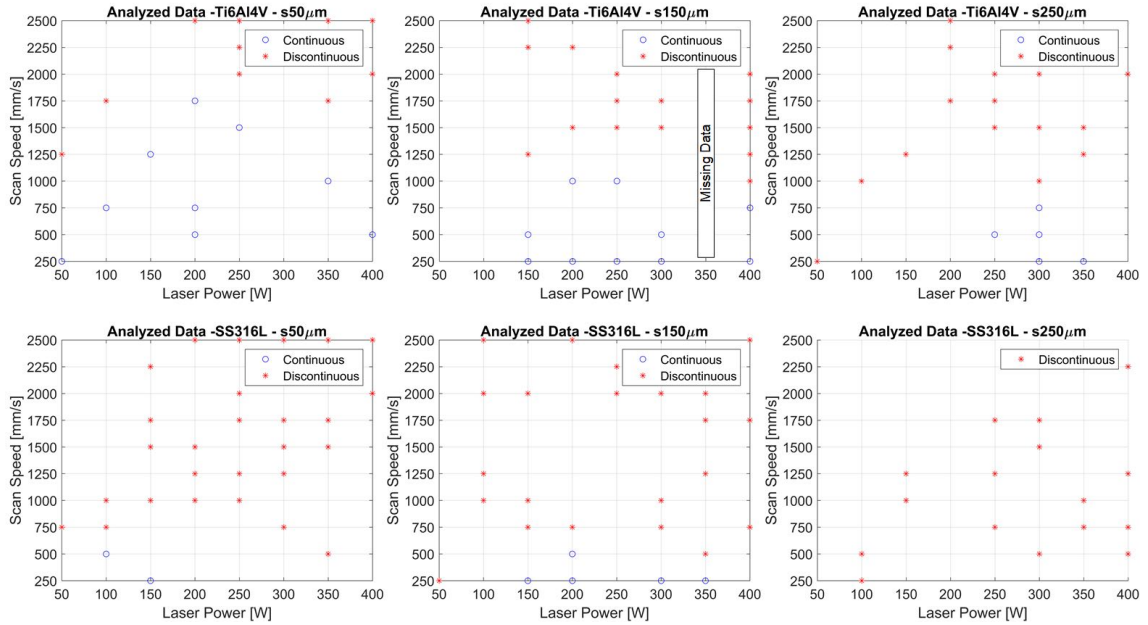


Figure 5.17: Representation of the computation dataset selected through *Mersenne Twister* algorithm.

To do this, data points were randomly chosen by the *Mersenne Twister* algorithm. The computation dataset selected this way can be seen in Figure 5.17. Therefore, the remaining data belonged to the validation dataset.

The e_{th} threshold was then estimated through computation dataset analysis and was subsequently applied for single track classification on validation dataset. As previously

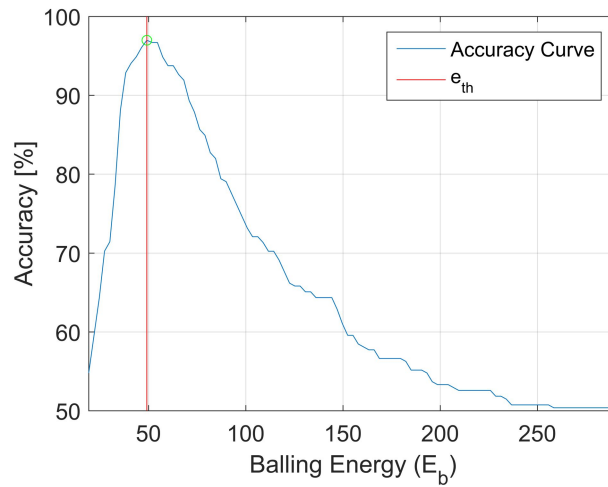


Figure 5.18: Accuracy function obtained by sliding e_{th} over the entire E_b -vector.

mentioned, the e_{th} threshold was defined by sliding it over the entire E_b -vector and by finding the value that maximizes the classification accuracy. The accuracy function can be seen in Figure 5.18. In case of computation dataset, the accuracy was about 97% with $e_{th} = 49.659$. By applying the same threshold on validation dataset, the accuracy was slightly higher (97.3%). Thus, the methodology was validated.

It is also worth reporting that the classification accuracy of all tracks, including also ambiguous ones, was 98.5%. Therefore, this algorithmic method can also be very useful to assist operators during situations where track morphology is unclear. Eventually, the single tracks classified incorrectly were only 7 and were mainly distributed in $50\mu m$ spot experiments. This is probably due to the high variability of the substrate topography and to the reduced dimensions of single tracks produced with the smallest level of spot size.

Lastly, make a parallel between the current methodology and the work presented in Chapter 3 (which was performed referring to the main literature works) is rather difficult, as the performed investigations and obtained results are different. As a matter of fact, a complete characterization was carried out in Chapter 3, while a rougher analysis was implemented in this methodology. Even just by deepening only the track morphology analysis, SEM inspection and 3D optical analysis are hardly comparable; SEM allows to obtain various information (e.g. microstructure, cross section views, etc.), while optical inspection acquires only the surface topography of the samples, even using the most precise acquisition technique (i.e. interferometry). It is also to be considered that the SEM images are 2D, while the image stacks provided by the optical profiler allow to obtain a 3D maps.

From the point of view of timing, it is well known that SEM inspections are very time consuming; the acquisition of a portion of the top surface of a single track took about 20 minutes (embedding 10 tracks at once). This is mainly due to the specific pre-processing operations required for a SEM analysis (e.g. grinding, polishing, vacuum sealing, etc.) and, it might actually be one of the reasons why many authors prefer to produce 3D benchmarks directly, thus avoiding single tracks studies.

On the over hand, optical inspection does not require any special preparation and, once the samples are placed in a specific holder, the measurement can be started. This implies also a certain degree of measurement automation (multi-measurement technique). Therefore, a shorter acquisition time is needed; the entire track topography can be acquired in about 10 minutes (loading 80 tracks in the samples holder). It is also worth reporting that the acquisition time can be further halved by adopting focus variation instead of interferometry, while reducing the measurements accuracy.

Another aspect that has to be taken into account is data analysis; the developed algorithmic framework for single tracks analysis allows to process a track topography in few minutes, providing repeatable results with a good reliability, as discussed above. This is the main advantage against manual SEM inspection, since it is possible to analyze a large number of experiments without strongly affecting time and costs of post-process inspections and, the obtained results are not affected by the operator subjectivity.

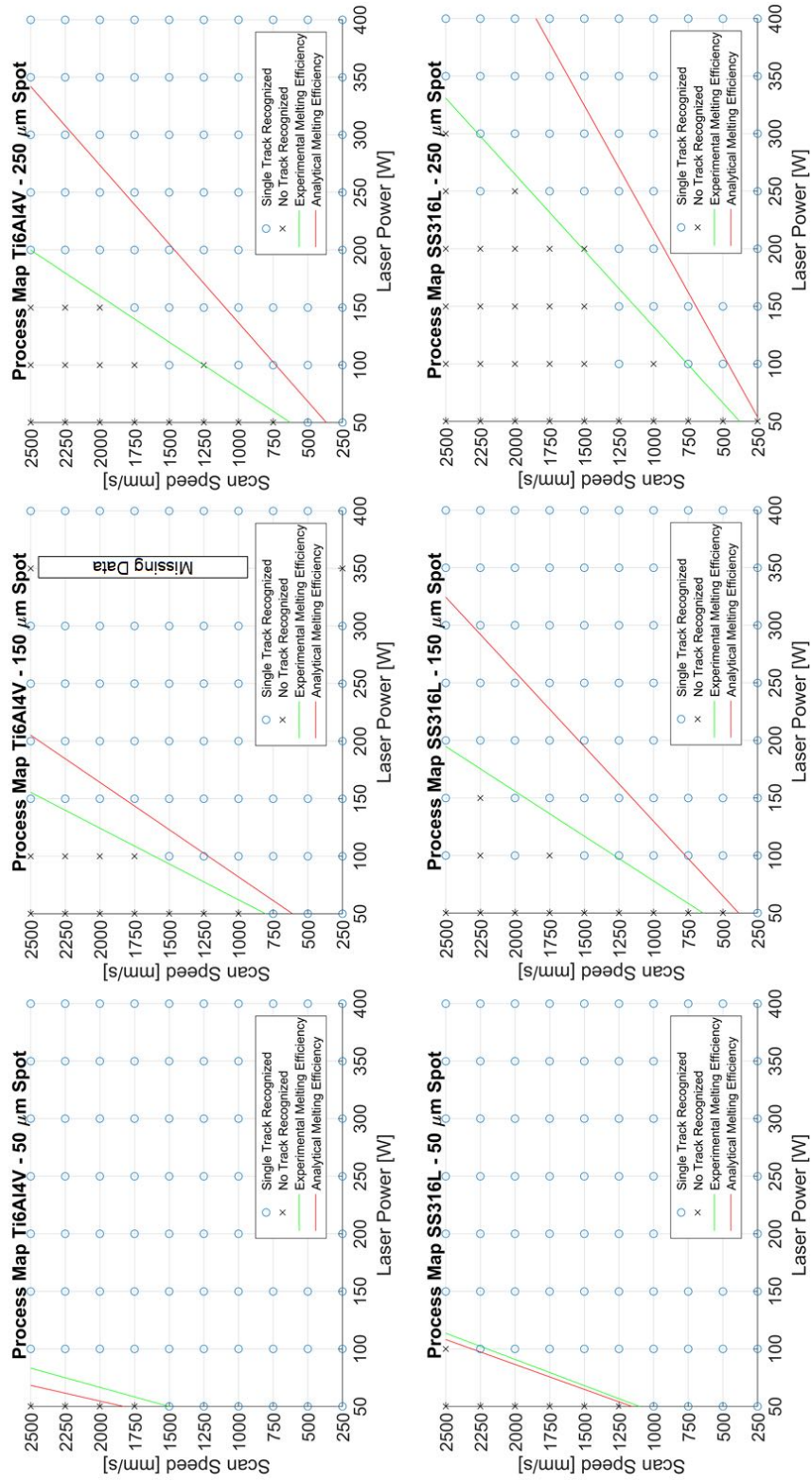


Figure 5.19: Melting efficiency curves at various laser spot size levels and different materials.

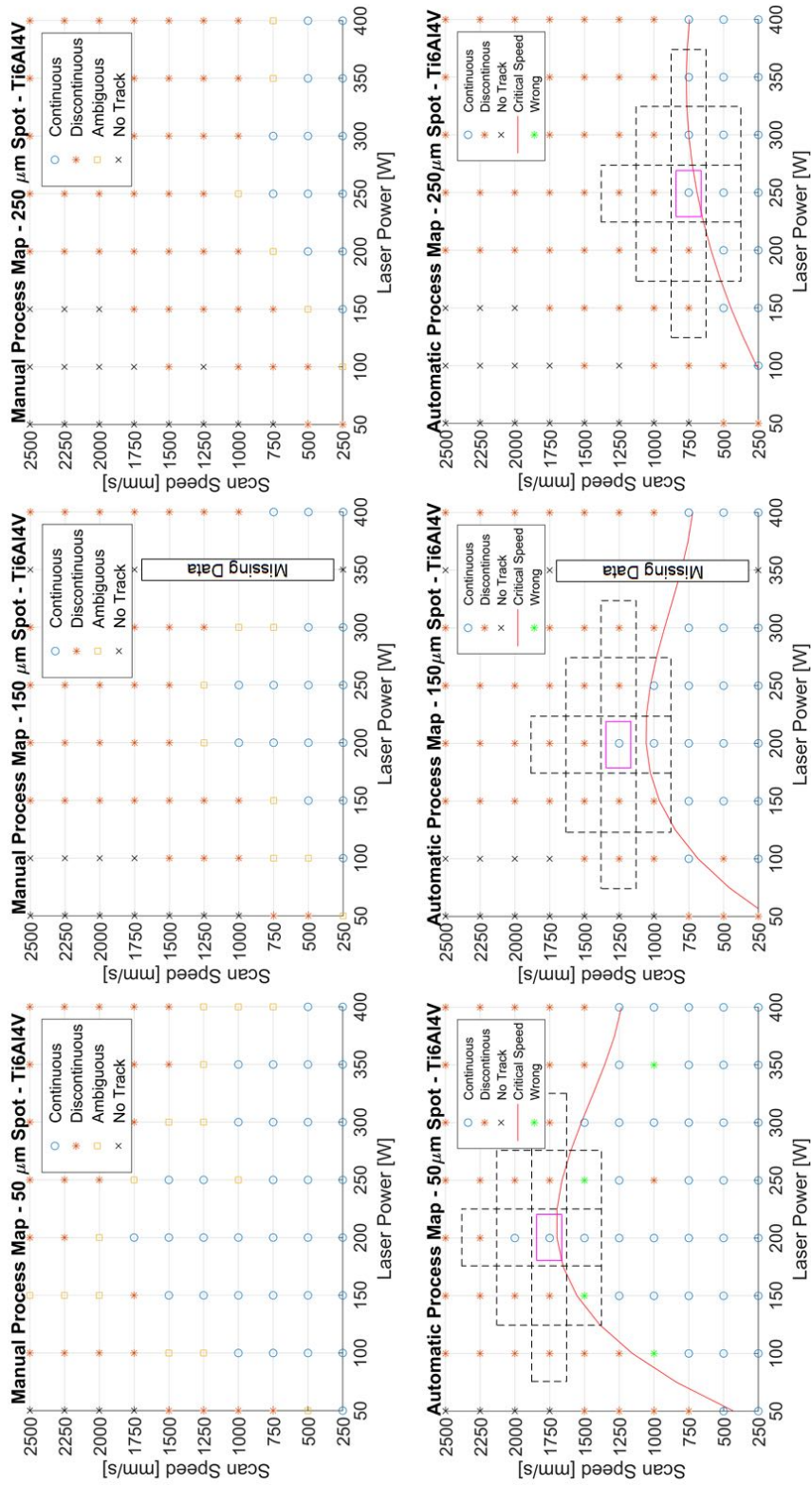


Figure 5.20: Manual and automatic process maps obtained from Ti6Al4V data analysis.

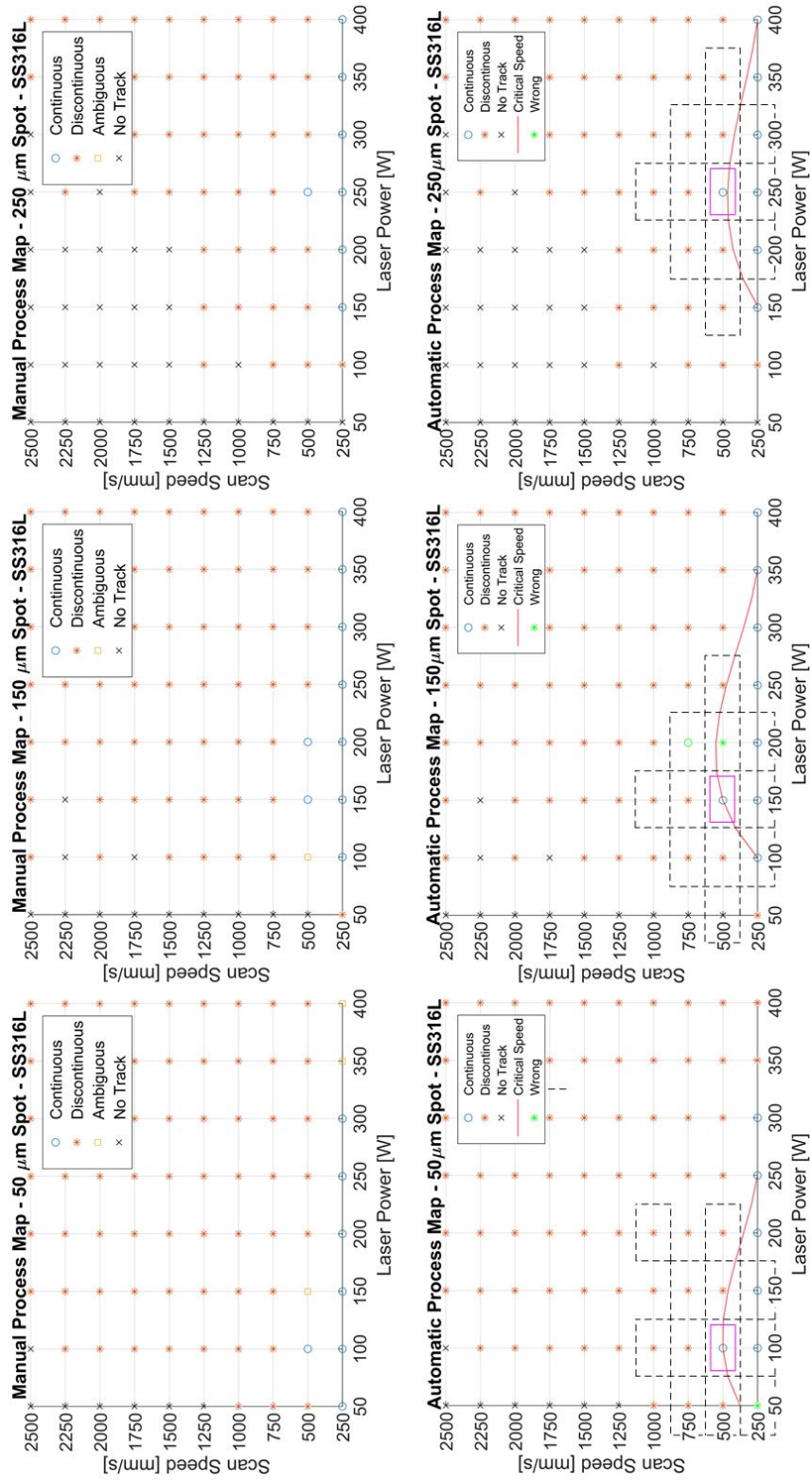


Figure 5.21: Manual and automatic process maps obtained from SS316L data analysis.

Chapter 6

3D Benchmarks Characterization

6.1 Input Data

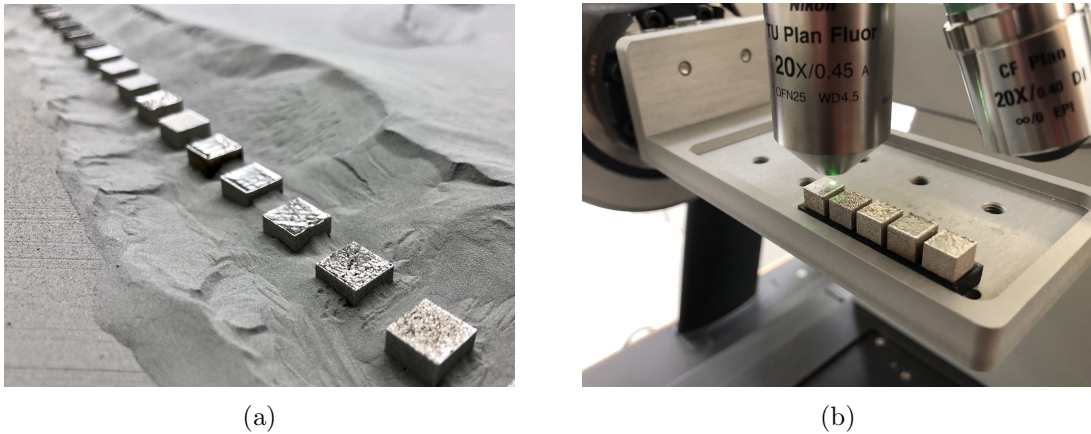


Figure 6.1: (a) Build chamber during removal of residual powder and, (b) setup for topographies acquisition.

The critical speed curve was used in the previous chapter to define the DoE for each spot size level and for each material (a total of six process windows). For each material, two build platforms with each 18 cubic samples (8 mm edge length) were fabricated. After production and some post-processing operations, the cubes were collected in 3D-printed holders for subsequent top-surface topography acquisition. In this case, two kinds of measures were performed with the 3D profiler for each cubic sample: the first measurement was performed by using an EPI 20x objective (4.7mm working distance), while the second measurement was executed with an EPI 5x objective (18.5mm working distance).

The measurement with higher magnification was performed in order to compute profile roughness measures. Indeed, a stitching area composed by a column of 15 FoVs with an overlapping of 20% was defined in order to scan, from side to side, a central band of the cube (see Figure 6.2a). The nominal acquisition area was $844.5 \times 8620 \mu\text{m}^2$, which corresponded to 1227×12492 pixels, since the resolution was set to $0.69 \mu\text{m}/\text{pixel}$.

It is worth reporting that the central band was taken so that it was perpendicular to tracks direction of the last cube-layer (tracks direction defines the *surface lay*).

The acquisition technique applied was focus variation, as the surface roughness was

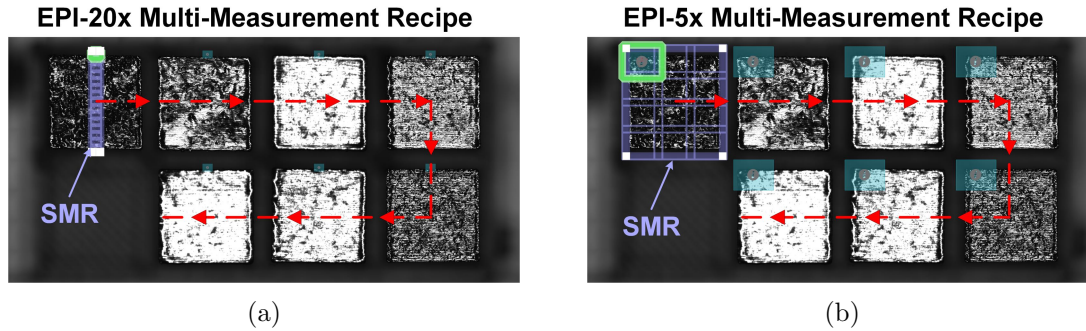


Figure 6.2: Scanning preview of the 3D optical profiler for (a) high magnification measurements and, (b) low magnification measurements.

sufficiently high. In addition, the Z stage acquisition range was $500\mu m$, 27% intensity of green light in HDR mode was used and autofocus algorithm was applied at each FoV. Once defined the Single Measurement Recipe (SMR) for one cube, the Multi-Measurement Recipe (MMR) was defined to acquire automatically, in one scanning operation, all cubes collected in a sample holder (one holder for each spot level). The output TXT files were comparable in size to single tracks ones; approximately 400 MB per file (about 15 million points). Regarding measures performed with EPI 5x objective, the purpose was to acquire the whole topography of the cubic samples. Hence, a stitching area composed by 4 rows and 3 columns with an overlapping of 20% was defined, as shown in Figure 6.2b. The resolution was set to $1.38\mu m/pixel$, which was as high as possible with such objective. Thus, the nominal acquisition area was $8783 \times 9609\mu m^2$, which correspond to 6364×6963 pixels. Even in this case, the adopted acquisition technique was focus variation and same setting were applied as for the first measurement type. Nevertheless, a higher Z stage acquisition range was set, since thermal warps were present at the edges of various cubic samples. Thus, the acquisition range was $1200\mu m$. In addition, the light intensity was also raised in order to acquire even the deepest areas of the surfaces (33% intensity). The outcome of cube topographies acquisition was a series of TXT files with approximately 1 GB size (about 27 million points). All topography files were then automatically renamed with a string containing the values of process parameters investigated in the various DoEs (e.g. ‘o30s50P150v2000.txt’ means a cube produced with an overlap rate of 30%, a spot size of $50\mu m$, a laser power of 150W and a scan speed of $2000mm/s$). Lastly, the relative density of all cubes was measured with Archimedes method and all data were imported in MATLAB environment.

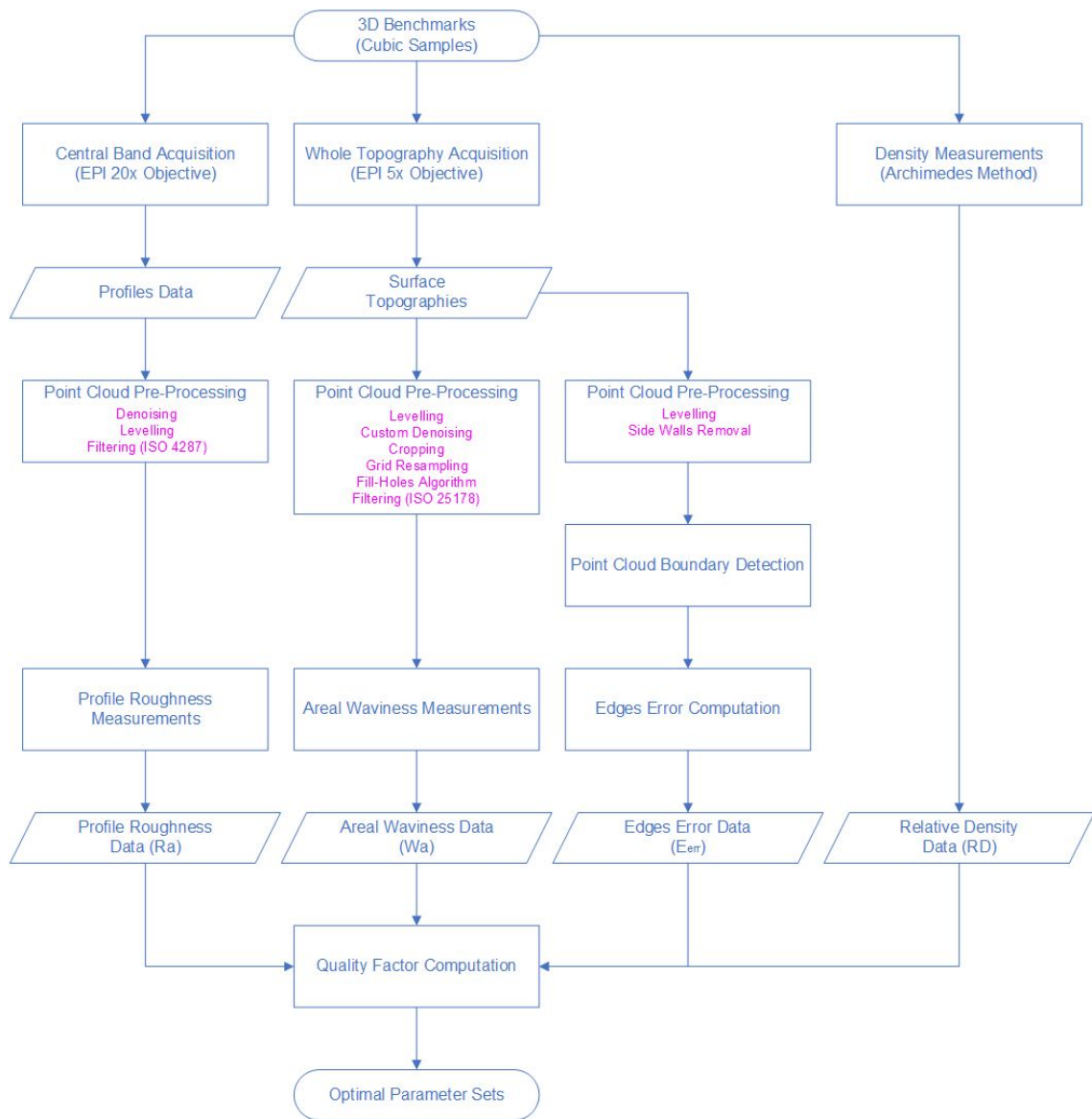


Figure 6.3: Flow chart of the methodology for 3D benchmarks characterization.

6.2 Profile Roughness

After topographies acquisition, all data of high magnification measurements (with EPI 20x objective) were manually elaborated with SensoVIEW 1.3 software in order to compute the profile roughness R_a in accordance with the ISO 4287 standard.

6.2.1 Point Cloud Pre-Processing

Denoising

Before computing roughness, all topographies were filtered with a denoising algorithm (in SensoVIEW, this operation is called “Despiking”). In this case, noise removal was necessary since the SMR was defined by averaging acquisition settings in order to adapt them to all conditions. Clearly in some cases, acquisition parameters (in particular light setting) were not optimal and some noise was acquired.

Levelling

After denoising operation, three profiles were manually chosen and subsequently elaborated. According to ISO 4287 standard, the first operation to be done was the form removal or, in this case, the levelling. The subtraction of nominal form from raw profiles can be performed by a high-pass filter with cut-off λ_f , which removes all large-wavelength components. However, the F-operator (form removal operator) is more often applied, since the profile length is typically not long enough to capture form. This mathematical operator firstly determines a best fit to the nominal form, and then subtracts the fitted form from raw data. In this case, the result of raw data interpolation was a levelling straight line, since the nominal shape of the surface was a plane. Therefore, the F-operator was applied to raw profiles and the primary profiles were obtained.

Filtering

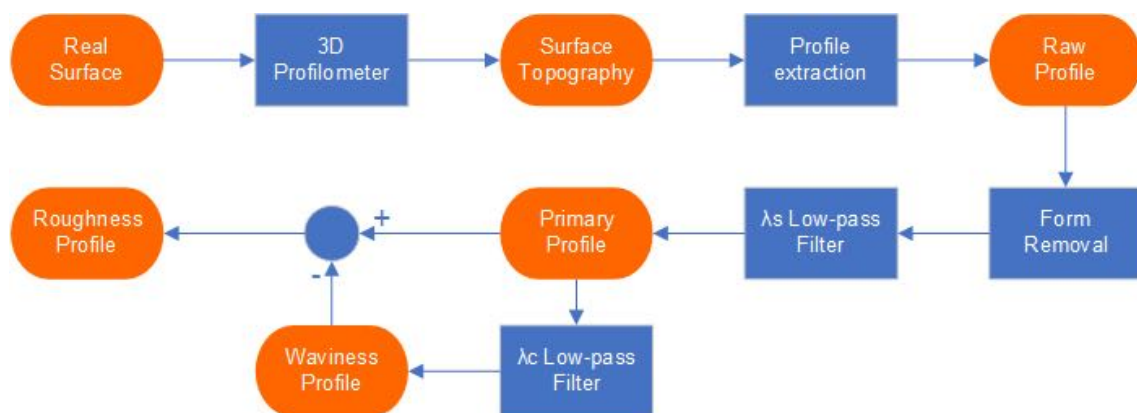


Figure 6.4: Flow chart of profiles elaboration.

The primary profiles were then filtered by a band-pass filter, according to ISO standard. The filter applied was characterized by two cut-offs:

- $\lambda_s = 2.5\mu m$ defines where the intersection occurs between the roughness and the presence of shorter-wavelength components in a profile;
- $\lambda_c = 2.5mm$ which defines the roughness and the waviness components.

The cut-off values were chosen according to ISO 4287. In particular, $\lambda_c = 2.5mm$ was chosen as the expected roughness values were in the range of $2 \div 10\mu m$.

From an operational perspective, after λ_s low-pass filtering, the waviness of the primary profile was computed by applying a Gaussian low-pass filter with λ_c cut-off. The waviness profile was then subtracted from primary profile and the result was the roughness profile (see Figure 6.5). Since the filters applied were of Gaussian type, the extremes of the profiles were removed from analysis.

It is also worth reporting that the profile length was not long enough to comply with the $5\lambda_c$ length recommended by the ISO standard.

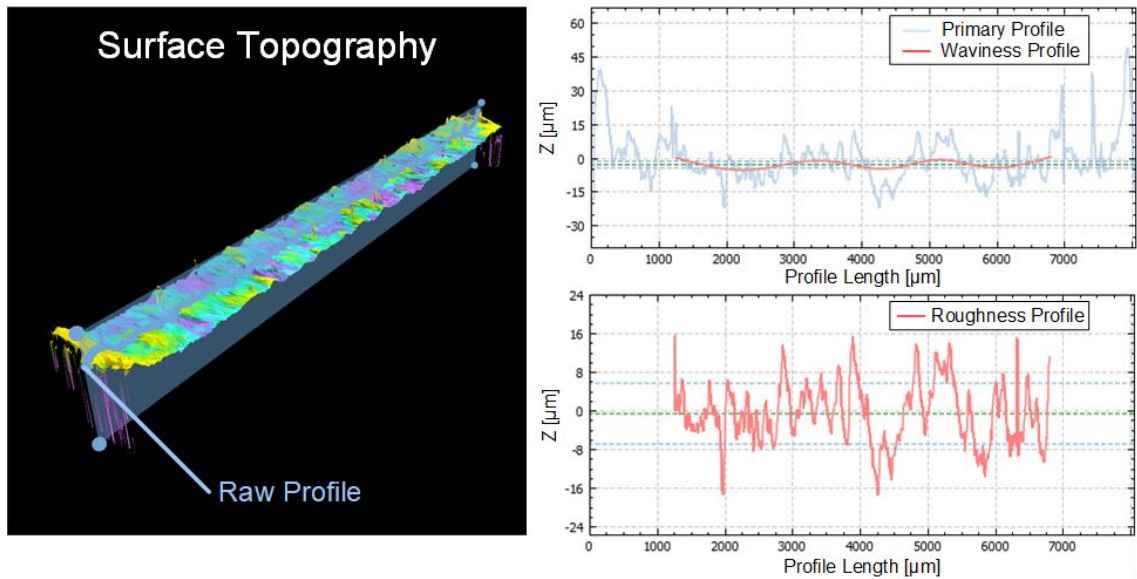


Figure 6.5: Raw profiles processing.

6.2.2 Ra Measurements

Once raw data was pre-processed and roughness profiles were obtained, Ra was computed for each cubic sample profile using the following:

$$Ra = \frac{1}{N} \sum_{n=1}^N |z(x_n) - z_{mean}| \quad (6.1)$$

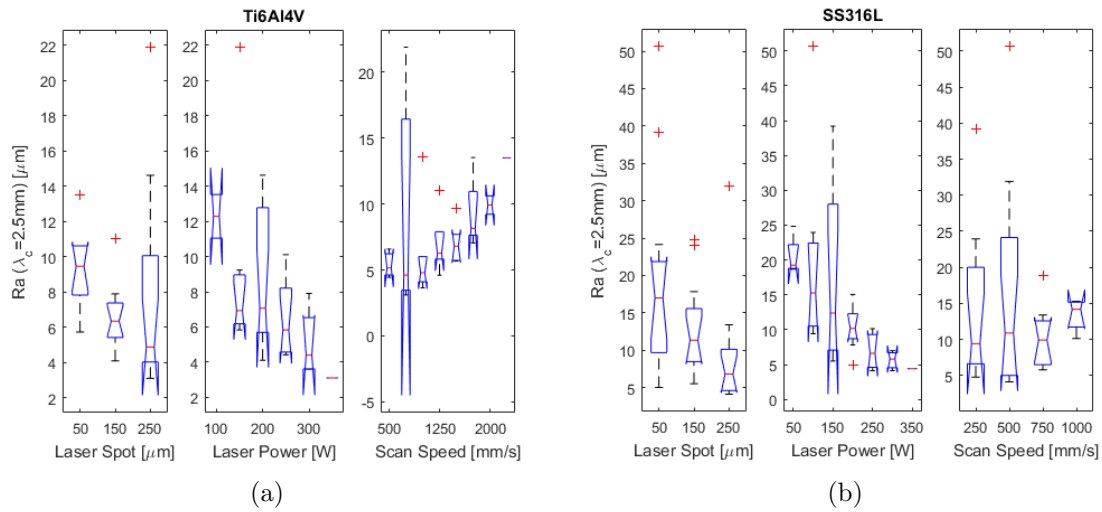


Figure 6.6: Box plots of roughness data as a function of spot diameter, laser power and scan speed for (a) Ti6Al4V and, (b) SS316L.

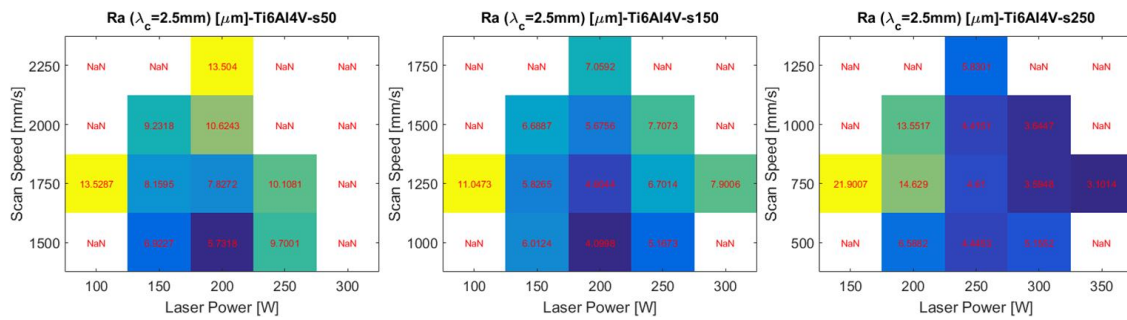


Figure 6.7: Roughness maps for Ti6Al4V benchmarks.

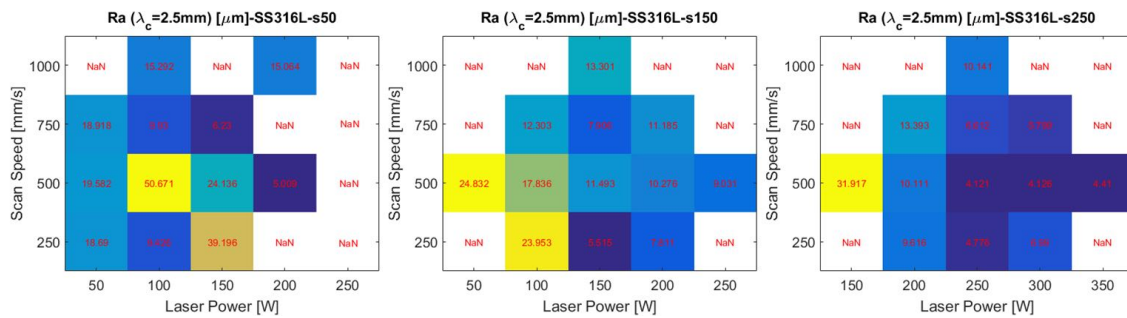


Figure 6.8: Roughness maps for SS316L benchmarks.

The profile roughness was computed for each 3D benchmark of the various DoEs and roughness maps were obtained. These maps can be seen in Figure 6.7 for Ti6Al4V and in Figure 6.8 for SS316L.

The data collected were then divided by type of material used and a preliminary statistical analysis was carried out. As can be seen from box plots in Figure 6.6, the increase in laser power had in general a positive effect on profile roughness, while the increase in scan speed had a negative influence (although the trend was less marked). These observations were in accordance with literature works. As a matter of fact, it is well known that an increase in linear energy density (that means an increase in power and a decrease in scan speed) entails a higher surface finish. Comparing the results of Ti6Al4V and SS316L, it was noticed that titanium benchmarks had lower roughness values than stainless-steel ones. The average value for Ti6Al4V was about $7.8\mu\text{m}$, while SS316L had a roughness average value of $13.8\mu\text{m}$.

Referring to laser power and scan speed variations, the aforementioned Ra trends were similar for both materials. However, the roughness trend as the speed varies was more marked for titanium samples. Nevertheless, it must be borne in mind that the speed range investigated in the case of titanium specimens was twice that of steel specimens. Either way, developing a reliable model of surface roughness is challenging due to the high variability of data, which in turn is due to the complex physics of the process. More interestingly, the trend of roughness values was inversely proportional to the laser spot size. Thus, the profile roughness was lower as the spot diameter increased. This effect might be due to the larger and smoother tracks produced with high values of spot diameter. Therefore, to produce components with low top-surface roughness, high spot size values are preferable.

6.3 Areal Waviness

The areal waviness measurements were performed on topographies acquired with the low magnification objective (EPI 5x). These point clouds represented the whole top surface of the various cubic samples and an “ad hoc” code was developed in MATLAB environment for an automated analysis.

Even in this case, the guidelines of ISO 25178 standard were followed as far as possible. It is also worth reporting that areal roughness measurements were not taken into account since point spacing was not optimal for this purpose.

6.3.1 Point Cloud Pre-Processing

Levelling

The first operation performed on raw point clouds was the form removal. As previously mentioned, the nominal form of the top surface of cubic samples was a plane. Thus, the F-operator firstly determined the best fit plane, interpolating the points belonging to the surface, and subsequently it subtracted the nominal form to the raw topography.

A similar surface levelling was performed in single track analysis. Thus, the mathematics of this operation can be found in Chapter 5.

Basically, the primary surfaces were obtained from raw data through this operation. Nevertheless, some extra-steps were needed in order prepare point clouds for filtering operation.

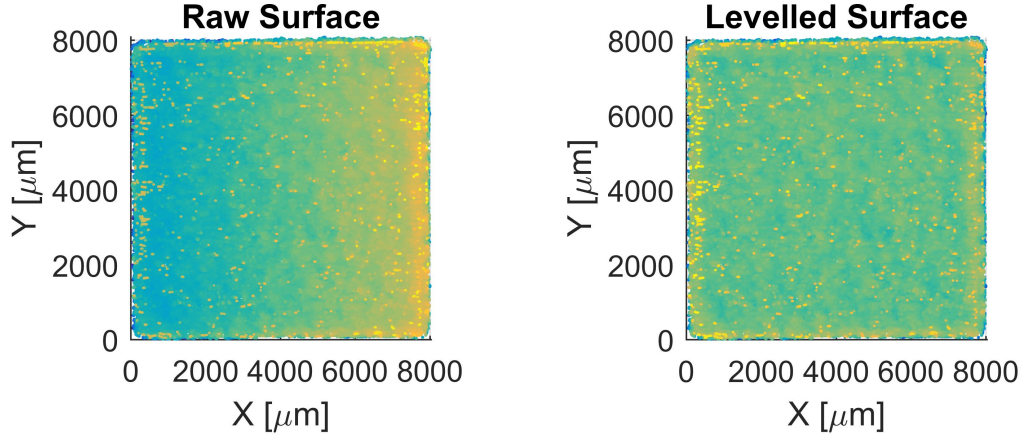


Figure 6.9: Surface topography before and after levelling operation.

Custom Denoising

Topographies acquired with low magnification objective were very noisy. This was due to the increased light intensity used during scanning operations. However, this light intensity level allowed to acquire even points in the deepest areas of the surface, which otherwise would not have been captured. Another issue related to the acquisition settings were the points acquired on side walls. As a matter of fact, the wide Z stage range of acquisitions had also allowed to capture points belonging to the side walls. Therefore, a two-steps denoising operation was needed in order to remove noise and unwanted points. The first step was a point cloud filtering with the denoise function of MATLAB. Basically, the outlier threshold was defined as 0.01 standard deviations from the mean of the average distance to neighbours of all points. Thus, an outlier was a point with an average distance to its k-nearest neighbours above the specified threshold. This filter drastically removed the noise of point clouds. Nevertheless, the points belonging to the side walls were not completely removed. Therefore, a second filtering step was performed to remove the remaining points. To do this, the points belonging to the area bordering the edges were detected. This area was defined by computing the centre of the point cloud in the (x,y) plane and by applying the following condition:

$$find((X > (x_c + 3700) | X < (x_c - 3700)) | (Y > (y_c + 3700) | Y < (y_c - 3700))) \quad (6.2)$$

where X is the vector of x-coordinates, Y is the vector of y-coordinates, x_c and y_c are the coordinates of the point cloud centre. Basically, a band of about $0.3mm$ was considered for each edge. Thus, the whole topography was divided into two areas: the central area and the peripheral area. After this operation, the central area was used to compute the mean height of the surface, while a threshold for Z-vector was applied on the peripheral area:

$$Z_{peripheral} > z_{mean,central} \quad (6.3)$$

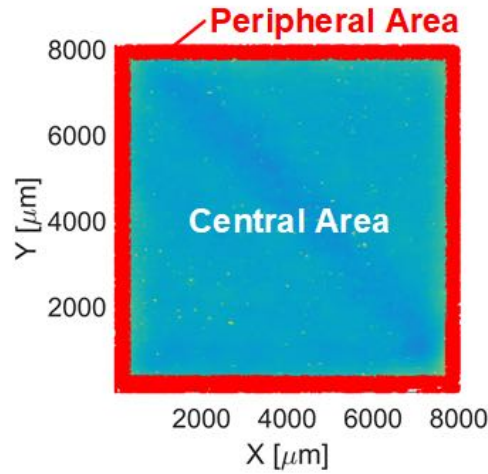


Figure 6.10: Surface topography divided into two areas: the central area and the peripheral area.

Therefore, the points belonging to the side walls were removed through this threshold. The result of this custom denoising function can be seen in Figure [6.11](#).

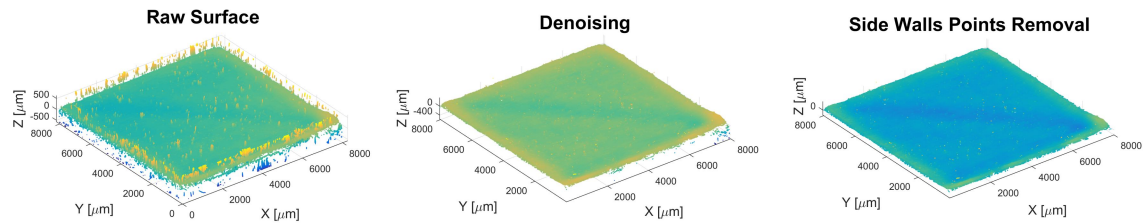


Figure 6.11: Surface topography two-step denoising operation.

Cropping

This step was performed in order to obtain point cloud boundaries as squared as possible. As a matter of fact, cube edges were in most cases non uniform due to thermal warps and other process issues. Thus, a cropping function was developed to cut the topographies edges and a rectangular surface area was obtained. To do this, points distribution was analysed along both x-axis and y-axis. An example of points distribution can be seen in Figure [6.4](#).

Then, a threshold on points numerosity was set in order to identify and remove points that did not have a consistent presence along the x-axis first, and along the y-axis later. The threshold for both axes was:

$$N_X, N_Y > n_{th} \quad (6.4)$$

where $n_{th} = 100000pt$. It is clear that if the topographies are not aligned with optical profiler reference system, this operation will cut more points than necessary. From this point of view, the special holder used for cubic samples positioning was sufficiently accurate. Therefore, the new point clouds were composed by only the points that satisfied Equation [6.4](#).

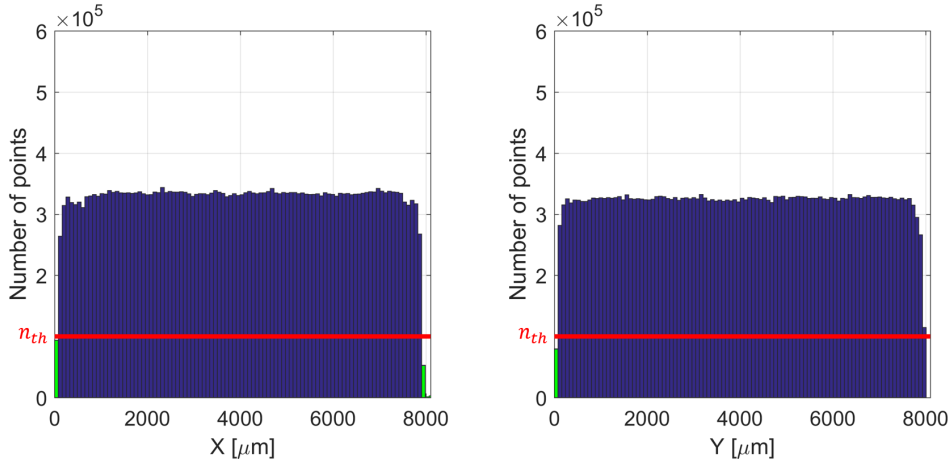


Figure 6.12: Topography points distribution along X axis and Y axis.

Grid Resampling

As for single tracks analysis, a resampling algorithm was applied to all topographies. In practice, a grid with a cell size of $2\mu m$ was applied to the (x,y) plane and the z-coordinates of the points within each cell were averaged. By considering the centre position of each cell as (x,y) coordinates and the average results as z-coordinates, a new equally spaced point cloud was obtained.

In this case, the resampling was necessary to slightly increase the points spacing (from $1.38\mu m$ to $2\mu m$), in order to reduce the computation time of the next step.

Fill-Holes Algorithm

In the previous step, a grid with a cell size of $2\mu m$ was applied to the point cloud and z-coordinates of the points within each cell were averaged. In practice, the point cloud was converted in a grayscale image (that is an $n \times m$ matrix) with $2\mu m$ of pixel size and the z-coordinates were the pixel intensity values.

Therefore, an algorithm was developed to fill the empty pixels. Basically, scrolling pixel by pixel the image, if an empty value was found, it was filled by the average of the neighbouring values.

However, if the image had multiple empty columns or empty rows, this algorithm didn't work, especially in the case of empty rows at the beginning of the scrolling function. It was therefore of great importance the previous cropping operation, which eliminated empty columns and rows in all analysed cases. Cropping function also drastically reduced the

computation time, since most of the holes were located along the edges of the topography. Eventually, the final result was a complete image representing the topography of the surface taken in analysis.

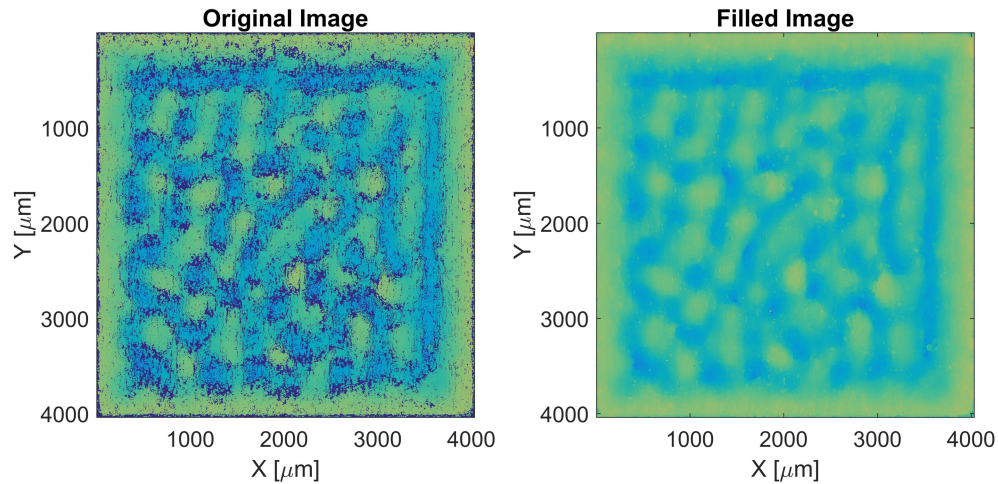


Figure 6.13: Surface topography before and after fill-holes algorithm application.

Filtering

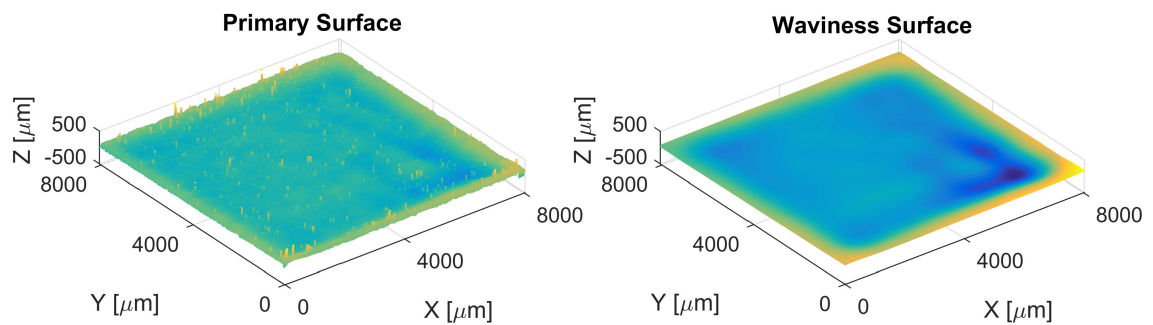


Figure 6.14: Surface topography before and after 2D Gaussian filtering ($\lambda_c = 2.5mm$ cut-off).

After pre-processing operations, the primary surface (in the form of an image) was obtained. So, it was possible to extract the waviness surface by filtering the image with a bidimensional low-pass filter. To carry out this operation, the filter was applied to the frequency spectrum of the image taken in analysis. Even in this case, the filter was of Gaussian type with same cut-off used for Ra measurements: $\lambda_c = 2.5mm$ (ISO 25178

standard). Basically, the waviness spectrum was obtained by calculating the product of the primary surface spectrum and a bidimensional Gaussian function with 50% transmission at cut-off length. This calculation corresponds to a convolution in the spatial domain. However, working in the frequency domain is more computationally efficient.

Once applied the filter, the image representing the waviness surface was obtained by computing the inverse FFT of the waviness spectrum.

Lastly, to reconvert the image to a point cloud, the (x,y) coordinates of each pixel were determined and the pixels intensity values were used as z -coordinates. Thus, a $n \times 3$ matrix was regained. An example of waviness surface obtained from this procedure can be seen in Figure 6.14.

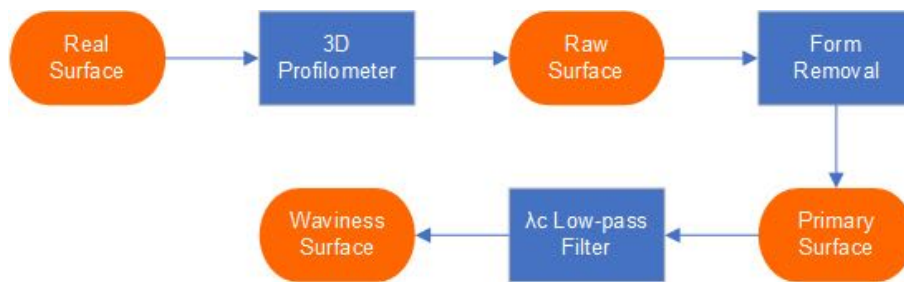


Figure 6.15: Simplified flow chart of surfaces elaboration.

6.3.2 W_a Measurements

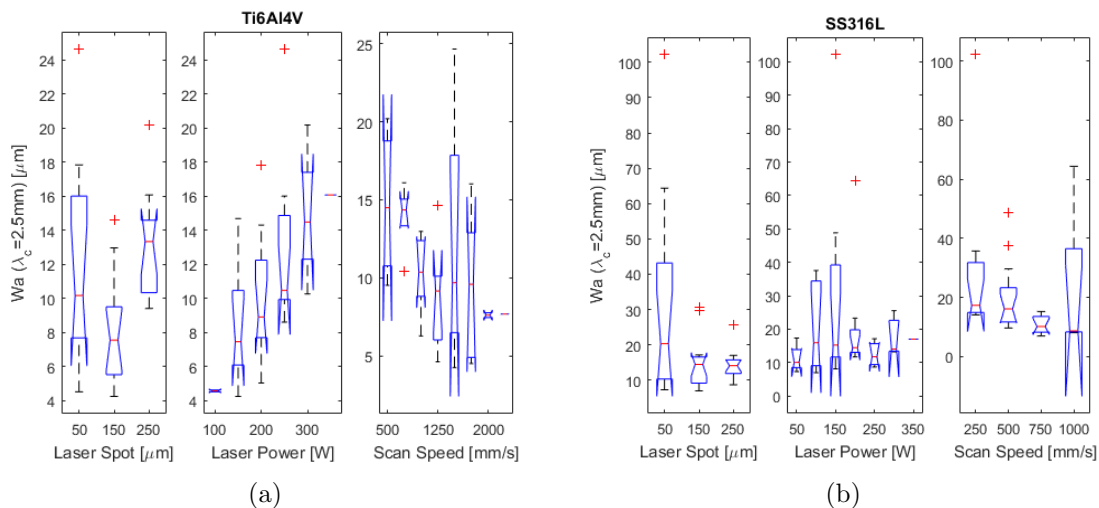


Figure 6.16: Box plots of waviness data as a function of spot diameter, laser power and scan speed for (a) Ti6Al4V and, (b) SS316L.

Once raw data was pre-processed and waviness surfaces were obtained, W_a was com-

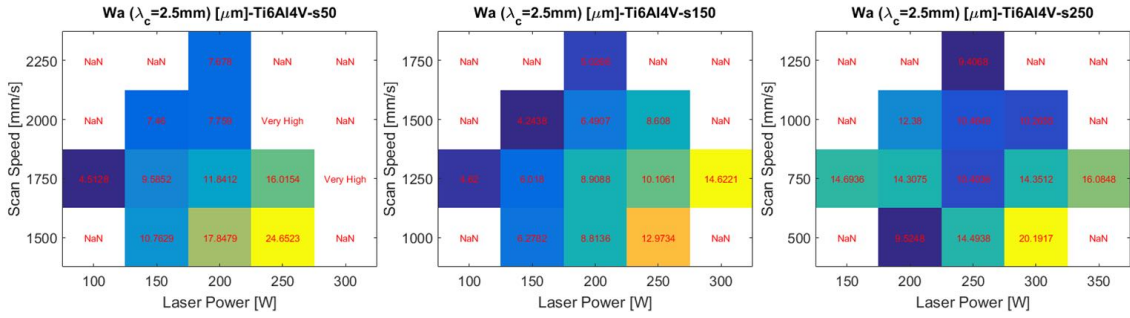


Figure 6.17: Areal waviness maps for Ti6Al4V benchmarks.

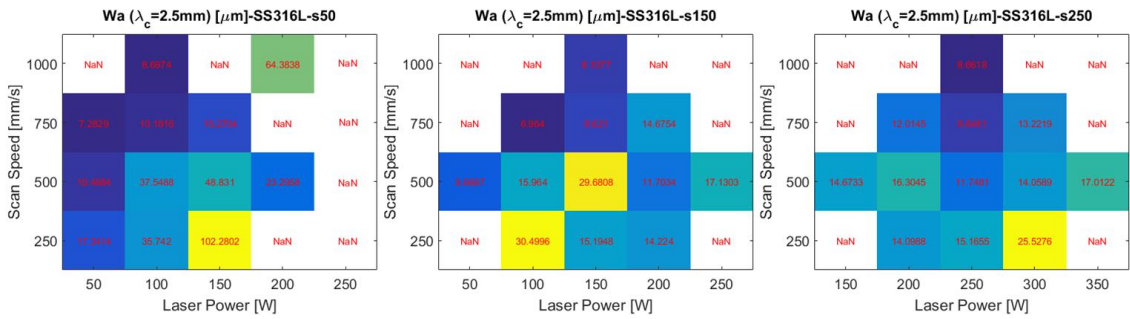


Figure 6.18: Areal waviness maps for SS316L benchmarks.

puted for each cubic sample using the following:

$$Wa = \frac{1}{N \cdot M} \sum_{m=1}^M \sum_{n=1}^N |z(x_n, y_m) - z_{mean}| \quad (6.5)$$

The areal waviness was computed for each 3D benchmark of the various DoEs and waviness maps were obtained. These maps can be seen in Figure 6.17 for Ti6Al4V and in Figure 6.18 for SS316L.

The data collected were then divided by type of material used and a preliminary statistical analysis was carried out. As can be seen from box plots in Figure 6.16, the increase in laser power had in general a negative effect on areal waviness, while the increase in scan speed had a positive influence (although the latter trend was less marked). Thus, it can be concluded that an increase in linear energy density (P/v) entails a higher surface waviness, which is detrimental for SLMed components quality.

Comparing the results of roughness measurements with waviness ones, it was noticed that they had opposite trends. Therefore, the optimal parameter set should be a compromise between these two descriptors. It is also worth reporting that no studies on surface waviness were found in the literature.

Another comparison was made on results of Ti6Al4V and SS316L. As for roughness, it was noticed that titanium benchmarks had lower waviness values than stainless-steel ones. The average value for Ti6Al4V was about $11\mu m$, while SS316L had a waviness average value of $20\mu m$.

Referring to laser power and scan speed variations, the aforementioned Wa trends were similar for both materials. However, the waviness trend as the laser power varies was more marked for titanium samples. On the other hand, the variability of waviness data was high with respect to scan speed changes, foreseeing a nonlinearity due to the complex physics of the process.

Moreover, the areal waviness data had different behaviours when spot size changed, depending on the material processed. In general, it was noticed that waviness had minimum values at $150\mu m$ spot; hence, this spot level was preferable to keep waviness low.

With respect to $50\mu m$ spot, the waviness data were the most scattered for both materials and it can be concluded that this operative condition was more sensitive to changes in laser power and scan speed. However, a larger experimental campaign would be needed to better understand the effect of laser spot size on waviness.

6.4 Boundary Characterization

In this section, a novel descriptor was proposed in order to evaluate the quality of top-surface edges. As a matter of fact, the latter can provide useful information on the applied operating conditions.

The data used were scans with low magnification objective (the same as those used for waviness measurements) and the algorithmic procedure was developed in MATLAB environment.

6.4.1 Point Cloud Pre-Processing

As for waviness measurements, the raw point clouds required some pre-processing operations before starting the actual analysis.

Firstly, a levelling operation (form removal) was applied in order to remove the surface tilt. Thus, the best fit plane was computed and subsequently subtracted from raw topography, obtaining a levelled surface.

Another pre-processing operation was then needed to remove points belonging to side walls. Therefore, the same function applied for waviness surface pre-processing was applied. It is worth reporting that the first denoising step (MATLAB *denoise* function) was not applied in order to preserve all points acquired, including noisy ones. Although the latter had wrong z -values, their (x,y) coordinates were correct and they were also included in the computation of point cloud boundary, which will be discussed in the following section.

6.4.2 Boundary Detection

The aim of this analysis was to objectively evaluate the edges of cubes top-surface. Thus, the first operation performed was the detection of the topography boundary in the (x,y) plane, which was actually composed by points belonging to the four edges of the cubic sample.

This operation was performed by the MATLAB's *boundary* function, which is linked to *alpha shape* algorithm. Basically, a 2D *alpha shape* can be described as the shape which

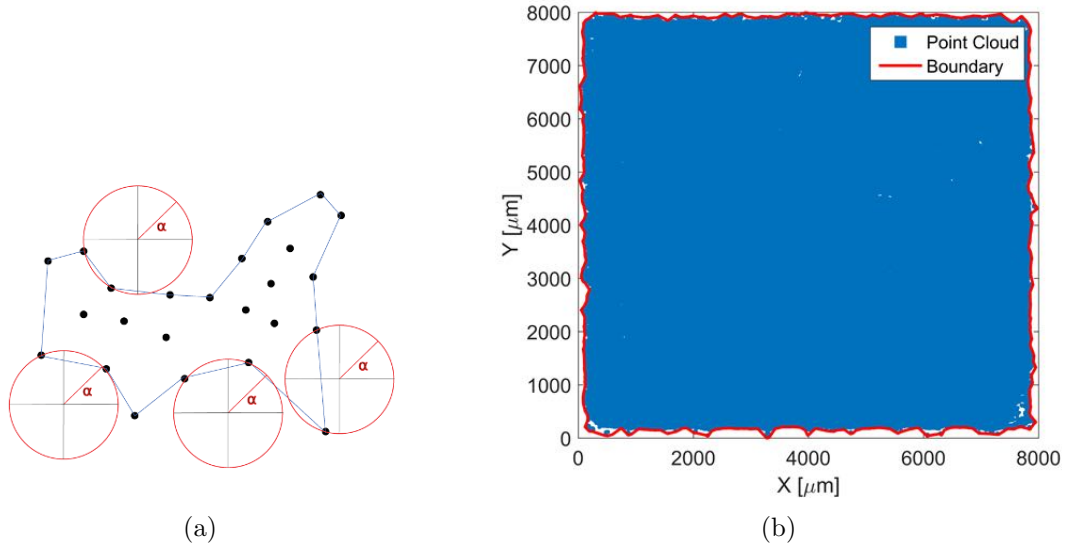


Figure 6.19: (a) Point cloud boundary detection through *alpha shape* disk [33] and, (b) example of boundary detection on cubic samples topography.

is generated if an impenetrable disk with radius α is rolled along the point cloud, starting with a border point. If a point is touched by the disk, it belongs to the boundary [33]. Clearly, the value of α defines the number of points involved in the boundary detection: if $\alpha \rightarrow 0$, all points of the dataset will be considered, while $\alpha \rightarrow \infty$ will only consider points that define the *convex hull* of the point cloud. The latter can be visualized as the shape enclosed by a rubber band stretched around the point cloud in the (x,y) plane.

However, *boundary* function does not allow to set directly α disk radius. Instead, the editable parameter is the *shrink factor*, specified as a scalar in the range of $0 \div 1$. When the *shrink factor* is zero, it corresponds to the *convex hull* of the point cloud, while a unitary *shrink factor* means the tightest single-region boundary around the points.

In this work, a *shrink factor* of 0.5 (default value) was applied in order to detect the points belonging to the boundary. An example of boundary detection can be seen in Figure 6.19b.

6.4.3 Edges Error Computation

After boundary detection, a regression line was computed for each cube edge. Thus, the points belonging to the point cloud perimeter were subdivided into four groups; one for each edge. To do this, a function was defined to search points along x-axis first and, then along y-axis. The vertices regions were not considered for line fitting as these regions were in some cases highly warped due to the excessive energy input and they would have increased the regression error. Hence, the beginning and the tail of each edge-points vector was ignored (the first millimetre and the last millimetre). Once the boundary point cloud was divided into the four edge-vectors, a linear regression was computed for every group of points and the edge lines were defined. An example of this operation can be seen in

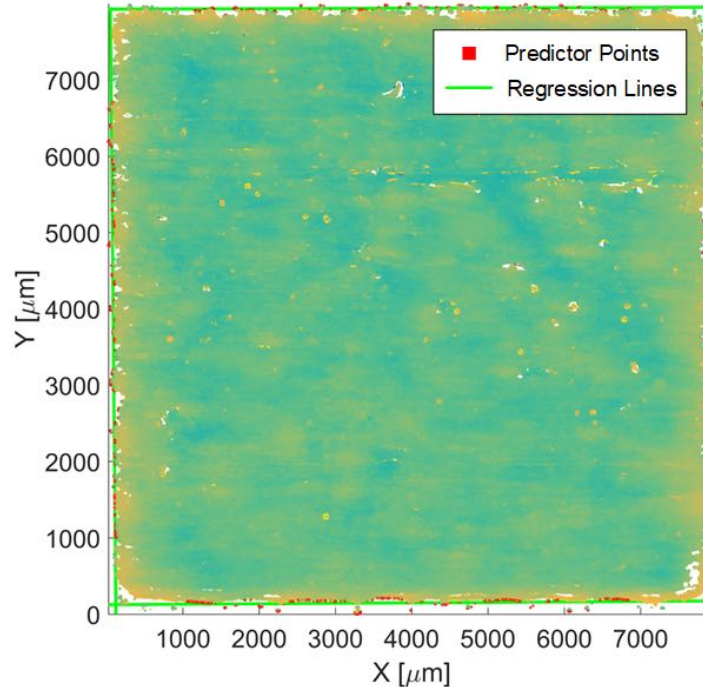


Figure 6.20: Computation of edges lines.

Figure 6.21. Lastly, the average distance of boundary points from the respective edge lines was computed. This parameter was proposed as a quality descriptor, since it represented the mean error of real edges with respect to the ideal edge lines of the cubic sample. In other words, it represented the extent of the edges jaggedness. It is worth noting that the geometrical relations between edges (e.g. angle between two edges) cannot be evaluated through this parameter and it was outside the scope of this descriptor.

These operations were automatically performed for each cubic sample and edges error maps were obtained (see Figure 6.23 for Ti6Al4V samples and Figure 6.24 for SS316L samples).

The data collected were then divided by type of material used and a preliminary statistical analysis was carried out. As can be seen from box plots in Figure 6.22, the increase in laser power had in general a negative effect on edges error, while the increase in scan speed had a positive influence. Thus, it can be concluded that an increase in linear energy density (P/v) entails a higher edges error, which means that the jaggedness of edges increased with energy input. This result had also physical sense as high energy input typically leads to high thermal stresses (and warps) and more powder particles could adhere to the build part due to the greater *mushy zone*.

Nevertheless, the most interesting result was related to the effect of spot size on edges error. As a matter of fact, it was noticed that the spot diameter had an almost exponential relation with this descriptor: when the spot size was decreased, the edges error decreased more rapidly. Hence, it was evident that more precise cubes were obtained with low values

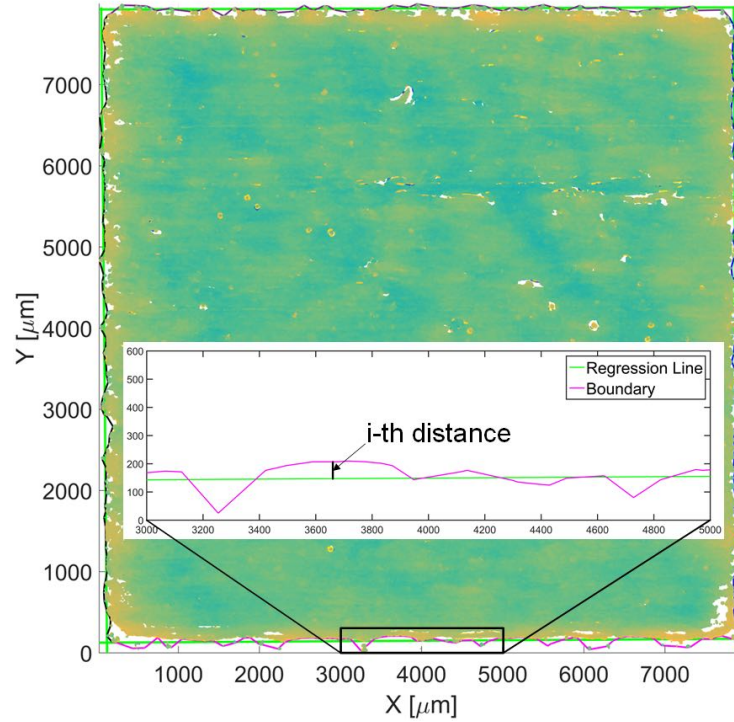


Figure 6.21: Representation of the distance between boundary points and the regression line. The average value represents the edges error.

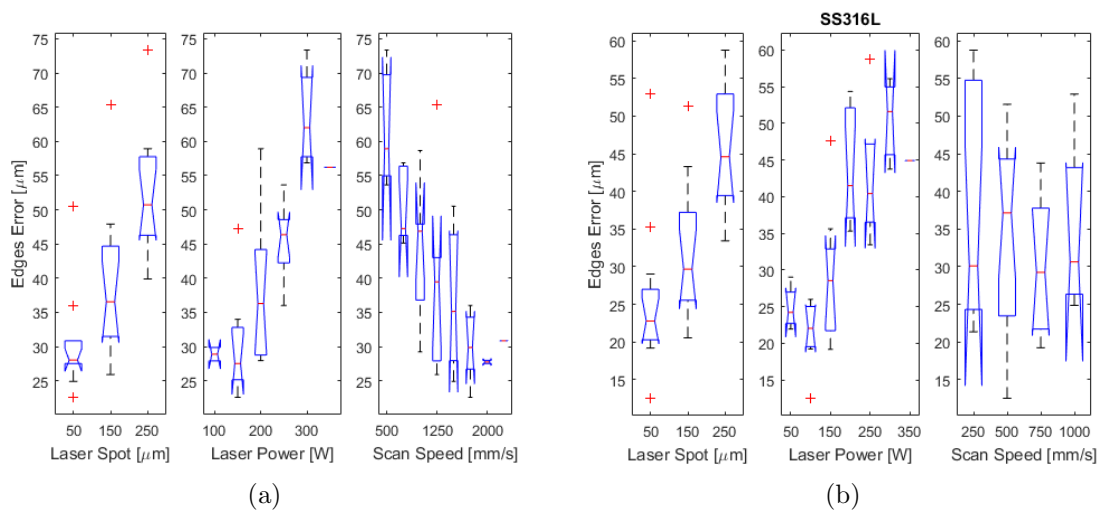


Figure 6.22: Box plots of edges error data as a function of spot diameter, laser power and scan speed for (a) Ti6Al4V and, (b) SS316L.

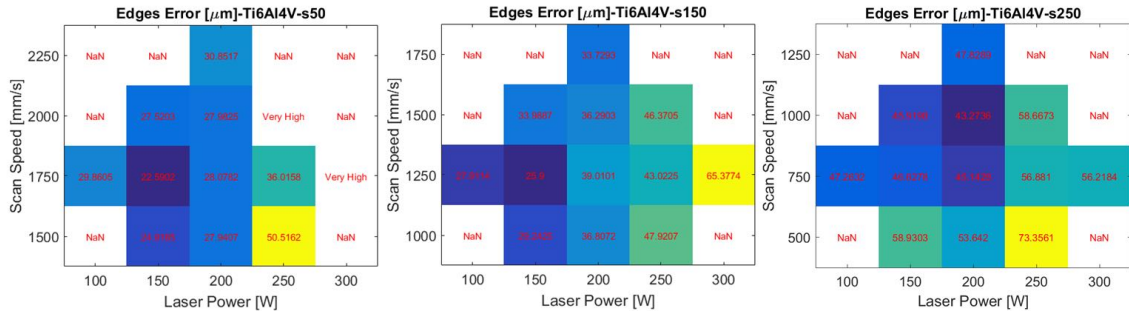


Figure 6.23: Edges error maps for Ti6Al4V benchmarks.

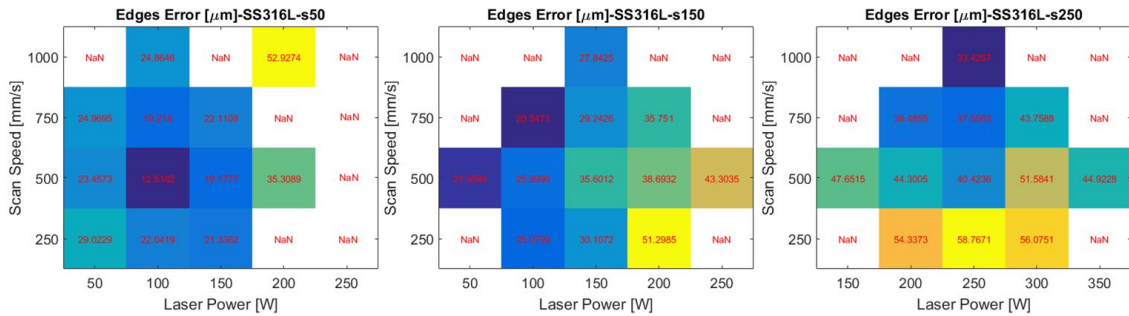


Figure 6.24: Edges error maps for SS316L benchmarks.

of spot diameter. In practice, by changing the spot size from $250\mu m$ to $50\mu m$, the median value of edges error was almost halved.

6.5 Relative Density

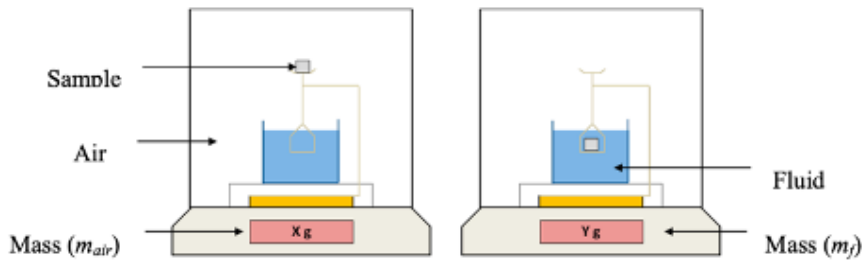


Figure 6.25: Schematic representation of the Archimedes method [7].

The Archimedes method was used to measure the density of all produced cubic samples. This method consists in weighing a specimen in a reference fluid (typically air) and in a second fluid, whose density is known. In this work, the second fluid was ethanol as it is more suitable for SLM components [7]. Once the measurements were performed, the

density was then determined by the following:

$$\rho_{sample} = \rho_f \cdot \frac{W_{air}}{W_{air} - W_f} \quad (6.6)$$

where ρ_f is the ethanol density, W_{air} is the weight of the sample weighed in air and W_f is the weight of the sample immersed in ethanol. The relative density was subsequently computed by the following:

$$RD = \frac{\rho_{sample}}{\rho_{reference}} \quad (6.7)$$

where $\rho_{reference}$ is the respective reference density for Ti6Al4V and SS316L, whose values are reported in Table 5.1.

Since this density measurement technique do not require any special sample preparation, it is actually one of the fastest methods that can be applied, and the accuracy of its results is comparable with those of other techniques (e.g. metallographic section analysis and tomography).

The data collected were then divided by type of material used and a preliminary statistical

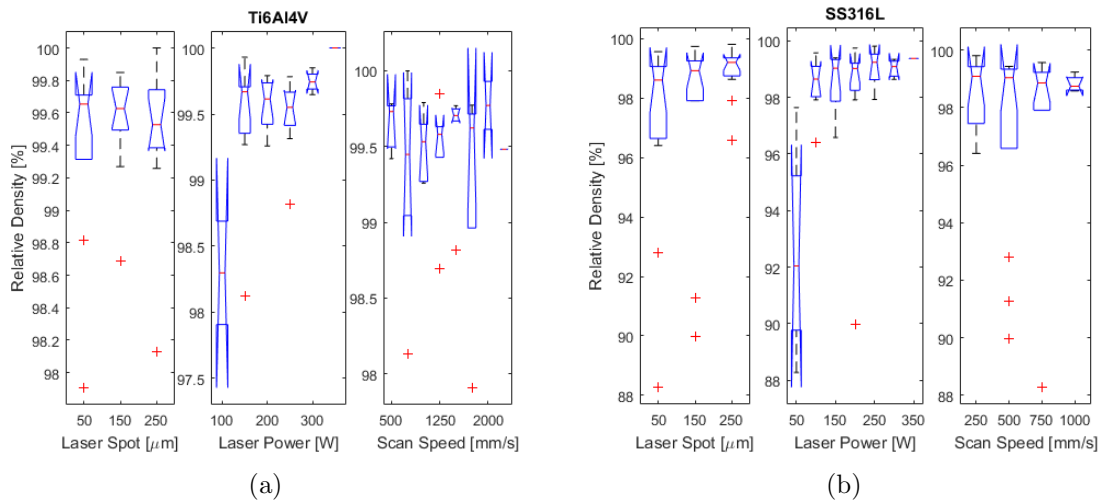


Figure 6.26: Box plots of relative density data as a function of spot diameter, laser power and scan speed for (a) Ti6Al4V and, (b) SS316L.

analysis was carried out. As can be seen from box plots in Figure 6.26, the only obvious trend was the one related to laser power. Indeed, it was noticed that a decrease in laser power led to a relative density reduction. In particular, the decrease in density was more rapid below a certain laser power threshold: 150W for Ti6Al4V and 100W for SS316L. In this operative condition, the energy input was probably not enough to completely melt the powder and a relevant number of pores were formed due to bad connection between neighbouring tracks and successive layers.

Neither scan speed nor spot size had a significant effect on relative density. With respect to spot diameter, this means that comparable density values can be obtained whatever the laser spot used.

Moreover, the relative density was probably not significantly affected by scan speed as the investigated range of this parameter was relatively small. In addition, the obtained values of relative density were generally high (more than 99%), excluding axial runs values. This proves that the process regions investigated were in the neighbourhood of the optimal ones. Thus, in these regions no major variations in track morphology (and therefore in relative density) due to scan speed changes were expected.

Comparing the results of Ti6Al4V and SS316L, it was noticed that the average value of relative densities was higher for titanium. This may be due to the not optimal value of overlap rate in case of stainless steel samples. Hence, an investigation on this parameter should be performed for parameters refinement.

Eventually, the relative density maps can be seen in Figure 6.27 for Ti6Al4V samples and Figure 6.28 for SS316L samples.

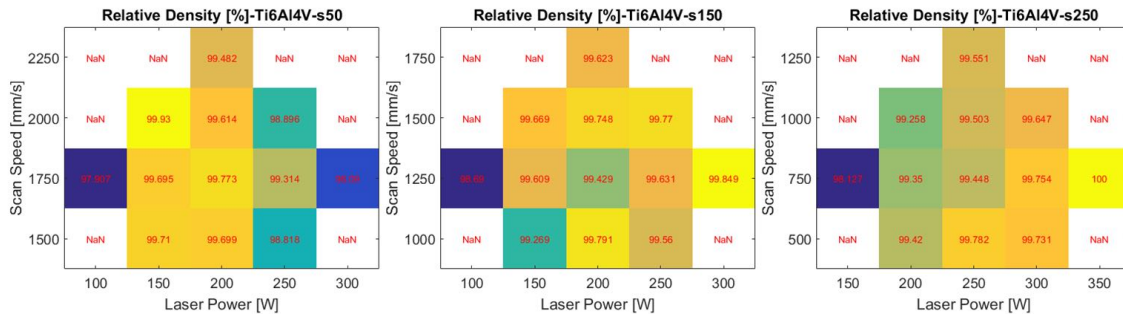


Figure 6.27: Relative density maps for Ti6Al4V benchmarks.

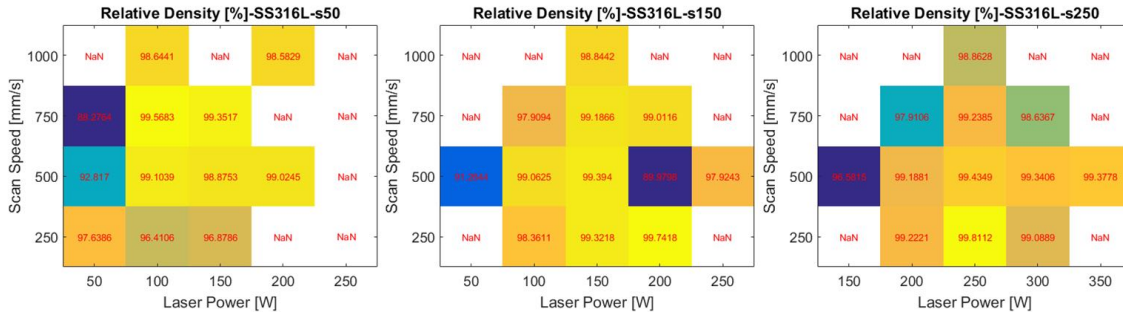


Figure 6.28: Relative density maps for SS316L benchmarks.

6.6 Optimal Parameter Sets

In summary, four quality descriptors were computed to evaluate the quality of each cubic sample: profile roughness, areal waviness, edges error and relative density. The profile roughness was measured to quantify the surface finish of the top surfaces, whose values can be easily compared with literature works since Ra is the most investigated parameter for this purpose. The areal waviness was studied to quantify the surface warps, while the

edges error was computed in order to measure the jaggedness of sample edges. Lastly, the relative density of 3D benchmarks was measured to verify that the specimens produced were dense enough to ensure good mechanical performance.

To define the optimal parameter set for each spot level, various optimization criteria can be applied depending on the required characteristics of the components to be produced. Therefore, the following methodology, used to define a unique parameter that expresses the quality of produced benchmarks, has to be considered a proposal.

Basically, the proposed method was based on describing the overall quality of a cubic sample with a novel index, which takes into account every quality descriptor previously defined; the *quality factor*. However, to sum non-homogeneous quantities in a final descriptor, it is first necessary to split descriptors values into class intervals or to convert them into dimensionless values.

As a first attempt, the values of each quality descriptor were classified according to a specific number of classes, which was computed by using the equation of Scott et al. [117]:

$$k = \frac{\text{range of data} \times \sqrt[3]{n_s}}{3.49 \times \sigma_s} \quad (6.8)$$

where n_s is the number of samples (values) and σ_s is the standard deviation of samples. The class interval was then calculated by dividing the range of data by the number of classes k . However, a different k value was found for the various descriptors, ranging from three to four classes. That implied a non-uniform weighing of the parameters when summed in a unique descriptor. Therefore, a different equation was tested to define the number of classes; the Sturges et al. [124] formula:

$$k = 1 + 3.3 \times \log 10n_s \quad (6.9)$$

Through Equation 6.9, the number of classes was six for each quality descriptor. Nevertheless, k value was not high enough to accurately describe the quality factor trend. In other words, the class intervals were too wide, and the trends of the various descriptors were too discretized. For this reason, it was decided to convert the various quality parameters into dimensionless descriptors. To do this, the following equation was applied:

$$X_{ND}(i) = \frac{X(i) - X_{min}}{X_{max} - X_{min}} \quad (6.10)$$

where X is a generic descriptor vector, $X(i)$ is its i -th element, while X_{min} and X_{max} are its minimum and maximum values, respectively. In addition, $X_{ND}(i)$ is the i -th element of the new dimensionless descriptor vector. By doing so, the values of the resultant vectors varied in the range of $0 \div 1$.

After the conversion of each quality descriptor, the *quality factor* was defined as follows:

$$\text{Quality Factor} = (RD)_{ND} - (Ra)_{ND} - (Wa)_{ND} - (E_{err})_{ND} \quad (6.11)$$

where ND is the acronym of non-dimensional (or dimensionless). The quality factor can ideally vary from 1, when $RD = (RD)_{max}$ and the other descriptors are equal to their minimum value (best condition), to -3 , which represents a minimum RD and the other

descriptors have maximum values (worst condition). Clearly, the higher the quality factor, the better the quality of cubic samples.

By including all the data collected, it was possible to define the quality factor maps for each spot size level, which can be seen in Figure 6.29 for Ti6Al4V, and in Figure 6.30 for SS316L. The maximum values of quality factor in each map represented the optimal processing condition; thus, the optimal parameter set.

However, by analysing the results of optimal process regions, it was noticed that relative

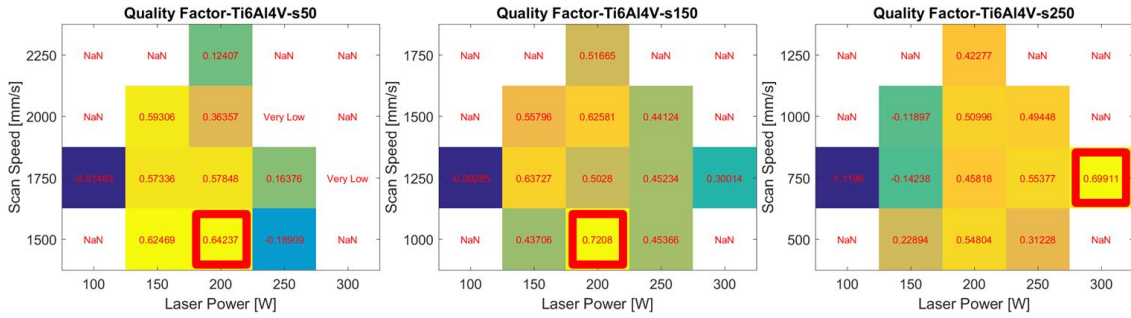


Figure 6.29: Quality factor maps for Ti6Al4V benchmarks (all data were included).

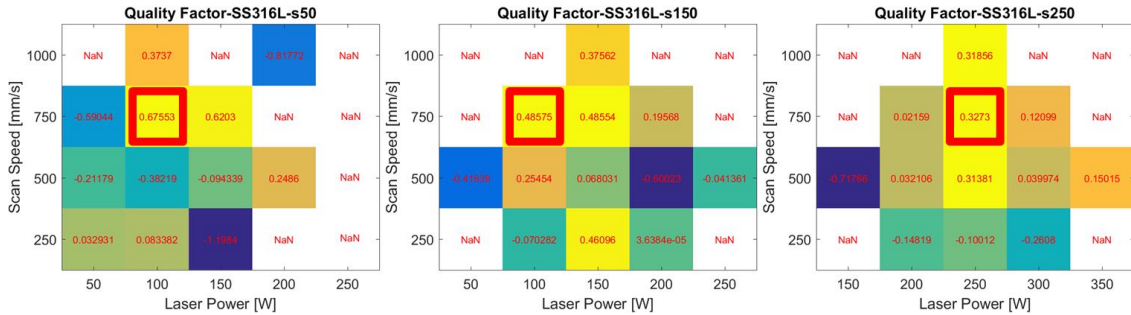


Figure 6.30: Quality factor maps for SS316L benchmarks (all data were included).

density values or areal waviness values were not acceptable in some cases. This discrepancy was probably due to how the *quality factor* had been formulated. As a matter of fact, each component of Equation 6.11 had a unitary weight coefficient and this choice was probably not suitable for evaluating the *quality factor* in every operating condition analysed. Nevertheless, finding a general criterion for the definition of non-unitary weight coefficients was challenging. Therefore, a different strategy was applied to solve this issue. Indeed, upstream of the *quality factor* calculation, two thresholds were applied to the data; one on relative density and one on areal waviness:

$$RD(i) > 99\% \quad (6.12)$$

$$Wa(i) < 2 \times mean(Ra) \quad (6.13)$$

where Ra is the roughness vector, while $RD(i)$ and $Wa(i)$ are the i -th elements of relative density vector and areal waviness vector, respectively.

6.6. Optimal Parameter Sets

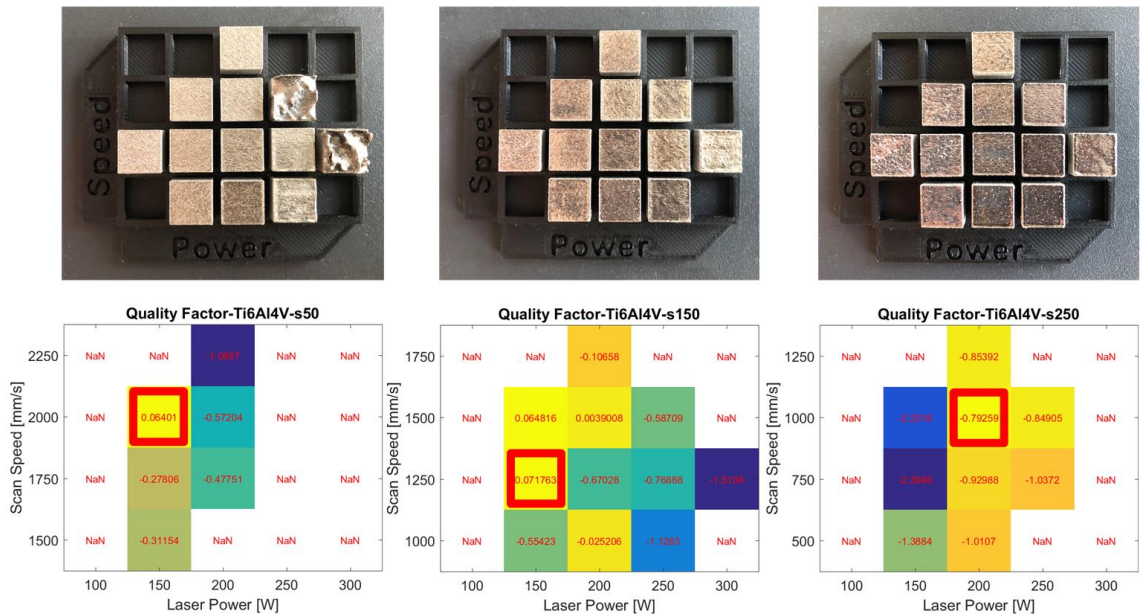


Figure 6.31: Quality factor maps for Ti6Al4V benchmarks. Only the data that satisfied $RD > 99\%$ and $Wa(i) > 2 \times mean(Ra)$ were considered.

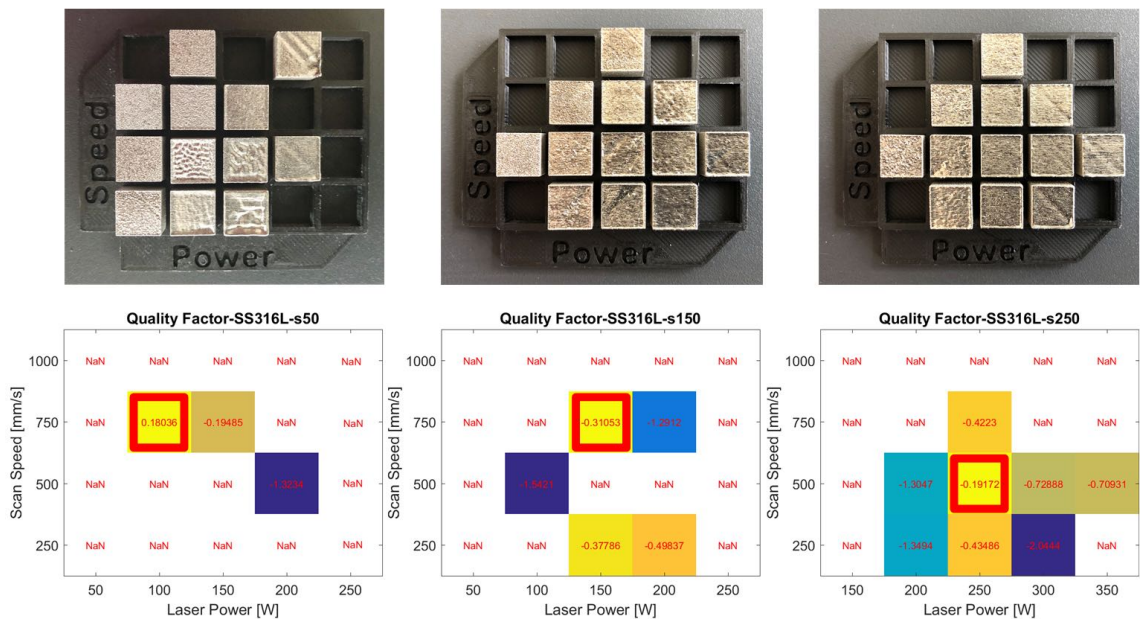


Figure 6.32: Quality factor maps for SS316L benchmarks. Only the data that satisfied $RD > 99\%$ and $Wa(i) > 2 \times mean(Ra)$ were considered.

Basically, all data that did not satisfy these conditions were removed from the analysis. As a matter of fact, relative densities below 99% are typically unacceptable for functional SLM components. With regard to waviness threshold, a surface warp entity above two times the mean roughness value was deemed unacceptable.

After the removal of samples with unacceptable characteristics, the *quality factor* was recalculated (Equation [6.11](#)) for the remaining samples.

Lastly, *quality factor* maps were defined, and more reliable optimal parameter sets were found for each spot level.

As can be seen in Figure [6.31](#) for Ti6Al4V and in Figure [6.32](#) for SS316L, the optimal parameter sets were at higher scan speed and/or lower laser power with respect to the maximum values of v_{cr} curves found with single tracks analysis (central point of each 3D benchmarks DoE). This was an expected result as it was in accordance with Di et al. [\[28\]](#) work. As a matter of fact, the authors studied SLM production through single track, multi-track and multi-layer (3D cubes) experiments. One of the main results of their analysis was that single track process window shifted to the upper left in multi-track and multi-layer production (referring to (P, v) plane). This means that lower laser power and/or higher scan speed was needed to obtain well-formed tracks in multi-track and multi-layer experiments. Moreover, the authors found that the heat accumulation on the workpiece during the production was the main cause of this effect, which was named *heat accumulation effect*.

Therefore, the results of this work supported their findings and demonstrated that the v_{cr} curve can be adopted to restrict the number of tests during 3D benchmarks production. It is true that optimal parameter set for 3D components cannot be defined only by the maximum value of v_{cr} curve; however, it was demonstrated that optimal parameters are in the neighbourhood of that process region. More precisely, at lower laser power levels and/or higher scan speed (upper left region).

Another validation can be made through the comparison between optimal parameters sets obtained with the presented methodology and those provided by the machine manufacturer. As a matter of fact, for each material, at least one level of the investigated spot diameters was comparable with the default value used by Concept Laser. The process parameters parallel is given in Table [6.1](#). As can be seen from the comparison, the optimal parameter sets slightly differed from Concept Laser ones. The main reason lies in the different hatch distance adopted for production; thus, further investigations on hatch distance (or overlap rate) should be made to make a more thorough parallel. Nevertheless, it is worth noting that, for each material, the volumetric energy density ($ED'_V = P/vth_d$) was almost the same for both parameter sets (3.9% and -8.8% of relative error for Ti6Al4V and SS316L, respectively), confirming that the results of the proposed methodology are suitable for production purposes. Another reason that justifies the slight discrepancy lies in the step size values adopted for the definition of power and speed levels of the DoEs. Clearly, not all operating condition were investigated in order to limit the number of experiments to be produced and analysed. Thus, the exact parameters values provided by Concept Laser were not investigated in the presented study and it was not possible to make a direct comparison. This consideration implies that the proposed methodology is rather crude. In fact, it will be necessary in the future to refine the method by introduc-

6.6. Optimal Parameter Sets

Material	Ti6Al4V		SS316L	
	Concept Laser	Current Study	Concept Laser	Current Study
Optimal Set Type				
Laser Power (P) [W]	225	150	180	150
Scan Speed (v) [mm/s]	1300	1250	600	750
Spot Size (d_s) [μm]	155	150	120	150
Hatch Distance (h_d) [μm]	90	60	105	78
Energy Density (ED'_V) [J/mm^3]	77	80	114	104
	Discrepancy 3.9%		Discrepancy -8.8%	

Table 6.1: Comparison between Concept Laser default parameters and optimal parameters obtained with the proposed methodology.

ing additional experimental stages, analysing further parameters and quality descriptors. For instance, mechanical properties were not considered in this work; however, as can be concluded from Table 4.1, tensile and fatigue properties are widely investigated in the literature for process optimization. Thus, mechanical testing will be for sure a point of interest for future development of the presented methodology.

Conclusions

This dissertation aimed to investigate the selective laser melting technology, focusing on process parameters optimization. The two main goals pursued were, on one hand, the definition of a new algorithmic optimization method based on optical metrology data and, on the other hand, the study of the effect of laser spot size variation on the quality of produced components. Therefore, various experiments were performed to achieve these objectives, varying the main process parameters according to a DoE approach and extending the study to different materials (Ti6Al4V and SS316L).

The first chapter was devoted to a brief introduction on metal additive manufacturing technologies, focusing on powder bed fusion processes. The general AM process chain was described and the main advantages, limitations and applications has been highlighted. From this first literature review, the following conclusions can be drawn:

- The most relevant metal AM technologies are selective laser melting and electron beam melting. The latter has higher build rates and the components produced are not significantly affected by thermal stresses as its counterpart. However, SLMed components are characterized by higher dimensional accuracy, surface finish and mechanical properties.
- Adapting slicing to part geometry can increase process productivity. Although adaptive slicing is not a recent concept, it is still difficult to apply in PBF processes, since the changes in layer thickness require appropriate adjustments of the other process parameters.
- The advantages of metal additive manufacturing are undeniable, especially to produce small batches of components with high buy-to-fly ratio. Nevertheless, due to the highly regulated industrial applications, there is a need to increase machines capabilities (build rate, density, dimensional accuracy, surface finish, etc.) and expand available materials that can be used.

In the second chapter, an extensive state of the art on selective laser melting was reported. The laser technology and the powder properties were widely discussed in order to understand the interaction between the heat source and the material involved in the process. Moreover, the process parameters that govern the melt pool dynamics were examined and the main physical phenomena that occur during the process were accurately addressed. Hence, the following conclusions can be drawn:

- The literature review on process parameters related to the adopted laser technology highlighted that there is a lack of comprehensive studies on laser spot size effect.
- The laser-material interaction is highly dynamic and it is one of the factors that complicate the process physics, since the laser interacts with a powder-coated substrate and not with a bare one, as it happens in laser welding.
- The most investigated process parameters in SLM are laser power, scan speed, layer thickness, hatch distance (or overlap rate) and scan strategy. These parameters, together with the spot size, define the energy input provided by the heat source and determine the thermal history of the produced parts.
- The main physical phenomena investigated in the literature are Rayleigh-Plateau instability, Marangoni convection, recoil pressure and keyhole phenomenon. With regard to Rayleigh-Plateau instability, two phenomena were recognized: the balling phenomenon and the humping effect. The first one is related to lack of fusion (not enough energy input), while the second one is the result of a combination of various forces, among which the most relevant is the recoil pressure.

The third chapter was firstly devoted to a review on process parameters optimization, from which the most adopted methodologies found in the literature were reported. Starting from literature works, a preliminary investigation on small laser spot size ($d_s = 50\mu m$) was carried out. The study was based on single tracks analysis; thus, 80 Ti6Al4V samples were produced by varying laser power and scan speed according to a full-factorial DoE and, a complete characterization was performed. The optimal process region for single tracks was defined and a preliminary 3D benchmark was printed, in order to verify the process performance when the new parameters are applied. The main results are listed below:

- Through the morphological analysis of single tracks, a process map was obtained by classifying tracks into five categories. The “Regular and thin shape” category represented the optimal process region for single tracks production when $50\mu m$ spot was applied.
- The width, depth, height and contact angle of single tracks were measured by SEM inspection and some statistical models were obtained through data analysis. In particular, track width and track depth models had a good fitting with experimental data (R^2 was 0.90 and 0.94, respectively), while track height and contact angle models had low statistical relevance. The latter result was also recognized by other authors and it is mainly due to the high variability of these two features along the track axis and thus to the position of analysed cross-section.
- From metallographic analysis, it was found that the microstructure was fully composed by Ti martensite and, through microhardness measurements, it was noticed that no appreciable differences in hardness values were present in the analysed samples.

- Lastly, a preliminary production of a lattice structure was carried out in order to verify that small spot parameters entailed higher process resolution. For this purpose, various measurements of beams diameter of the lattice structure produced were performed and it was confirmed that the dimensional accuracy was increased by 22% with respect to standard parameter set adoption.
- This study was very useful to understand the criticalities of process optimization methods currently proposed in the literature.

In the fourth chapter, an updated review on SLM process optimization was reported. The novel process optimization methodology was subsequently described in its entirety, giving an overview of the general procedure and highlighting the DoE details. An overview on the optical metrology techniques adopted for specimens inspection was also given in this chapter. The following conclusions can be drawn:

- The updated literature review highlighted that no works were performed on areal waviness characterisation applied to process optimization. In addition, a few studies on advanced AM surface characterization were found; however, none of them were aimed to process optimization.
- The 3D optical profiler adopted in this work has three acquisition techniques available: confocal microscopy, focus variation and interferometry. The latter was preferred for single track topography acquisition, since it is the most accurate measuring technique. With regard to 3D benchmarks characterization, focus variation was found out to be the most suitable since it is very fast and the area to be measured was much larger than single track acquisitions.
- A novel process optimization methodology was defined by exploiting the capabilities of the aforementioned optical 3D profiler and the automation of the analysis procedure, due to the algorithmic frameworks developed in MATLAB environment.
- The method presented does not provide a complete characterization of the single tracks, as was done in the work of Chapter 3. In fact, time-consuming measures, such as SEM analysis of cross-sections, were not performed and some information was not considered in this methodology. However, the useful information provided by the surfaces of analysed samples will be sufficient to quickly, reliably and objectively define the optimal parameters combinations for 3D benchmarks production.

The fifth chapter was devoted to the description of all steps that define the single tracks analysis. The procedure started with the automatic acquisition, through the 3D optical profiler, of all single tracks produced and each topography scanned was then elaborated in MATLAB environment. Single tracks were first recognized in the topography and then their mean profile was extracted in order to analyse the frequency spectrum. Through a novel parameter, single tracks were subsequently classified and the optimal process regions were identified. The main results are listed below:

- The algorithm developed in this work allowed to automatically recognize a single track on a SLMed substrate and extract it from the entire topography.

- A novel parameter that quantifies the track continuity was defined; the *balling energy*. Basically, this descriptor represented the energy associated with the frequency components due to humping or balling phenomena in the frequency spectrum of the single track profile. From a more practical point of view, the balling energy quantified the extent of discontinuity of the analysed profiles.
- The accuracy of the classification algorithm was determined by comparing the process maps obtained from the aforementioned methodology with those obtained manually by an experienced operator. Hence, the accuracy was about 97%, validating the methodology.
- One process map for each data set was obtained, dividing the samples into three categories: continuous track, discontinuous track and absent track (no track). In addition, two separation lines, which divided the samples into the various categories, were determined in the experimental data analysis: the single track melting efficiency curve and the critical speed curve. The latter curve, which separates continuous from discontinuous tracks, was the most interesting one, since it was never recognized before in SLM process optimization works. The critical speed represents the maximum scan speed that produces a continuous single track, given a specific laser power value. However, due to the complex physics of the process and the insufficient number of materials investigated, it was not possible to define any general rule that could describe the behaviour of these curves as the spot and material varied. The maximum of the critical speed curve is the optimal process region for single tracks experiments, since it represents the $P - v$ combination that maximizes the productivity.
- The laser spot size had an evident effect on the process performance; the track width increased as the spot size increased, while the maximum of the critical speed curve rapidly decreased as the the spot diameter increased in case of Ti6Al4V powder. The latter effect was not recognized in SS316L experiments, since the continuous region was generally small for this material and, to recognize the aforementioned effect, the experiments should have intensified in that region. Therefore, further investigations should be performed in order to deepen the understanding of this effect.

In the sixth chapter, the description of all steps that define the 3D benchmarks characterization was given. The procedure started with the automatic acquisition of all top surfaces of the 3D benchmarks produced and, for each topography scanned, the profile roughness, areal waviness and edges error were semi-automatically computed. In addition, density measurements were carried out in order to evaluate the relative density of samples. Lastly, an overall quality descriptor was proposed and the process maps for 3D benchmarks were obtained. Hence, the optimal process parameter sets were found. The main results are listed below:

- A novel descriptor that quantified the extent of the edges jaggedness was defined. Basically, this descriptor represented the mean error of real edges with respect to the ideal edge lines of the cubic samples.

- From a preliminary statistical analysis, it was found that profile roughness decreased as the laser power increased and the scan speed decreased. This was in accordance with literature works. In addition, the profile roughness trend was inversely proportional to the spot size increase.
- On the other hand, areal waviness had an opposite behaviour: it increased as the laser power increased and the scan speed decreased. No correspondence was found with the literature works, as this parameter was never investigated in order to optimize the process. Moreover, no statistically relevant trend was found with respect to laser spot size variation.
- The edges error had similar trends as waviness when laser power and scan speed varied. In addition, through this descriptor, it was possible to demonstrate that small spot size levels entailed more precise edges. As a matter of fact, there is a direct proportionality between laser spot diameter and edges error.
- The relative density values were significantly influenced only by laser power. No clear trends were noticed with respect to variations of both scan speed and spot size.
- The non-dimensional values of all quality descriptors were computed and a overall quality factor was then proposed, in order to find the optimal process region for each dataset. Thus, the optimal process parameter sets were defined for each spot level and for each material.
- Comparing the optimal process parameters for 3D benchmarks production and the optimal regions in the single tracks process maps, it was found that these regions were slightly shifted in the (P, v) plane. More specifically, the process window of 3D benchmarks was at higher scan speed and/or lower laser power compared to that of single tracks. This was an expected result as it was also demonstrated by Di et al. [28]. Therefore, this result confirmed that the maximum of the critical speed curve was a powerful tool for the process window identification. As a matter of fact, the 3D benchmarks DoE was considerably smaller than single tracks experimental campaign and it was centred in the correct position in the (P, v) plane.

As a consequence, the proposed methodology has made it possible to objectively, reliably and efficiently find the optimal parameter sets for various laser spot diameters and different materials. It is therefore considered that the thesis objective was successfully achieved.

In closing, this methodology can be applied for the characterization of a large number of specimens and more process parameters (which were not considered in this work) can be involved in the DoE. Furthermore, this optimization method can be adopted to existent production strategies that require more than one process parameter set, such as hull and core strategy and multi-laser scanning, and opens the door to new production strategies. For instance, the development of scanning strategies that adapt the process parameters to part geometry (e.g. spot size and layer thickness) could benefit from this methodology. Clearly, the proposed method requires various refinements and there is still room for

improvement. First of all, more powder materials should be tested in order to better validate the methodology, develop an analytical model that describes the critical speed curve behaviour and deepen the understanding of spot size effect. Secondly, more process parameters should be added to the experimental campaign in order to refine the optimal process region detection.

Eventually, more quality descriptor and different geometries should be introduced for 3D benchmarks characterization. For instance, an ad hoc 3D benchmark could be designed for overhanging surfaces evaluation and thus a specific characterization procedure should be developed. Moreover, tensile specimens should be added to the experimentation in order to assess tensile and fatigue behavior of the manufactured components.

Bibliography

- [1] 3dlink. Understand and fix common errors in stl files, 2018. <https://3dlink.me/entender-y-reparar-errores-comunes-en-archivos-stl/>.
- [2] N. T. Aboulkhair, N. M. Everitt, I. Ashcroft, and C. Tuck. Reducing porosity in als10mg parts processed by selective laser melting. *Additive Manufacturing*, 1:77–86, 2014.
- [3] I. H. Ahn. Determination of a process window with consideration of effective layer thickness in slm process. *The International Journal of Advanced Manufacturing Technology*, 105(10):4181–4191, 2019.
- [4] A. Amado, M. Schmid, and K. Wegener. Flowability of sls powders at elevated temperature. Technical report, ETH Zurich, 2014.
- [5] K. Arafune and A. Hirata. Thermal and solutal marangoni convection in in-ga-sb system. *Journal of Crystal Growth*, 197(4):811–817, 1999.
- [6] ARCAM. Arcam q20 - pushing the envelope for additive manufacturing, 2013. <http://www.arcam.com/wp-content/uploads/Arcam-Q20-final.pdf>.
- [7] C. Arvieu, C. Galy, E. Le Guen, and E. Lacoste. Relative density of slm-produced aluminum alloy parts: Interpretation of results. *Journal of Manufacturing and Materials Processing*, 4(3):83, 2020.
- [8] M. Balbaa, S. Mekhiel, M. Elbestawi, and J. McIsaac. On selective laser melting of inconel 718: Densification, surface roughness, and residual stresses. *Materials & Design*, page 108818, 2020.
- [9] A.-M. Bandar. Powder metallurgy of stainless steel: state-of-the art, challenges, and development. *MICROSTRUCTURE, MECHANICAL PROPERTIES AND METHODS OF APPLICATION*, page 37, 2019.
- [10] J. L. Bartlett and X. Li. An overview of residual stresses in metal powder bed fusion. *Additive Manufacturing*, 27:131–149, 2019.
- [11] U. S. Bertoli, A. J. Wolfer, M. J. Matthews, J.-P. R. Delplanque, and J. M. Schoenung. On the limitations of volumetric energy density as a design parameter for selective laser melting. *Materials & Design*, 113:331–340, 2017.

- [12] V. Bhavar, P. Kattire, V. Patil, S. Khot, K. Gujar, and R. Singh. A review on powder bed fusion technology of metal additive manufacturing. In *Additive Manufacturing Handbook*, pages 251–253. CRC Press, 2017.
- [13] F. Bosio, A. Aversa, M. Lorusso, S. Marola, D. Gianoglio, L. Battezzati, P. Fino, D. Manfredi, and M. Lombardi. A time-saving and cost-effective method to process alloys by laser powder bed fusion. *Materials & Design*, 181:107949, 2019.
- [14] D. Bourell, B. Stucker, A. Spierings, N. Herres, and G. Levy. Influence of the particle size distribution on surface quality and mechanical properties in am steel parts. *Rapid Prototyping Journal*, 2011.
- [15] D. Buchbinder, W. Meiners, N. Pirch, K. Wissenbach, and J. Schrage. Investigation on reducing distortion by preheating during manufacture of aluminum components using selective laser melting. *Journal of laser applications*, 26(1):012004, 2014.
- [16] F. Calignano. Investigation of the accuracy and roughness in the laser powder bed fusion process. *Virtual and Physical Prototyping*, 13(2):97–104, 2018.
- [17] S. L. Campanelli, G. Casalino, N. Contuzzi, A. Angelastro, and A. D. Ludovico. Analysis of the molten/solidified zone in selective laser melted parts. In *High-Power Laser Materials Processing: Lasers, Beam Delivery, Diagnostics, and Applications III*, volume 8963, page 896311. International Society for Optics and Photonics, 2014.
- [18] L. Caprio, A. G. Demir, and B. Previtali. Influence of pulsed and continuous wave emission on melting efficiency in selective laser melting. *Journal of Materials Processing Technology*, 266:429–441, 2019.
- [19] R. Casati, M. Hamidi Nasab, M. Coduri, V. Tirelli, and M. Vedani. Effects of platform pre-heating and thermal-treatment strategies on properties of als10mg alloy processed by selective laser melting. *Metals*, 8(11):954, 2018.
- [20] Q. Chen, G. Guillemot, C.-A. Gandin, and M. Bellet. Numerical modelling of the impact of energy distribution and marangoni surface tension on track shape in selective laser melting of ceramic material. *Additive Manufacturing*, 21:713–723, 2018.
- [21] S. Chen, J. Huang, C. Pan, C. Lin, T. Yang, Y. Huang, C. Ou, L. Chen, D. Lin, H. Lin, et al. Microstructure and mechanical properties of open-cell porous ti-6al-4v fabricated by selective laser melting. *Journal of Alloys and Compounds*, 713:248–254, 2017.
- [22] B. Cheng, L. Loeber, H. Willeck, U. Hartel, and C. Tuffile. Computational investigation of melt pool process dynamics and pore formation in laser powder bed fusion. *Journal of Materials Engineering and Performance*, 28(11):6565–6578, 2019.
- [23] Comsol. The marangoni effect, 2017. <https://www.comsol.it/multiphysics/marangoni-effect>.

-
- [24] Controllaser. Buyer's guide: Understanding laser machines, 2020. <https://www.controllaser.com/articles/buyers-guide/how-can-i-select-the-right-laser-source-for-my-application/>.
- [25] M. Courtois, M. Carin, P. Le Masson, S. Gaied, and M. Balabane. A complete model of keyhole and melt pool dynamics to analyze instabilities and collapse during laser welding. *Journal of Laser applications*, 26(4):042001, 2014.
- [26] D. Dai and D. Gu. Influence of thermodynamics within molten pool on migration and distribution state of reinforcement during selective laser melting of aln/alsi10mg composites. *International Journal of Machine Tools and Manufacture*, 100:14–24, 2016.
- [27] C. de Formanoir, U. Paggi, T. Colebrants, L. Thijs, G. Li, K. Vanmeensel, and B. Van Hooreweder. Increasing the productivity of laser powder bed fusion: Influence of the hull-bulk strategy on part quality, microstructure and mechanical performance of ti-6al-4v. *Additive Manufacturing*, 33:101129, 2020.
- [28] W. Di, Y. Yongqiang, S. Xubin, and C. Yonghua. Study on energy input and its influences on single-track, multi-track, and multi-layer in slm. *The International Journal of Advanced Manufacturing Technology*, 58(9-12):1189–1199, 2012.
- [29] O. Diegel, A. Nordin, and D. Motte. *A Practical Guide to Design for Additive Manufacturing*. Springer, 2019.
- [30] C. Dixon. Atomizing molten metals—a review. *Canadian Metallurgical Quarterly*, 12(3):309–322, 1973.
- [31] T. Duda and L. V. Raghavan. 3d metal printing technology. *IFAC-PapersOnLine*, 49(29):103–110, 2016.
- [32] G. Dursun, S. Ibekwe, G. Li, P. Mensah, G. Joshi, and D. Jerro. Influence of laser processing parameters on the surface characteristics of 316l stainless steel manufactured by selective laser melting. *Materials Today: Proceedings*, 2020.
- [33] M. Eich, M. Dabrowska, and F. Kirchner. Semantic labeling: Classification of 3d entities based on spatial feature descriptors. In *IEEE International Conference on Robotics and Automation (ICRA2010) in Anchorage, Alaska*, 2010.
- [34] Z. Fan, M. Lu, and H. Huang. Selective laser melting of alumina: A single track study. *Ceramics International*, 44(8):9484–9493, 2018.
- [35] Fraunhofer. Automated support removal for slm components, 2017. https://www.ilt.fraunhofer.de/content/dam/ilt/en/documents/annual-reports-/AR16/TF2/AR16.P59_automated-support-removal-SLM-components.pdf.
- [36] FreesteelBlog. We have some slicing, 2015. <https://www.freesteel.co.uk/wpblog/2015/01/05/we-have-some-slicing/>.

- [37] GeneralElectricAdditive. Direct metal laser melting (dmlm) machines, 2020. <https://www.ge.com/additive/additive-manufacturing/machines/dmlm-machines/x-line-2000r>.
- [38] I. Gibson, D. W. Rosen, B. Stucker, et al. *Additive manufacturing technologies*, volume 17. Springer, 2014.
- [39] X. Gong, B. Cheng, S. Price, and K. Chou. Powder-bed electron-beam-melting additive manufacturing: powder characterization, process simulation and metrology. In *Early Career Technical Conference, Birmingham, AL*, pages 55–66, 2013.
- [40] J. V. Gordon, S. P. Narra, R. W. Cunningham, H. Liu, H. Chen, R. M. Suter, J. L. Beuth, and A. D. Rollett. Defect structure process maps for laser powder bed fusion additive manufacturing. *Additive Manufacturing*, 36:101552, 2020.
- [41] D. Gu. *Laser additive manufacturing of high-performance materials*. Springer, 2015.
- [42] D. Gu, Y.-C. Hagedorn, W. Meiners, K. Wissenbach, and R. Poprawe. Nanocrystalline tic reinforced ti matrix bulk-form nanocomposites by selective laser melting (slm): Densification, growth mechanism and wear behavior. *Composites Science and Technology*, 71(13):1612–1620, 2011.
- [43] V. Gunenthiram, P. Peyre, M. Schneider, M. Dal, F. Coste, and R. Fabbro. Analysis of laser–melt pool–powder bed interaction during the selective laser melting of a stainless steel. *Journal of Laser Applications*, 29(2):022303, 2017.
- [44] C. Guo, S. Li, S. Shi, X. Li, X. Hu, Q. Zhu, and R. M. Ward. Effect of processing parameters on surface roughness, porosity and cracking of as-built in738lc parts fabricated by laser powder bed fusion. *Journal of Materials Processing Technology*, page 116788, 2020.
- [45] X. Han, H. Zhu, X. Nie, G. Wang, and X. Zeng. Investigation on selective laser melting als10mg cellular lattice strut: molten pool morphology, surface roughness and dimensional accuracy. *Materials*, 11(3):392, 2018.
- [46] D. Hann, J. Iammi, and J. Folkes. A simple methodology for predicting laser-weld properties from material and laser parameters. *Journal of Physics D: Applied Physics*, 44(44):445401, 2011.
- [47] J. Hecht. *Understanding lasers: an entry-level guide*. John Wiley & Sons, 2018.
- [48] B. Hughes and G. Wilson. 3d/additive printing manufacturing: a brief history and purchasing guide. *Technology and Engineering Teacher*, 75(4):18, 2015.
- [49] InsideMetalAdditiveManufacturing. Design: optimising supports for complex components, 2015. <https://www.insidemetaladditivemanufacturing.com/blog/design-optimising-supports-for-complex-components>.
- [50] ISO/ASTM-52900. Additive manufacturing - general principles - terminology, 2015.

-
- [51] ISO/DIS-7296-2. Additive manufacturing - general principles - part 2 overview of process categories and feedstock, 2015.
- [52] A. Iveković, M. L. Montero-Sistiaga, K. Vanmeensel, J.-P. Kruth, and J. Vleugels. Effect of processing parameters on microstructure and properties of tungsten heavy alloys fabricated by slm. *International Journal of Refractory Metals and Hard Materials*, 82:23–30, 2019.
- [53] P. Jamshidi, M. Haddad, and S. Mansour. A new database approach to improve stl files correction algorithms. In *18th International Conference on Production Research*, 2005.
- [54] J. Jiang, X. Xu, and J. Stringer. Support structures for additive manufacturing: a review. *Journal of Manufacturing and Materials Processing*, 2(4):64, 2018.
- [55] N. Karapatis, G. Egger, P. Gygax, and R. Glardon. Optimization of powder layer density in selective laser sintering. In *1999 International Solid Freeform Fabrication Symposium*, 1999.
- [56] K. Kempen, B. Vrancken, S. Buls, L. Thijs, J. Van Humbeeck, and J.-P. Kruth. Selective laser melting of crack-free high density m2 high speed steel parts by baseplate preheating. *Journal of Manufacturing Science and Engineering*, 136(6), 2014.
- [57] S. Khademzadeh, F. Zanini, J. Rocco, K. Brunelli, P. Bariani, and S. Carmignato. Quality enhancement of microstructure and surface topography of niti parts produced by laser powder bed fusion. *CIRP Journal of Manufacturing Science and Technology*, 2020.
- [58] S. A. Khairallah, A. T. Anderson, A. Rubenchik, and W. E. King. Laser powder-bed fusion additive manufacturing: Physics of complex melt flow and formation mechanisms of pores, spatter, and denudation zones. *Acta Materialia*, 108:36–45, 2016.
- [59] W. E. King, H. D. Barth, V. M. Castillo, G. F. Gallegos, J. W. Gibbs, D. E. Hahn, C. Kamath, and A. M. Rubenchik. Observation of keyhole-mode laser melting in laser powder-bed fusion additive manufacturing. *Journal of Materials Processing Technology*, 214(12):2915–2925, 2014.
- [60] C. Körner, A. Bauereiß, and E. Attar. Fundamental consolidation mechanisms during selective beam melting of powders. *Modelling and Simulation in Materials Science and Engineering*, 21(8):085011, 2013.
- [61] S. Kou. *Welding metallurgy*. New Jersey, USA, pages 431–446, 2003.
- [62] I. Koutiri, E. Pessard, P. Peyre, O. Amlou, and T. De Terris. Influence of slm process parameters on the surface finish, porosity rate and fatigue behavior of as-built inconel 625 parts. *Journal of Materials Processing Technology*, 255:536–546, 2018.

- [63] D. Koutny, D. Palousek, L. Pantelejev, C. Hoeller, R. Pichler, L. Tesicky, and J. Kaiser. Influence of scanning strategies on processing of aluminum alloy en aw 2618 using selective laser melting. *Materials*, 11(2):298, 2018.
- [64] A. Kreitchberg, V. Brailovski, and S. Prokoshkin. New biocompatible near-beta ti-zr-nb alloy processed by laser powder bed fusion: Process optimization. *Journal of Materials Processing Technology*, 252:821–829, 2018.
- [65] J.-P. Kruth, M. Badrossamay, E. Yasa, J. Deckers, L. Thijs, and J. Van Humbeeck. Part and material properties in selective laser melting of metals. In *Proceedings of the 16th International Symposium on Electromachining (ISEM XVI)*, pages 3–14. SHANGHAI JIAO TONG UNIV PRESS, 2010.
- [66] J. P. Kruth, M. Bartscher, S. Carmignato, R. Schmitt, L. De Chiffre, and A. Weckenmann. Computed tomography for dimensional metrology. *CIRP annals*, 60(2):821–842, 2011.
- [67] T. S. Kumar and A. Vijai. 3d reconstruction of face from 2d ct scan images. *Procedia Engineering*, 30:970–977, 2012.
- [68] M. Langelaar. Combined optimization of part topology, support structure layout and build orientation for additive manufacturing. *Structural and Multidisciplinary Optimization*, 57(5):1985–2004, 2018.
- [69] R. Leach. *Optical measurement of surface topography*, volume 14. Springer, 2011.
- [70] H. Lee, C. H. J. Lim, M. J. Low, N. Tham, V. M. Murukeshan, and Y.-J. Kim. Lasers in additive manufacturing: A review. *International Journal of Precision Engineering and Manufacturing-Green Technology*, 4(3):307–322, 2017.
- [71] Y. Lee and W. Zhang. Mesoscopic simulation of heat transfer and fluid flow in laser powder bed additive manufacturing. In *International Solid Free Form Fabrication Symposium, Austin*, pages 1154–1165, 2015.
- [72] Z. Lei, J. Bi, Y. Chen, X. Chen, X. Qin, and Z. Tian. Effect of energy density on formability, microstructure and micro-hardness of selective laser melted sc-and zr-modified 7075 aluminum alloy. *Powder Technology*, 356:594–606, 2019.
- [73] Let’sScience. Rocce sedimentarie. <http://letscience.altervista.org/html/geologia/rocce-sedimentarie.php>.
- [74] G. N. Levy. Additive manufacturing - a revolutionary enabling innovation-space past present and future, 2018. AITeM AM Conference.
- [75] C. Li, Y. Guo, and J. Zhao. Interfacial phenomena and characteristics between the deposited material and substrate in selective laser melting inconel 625. *Journal of Materials Processing Technology*, 243:269–281, 2017.

- [76] R. Li, J. Liu, Y. Shi, L. Wang, and W. Jiang. Balling behavior of stainless steel and nickel powder during selective laser melting process. *The International Journal of Advanced Manufacturing Technology*, 59(9-12):1025–1035, 2012.
- [77] R. Li, Y. Shi, Z. Wang, L. Wang, J. Liu, and W. Jiang. Densification behavior of gas and water atomized 316l stainless steel powder during selective laser melting. *Applied surface science*, 256(13):4350–4356, 2010.
- [78] D. Lin, L. Xu, Y. Han, Y. Zhang, H. Jing, L. Zhao, and F. Minami. Structure and mechanical properties of a fecocorni high-entropy alloy fabricated via selective laser melting. *Intermetallics*, 127:106963, 2020.
- [79] B. Liu, R. Wildman, C. Tuck, I. Ashcroft, and R. Hague. Investigation the effect of particle size distribution on processing parameters optimisation in selective laser melting process. *Additive manufacturing research group, Loughborough University*, pages 227–238, 2011.
- [80] Y.-L. Lo, B.-Y. Liu, and H.-C. Tran. Optimized hatch space selection in double-scanning track selective laser melting process. *The International Journal of Advanced Manufacturing Technology*, 105(7-8):2989–3006, 2019.
- [81] S. Longo. *Analisi Dimensionale e Modellistica Fisica: Principi e applicazioni alle scienze ingegneristiche*. Springer Science & Business Media, 2011.
- [82] S. Lou, X. Jiang, W. Sun, W. Zeng, L. Pagani, and P. Scott. Characterisation methods for powder bed fusion processed surface topography. *Precision Engineering*, 57:1–15, 2019.
- [83] M. Lutter-Günther, C. Gebbe, T. Kamps, C. Seidel, and G. Reinhart. Powder recycling in laser beam melting: strategies, consumption modeling and influence on resource efficiency. *Production Engineering*, 12(3-4):377–389, 2018.
- [84] O. Lyckfeldt. Powder rheology of steel powders for additive manufacturing. In *International Powder Metallurgy Congress and Exhibition, Euro PM 2013*. European Powder Metallurgy Association (EPMA), 2013.
- [85] A. H. Maamoun, Y. F. Xue, M. A. Elbestawi, and S. C. Veldhuis. Effect of selective laser melting process parameters on the quality of al alloy parts: Powder characterization, density, surface roughness, and dimensional accuracy. *Materials*, 11(12):2343, 2018.
- [86] T. Maconachie, M. Leary, B. Lozanovski, X. Zhang, M. Qian, O. Faruque, and M. Brandt. Slm lattice structures: Properties, performance, applications and challenges. *Materials & Design*, page 108137, 2019.
- [87] L. Magazine. Digital micromirror devices enable dynamic stage lighting, 2018. <https://www.ledsmagazine.com/leds-ssl-design/microcontrollers/article/16695785/digital-micromirror-devices-enable-dynamic-stage-lighting-magazine>.

- [88] N. W. Makoana, I. Yadroitsava, H. Möller, and I. Yadroitsev. Characterization of 17-4ph single tracks produced at different parametric conditions towards increased productivity of lpb systems—the effect of laser power and spot size upscaling. *Metals*, 8(7):475, 2018.
- [89] A. Manmadhachary, R. Kumar, and L. Krishnanand. Improve the accuracy, surface smoothing and material adaption in stl file for rp medical models. *Journal of Manufacturing Processes*, 21:46–55, 2016.
- [90] C. Marangoni. *Sull'espansione delle gocce d'un liquido galleggianti sulla superficie di altro liquido*. 1865.
- [91] I. Marin, I.-B. Păvăloiu, N. Goga, A. Vasilăţeanu, and G. Drăgoi. Automatic contour detection from dental cbct dicom data. In *2015 E-Health and Bioengineering Conference (EHB)*, pages 1–4. IEEE, 2015.
- [92] A. Matilla, J. Mariné, J. Pérez, C. Cadevall, and R. Artigas. Three-dimensional measurements with a novel technique combination of confocal and focus variation with a simultaneous scan. In *Optical Micro-and Nanometrology VI*, volume 9890, page 98900B. International Society for Optics and Photonics, 2016.
- [93] J. Metelkova, Y. Kinds, K. Kempen, C. de Formanoir, A. Witvrouw, and B. Van Hooreweder. On the influence of laser defocusing in selective laser melting of 316l. *Additive Manufacturing*, 23:161–169, 2018.
- [94] S. Metrology. S neox five axis, 2020. <https://www.sensofar.com/metrology/products/sneox-fiveaxis/>.
- [95] MidwestCompositeTechnologies. Direct metal laser sintering (dmls), 2020. <https://www.midwestcomposite.com/capabilities/direct-metal-laser-sintering-dmls/>.
- [96] D. L. Millis. Responses of musculoskeletal tissues to disuse and remobilization. In *Canine rehabilitation and physical therapy*, pages 92–153. Elsevier, 2014.
- [97] MIMA. Mim materials range, 2020. <https://mimaweb.org/design-center/materials-range/>.
- [98] A. K. Mishra and A. Kumar. Effect of surface morphology on the melt pool geometry in single track selective laser melting. *Materials Today: Proceedings*, 27:816–823, 2020.
- [99] B. Nagarajan, Z. Hu, X. Song, W. Zhai, and J. Wei. Development of micro selective laser melting: The state of the art and future perspectives. *Engineering*, 5(4):702–720, 2019.
- [100] L. Newton, N. Senin, C. Gomez, R. Danzl, F. Helmlı, L. Blunt, and R. Leach. Areal topography measurement of metal additive surfaces using focus variation microscopy. *Additive Manufacturing*, 25:365–389, 2019.

-
- [101] T. D. Ngo, A. Kashani, G. Imbalzano, K. T. Nguyen, and D. Hui. Additive manufacturing (3d printing): A review of materials, methods, applications and challenges. *Composites Part B: Engineering*, 143:172–196, 2018.
- [102] X. Nie, H. Zhang, H. Zhu, Z. Hu, L. Ke, and X. Zeng. Analysis of processing parameters and characteristics of selective laser melted high strength al-cu-mg alloys: From single tracks to cubic samples. *Journal of Materials Processing Technology*, 256:69–77, 2018.
- [103] S. Pal, I. Drstvensek, and T. Brajliah. Physical behaviors of materials in selective laser melting process. *DAAAM Int Sci B., Vienna*, pages 239–256, 2018.
- [104] D. Palousek, M. Kocica, L. Pantelejev, L. Klakurkova, L. Celko, D. Koutny, and J. Kaiser. Slm process parameters development of cu-alloy cu7. 2ni1. 8si1cr. *Rapid Prototyping Journal*, 2019.
- [105] S. Patel and M. Vlasea. Melting modes in laser powder bed fusion. *Materialia*, 9:100591, 2020.
- [106] J. A. F. Plateau. *Mémoire sur les phénomènes que présente une masse liquide libre et soustraite à l'action de la pesanteur*, volume 16. Hayez, 1843.
- [107] PrimaAdditive. Il processo powder bed fusion, 2020. <https://www.primaadditive.com/it/il-processo-powder-bed-fusion/>.
- [108] PYROIStech. Superluminiscent diode (sled) lighting principles unveiled, 2019. <https://www.pyroistech.com/sled-principles/>.
- [109] C. Qiu, C. Panwisawas, M. Ward, H. C. Basoalto, J. W. Brooks, and M. M. Attallah. On the role of melt flow into the surface structure and porosity development during selective laser melting. *Acta Materialia*, 96:72–79, 2015.
- [110] M. Quinten. *A Practical Guide to Surface Metrology*. Springer, 2019.
- [111] L. Rayleigh. On the capillary phenomena of jets. *Proc. R. Soc. London*, 29(196-199):71–97, 1879.
- [112] T. Rayna and L. Striukova. From rapid prototyping to home fabrication: How 3d printing is changing business model innovation. *Technological Forecasting and Social Change*, 102:214–224, 2016.
- [113] F. Savart. Memoire sur la constitution des veines liquids lancees par des orifices circulaires en mince paroi. *Ann. de chim.*, 53:337–386, 1833.
- [114] R. Savino, A. Cecere, and R. Di Paola. Surface tension-driven flow in wickless heat pipes with self-rewetting fluids. *International Journal of Heat and Fluid Flow*, 30(2):380–388, 2009.
- [115] SCANLAB. varioscan data sheet, 2015. <https://www.scanlab.de/en/products/z-achsen-3d-erweiterungen/varioscan>.

- [116] D. Schulze. Powders and bulk solids: Behavior, characterization, storage and flow. 2008, 2003.
- [117] D. W. Scott. On optimal and data-based histograms. *Biometrika*, 66(3):605–610, 1979.
- [118] N. Senin, A. Thompson, and R. Leach. Feature-based characterisation of signature topography in laser powder bed fusion of metals. *Measurement Science and Technology*, 29(4):045009, 2018.
- [119] W. Shi, Y. Liu, X. Shi, Y. Hou, P. Wang, and G. Song. Beam diameter dependence of performance in thick-layer and high-power selective laser melting of ti-6al-4v. *Materials*, 11(7):1237, 2018.
- [120] S. Shrestha and K. Chou. Single track scanning experiment in laser powder bed fusion process. *Procedia Manufacturing*, 26:857–864, 2018.
- [121] T. G. Spears and S. A. Gold. In-process sensing in selective laser melting (slm) additive manufacturing. *Integrating Materials and Manufacturing Innovation*, 5(1):16–40, 2016.
- [122] A. B. Spierings, M. Voegtlin, T. Bauer, and K. Wegener. Powder flowability characterisation methodology for powder-bed-based metal additive manufacturing. *Progress in Additive Manufacturing*, 1(1-2):9–20, 2016.
- [123] K. Stevenson. Slm solutions making things easier, 2018. <https://www.fabbaloo.com/blog/2018/7/27/slm-solutions-making-things-easier>.
- [124] H. A. Sturges. The choice of a class interval. *Journal of the american statistical association*, 21(153):65–66, 1926.
- [125] Y. Sun, S. Gulizia, C. Oh, C. Doblin, Y. Yang, and M. Qian. Manipulation and characterization of a novel titanium powder precursor for additive manufacturing applications. *Jom*, 67(3):564–572, 2015.
- [126] T. T. Wohler. *History of additive Manufacturing*. Wohler Report, 2014.
- [127] C. Tan, S. Li, K. Essa, P. Jamshidi, K. Zhou, W. Ma, and M. M. Attallah. Laser powder bed fusion of ti-rich tini lattice structures: Process optimisation, geometrical integrity, and phase transformations. *International Journal of Machine Tools and Manufacture*, 141:19–29, 2019.
- [128] C. Tang, K. Q. Le, and C. H. Wong. Physics of humping formation in laser powder bed fusion. *International Journal of Heat and Mass Transfer*, 149:119172, 2020.
- [129] TheEconomist. The third industrial revolution – the economist publishes a special report on 3d printing, 2011. <http://on3dprinting.com/2012/04/20/the-third-industrial-revolution-the-economist-publishes-a-special-report-on-3d-printing/>.

- [130] M. K. Thompson, G. Moroni, T. Vaneker, G. Fadel, R. I. Campbell, I. Gibson, A. Bernard, J. Schulz, P. Graf, B. Ahuja, et al. Design for additive manufacturing: Trends, opportunities, considerations, and constraints. *CIRP annals*, 65(2):737–760, 2016.
- [131] J. Thomson. Xlii. on certain curious motions observable at the surfaces of wine and other alcoholic liquors. *The London, Edinburgh, and Dublin Philosophical Magazine and Journal of Science*, 10(67):330–333, 1855.
- [132] L. Tonelli, A. Fortunato, and L. Ceschini. Cocr alloy processed by selective laser melting (slm): Effect of laser energy density on microstructure, surface morphology, and hardness. *Journal of Manufacturing Processes*, 52:106–119, 2020.
- [133] A. Townsend, N. Senin, L. Blunt, R. Leach, and J. Taylor. Surface texture metrology for metal additive manufacturing: a review. *Precision Engineering*, 46:34–47, 2016.
- [134] J. Trapp, A. M. Rubenchik, G. Guss, and M. J. Matthews. In situ absorptivity measurements of metallic powders during laser powder-bed fusion additive manufacturing. *Applied Materials Today*, 9:341–349, 2017.
- [135] A. Ünal. Production of rapidly solidified aluminium alloy powders by gas atomisation and their applications. *Powder metallurgy*, 33(1):53–64, 1990.
- [136] E. Vaglio, T. De Monte, A. Lanzutti, G. Totis, M. Sortino, and L. Fedrizzi. Single tracks data obtained by selective laser melting of ti6al4v with a small laser spot diameter. *Data in Brief*, 33:106443, 2020.
- [137] A. Vilardell, I. Yadroitsev, I. Yadroitsava, M. Albu, N. Takata, M. Kobashi, P. Krakhmalev, D. Koupryanoff, G. Kothleitner, and A. du Plessis. Manufacturing and characterization of in-situ alloyed ti6al4v (eli)-3 at.% cu by laser powder bed fusion. *Additive Manufacturing*, 36:101436, 2020.
- [138] VisionSystemsDesign. Near-infrared camera monitors selective laser melting process, 2011. <https://www.vision-systems.com/cameras-accessories/article/16744806/nearinfrared-camera-monitors-selective-laser-melting-process>.
- [139] S. Vock, B. Klöden, A. Kirchner, T. Weißgärber, and B. Kieback. Powders for powder bed fusion: a review. *Progress in Additive Manufacturing*, pages 1–15, 2019.
- [140] B. Vrancken, S. Buls, J.-P. Kruth, and J. V. Humbeeck. Preheating of selective laser melted ti6al4v: microstructure and mechanical properties. In *Proceedings of the 13th World Conference on Titanium*, pages 1269–1277. Wiley Online Library, 2016.
- [141] D. Wang, Y. Yang, Z. Yi, and X. Su. Research on the fabricating quality optimization of the overhanging surface in slm process. *The International Journal of Advanced Manufacturing Technology*, 65(9-12):1471–1484, 2013.

- [142] G. Wang, L. Huang, Z. Liu, Z. Qin, W. He, F. Liu, C. Chen, and Y. Nie. Process optimization and mechanical properties of oxide dispersion strengthened nickel-based superalloy by selective laser melting. *Materials & Design*, 188:108418, 2020.
- [143] Z. Wang and M. Liu. Dimensionless analysis on selective laser melting to predict porosity and track morphology. *Journal of Materials Processing Technology*, 273:116238, 2019.
- [144] Y. Xiang, S. Zhang, Z. Wei, J. Li, P. Wei, Z. Chen, L. Yang, and L. Jiang. Forming and defect analysis for single track scanning in selective laser melting of ti6al4v. *Applied Physics A*, 124(10):685, 2018.
- [145] W. Xiong, L. Hao, Y. Li, D. Tang, Q. Cui, Z. Feng, and C. Yan. Effect of selective laser melting parameters on morphology, microstructure, densification and mechanical properties of supersaturated silver alloy. *Materials & Design*, 170:107697, 2019.
- [146] J. Xu, X. Gu, D. Ding, Z. Pan, and K. Chen. A review of slicing methods for directed energy deposition based additive manufacturing. *Rapid Prototyping Journal*, 2018.
- [147] I. Yadroitsev, P. Krakhmalev, I. Yadroitsava, S. Johansson, and I. Smurov. Energy input effect on morphology and microstructure of selective laser melting single track from metallic powder. *Journal of Materials Processing Technology*, 213(4):606–613, 2013.
- [148] I. Yadroitsev and I. Smurov. Selective laser melting technology: from the single laser melted track stability to 3d parts of complex shape. *Physics Procedia*, 5:551–560, 2010.
- [149] I. Yadroitsev and I. Smurov. Surface morphology in selective laser melting of metal powders. *Physics Procedia*, 12:264–270, 2011.
- [150] M. Yakout, M. Elbestawi, and S. C. Veldhuis. Density and mechanical properties in selective laser melting of invar 36 and stainless steel 316l. *Journal of Materials Processing Technology*, 266:397–420, 2019.
- [151] J. Yang, J. Han, H. Yu, J. Yin, M. Gao, Z. Wang, and X. Zeng. Role of molten pool mode on formability, microstructure and mechanical properties of selective laser melted ti-6al-4v alloy. *Materials & Design*, 110:558–570, 2016.
- [152] P.-M. Yang, Y.-L. Lo, and Y.-H. Chang. Laser galvanometric scanning system for improved average power uniformity and larger scanning area. *Applied optics*, 55(19):5001–5007, 2016.
- [153] C. Y. Yap, C. K. Chua, Z. L. Dong, Z. H. Liu, D. Q. Zhang, L. E. Loh, and S. L. Sing. Review of selective laser melting: Materials and applications. *Applied physics reviews*, 2(4):041101, 2015.

- [154] M. Zavala-Arredondo, T. London, M. Allen, T. Maccio, S. Ward, D. Griffiths, A. Allison, P. Goodwin, and C. Hauser. Use of power factor and specific point energy as design parameters in laser powder-bed-fusion (l-pbf) of alsil0mg alloy. *Materials & Design*, 182:108018, 2019.
- [155] B. Zhang, Y. Li, and Q. Bai. Defect formation mechanisms in selective laser melting: a review. *Chinese Journal of Mechanical Engineering*, 30(3):515–527, 2017.
- [156] J. Zhang, D. Gu, Y. Yang, H. Zhang, H. Chen, D. Dai, and K. Lin. Influence of particle size on laser absorption and scanning track formation mechanisms of pure tungsten powder during selective laser melting. *Engineering*, 5(4):736–745, 2019.
- [157] X. Zhou, Y. Zhong, Z. Shen, and W. Liu. The surface-tension-driven benard convections and unique sub-grain cellular microstructures in 316l steel selective laser melting. *arXiv preprint arXiv:1801.01408*, 2018.
- [158] Y. Zhou, W. Li, L. Zhang, S. Zhou, X. Jia, D. Wang, and M. Yan. Selective laser melting of ti-22al-25nb intermetallic: Significant effects of hatch distance on microstructural features and mechanical properties. *Journal of Materials Processing Technology*, 276:116398, 2020.
- [159] F. Zigunov. The anti-gravity piddler: A demonstration of aliasing, 2020. <https://zigunov.com/2020/04/25/the-anti-gravity-spout-a-demonstration-of-aliasing/>.